

Investigations of radial transport in the scrape-off layer of JET-ILW

Alasdair Patrick Wynn

Doctor of Philosophy

UNIVERSITY OF YORK

PHYSICS

August 2017

Abstract

In the open magnetic field line boundary plasma (or Scrape-Off Layer (SOL)) of tokamaks, the stronger than diffusive transport of particles is to a large extent due to the convection of coherent, filamentary like structures when operating in divertor configuration. Reliable predictions of this transport are vital for the understanding of wall erosion, subsequent impurity release and the retention of fuel in future fusion devices. This thesis investigates factors which influence the quantity and properties of this cross-field transport, both from a steady state and time resolved perspective. Data have been analysed and interpreted from experiments conducted at the Joint European Torus with ITER-like wall (JET-ILW). The experiments used were designed either specifically, or for other purposes, but still provide relevant data.

The magnitude of the main chamber radial particle flux density has been investigated via two methods. Firstly, a particle balance model has been used to infer the effective convective cross-field velocity v_{eff} for Ohmically heated L-mode plasmas performed at a range of plasma current, I_p , and density. The sensitivity to assumptions together with measurement uncertainties found v_{eff} to be reliable to within a factor three. Secondly, analysis of a flush mounted Langmuir probe on the outboard poloidal limiter suggests that the particle flux density scales proportional to core density and inversely with the square of I_p for the plasmas studied, although there may also be some unidentified effect of the ion-gyroradius. The expected duration time of intermittent structures was also observed to scale with I_p^2 for a wide range of plasma density, consistent with an increase in size and/or a reduction of velocity of filaments perpendicular to the magnetic field.

The collisionality was found not to be the general control parameter of the cross-field transport. *Only* in the Deuterium fuelled, horizontal target cases was cross field transport observed to increase with increasing collisionality. When using any other method to modify the collisionality, this correlation was not observed. This independence of the cross-field transport from collisionality is a key result of this thesis and contributes to similar conclusions of other recent studies.

The plasma-neutral interaction of the fuel species in the divertor region, indicated by D_α emission, was found to more generally correlate with the main chamber cross-field transport than collisionality. Candidate plasma-neutral interactions include ionisation and or charge exchange (CX). Despite being unsure of the precise mechanism, undoubtedly plasma-neutral interaction of the fuel species in the divertor region plays a significant role in setting the main chamber cross field transport.

Contents

Abstract	3
List of Tables	9
List of Figures	11
Acknowledgments	15
Declaration	17
1 Introduction	19
1.1 Global energy demand and supply	19
1.1.1 Fossil fuels	19
1.1.2 Renewable energy	20
1.1.3 Nuclear fission	21
1.2 Nuclear Fusion	22
1.2.1 Terrestrial fusion fuel	22
1.2.2 Societal and environmental impact of nuclear fusion	23
1.3 Definition of a plasma	24
1.4 Fusion gain and ignition	25
1.4.1 The Lawson criterion and energy gain	25
1.5 Confinement methods	26
1.5.1 Inertial confinement fusion	26
1.5.2 Magnetic confinement fusion	27
1.5.3 Tokamak co-ordinate system	30
1.5.4 Current and future tokamaks	31
1.6 The scrape-off layer	32
1.6.1 Limiter configuration	32
1.6.2 Divertor configuration	33
1.6.3 High power densities on divertor target plates	33
1.7 Purpose and outline of thesis	35
2 Literature Review	37
2.1 Transport in the main chamber SOL	37
2.1.1 Introduction	37

2.1.2	Filament origins	38
2.1.3	Filament structure and concept	39
2.1.4	Statistical evidence of filaments	40
2.2	Filament equivalent circuit	43
2.3	The two region model	45
2.4	Time average profiles	47
2.5	Divertor physics	51
2.5.1	Plasma-neutral interactions	51
2.5.2	Divertor operating regimes	52
2.5.3	Divertor geometries	55
2.6	Summary	57
3	Methodology	59
3.1	SOL density profile measurement	59
3.1.1	Neutral Li beam injection	59
3.1.2	Shoulder amplitude metric	62
3.1.3	Profile mapping	62
3.2	SOL T_e profile estimation	63
3.3	Pressure gauges	63
3.4	Optical cameras	64
3.4.1	Brightness calibration	65
3.4.2	Spatial calibration	66
3.4.3	Inversion methods	69
3.4.4	Ionisation profiles	69
3.4.5	Radial D_α view-chord	71
3.5	Langmuir probes	71
3.5.1	Identifying intermittent events	71
3.6	Radial flux analysis method	74
4	Radial velocities in the SOL	77
4.1	Introduction	77
4.2	Experiments	77
4.3	Time averaged radial flux analysis	77
4.3.1	Results	77
4.3.2	Sensitivity analysis	79
4.4	Limiter probe statistical analysis	85
4.4.1	Results	85
4.5	Discussion	87
4.6	Conclusions	94
5	The role of collisionality	97
5.1	Introduction	97
5.2	Λ_{div} in horizontal target	98

5.3	Λ_{div} in vertical target	102
5.4	Λ_{div} in N seeded horizontal target	104
5.5	Density shoulder in H-mode	108
5.5.1	H-mode D ₂ ramp	108
5.5.2	H-mode N ₂ seeding ramp	111
5.6	Discussion	114
5.7	Conclusion	117
6	The influence of divertor neutrals	121
6.1	Introduction	121
6.2	Strike point sweeping	121
6.2.1	Small amplitude sweeping	121
6.2.2	Large amplitude sweeping	123
6.2.3	Strike point sweeping in H-mode	125
6.3	D _α in the presence of N	125
6.4	The role of mid-plane neutrals	127
6.5	Comparison of HT and VT	128
6.6	Discussion	130
6.7	Conclusions	132
7	Conclusions and future work	139
	Appendix 1 - High frequency Li-beam measurements	143
	Bibliography	147

List of Tables

7.1	Summary of conclusions	139
-----	----------------------------------	-----

List of Figures

1.1	(a) Population estimates to 2100 (b) Historical global emissions	20
1.2	Fusion reaction rates	23
1.3	Tokamak schematic	28
1.4	Wendelstein 7-X	30
1.5	Limited and diverted tokamak configurations	31
1.6	Divertor heat flux mitigation methods	34
2.1	Example image of filaments from MAST	38
2.2	Illustration of cross field filament structure	40
2.3	TCV SOL plasma statistics	41
2.4	PDFs from Langmuir probes from several tokamaks	42
2.5	Experimental measurement of cross field filament structure from VTF .	43
2.6	TCV intermittent events and conditional average	44
2.7	Filament circuit diagram	45
2.8	Flux tube flattening near the x-point	46
2.9	Regime diagram for the two-region model	47
2.10	Example relationship between density profile structure and the intermit- tent nature of ion saturation current.	48
2.11	Example flattening of SOL density profile with increasing density	49
2.12	SOL λ_n in AUG and JET	50
2.13	Example v_{eff} profiles taken on TCV and C-mod.	51
2.14	Plasma-neutral interaction rate coefficients of the atomic and molecular hydrogen	52
2.15	Divertor regime schematic	54
2.16	Divertor geometries	55
2.17	JET-ILW divertor configurations	57
3.1	Diagnostic locations and equilibria	60
3.2	Diagnostic locations and equilibria, close up of divertor	61
3.3	Neutral diagnostic beam principle	61
3.4	Shoulder amplitude A_s definition	62
3.5	Steeping density profile in limiter shadow	63
3.6	Optical camera views	64
3.7	KL1 brightness calibration fitting	66

3.8	(a) Spatial calibration example. (b) Example tangent pixels.	68
3.9	1D inversion geometry	70
3.10	Filament detection thresholds	72
3.11	Measured and assumed Mach profiles	75
4.1	Time traces for Horizontal target L-mode D fuelling ramps.	78
4.2	D_α radial view-chord and the integrated LFS emissivity derived from the brightness profile measured by the camera.	79
4.3	Radial flux analysis input and output profiles	80
4.5	Comparison of the neutral and plasma fluxes at the limiter radius . . .	81
4.6	Sensitivity of radial flux analysis to T_e variation	82
4.7	Sensitivity of radial flux analysis to variations in profile shifting and separatrix location uncertainty.	83
4.8	Dependence of radial flux analysis on M profile	84
4.9	(a) Dependence of J_{sat} on \bar{n}_e for a range of I_p . (b) Dependence of the signal fraction below the noise floor, f_{nf} on \bar{n}_e	84
4.10	Scaling of J_{sat} with f_{gw}/I_p for a range of I_p	86
4.11	Relative contribution of intermittent events to total J_{sat} for different thresholds.	87
4.12	Density profiles for different I_p with fixed $n_{e,lim}$	88
4.13	PDFs of J_{sat} taken over 0.5s windows spanning the time of profiles shown in figure 4.12.	88
4.14	Conditional averages and auto-correlations of J_{sat} taken over 0.5s windows spanning the time of profiles shown in figure 4.12.	89
4.15	Waiting and duration time statistics for intermittent events at fixed limiter n_e	89
4.16	Dependence of fitted τ_w and τ_d on $ B (T)$ and $ B ^2(T^2)$ for data at fixed limiter n_e	90
4.17	Dependence of fitted τ_w and τ_d on $ B ^2$ for a range of \bar{n}_e	90
4.18	v_{eff} profiles from multiple tokamaks. The radial co-ordinate has been normalised to the minor radius.	91
5.1	Horizontal target L-mode upstream and divertor profiles	98
5.2	Horizontal target L-mode SOL property time traces	99
5.3	Horizontal target L-mode: correlation between Λ_{div} and A_s in the near and far SOL	100
5.4	Radial movement of A_s with Λ_{div} , Greenwald fraction f_{gw} and \bar{n}_e	101
5.5	Vertical target L-mode D ₂ fuelling ramp pulse time traces	102
5.6	Vertical target L-mode D ₂ fuelling ramp upstream and divertor profiles	103
5.7	Vertical target L-mode: correlation between Λ_{div} and A_s in the near and far SOL	104
5.8	Vertical Target D ₂ fuelled L-mode PDFs	105
5.9	Nitrogen seeded Horizontal target L-mode pulse time traces	106

5.10	Nitrogen seeded Horizontal target L-mode upstream and divertor profiles	107
5.11	Nitrogen seeded Horizontal target L-mode shoulder amplitude, A_s , as a function of Λ_{div}	108
5.12	NII brightness as a function of N_2 seeding rate in loaded and unloaded cases	109
5.13	Filament properties in N_2 seeded horizontal target L-mode	110
5.14	Pulse time traces for horizontal target H-mode D_2 fuelling ramp.	111
5.15	Horizontal target H-mode D_2 fuelling ramp upstream and divertor profiles	112
5.16	Horizontal target H-mode D_2 fuelling ramp ELM removal and thresholds example	113
5.17	Horizontal target H-mode D_2 fuelling ramp PDFs	113
5.18	Horizontal target H-mode D_2 fuelling ramp τ_w and τ_d for different intermittent thresholds.	114
5.19	Horizontal target H-mode D_2 fuelling ramp conditional averages for different intermittent thresholds.	115
5.20	Horizontal target H-mode N_2 seeding ramp pulse time traces	116
5.21	Horizontal target H-mode N_2 seeding ramp upstream and divertor profiles	117
5.22	Horizontal target H-mode N_2 seeding ramp limiter probe J_{sat} and total divertor flux.	118
5.23	Horizontal target H-mode N_2 seeding ramp limiter probe PDFs	118
5.24	Horizontal target H-mode N_2 seeding ramp waiting time and duration time distributions	119
5.25	Horizontal target H-mode N_2 seeding ramp conditional averages and auto-correlations	119
6.1	Small amplitude strike point sweeping pulse time traces.	122
6.2	Small amplitude strike point sweeping correlations.	123
6.3	Large amplitude strike point sweeping extrema.	124
6.4	Large amplitude strike point sweeping time traces	125
6.5	Normalised density profiles at the large amplitude strike point sweeping extrema.	126
6.6	Large amplitude strike point sweeping correlations	127
6.7	H-mode strike point sweeping time traces	128
6.8	Effect of N_2 seeding on divertor D_α measured by vertical view-chords.	129
6.9	Effect of N_2 seeding on divertor D_α and NII 2D emission maps.	133
6.10	A_s dependence on $I - D_\alpha$ in cases with and without the presence of N 'loaded' vessel surfaces.	134
6.11	Comparison of horizontal and vertical target n_e and S_{ion} profiles and the functional dependence of mid-plane pressure on \bar{n}_e .	134
6.12	Comparison of 2D D_α emission maps of horizontal and vertical target	135
6.13	Comparison of 2D D_γ emission maps of horizontal and vertical target	136

6.14	Time traces of 2D D_α emission profiles integrated in flux tubes for horizontal and vertical target	137
1	Appendix: Fourier spectra of the high frequency Li-beam diagnostic . .	143
2	Appendix: Comparison of PDFs from the OLP and fast Li-beam diagnostic	144
3	Appendix: Correlation of adjacent high frequency Li-beam channels . .	144
4	Appendix: Calculation of SOL velocity from cross-correlations	145

Acknowledgements

Thanks to my wife Hannah, who in her opinion should also be an author on this thesis. As usual, she is probably right. Thanks also to my children, Florence and Evelyn. The continuous presence of the thesis in one's mind is a stress acknowledged by anyone who has undertaken a PhD. Florence and Evelyn have provided an all consuming distraction that has been of great help in keeping my feet on the ground (although a little more sleep may have made things easier).

Hannah and I have also benefited greatly from our wider support network, most of all our parents. They have been fantastically supportive during countless early mornings, often at short notice, which has allowed Hannah and I to pursue our careers, as well as have a family. Thank you to Geoff, Jules, Ed and Gill.

My long suffering supervisor, Bruce Lipschultz, has invested a great deal of his time in my thesis. Many others have contributed ideas and advice, or gone out of their way to support me including Guy Matthews, Fulvio Militello, Nick Walkden, Istvan Cziegler, James Harrison, Aaro Jaervinen, Balazs Tal, Mathias Brix, Alexander Huber, Valentina Huber, Uron Kruzei, Sven Wiesen. Thank you to all.

Declaration

I declare that the work presented in this thesis, except where it is otherwise stated, is based on my own research and has not been submitted previously for a degree in this or any other university.

- Parts of section 5.2, 5.3, 5.4, 5.5, 5.6, 6.2, 6.3, 6.4 and 6.5 have been published in *Nuclear Fusion* **58**(5):056001 and has been invited to Plasma Surface Interaction in controlled Fusion Devices Conference (2018).
- Section 4.1 - 4.3 were presented as a poster at the Plasma Surface Interaction in controlled Fusion Devices Conference (2016).
- Parts of section 5.2, 5.3, 5.4 and 6.4 were presented orally at the European Physical Society Conference on Plasma Physics (2016).
- Parts of section 5.2, 5.3, 5.4, 5.5, 6.2 and 6.3 were presented orally at the International Tokamak Physics Activity, Scrape-off Layer and Divertor Topical Group (2017).
- 2D tomographical inversions in section 6.3 and 6.5 were performed by Janina Schmitz using the `k111` code developed by Dr. James Harrison.

Chapter 1

Introduction

1.1 Global energy demand and supply

The supply of energy in various forms, principally of heat and electricity, is essential to modern civilisation. In the UK for example, the average continuous consumption of electrical power is around 600W per capita. The world average is around 400W and has roughly doubled over the last 40 years, following a linear progression [1]. However, in many developed nations, average power consumption is either stagnant or falling. For example, power consumption levels in the UK have been falling since 2005. However, developed nations represent only a fraction of the world and most nations are developing rapidly. Concurrently, the world population is increasing. Different projections of the world population to 2100 by the UN [2] are shown in figure 1.1 (a). The two factors of increasing population and growing energy demand per capita are driving the increase in total global energy consumption.

1.1.1 Fossil fuels

Today, fossil fuels still dominate global energy supply, providing over 80%. Alarmingly, this fraction is stagnant or even slightly growing over time [1]. This is driven by developing nations choosing fossil fuels over alternatives. Total energy production from fossil fuels is predicted to approximately double from 2010 to 2040 [3]. During that period, more carbon will be burnt than in the previous 300 years combined. This dominance coupled with predicted population growth will likely result in global CO_2 equivalent emissions increasing strongly, as they have been for the last 40 years, shown in figure 1.1 (b) [1].

Such strong increases in CO_2 emissions result in the increase of globally averaged surface temperatures through radiative forcing, commonly referred to as the greenhouse gas effect. The complexity and chaotic nature of the global climate system make predicting the effect of this forcing difficult in the long term [4]. Nevertheless, to a high degree of certainty, anthropogenic emission of greenhouse gases is having a strong impact on the climate. The effects are diverse and increasingly visible [4]. For example, the global mean sea level rose by 20mm from 2005-2012, not only due to the increase

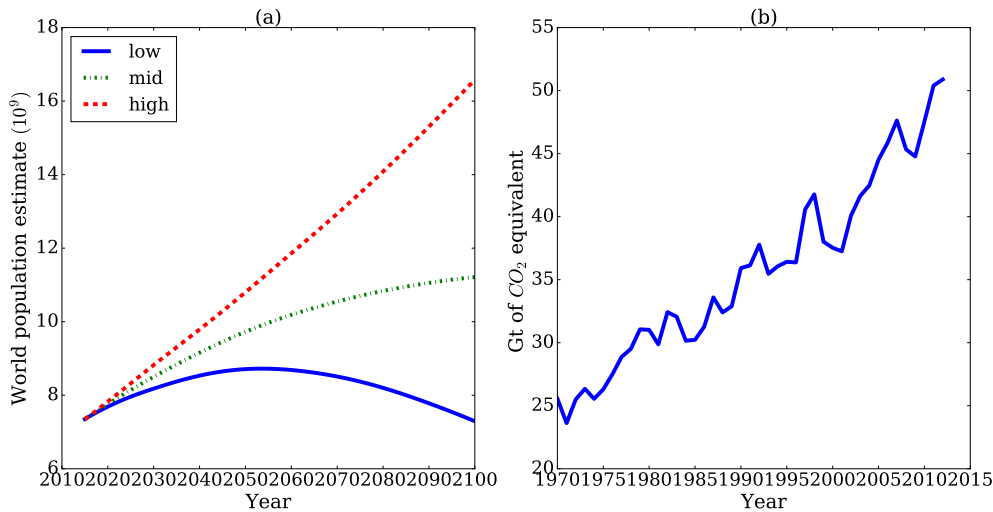


Figure 1.1: (a) Different population scenarios for the 21st century. Significant growth is likely to occur. (b) Total green house gas emission in terms of CO₂ equivalent units.

in water mass but also due to thermal expansion of the oceans [5].

Further, fossil fuels are a finite resource. Projections of fossil fuel reserves suggest coal will be the only fossil fuel available after the mid 2040s [6], lasting until ≈ 2110 . However, there are significant uncertainties in the modelling [3]. Reserves may be extended by factors including the advancement of extraction technology and increasing amount of commercially available reserves as global prices increase.

In any case, the rapid transition away from a fossil fuel dominated economy is undoubtedly necessary for the long term stability of the climate, protection of the ecosystem and the long term improvement of average global living standards.

1.1.2 Renewable energy

Renewable energy technologies have received substantial political and financial backing in attempting to realise this transition. Hydropower, particularly from dams, has proved enormously successful in terms of cost and reliability relative to fossil fuels but is not as scalable due to the limited number of feasible locations. Wind and solar energy are subsidised by \$100bn a year globally, but provide only around 7% of the world's electricity [7]. Further, due to the intermittent nature of wind and solar, each Watt of installed renewable capacity must be matched by at least another Watt of back-up capacity, usually from gas which has the required flexibility [8]. This unavoidably increases prices which developed nations may be able to afford, but is a much less attractive option for developing countries whose economies and populations will grow the most in coming decades and do not want to pay for more infrastructure than necessary. Increased energy storage capacity improves the viability of renewable sources providing the majority of global supply, but again this is an additional cost and no scalable technology has been implemented cost effectively yet. Undoubtedly, enough renewable power exists. Whether it can be delivered in a way which is as scalable, reliable and as cheap as fossil fuels is currently unproven.

A less publicly prominent form of renewable energy is the use of wood-chippings. However, a recent report [9] questions whether wood-chippings are a truly renewable energy source. In the report the author suggests that burning wood chippings may indeed be worse than coal in terms of carbon emissions per unit of energy delivered, chiefly due to the use of virgin forests as an wood source rather than purely waste from industrial processes. Newly planted trees take many years to mature and trap the carbon that was once stored. Moreover, forests that are mature are not carbon stable and are in fact very effective carbon sinks [10] due to the rising CO₂ in the atmosphere which is the raw material of plant matter.

Reports such as [8] and [9] highlight the inefficacy of political efforts to prevent climate change to date and suggest the solution is routed in technology and not in policy.

1.1.3 Nuclear fission

One energy source that has suffered the negative effect of politics is the exploitation nuclear fission. With the exception of hydropower, it is the only technology which provides a reliable base load supply of electricity that is carbon free, however the cost is substantially higher. Hinckley Point C, a proposed reactor in the UK will produce electricity that is roughly twice as expensive as fossil fuels [11] with a strike price of ~90 as of 2013. Perhaps the most obvious cause of the increase in price of nuclear power over time are the infamous accidents in the 20th century such as Three Mile Island and Chernobyl. However, a study of the historical costs of nuclear power generation indicates that the other factors, such as nuclear regulatory cultures, play a stronger role [12].

Despite the average increase of nuclear power over time in most countries, safe, cheap and scalable electricity from fission has been demonstrated on a national scale in France. Further, in South Korea the costs of construction have steadily reduced [12] over time. However, in its current form, nuclear fission could not replace fossil fuels globally due to the inefficient use of Uranium reserves by typical 'once through' fuel rod usage. The International Atomic Energy Agency (IAEA) estimate current reserves of 150 years [13]. Current fission technology is a product of the 20th century nuclear arms race. Nuclear fission may be made scalable if more efficient use of nuclear fuels are implemented and this is indeed the object of the global nuclear renaissance which is gathering momentum. In the UK for example, government incentives have initialised the development of small modular reactors and advanced fission technology [14]. China is also investing heavily in this area [15].

Such advanced fission technology undoubtedly has a place in the near future of global energy supply, but the desired paradigm shift in fission technology is far from being realised. Public and political opposition may also stagnate change.

1.2 Nuclear Fusion

A key option that has not yet been realised in global energy supply is nuclear fusion. The fusion community has been effective in separating itself from nuclear fission in the minds of policy makers. Consequently, a thriving global research community exists to advance the physics and technological understanding required to make fusion power a reality. The basics of nuclear fusion are included here for completeness.

Nuclear fusion is the process by which lighter nuclei are combined to form heavier nuclei. The binding energy per nucleon increases with increasing mass number up to Iron. Therefore, fusing nuclei lighter than Iron results in a net release of energy which may be utilized for the purposes of electricity production. Eddington first postulated nuclear fusion as the energy source of stars [16]. This was later detailed by Bethe in 1939 [17].

In order for two nuclei to fuse, they must be brought sufficiently close together such that the attractive strong nuclear force may act. In order to achieve this however, the repulsive Coulomb force between the nuclei must be overcome by raising their kinetic energy typically to 10keV or more [18].

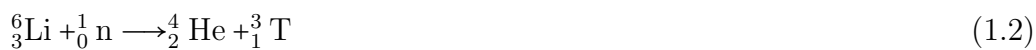
1.2.1 Terrestrial fusion fuel

Terrestrial attainment of fusion power is concerned with the fusion of two isotopes of Hydrogen. These are Deuterium (D) and Tritium (T) which have one and two additional neutrons respectively. The combination of these isotopes offers the largest fusion reaction rate by an order of magnitude or more at temperatures below 60-70keV as shown in figure 1.2.

The DT fusion reaction is given by



Regardless of the fusion concept used in a reactor, the production of T, known as breeding, will be an essential technology of a fusion reactor. Unlike D which is stable and abundantly available in water, T has a half-life of 12.5 years and therefore no naturally extractable deposits exist. Consequently, T must be bred from Li which is available in salt flats or the ocean. The amount of Li in the oceans is finite, but for the purposes of producing T for fusion, the quantity is practically inexhaustible [20]. Using fusion neutrons to bombard Li nuclei causes them to fission and produce T. Production of T takes place for both naturally occurring isotopes of Li via the reactions [18]



Thermal energy neutrons are sufficient to fission ${}^6_3\text{Li}$, but ${}^7_3\text{Li}$ fusion require neutrons with an energy of 2.47MeV or more. Further, ${}^6_3\text{Li}$ and ${}^7_3\text{Li}$ are present in nature in fractions of 7.5% and 92.5% respectively. This may mean that breeding technology of

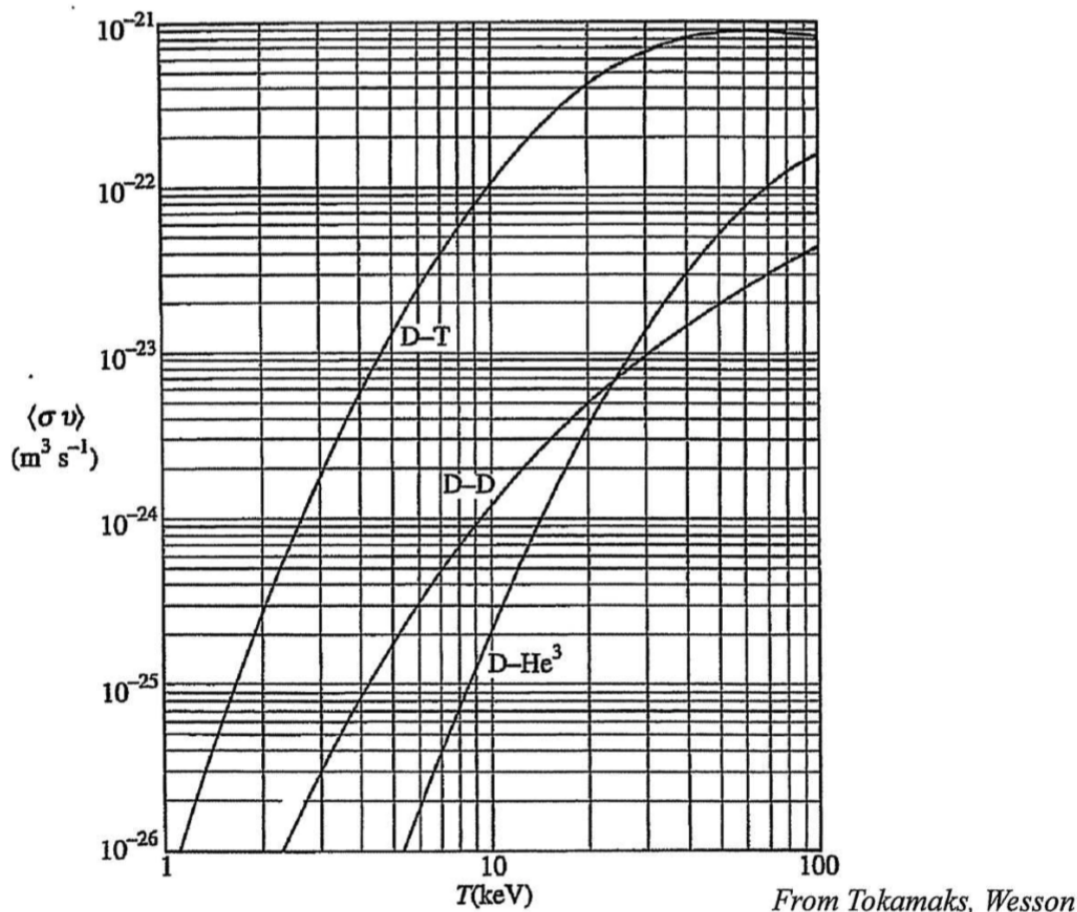


Figure 1.2: Fusion reaction rate coefficient for different reactant combinations as a function of temperature [19]. The DT reaction clearly offers the best choice for terrestrial fusion reactors.

a fusion reactor must use ${}^6_3\text{Li}$ enriched material, potentially raising the costs. However the ${}^7_3\text{Li}$ reaction produces an extra neutron which aids the production of T.

The DT fusion reaction produces only a single neutron. Therefore to achieve a net increase in usable T reserves, which is required to account for finite T escape from the handling system and to produce fuel for future fusion reactors, a neutron multiplier must be used. Suitable materials include Pb and Be.

1.2.2 Societal and environmental impact of nuclear fusion

Utilising nuclear fusion as an energy source offers clear advantages over existing technology. Firstly, unlike fission, there is no remnant fusion product which presents a radiation risk. In fact the He produced from DT fusion reaction is useful. Due to the high neutron flux, there will undoubtedly be irradiated material which will require decommissioning, such as the reactor vessel. However, materials may be chosen for the reactor which present less nuclear liability and isotopic enrichment may also be used to minimise transmutation effects [21]. Further as mentioned in 1.2.1, the fuel for fusion is practically inexhaustible and accessible to everyone. Clearly this is advantageous over fossil fuels and once through nuclear fission. The universal accessibility of the fuel will also not enhance geopolitical tensions which have dogged fossil fuels. Further, fusion

will not suffer from the intermittency of renewable energy and would instead provide reliable base load power.

Due to the projected time scales of fusion power delivery and the onset of climate change, it is highly unlikely that fusion can play an active role in the short term prevention of climate change. If fossil fuels continue to be used in the same manner, it is likely in a few decades time enough carbon will be present in the climate system to cause 2°C of warming above pre-industrial temperatures, which is considered catastrophic climate change [4]. Fusion is first expected to deliver energy in the second half of the century, and will likely start with a single reactor. Nevertheless, the long term prevention of climate change is still essential and fusion can play an active role in this continuing effort.

1.3 Definition of a plasma

As mentioned in section 1.2, fusion fuel must be raised to high temperatures before a useful number of fusion reactions begin to occur. At such temperatures, and assuming a thermal distribution, almost all electrons are free from nuclei and the matter exists in a state known as a plasma.

In order to be considered a plasma, the collection of charged particles must satisfy three conditions which are

$$\lambda_D \ll L, \tag{1.4}$$

$$\Gamma_D \gg 1, \tag{1.5}$$

$$\omega\tau_c \gg 1. \tag{1.6}$$

The Debye length is defined by $\lambda_D = \sqrt{\frac{\epsilon_0 kT}{e^2 n}}$ where ϵ_0 is the classical vacuum permittivity, k is the Boltzmann constant, T is the temperature in K , e is the electron charge and n is the number density. Physically, λ_D is the characteristic fall off length of the potential of a free charge in a plasma. In other words, it is the length scale over which the plasma shields the electric field of a free charge. Equation 1.4 states that the total length scale of the system, L , must be sufficiently large that electric fields of individual particles are completely screened out.

The plasma parameter, is defined by $\Lambda_D = 4\pi n\lambda_D^3$ and is the number of particles within the Debye sphere. The third condition given by equation 1.6, states that plasma interactions, taking place at frequency ω must exceed the rate of plasma-neutral interactions, occurring on a time scale τ_c . Physically, this condition implies that the motion of the particles is governed by their charged nature and not by hydrodynamic forces. The electric forces between electrons and atomic nuclei serve to maintain the quasi neutrality of the plasma.

1.4 Fusion gain and ignition

The objective of performing nuclear fusion experiments is ultimately to produce more energy than is required to tailor the plasma into the correct conditions and operate the other reactor systems, taking into account conversion efficiencies. This may be simply expressed as $E_{out}^* > E_{in}^*$ where E_{out}^* is the *recoverable* energy from a fusion reactor and E_{in}^* is the energy supplied to sustain the fusion reaction. Relating this condition to the properties of the plasmas yields useful information on the conditions fusion reactors are likely to have to achieve net fusion energy.

1.4.1 The Lawson criterion and energy gain

A commonly used condition to estimate the required reactor conditions for fusion gain is the Lawson criterion [22]. Energy inputs and outputs are balanced as follows, using the derivation from [18]. The recoverable energy from a fusion reactor may be expressed in different forms of energy, E , as

$$E_{out}^* = \eta_{fu} E_{fu}^* + \eta_{rad} E_{rad}^* + \eta_{th} E_{th}^* \quad (1.7)$$

where η refers to relative efficiencies of recovering energy from fusion, fu , radiation, rad and thermal energy, th . Energy supplied to the plasma may be expressed as

$$\eta_{in} E_{in}^* = E_{rad}^* + E_{th}^* \quad (1.8)$$

where η_{in} is the fraction of input energy which actually couples to the plasma. One may make a number of assumptions in order to combine equations 1.7 and 1.8. Firstly, an average efficiency of those expressed in equation 1.7 may be taken as η_{out} . One may also assume a global energy confinement time, τ_e , and that the radiation is dominated by bremsstrahlung so that $P_{rad} \approx P_{br}$, where P is the power. One may then express equations 1.7 and 1.8 as a condition for fusion gain as

$$\eta_{in} \eta_{out} (\tau_E P_{fu} + \tau_E P_{br} + 3NT) > \tau_E P_{br} + 3NT \quad (1.9)$$

where N is the temperature and T is the density. The total thermal energy is made up of contribution from both ions and electrons such that $E_{th} = \frac{3}{2}(N_i T_i + N_e T_e) = 3NT$, assuming equivalent ion and electron temperatures and densities. Introducing the temperature and density dependence of P_{fu} and P_{br} and rearranging for $N\tau_E$ and yields

$$N\tau_e > \frac{12(1 - \eta_i \eta_{out})T}{\eta_i \eta_{out} < \sigma v >_{DT} (T) Q_{DT} - (1 - \eta_i \eta_{out}) A_{br} \sqrt{T}} \quad (1.10)$$

where DT fusion has been assumed with $< \sigma v >_{DT} (T)$ being the DT fusion reaction rate which has a strong temperature dependence as shown in figure 1.2. Q_{ab} is the energy per fusion reaction, A_{br} is a constant associated with the bremsstrahlung radiation.

Inequality 1.10 has the assumption of homogeneity through out the plasma volume which will clearly not hold in an actual fusion reactor. There is a strong dependence on T . For DT fusion the minimum of the RHS of 1.10, as a function of ion temperature, occurs at approximately 15keV with $N\tau_E \sim 10^{20}$. Further, 1.10 is for net fusion gain in a scientific sense. From a practical perspective, the minimum Lawson limit may have to be exceeded by an order of magnitude or more.

Going further than simply fusion gain, the ultimate goal of fusion research is to achieve what is known as ignition. This is where the fusion reactions within the plasma are sufficient to sustain both the temperature of the plasma, known as self-heating, and also to power all the reactor systems, with no power being used to directly heat the plasma. In other words the plasma is self sustaining. A more modern, but similar, figure of merit than the Lawson criterion for fusion reactors is the fusion triple product, $NT\tau_E$. The conditions required to achieve ignition are usually expressed as [23]

$$NT\tau_E > 5 \times 10^{21} \text{m}^{-3} \text{ s keV} \quad (1.11)$$

which provides an intuitive threshold; the plasma must be sufficiently hot, dense and contained for enough time in order to ignite.

Clearly there is a large range in reactor performance between achieving power balance and an ignited plasma. This performance is quantified by the Q factor given by

$$Q = \frac{E_{fu}^*}{\eta_{in} E_{in}^*}. \quad (1.12)$$

Fusion experiments today have $Q < 1$. Scientific break-even is where $Q = 1$ and ignition is $Q = \infty$. Typically, $Q = 10$ is stated as the realistic performance requirement in order to make fusion commercially viable and is often referred to as *engineering* break-even.

1.5 Confinement methods

Confining the plasma in order to achieve the required fusion performance in a controlled and repeatable manner has thus proved challenging. Multiple strategies have been investigated since the inception of controlled fusion research in the mid 20th century.

Currently there are two confinement methods which are the most prevalent in the fusion research community. These are inertial confinement fusion (ICF) and magnetic confinement fusion (MCF). The way in which ICF and MCF attempt to satisfy inequality 1.11 are starkly contrasted. This thesis is concerned with MCF, but for completeness, ICF is briefly described below.

1.5.1 Inertial confinement fusion

Inertial confinement fusion will attempt to achieve ignition via the compression of a \sim mm sized capsule using lasers. The capsule is comprised of different layers of DT ice

and gas along with an outer layer which, by design, ablates under the intensity of the lasers. The ablation causes an inward force which compresses the DT ice and gas. The concept is to create a central hotspot where DT fusion initiates and results in a self sustaining wave of fusion reactions propagating into the rest of the capsule. In terms of the fusion triple product, ICF balances very short $\tau_E \sim 10^{-9}$ s with very high densities on the order 10^{32}m^{-3} [18]. Temperatures are of the order 10keV.

The National Ignition Facility is the largest and most powerful existing ICF experiment [24], where 192 laser beams accurately deliver 2MJ of energy onto the target. Recently on NIF, experiments recorded more energy emitted than was absorbed by the fuel [25]. Although progress is being made, overcoming the asymmetry of the implosion, resulting from hydrodynamic effects such as the Rayleigh-Taylor instability, is still the primary concern of ICF research.

There are also significant technical challenges. For example, the high rate of capsule implosions, on the order of Hz, and large increases in the required heating efficiency.

1.5.2 Magnetic confinement fusion

Magnetic confinement fusion is perhaps the branch of fusion research that is closest to an energy producing reactor. Modern magnetic confinement devices are toroidal and there are main two types; tokamaks and stellarators.

1.5.2.1 Tokamaks

Magnetic confinement fusion devices exploit the gyromotion of charged particles around magnetic field lines to restrict their expansion. A single charged particle in a magnetic field and under no other forces will gyrate perpendicular to the direction of the magnetic field with a radius $r_L = mv_{\perp}/q|B|$ known as the gyro-radius or Larmor radius. Here m and q are the particles mass and charge, B is the magnetic field strength and v_{\perp} is the velocity of the particle perpendicular to the magnetic field, referred to as the perpendicular direction. The particle is free to move along the field. The initial exploitation of this effect was realised in the form of a magnetic mirror where two current carrying coils face one another [18]. This configuration offered poor confinement parallel to the magnetic field. The obvious next step is to link several magnetic mirrors [27] such that parallel losses from each magnetic mirror flowed into the next, known as a bumpy torus. The magnetic field of the bumpy torus is curved and stronger in the centre of the device. Consequently the curvature and ∇B particle drifts, which are charge dependent, set up an electric field. The electric field results in an $E \times B$ drift directed radially away from the axis of the machine, which is not charge dependent, thus resulting in a loss of the plasma confinement. The addition of a poloidal magnetic field causes magnetic field lines to be helically shaped and introduces a rotational transform which acts to cancel the net effect of the curvature and ∇B drifts, thus preventing the $E \times B$ and the loss of the plasma. The combination of the toroidal field

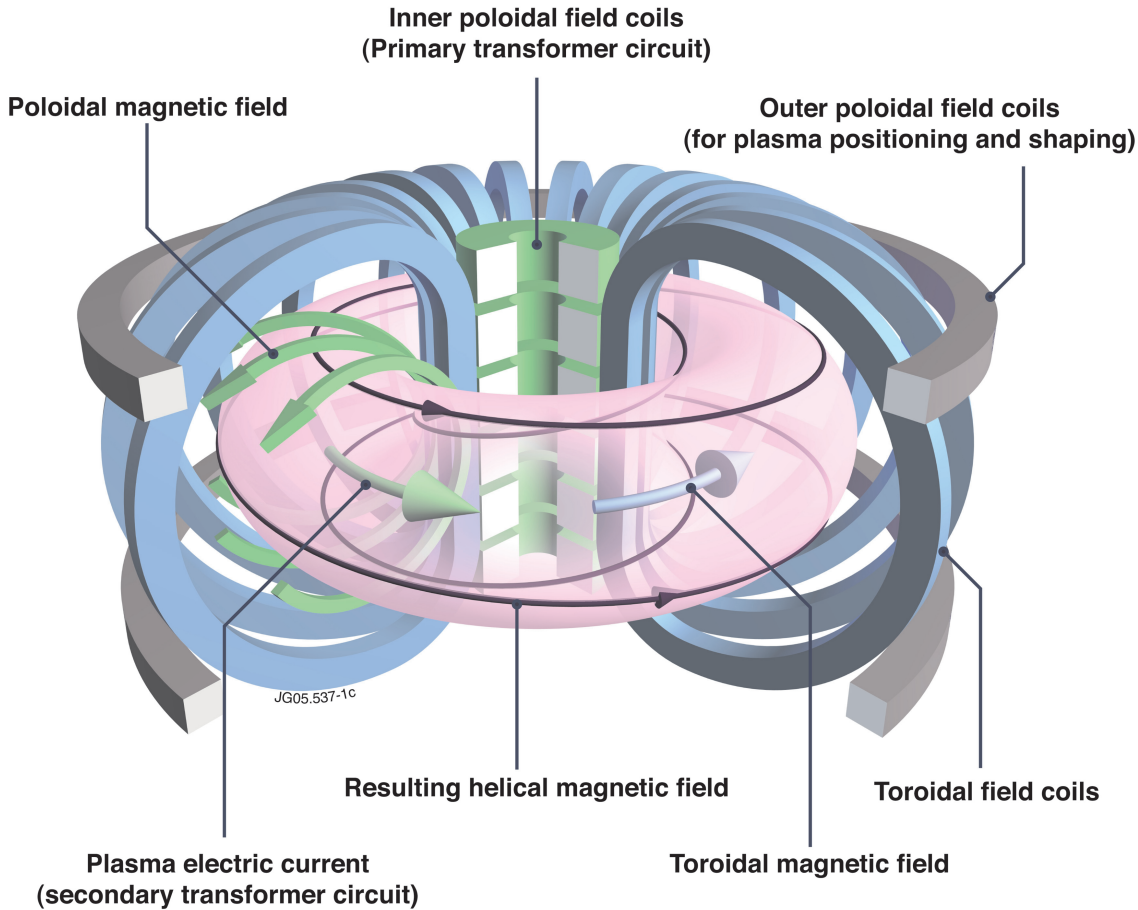


Figure 1.3: Modern tokamak schematic. Toroidal and inner and outer poloidal field coils are shown. Together with the plasma current, they produce the helical magnetic field [26]

coils together with the poloidal field *is* the tokamak concept. The poloidal magnetic field in a tokamak is usually produced by inducing a toroidal current in the plasma via transformer action using a solenoid in the centre of the device. A schematic of the tokamak concept is shown in figure 1.3 [26].

The outer poloidal magnetic field coils in figure 1.3 are used to shape the plasma and restrict it from expanding. The thermal pressure from the plasma is balanced by the pressure of the magnetic field. The magnetic field at the inner edge of the plasma is stronger than the outside and hence there is a pressure imbalance which forces the entire plasma radially outwards. The outer poloidal magnetic field coils produce a vertical field and together with the plasma current result in a balancing radially inward force. Tailoring the shape of the plasma with the outer poloidal field coils has also been shown to impact the fusion performance and is why most modern tokamak experiments are 'D' shaped in their cross-section rather than circular.

The volume within which the plasma is generated and confined by the magnetic field is separated from the atmosphere by a vacuum vessel which is typically located inside the toroidal field coils. High vacuum's are required as tokamak plasma densities are 4-5 orders of magnitude lower than the atmosphere.

The plasma is also heated using two mechanisms in addition to its own Ohmic resistance in order to improve fusion performance. External heating is required as the resistivity of a plasma is proportional to $T^{-3/2}$ [18] and therefore increases in I_p

offer diminishing amounts of power deposited in the plasma. The first of the additional methods is the application of electromagnetic waves. Specific wavelengths of EM radiation are chosen to resonate with the oscillation frequencies of the plasma, for example, the gyration frequency of the ions and electrons. Resonances in the plasma also arise through its multi-species nature, which are then exploited to couple incident energy and heat the plasma [19]. Deliberate introduction of non-fuel isotopes to the plasma can be used to control these resonances. The second external heating method is the injection of high-energy neutrals, usually of the fuel species, which slow down in plasma and thus deposit energy. The high energy incident neutrals, not affected by the magnetic field, couple to the plasma via charge-exchange (CX) and ionisation.

The α particles produced from fusion reactions inside the plasma are also a heating mechanism. In existing tokamaks where $Q \ll 1$, α particle heating is negligible. In progressing toward a fusion reactor an increasing, and eventually dominant, fraction of the heating will originate from α particles, with ignition ($Q = \infty$) occurring when the alpha particles provide 100% of the heating required to sustain the plasma temperature.

Perhaps the most salient achievement in tokamak research was the discovery that above a certain input power threshold, the plasma spontaneously transitions into a high confinement mode, commonly referred to as the *H-mode* [28]. The mode below this power threshold is correspondingly called the Low confinement mode or *L-mode*. The H-mode is so called because of the factor ~ 2 increase in τ_E as evidenced by strong enhancements of the core temperature and density. These increases are the result of the formation of a region with enhanced gradients, of both temperature and density, at the edge of the confined region. The width of this region is dependent on machine size, but is typically on the order \sim cm and is known as the edge transport barrier (ETB) or *pedestal*. In the pedestal, the presence of strong flows acts to suppress the turbulent transport of energy perpendicular to the magnetic field. However, tokamak plasmas in H-mode regime suffer from the effect of edge-localised modes (ELMs), which are driven by the strong gradients. An ELM results in the ejection of high energy plasma toward material surfaces which may cause damage there. Significant progress has been made in understanding the cause of ELMs [29] [30]. Consequently, it has been possible to mitigate their effects through mechanisms such as the application of additional magnetic fields [31]. An H-mode where the ELMs are somehow mitigated provides the current most reactor relevant regime. However, the discovery and optimisation of regimes different to the H-mode is an active area of research [32][33].

Regardless of the regime operated under, substantial interaction of the plasma and reactor surfaces will occur. Therefore, the material that components which face the plasma (PFCs) are made from is critical to the fusion performance. PFC materials must have high melting temperatures, be ideally of low atomic number and possess a resistance to erosion by the plasma. Historically, carbon was chosen not least because it sublimates rather than melts under intense power densities. However, the disadvantage of C is the formation of hydrocarbons which have the potential to trap scarce resources

of T by co-depositing with eroded C present in the machine. For this reason, PFCs in future MCF devices are likely to be metals such and W. Despite its high Z , W is advantageous through its high melting point and resistance to sputtering.

1.5.2.2 Stellarators

Stellarators generate a rotational transform without a toroidal plasma current. The world's most advanced stellarator, Wendelstein 7-X [34] achieves a rotational transform by using a set of twisting field coils, illustrated in figure 1.4 [35]. The complex nature of the coils is a consequence of the computational optimisation used to design them. The demanding nature of designing and manufacturing stellarators has resulted in the construction of fewer devices compared to tokamaks. Arguably, the physics understanding of stellarators is behind tokamaks and is why future fusion relevant devices are currently intended to be tokamaks. However, the lack of toroidal current in a stellarator removes the risk of potentially damaging disruptions [18]. For this reason, in the long term fusion reactors may potentially be more similar to current stellarators than tokamaks.

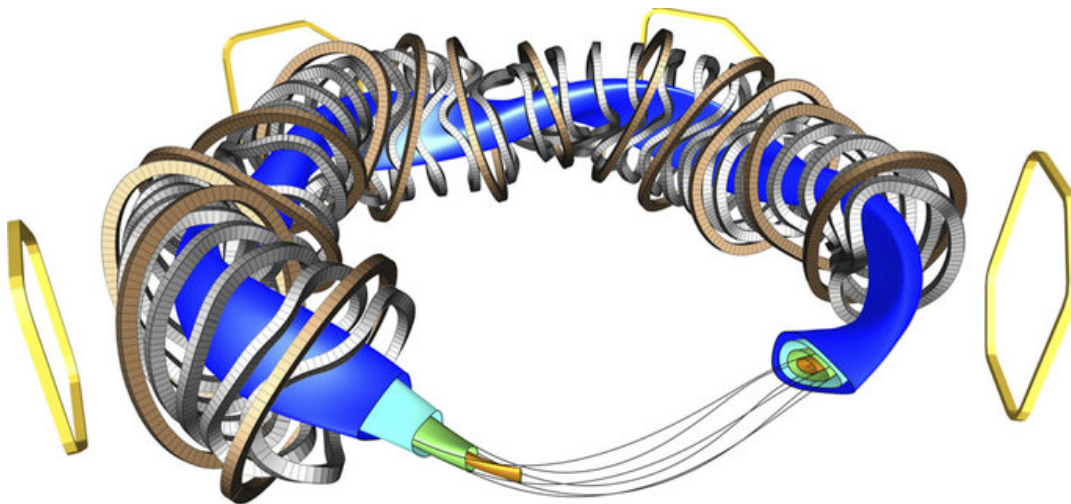


Figure 1.4: Different types of field coil used to create the magnetic topology of Wendelstein 7-X. Non-planar coils (grey) are complemented by planar correction coils (brown) and external trim coils (yellow). Nested magnetic surfaces produced by the coils are shown [35]

1.5.3 Tokamak co-ordinate system

The definition of the tokamak co-ordinate system used throughout this thesis is illustrated in figure 1.5 (a) and (b). The major radius, R , extends from the centre of rotation of the tokamak. The minor radius coordinate, r , together with the poloidal angle θ define locations in the poloidal plane. The toroidal direction, ϕ , is the same as

the azimuthal direction in cylindrical polar coordinates. Poincaré plots of the magnetic field in the poloidal plan are known as surfaces of constant poloidal flux. Denoted ψ , and provide a similar coordinate to r . It is common to normalise the flux surface coordinate to 1 at the separatrix, with $\psi > 1$ being in the SOL. This definition is used throughout this thesis.

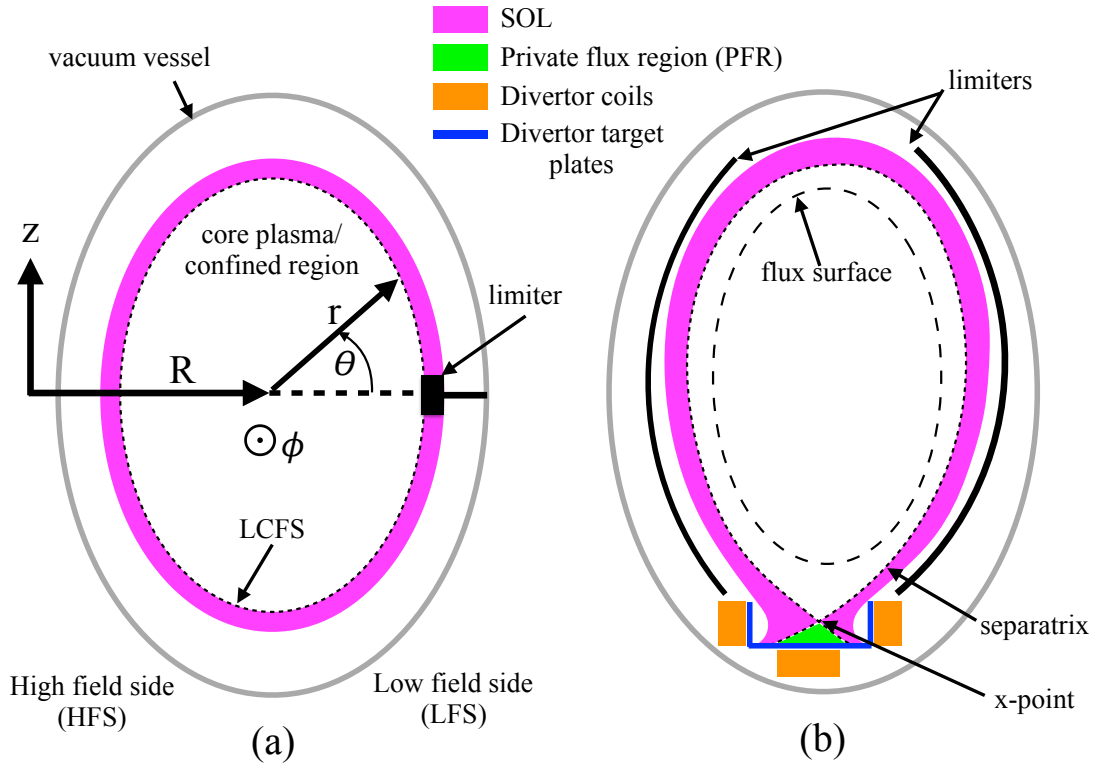


Figure 1.5: (a) Limited configuration where the limiter controls the extent of the plasma. Definitions of the tokamak coordinates are also shown. (b) Divertor magnetic geometry. The core plasma is not in direct contact with any material surface.

1.5.4 Current and future tokamaks

The eurofusion roadmap frames the path to fusion energy on a series of key devices [36]. Currently these devices are tokamaks. They are briefly reviewed in this section.

The joint European Torus (JET) is the world's largest and most powerful existing tokamak, with a plasma volume of 100m^3 and maximum heating power $\sim 30\text{MW}$ [37]. Peak I_p durations are typically 10s. JET holds the world record for fusion performance, achieving $Q \approx 0.7$ momentarily, with a corresponding fusion power of 16MW [38]. JET's main purpose is to enhance the physics understanding of future large tokamaks, specifically ITER, the successor to JET. The world record fusion results from JET were achieved with C PFCs. Due to the unacceptably high retention of T that would occur in a reactor with C PFCs, ITER was originally planned to have C PFC only for those parts that would experience the highest power densities [39]. However, the decision was made to remove C from the divertor altogether [40] and will now instead be made entirely from Be and W. Prior to this decision, JET was upgraded to have W

and Be PFCs, which now mirror the ITER design choice. JET therefore provides the most ITER relevant conditions for plasma and materials research.

The goal of ITER is to achieve $Q = 10$ for 400s, generating 500MW of fusion power [41]. ITER is twice the size of JET in each linear dimension and will have a plasma volume of 840m³. Although the goal is to achieve fusion gain that is of commercial relevance, ITER will not produce electricity and is still purely an experimental device. In addition to plasma physics experiments, ITER also intends to demonstrate the key reactor relevant technologies, such as long pulse duration super-conducting magnets, tritium breeding blankets and remote handling in an irradiated environment. ITER is currently under construction in Cadarache and is due deliver its first plasma in the mid 2020's, with DT operation beginning possibly a decade later.

The realisation of the next stage of fusion reactors will rest heavily on the success of ITER. The successor to ITER is known as DEMO. It is currently not known what form DEMO will take and whether it will depart significantly from the ITER design. Progressing with DEMO is challenging given current uncertainties.

For ITER, and for whichever design of DEMO is chosen, there will inevitably be significant interaction between the plasma and the PFCs. Understanding the physics governing the plasma in the boundary layer between the core plasma and the PFCs is therefore critical to the future of fusion. In the next section, the basic concepts of this boundary layer in a tokamak, called the scrape-off layer (SOL) are introduced.

1.6 The scrape-off layer

Despite the effective confinement of the helical magnetic field in a tokamak, the plasma will still expand to fill the vacuum vessel unless it is in some way restricted. There are two methods to used to restrict the extent of the plasma, illustrated in figure 1.5 where (a) shows the use of a limiter and (b) shows the divertor plasma concept.

1.6.1 Limiter configuration

A limiter is a piece of material inserted into the tokamak which the plasma and field lines come into contact with. The size of the plasma is restricted by the dominance of the parallel transport, which may be up to the sound speed c_s , compared to the perpendicular direction, which may be due to diffusion or convection, dependent upon the conditions. Upon contacting a limiter, the plasma on the flux surface which contacts the limiter flows to the material surface and neutralises, known as recycling, while traversing a relatively minimal distance in the perpendicular direction before the plasma density, and temperature, drops to very low values. In limited configuration, the perpendicular SOL width is typically characterized by an exponential fall off length. The region outside several fall off lengths is a rarefied gas. Different limiter geometries exist, most of which exploit either the poloidal or toroidal symmetry [42].

Flux surfaces, or magnetic field lines, that intersect material surfaces are referred

to as 'open', where as flux surfaces which close on themselves are 'closed'. The outer most closed flux surface which does not intersect the limiter, is referred to as the last close flux surface(LCFS) and provides the distinction between the confined plasma and the SOL region.

The limiter is in direct contact with the hot confined plasma which results in multiple issues undesirable for a fusion reactor. Firstly, the aggressive plasma environment erodes the limiter at a rate which is not conducive to reactor relevant time scales. Limiters would have to be replaced often, resulting in significant downtime, but this is technical challenge not associated with the plasma physics. The plasma physics motivation behind the avoidance of limiters for a reactor is due to two related reasons. These are firstly that the eroded material will have a higher Z than the fuel species and has direct access to the confined region, resulting in strong radiation. Secondly that H-mode has a higher power threshold when using limiters compared to divertor configuration plasmas.

1.6.2 Divertor configuration

The fusion performance advantages provided by divertors over limiters has resulted in almost all modern tokamak experiments using a divertor. The diverted plasma configuration is shown in figure 1.5 (b). Additional coils, carrying current in the same direction as the plasma, cause a null in the poloidal magnetic field called an x-point due to its shape in the poloidal plane in figure 1.5. At the x-point, the magnetic field is only toroidal. In diverted configuration, the LCFS is known as the separatrix. Plasma particles outside the separatrix travel along the field lines and onto remote target plates and undergo plasma material interaction there.

The separation between the core plasma and the plasma-material interaction offers multiple advantages. Eroded material from the divertor target plates does not have direct access to the hot core plasma. Further, the divertor and core plasmas can be treated somewhat separately. Not entirely, but sufficiently to allow specific tailoring of the divertor plasma to reduce the erosion of material surfaces. Despite this enhanced flexibility, mitigating the high power densities incident on the divertor targets will be a significant challenge for ITER and is currently an unresolved issue for DEMO as will be discussed in the next section.

1.6.3 High power densities on divertor target plates

The characteristic perpendicular to B e-folding width over which the heat flux decays outside the separatrix, λ_q , is thinner in H-modes than L-modes. This is due to the fact that turbulence in the edge region which spreads out the heat in when crossing the separatrix in L-mode is suppressed in H-mode. Also it has been recently found that the λ_q scales most strongly with the poloidal magnetic field, B_p , at the midplane, essentially defined by I_p , and that it does not scale strongly with the machine size [43]. Consequently, despite ITER being significantly larger than JET, it is projected to have

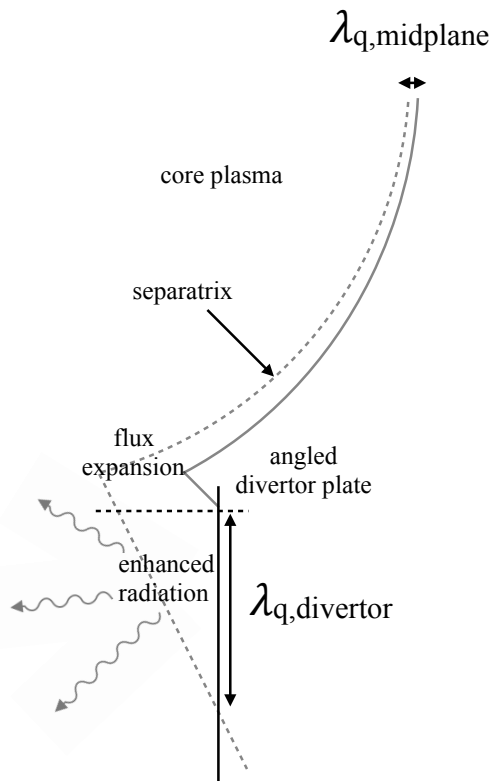


Figure 1.6: The different methods used to mitigate high divertor heat fluxes. A poloidal cross-section is shown. Expanding magnetic field lines, angling divertor target plates and enhancing radiative losses from the plasma are the key methods used.

a smaller λ_q , being on the order 1mm at the LFS midplane. ITER was designed on the assumption that λ_q would scale with machine size and be of the order 5mm. In terms of engineering limits, assuming a $Q = 10$, 500MW fusion power plasma with $\lambda_q = 1\text{mm}$, the power density at the outboard mid-plane of ITER will be on the order 1GWm^{-2} . The maximum power density that the actively cooled W divertor can tolerate in steady state is 10MWm^{-2} and 20MWm^{-2} for transients [44]. Therefore, handling the significantly larger power densities than were expected in order to protect the divertor target plates from melting is a key research focus of the international tokamak community and presents possibly the largest challenge in the realisation of fusion power.

The methods used to achieve this reduction are illustrated in figure 1.6. Expanding a given bundle of magnetic flux tubes prior to intersecting the target will increase the area over which power is deposited. This area may again be increased by inclining the target plates. Radiating the plasma power away volumetrically to reduce the intensity at the target is also commonly used. The most effective way to perform this is via the injection of a so called impurity species. Common impurities used in JET are N and Ne and will likely be used in ITER. The volumetric radiation deposits the

power over a larger area of the vessel.

Even with these methods, achieving sufficiently low power densities at the target remains a challenge, even more so when the effect of ELM transients are included in the mitigation of high divertor heat fluxes. Indeed unless ELMs are effectively mitigated, there is likely to be melting of the divertor surface [45].

1.7 Purpose and outline of thesis

For the reasons in the above section, the divertor heat flux challenge will likely be the main driving factor behind operational decisions regarding the boundary plasma in ITER. However it is important to consider whether the active divertor heat flux mitigation mechanisms impact upon the total particle flux toward main chamber surfaces and thus enhance deleterious plasma-material interaction. The purpose of this thesis is to further the current understanding of this issue. This question is increasingly important with progression toward a fusion reactor as erosion will limit the main chamber component lifetime and there may be regulatory constraints on the retention of T in the reactor.

The remainder of this thesis is structured as follows. Chapter 2 reviews the current literature and physics understanding of perpendicular transport in the main chamber SOL along with the basic concepts of divertor physics. The motivation of the research direction is also provided. Chapter 3 provides a methodology which details the SOL diagnostics used to collect data from the performed experiments along the methods used for analysis. Chapter 4 is in two parts. The first provides results of an interpretative analysis of the SOL radial flux and characterizes the radial transport using an effective convective velocity, v_{eff} . Results from similar studies are collated and the implications for ITER are given. The second part presents a statistical analysis of the ion current measured by the a flush mounted limiter probe, and its dependence on discharge parameters. Chapter 5 examines the role of parallel collisionality in determining upstream radial ion transport. In light of the results from Chapter 5, Chapter 6 examines the role of plasma-neutral interaction of the fuel species in the divertor region in determining the upstream transport. Chapter 7 summarises the main conclusions of the work and identifies potential avenues of further research.

Chapter 2

Literature Review

This chapter is structured into two sections. Section 2.1 reviews the current understanding of main chamber perpendicular ion transport. Section 2.5 reviews the divertor physics concepts required to interpret the results presented in this thesis. The summary relates the two main sections in order to motivate direction of research undertaken in this thesis.

2.1 Transport in the main chamber SOL

2.1.1 Introduction

By design in divertor configuration, the majority of the power and particles that cross the separatrix are directed toward the divertor. However, a substantial fraction of the *particles* leaving the confined region are incident upon the main chamber surfaces, despite the dominance of parallel transport compared to perpendicular transport (also referred to as cross-field transport).

The reason there is such strong particle flux incident on main chamber surfaces in tokamaks is due to the radial transport in the SOL being convective in nature, rather than diffusive. Initial experimental observations of the turbulent and convective nature of the SOL plasma were made in the early 1980's [46, 47]. However, it was not until the late 1990s that convection started to become increasingly accepted as an important transport mechanism in the SOL that more appropriately describes the SOL than diffusion [48]. This was motivated by the somewhat unphysical observation that the effective diffusion coefficient characterising the cross-field transport would have to increase by an order of magnitude or more in order to explain experimentally observed density profiles. Indeed, characterizing the radial flux via a effective diffusion coefficient D_{eff} such that $\Gamma_1(r) = D_{eff}(r)\nabla n(r)$, infinite D_{eff} were required to reconcile flat radial density profiles [49]. Convective transport on the other hand is consistent with observed profiles. Despite the transport being clearly convective nature, the diffusive interpretation persisted until the mid 2000s [49] and diffusive radial transport is still used in fluid modelling of the SOL region [50].

The convective transport in the SOL is structured and is manifested in the form

of coherent objects known as filaments. An illustration of filaments is given in figure 2.1, taken from [51], in order to provide an intuition of their nature. The Mega Amp Spherical Tokamak (MAST) is viewed with a wide angle camera and a background subtraction imaging technique [52] has been used to accentuate the filamentary structures. Three states of the edge plasma are shown. Figure 2.1 (a) shows the presence of filaments in between ELMs and are similar to filaments in L-mode, shown in (b). Edge plasma emission during an ELM Figure is shown in (c) which has a strong toroidal asymmetry, unlike (a) and (b). The review of literature in this chapter will focus mainly on filaments and time average profiles in L-mode which have received much attention in the field. In addition to the review here, the review of filaments in [53] should be considered for reference. ELMs are not considered in this thesis.

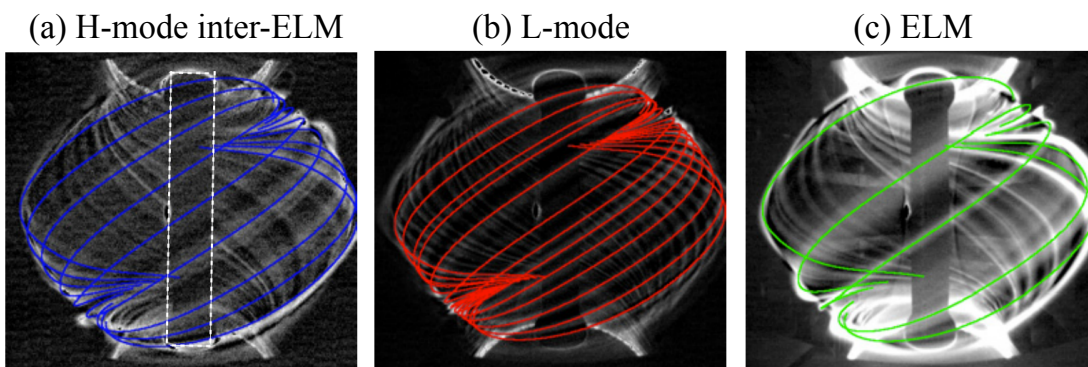


Figure 2.1: Imaging of filamentary structures in different regimes in MAST, images taken from [51]

2.1.2 Filament origins

There is not a consensus on the birth location of filaments. Some studies suggest the location is inside the separatrix, while others suggest outside. Understanding blob birth is of importance to know whether parallel dynamics in the SOL may play a role in their production.

Measurements from JET indicate that filaments might form inside the separatrix in a region called the edge shear layer (ESL) [54]. They are likely, but not certainly, a result of interchange instabilities [55] in tokamaks. The prevalence of filaments is generally dependent on the strength of the sheared flows in the region in which they are born. The flow direction referred to here is the direction perpendicular to both total magnetic field and the minor radius (similar to the poloidal direction) known as the bi-normal direction, and the shear direction is the minor radial direction. This can be visualized as the fluid at each flux surface having an approximately poloidal velocity different to adjacent flux surfaces. The turbulence that creates the filaments is suppressed with increasing shear flow.

In linear plasma devices and tokamak experiments with relatively low I_p , where shear flows are weak, plasma structures that are significantly extended in the radial

direction have been observed [56, 57, 58]. These structures have densities significantly higher than the surrounding background plasma. Their radially extended structure resulted in their common designation of 'streamer'.

When operating a tokamak with a more typical ratio of toroidal to poloidal magnetic field ($I_p(\text{MA})/B_t(\text{T}) \sim 1$), where B_t is the toroidal magnetic field, the increased presence of shear flows inside the separatrix acts to break up the radial streamers and reduce their radial size. The resulting structures are localized in the direction perpendicular to the magnetic field, typically on the order of cm, but are elongated along the magnetic field line. These structures are filaments.

Increasing the sheared flows still further, such as in H-mode, the linear growth rate of the instabilities which form the filaments are suppressed; the flows tear apart coherent structures [59]. The reduced turbulence in the edge is characteristic of the presence of the pedestal in H-mode and indeed the SOL turbulence is substantially reduced during inter-ELM periods.

Xu et al. [54] detailed the creation and subsequent motion of filaments into the SOL. The same flows which break streamers into filaments also result in coherent regions of reduced density, known as holes which are effectively the antithesis of filaments. In that study, they report that the interchange drive forces filaments and holes radially outwards and inwards respectively. Only filaments of sufficient size both radially (wider than the ESL) and poloidally, such that the life time is greater than the characteristic shear flow rate, can 'stick out' of the ESL, shear off, and become a permanently formed filament.

In contrast, gas puff imaging (GPI) of the SOL on NSTX [60] concluded that filaments formed in the SOL and have densities similar to the background of the region in which they are born. However, GPI imaging will only have a limited penetration into plasma; accelerated beams are usually used for measuring inside the separatrix and the pedestal. In that study it was argued that filaments acquire their density via interchange with the background profile and therefore the density of a particular filament was indicative of the region in which it was born. However, filaments also drain their density as they propagate radially. This study may have therefore only measured a filament's density when it was possible for the GPI technique to observe the filament, and may not account for earlier times in the filaments life at higher densities, further into the plasma. Further, at greater depths into the plasma filaments are more difficult to detect due to smaller relative density perturbations, $\delta n/n$.

2.1.3 Filament structure and concept

Unlike the relatively sparse literature on the formation of filaments, the structure of filaments once they are in the SOL has been extensively characterized such that a general definition of filaments now exists [53]:

- A filament has a singly peaked density, the peak of which is substantially higher than typically occurs with the rms fluctuations. This density peak is coherent

under propagation of the filament.

- $\lambda_{\parallel} \gg \delta_{\perp}$ where λ_{\parallel} is the extent of the filament parallel to the magnetic field line and is typically on the order of several metres or more. δ_{\perp} is the extent of the filament in the perpendicular direction and is typically on the order of cm.
- In the perpendicular direction, internal charge separation and vorticity result in a dipole structure which sets up an $\vec{E} \times \vec{B}$ motion of the entire structure. This motion may be both poloidal and radially outward.

While figure 2.1 gives an indication of the parallel structure of filaments, figure 2.2 gives an indication of their structure in the perpendicular direction. Notable is the order 1 density perturbation, typical in the far SOL. Although the concept shown in figure 2.2 is generally correct, there exists a rich phenomenology of filaments that have been investigated, especially from a numerical perspective.

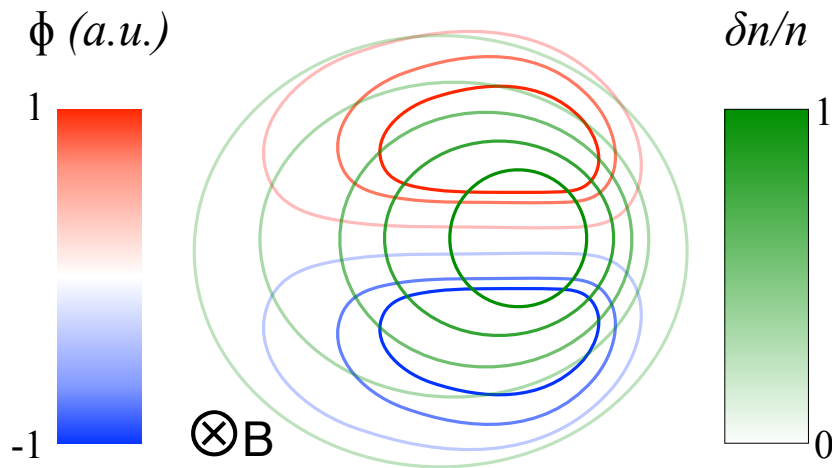


Figure 2.2: Typical cross field structure of a filament. The dipole in electrostatic potential Φ is shown along with a representative density perturbation. The direction of propagation is to the right.

2.1.4 Statistical evidence of filaments

Langmuir probes have been used on a large number of devices to confirm the presence of filaments in the SOL of magnetic confinement devices via statistical analysis of the measured currents and voltages.

A single LP is an electrode that is inserted into the plasma and can be electrically biased as required or left to float. In order to collect ions, and repel electrons, LPs are negatively biased (in JET, typically $\sim -100\text{V}$). The collected current is known as the ion saturation current, I_s .

Filaments, as regions of relatively higher density than the background, act to positively skew the time signal in the far SOL. Examples of such time signals can be seen in figure 2.3 (a) which were taken on TCV [61] using a reciprocating Langmuir

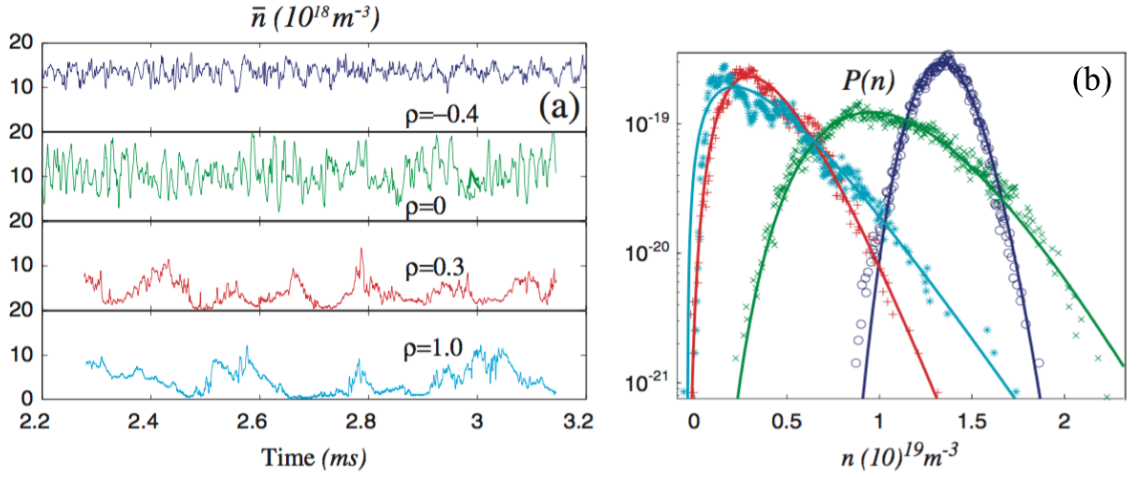


Figure 2.3: (a) Example time traces at different depths into the plasma. With increasing ρ (away from the separatrix), the PDF skew (b) increases. Figure reproduced from [61]

probe. In (a), $\rho = 0$ at the separatrix and 1 at the limiter radius. Advancing towards the separatrix from the limiter radius, the signal becomes less positively skewed, until it is essentially Gaussian at $\rho = -0.4$. It should be noted that negatively skewed signals are measured inside the separatrix on other devices such as JET[54] as NSTX [62].

Remarkably, the positively skewed I_s measurements in the far SOL of tokamaks show a high degree of similarity when shifted and scaled by the mean and standard deviation, respectively. Examples of this similarity are shown in figure 2.4. In (a) (taken from [63]) the scaled PDFs of several machines have been over plotted, where as (b) shows discharges of different density, all in TCV [55].

The q th moment, H , of the signal $y(t)$, which in the LP case is I_{sat} , is given by

$$H(q) = \frac{1}{N} \sum_{i=1}^N \frac{(y_i - \bar{y})^q}{\sigma_y^q} \quad (2.1)$$

where there are N points indexed by i , and \bar{y} and σ_y are the mean and standard deviation of y respectively. The skewness is defined as $S = H(3)$. The kurtosis, $K = H(4)$, quantifies the tendency of the distribution to have a tail. For a Gaussian distribution $K = 3$.

It has been shown that K and S are generally related via the inequality [64]

$$K \geq S^2 + 1. \quad (2.2)$$

Experimental data may be used to define the quadratic curve in (K, S) space. The coefficients of the quadratic indicate toward the analytical distribution which may be used to fit the measured PDFs. A common choice when measuring tokamak SOLs is the Γ distribution defined by

$$f_{\Gamma}(y; k, \theta) = \frac{y^{k-1} \exp(-y/\theta)}{\theta^k \Gamma(k)} \quad (2.3)$$

where $\Gamma(k)$ is the gamma function evaluated at k . In reference [65], it was remarked that the universal character of the PDFs and the unique relationship between S and K suggested that the events in the whole SOL and edge region are related and that the edge (being the separatrix and just inside) is likely the source of the intermittent events, consistent with the conclusions of reference [54].

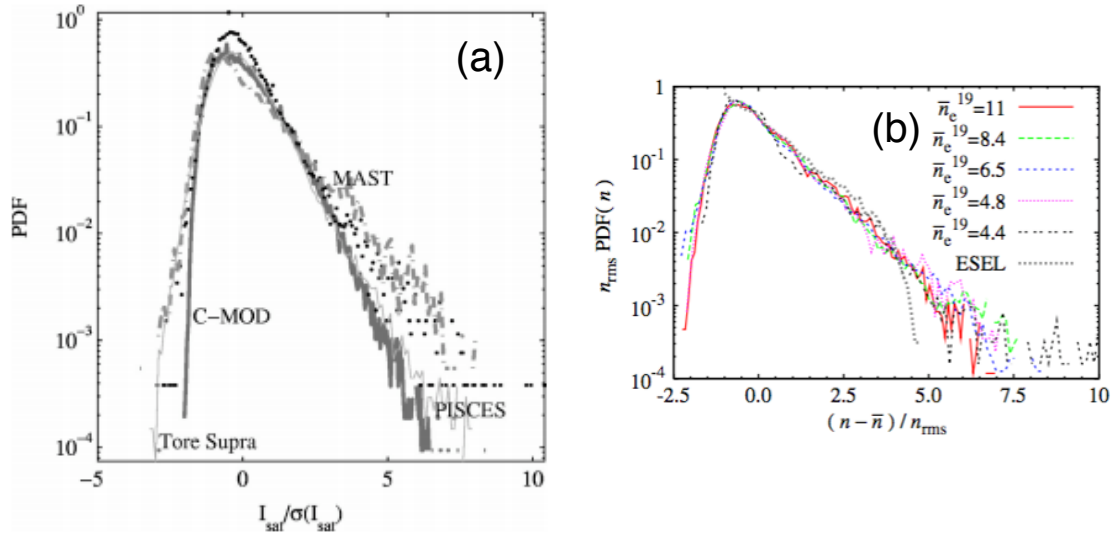


Figure 2.4: (a) Overlaid PDFs from several tokamaks, measured using Langmuir probes [63]. (b) PDFs from TCV for a range of \bar{n}_e [55]. The rescaled shape of the PDF is almost universal

2.1.4.1 Experimental measurements of cross field structure

By utilizing 2D arrays of Langmuir probes (LPs) the cross field structure of filaments shown in figure 2.2 can be measured experimentally. An example of such a measurement is shown in figure 2.5, taken from [66], conducted at the Versatile Toroidal Facility (VTF), where such a 2D probe array has been used to measure the floating potential, V_f , of the plasma and to infer the velocity field. Clearly visible is the dipole structure in both V_f and vorticity. Measurements in figure 2.5 are instantaneous but similar measurements that average over many identified filaments at the TORPEX device show a similar structure [67, 68].

2.1.4.2 Conditionally averaged measurements

It is typical to consider the SOL plasma as the superposition of filaments, driven by convection, on top of a background plasma, assumed to be subject to diffusive transport, but possibly convection also. In order to identify those parts of the signal that are due to the intermittent transport, it is common to define a threshold. Parts of the signal which rise above the threshold are considered to be due to a filaments. Once identified, those conditionally selected parts of the signal are temporally aligned to their respective peaks and averaged over. Across multiple tokamaks, the resultant, conditionally averaged pulse shape has a rise time typically shorter than the decay

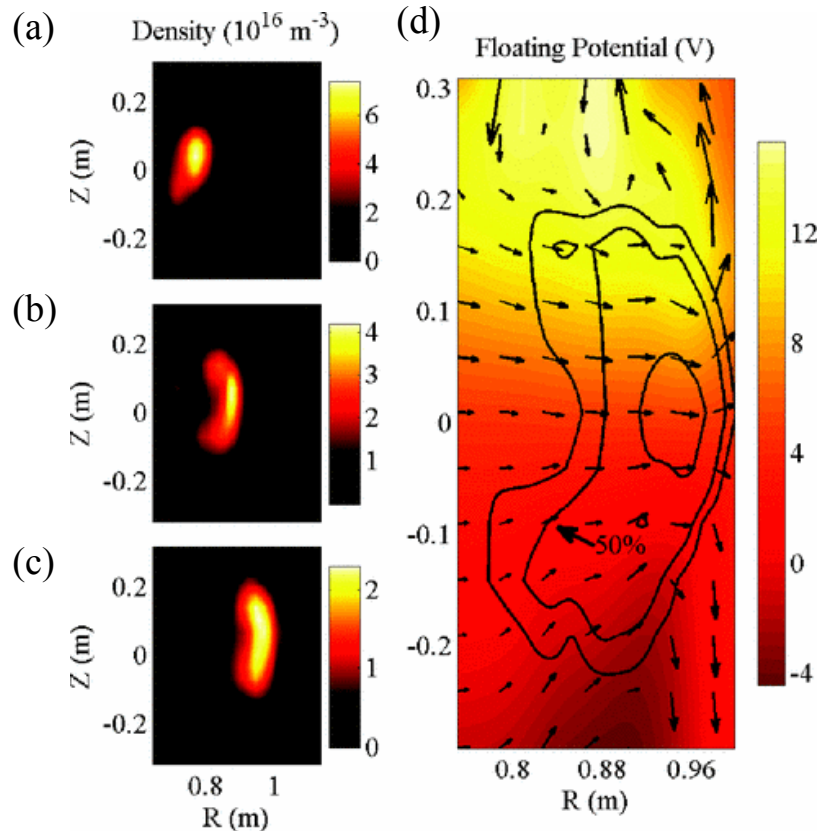


Figure 2.5: (a)-(c) density measurements separated by $100\mu\text{s}$. (d) Floating potential showing the dipole structure of the filament. Overlaid arrows indicate the local $\vec{E} \times \vec{B}$ velocity.

time, as depicted in figure 2.6, taken from [69]. Although somewhat limited, single point probe measurements can be used to determine the change to the waveform with plasma conditions. The contraction of the conditionally averaged shape with density is typical and indicates a reduction of the average size/velocity ratio. Such a contraction has also been observed with decreasing I_p [70, 71].

Multi-headed probe measurements yield more insightful information. As described in section 2.2 the radial and poloidal motion of filaments is driven by $\vec{E} \times \vec{B}$ motion, arising from their dipole nature structure. By measuring the electric field between two spatially separated Langmuir probe heads, the effective velocity may be determined as $v_{\vec{E} \times \vec{B}} = E_{\text{measured}} \times B/B^2$. A velocity may also be obtained by cross-correlating one probe head with another with the time delay between probe heads indicating the filament velocity. Together with the auto-correlation time, this yields both size and velocity information on the filaments. These operations may be performed in an ensemble averaged sense or on individual filaments to obtain distributions.

2.2 Filament equivalent circuit

Models of filaments are concerned with either the numerical or analytical solution of two equations which describe the conservation of charge and density. The equation for

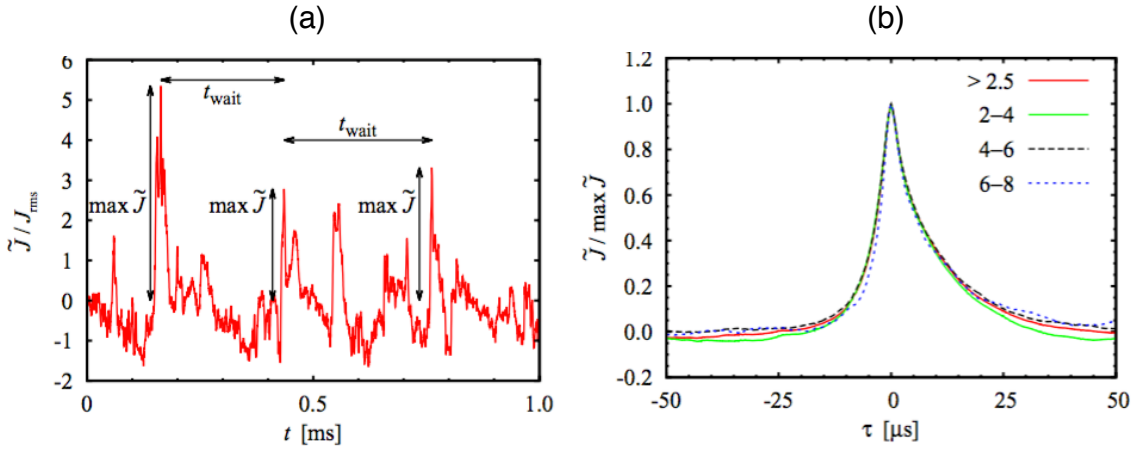


Figure 2.6: (a) Example identification of intermittent events using a 2.5σ threshold on data from TCV. Example waiting times are also indicated. (b) Conditionally averaged waveforms showing the invariance of the waveform shape with threshold window. Both (a) and (b) are taken from [69]

charge conservation is

$$\nabla_{\perp} \cdot \frac{d}{dt} \left(\frac{n_e m_i}{B^2} \nabla_{\perp} \phi \right) = \nabla_{\parallel} j_{\parallel} + \nabla_{\perp} \cdot \left(\frac{\vec{F} \times \hat{b}}{B} \right). \quad (2.4)$$

The equation for density continuity is

$$\frac{dn}{dt} \equiv \frac{\partial n_e}{\partial t} + \vec{v}_e \cdot \nabla \cdot (n_e) = S_{ion}. \quad (2.5)$$

The LHS of equation 2.4 is the polarization current density \vec{j}_{pol} which arises due to the inertial force. On the RHS, j_{\parallel} is the magnitude of the parallel current density \vec{j}_{\parallel} . The term $\frac{\vec{F} \times \hat{b}}{B} = \vec{j}_F$ is the current which flows due to a net species summed force \vec{F} , where $B = |\vec{B}|$ and $\hat{b} = \vec{B}/B$. Physically, equation 2.4 describes how the force \vec{F} drives the formation of the electrostatic potential, ϕ , with j_{\parallel} mitigating the build up of charge. In the case of a filament, which is essentially a perturbation in the pressure, p , \vec{F} is due predominantly to the pressure gradient which gives rise to the diamagnetic current

$$\vec{j}_{dia} = \frac{\hat{b} \times \vec{\nabla} p}{B}. \quad (2.6)$$

Equation 2.5 also defines the convective derivative used in equation 2.4. S_{ion} is the volumetric ionisation source. The nature by which the currents in equation 2.4 close determine the manner in which the filament propagates. It is useful to consider these currents as a circuit diagram as shown in figure 2.7, figure taken from [72]. Clearly the parallel currents themselves cannot close the circuit. Instead they enable the closure of the circuit by perpendicular currents at different locations along the field line.

There are two main locations in the tokamak where perpendicular currents may

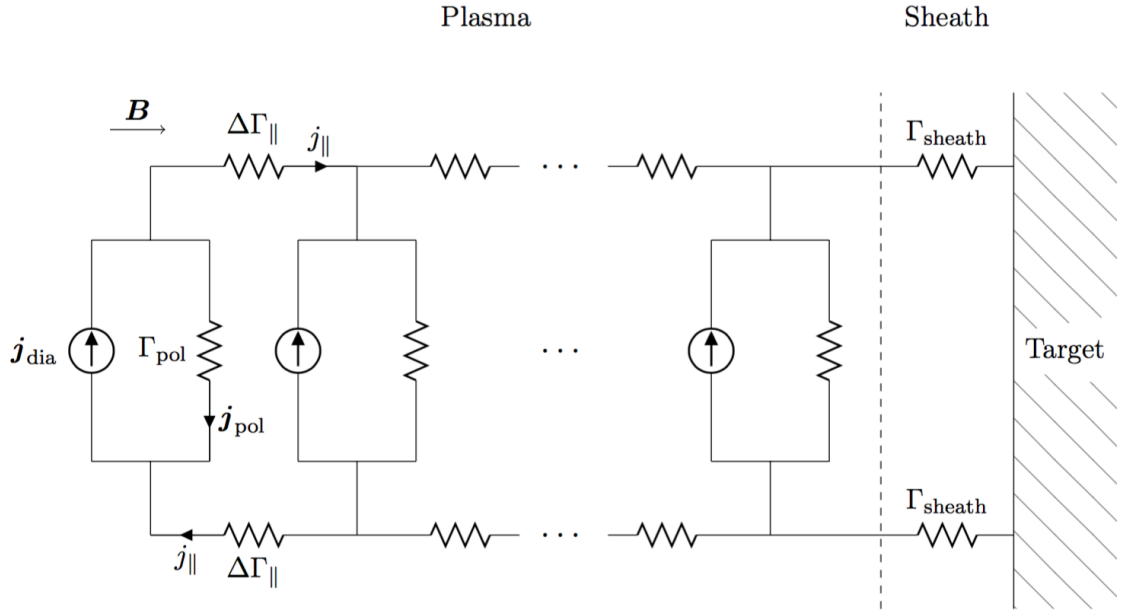


Figure 2.7: Current paths in a filament. The pressure perturbation drives j_{dia} . Other currents which close the circuit are impeded by resistances Γ . The currents may also be closed by flowing through the target material itself. Figure taken from [72]

flow more easily. These are the x-point and the target. At the x-point, there is strong magnetic shear. Consequently, a filament that is circular in cross-section at the mid-plane will be flattened substantially in the x-point region. This flattening is depicted in figure 2.8 [73] and may reduce the width to the order of the ion gyroradius. When the flux tube flattens, the perpendicular current can flow much more easily across the thin dimension. Assuming the target material is conducting, the perpendicular current may also flow through the target material itself. This closure was proposed originally in reference [74].

2.3 The two region model

Clearly, a main objective of modelling filaments is to obtain relations between the size and velocity in different scenarios which are relevant to a tokamak. A common model used to derive such relations is the 'two region model', the two regions being the outboard midplane and the x-point [75]. In the model, parallel currents are allowed to flow between the regions and the flattening of magnetic flux tubes, depicted in figure 2.8 is also accounted for in the x-point region by geometrically mapping between the coordinate systems. The four parameters which characterize the model are the collisionality, Λ , the perpendicular size, Θ , the flux tube flattening ϵ_x and a scaled blob velocity \hat{v} . The collisionality is defined as

$$\Lambda = \frac{L_{\parallel} \nu_{ei} \Omega_i}{c_s \Omega_e} = \varrho \frac{n_e L_{\parallel}}{T_e^2} \quad (2.7)$$

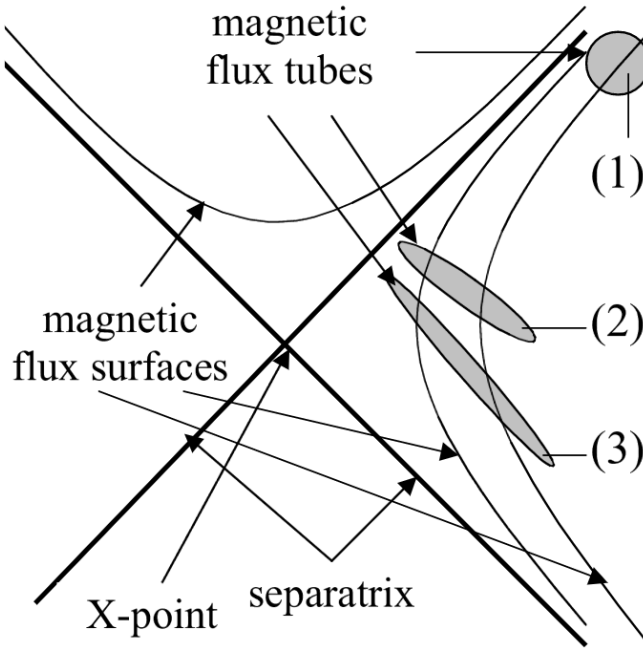


Figure 2.8: Flattening of flux tubes with proximity to the x-point due to magnetic shear. Sufficient flattening may provide an alternative current closure not depicted in 2.7. Figure taken from [73]

where L_{\parallel} is the parallel connection length, ν_{ei} is the electron-ion collision frequency, $\Omega_{i/e}$ is the gyrofrequency of electrons and ions and c_s is the sound speed. The constant factor $\varrho = 1.7 \times 10^{-18}$ is for s.i. units. The perpendicular size parameter is defined as

$$\Theta = \hat{\delta}^{5/2} = \left(\frac{\delta_{\perp}}{\delta_{*}} \right)^{5/2} \quad (2.8)$$

where $\delta_{*} = \frac{c_s}{\Omega_i} \left(\frac{L_{\parallel}^2 \Omega_i}{R c_s} \right)^{1/5}$. The blob velocity parameter is defined as $\hat{\nu} = \frac{\nu_x}{c_s} \left(\frac{R}{\delta_{*}} \right)^{1/2}$, where x refers to the direction in which the filament is propelled, which in a tokamak is some combination of the radial and poloidal directions. The flattening parameter, ϵ_x , is defined to be 1 for no distortion (circular cross section) and tends to 0 as a given flux tube loses its width near the x-point.

These parameters were used to define four different regimes of filaments, a diagram of which is shown in figure 2.9. These four regimes are:

- (a) C_s : The sheath connected interchange regime occurs for large filaments ($\delta_{\perp} > \delta_{*}$) for low collisionality ($\Lambda < 1$). The parallel currents, connecting to the target through the sheath, dominate the closure than polarization currents. Filament velocities scale as $\hat{\nu} \propto \hat{\delta}^{-2}$.
- (b) C_i : The ideal interchange regime occurs when j_{dia} in small filaments is closed via enhanced polarization currents in the x-point region. The magnetic shear appears in the velocity scaling as $\hat{\nu} \propto \epsilon_x \hat{\delta}^{1/2}$.
- (c) RX: The resistive x-point regime exists for large filaments at high collisionality. The sheath provides the current closure, but the enhanced resistivity results in a

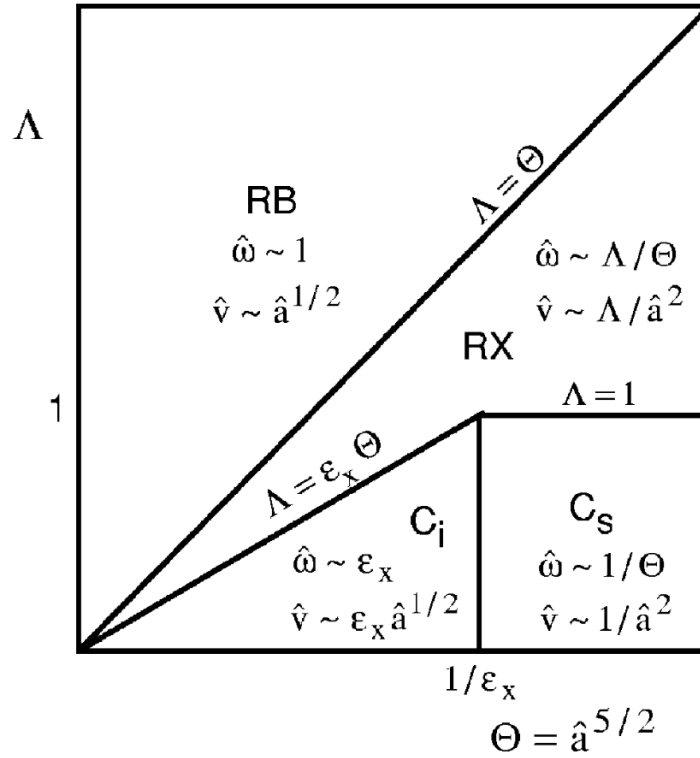


Figure 2.9: Regime diagram for the two region model. The filament velocity scaling for each region is given. Figure taken from [75]

velocity scaling of $\hat{v} \propto \Lambda \hat{\delta}^{-2}$.

- (d) RB: The resistive ballooning regime applies to small blobs at high collisionality. The polarisation currents are sufficient to close j_{dia} in the mid-plane and consequently $\hat{v} \propto \hat{\delta}^{1/2}$.

One of the most important predictions of this model is that enhanced resistivity increases the radial velocities of filaments, potentially enhancing net transport of plasma to the main wall. This has also been suggested by recent 3D modelling of filaments in slab geometry where the collisionality was artificially increased in the last 25% of the filaments length, emulating enhanced divertor resistances [72]. However, the authors noted that the increases required were perhaps unphysically large.

2.4 Time average profiles

Understanding the motion of individual filaments is undoubtedly important in the picture of SOL transport but understanding the net transport, both in a time averaged and statistical sense is ultimately more important for the predicting radial fluxes in future devices such as ITER and DEMO. As mentioned in section 2.1.1, the structure of time averaged density profiles is indicative of the convective transport which is manifested in the form of filaments. One of the first observations that connected the flatness of the radial density profile and the prevalence of large intermittent events was made LaBombard [76], reproduced in figure 2.10.

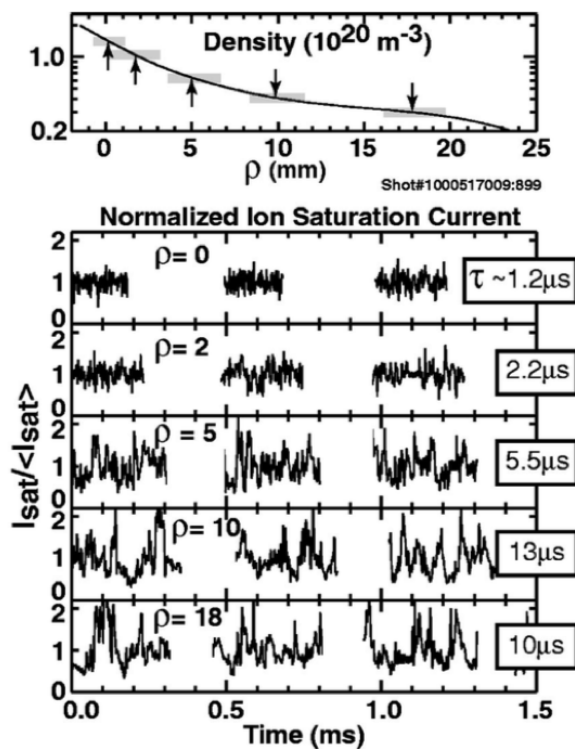


Figure 2.10: Example relationship between density profile structure and the intermittent nature of ion saturation current, measured on C-mod. Inset τ show the increasing auto-correlation time with distance from the separatrix ρ . Figure taken from [76].

A key and ubiquitous observation made by the community is the sensitivity of time averaged density profiles to increasing line-averaged density. A typical example is shown in figure 2.11 [77] where strong gas puffing in C-mod was used to raise line average density, \bar{n}_e , by around a factor ~ 2.5 . Shown in (a), the SOL density profile changes dramatically by becoming much flatter, resulting in the limiter density increasing by over an order of magnitude. Another study on C-mod found the relationship between the time averaged radial flux Γ_{perp} and \bar{n}_e to be almost exponential, with a factor ~ 4 increase in the \bar{n}_e leading to a factor ~ 20 increase in the radial flux [78]. Figure 2.11 shows another typical observation; despite strong increases in local n_e , T_e profiles remain relatively unchanged. Perhaps unsurprisingly, the midplane pressure shows an approximately linear relationship with plasma flux to the limiter, where the plasma neutralizes.

Figure 2.11 (a) also shows the two region structure that is commonly observed in divertor configuration. These two regions are the near and far SOL, referring to the distance from the separatrix. The near SOL ($\rho \approx 0 - 5$ mm in figure 2.11 (a)) is characterized by relatively short radial decay length λ_n . The far SOL ($\rho > 5$ mm in figure 2.11 (a)) has much larger λ_n and at high densities can be almost flat. Increases in \bar{n}_e initially affects λ_n in the far SOL. At sufficiently high \bar{n}_e , the flattening can extend to the near SOL and even inside the separatrix.

The intrusion of the turbulent transport, associated with the profile flattening, into the confined region has been suggested to play a role in setting the empirically observed upper limit of achievable density in toroidally confined plasmas [76]. This

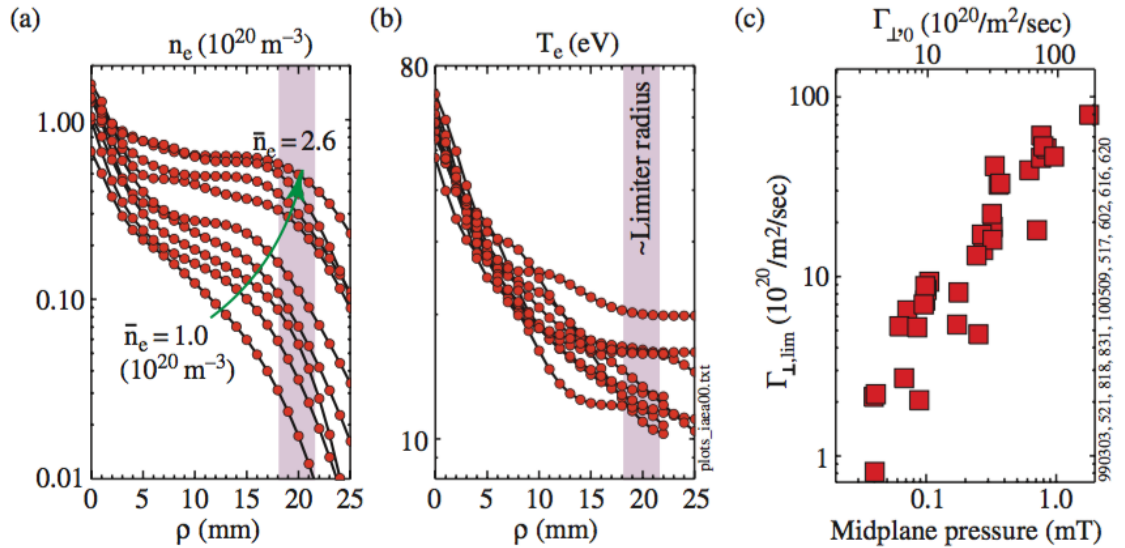


Figure 2.11: (a) Example flattening of SOL density profile with increasing density. (b) T_e profiles which remain relatively unaffected during the increase in \bar{n}_e . (c) Correlation between inferred limiter flux, $\Gamma_{L,lim}$, and midplane pressure or equivalently neutral flux $\Gamma_{L,0}$. Figure taken from [77].

limit is expressed as [79]

$$n_G = \frac{I_p}{\pi a^2} \quad (2.9)$$

where n_G is in units of 10^{20} m^{-3} , I_p is in units of MA and the minor radius of the machine, a , is in m. In that study, it was argued that the strong convective transport may act to cool the edge plasma, enhancing the resistivity thus shrinking the area through which the current flows, forcing the plasma to be magneto-hydrodynamic (MHD) unstable. The authors also state such cooling would increase the radiation, complementing the power losses from turbulence.

The predicted role of collisionality in the properties of filaments from analytical and numerical modelling has prompted its use in interpreting the behaviour of time averaged density profiles. L-mode experiments on TCV [70] concluded that the electrical disconnection of filaments from the target sheath at high collisionality was the likely cause of flattened density profiles. In those experiments, I_p was varied at fixed B_t and \bar{n}_e in order to modify L_{\parallel} . Other L-mode experiments on AUG also concluded that collisionality, expressed in that case as $\Lambda_{div} = \Lambda/5$, to be the parameter controlling the upstream radial ion transport [80]. The AUG experiments used N_2 seeding to enhance Λ_{div} without modifying either \bar{n}_e or L_{\parallel} . Those results were also interpreted as evidence of the two region model [80]. The key result from this study is shown in figure 2.12, figure taken from [80]. It was argued that the general behaviour of λ_n with Λ_{div} demonstrated Λ_{div} as being the control parameter. The effect of N_2 seeding on filament sizes and velocities was not supplied.

More recent studies question the role of collisionality. Experiments similar to

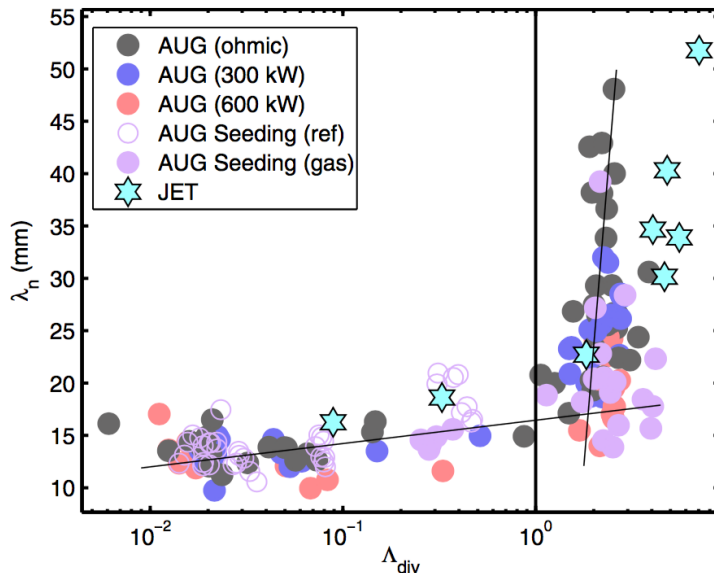


Figure 2.12: Density e-folding lengths λ_n in a variety of discharges from AUG and JET measured over 25mm outside the separatrix. Figure taken from [80]

those reported in [80] performed in H-mode did not observe the same effect when seeding with N_2 . Further, a study of L-mode experiments on TCV which varied L_{\parallel} using divertor coils, whilst keeping I_p and B_t constant concluded that increasing $\Lambda_{div} > 1$ maybe a necessary condition for flat profiles, but it was not sufficient. Whether collisionality has a central role in determining the radial transport is being examined by the community, and will be examined in this thesis in chapter 5.

The time average radial flux and density profile are connected via the relation $\Gamma_{\perp} = nv_{eff}$, where v_{eff} is an *effective* convective velocity. Quasi-neutrality is assumed such that $n \approx n_i \approx n_e$. v_{eff} is not a direct measure of the velocity, but is rather the velocity required to yield the observed fluxes. Expressing the radial transport in this manner is undoubtedly an over simplification. Arguably however, it is more representative than the diffusive approximation given the turbulent nature of the transport. Consequently, v_{eff} has been used more commonly by the community in recent times.

A surprisingly common result from studies of v_{eff} across multiple tokamaks is that $v_{eff} \sim 100\text{ms}^{-1}$ in the far SOL near the limiter radius, with approximately a factor two variation [49, 81, 82]. Example profiles of v_{eff} are shown in figure 2.13. An I_p scan in TCV [70], shown in (a), suggested the major effect of I_p on v_{eff} was near the separatrix ($\rho = 0$), with v_{eff} remaining fixed near the limiter radius ($\rho = 1$). These measurements were made using a RCP. Comparatively, a study of C-mod plasmas, shown in (b), suggested v_{eff} was relatively insensitive to either core or local densities [49]. In that study, v_{eff} was calculated using an interpretive transport method that has also been utilized in this thesis in chapter 4.

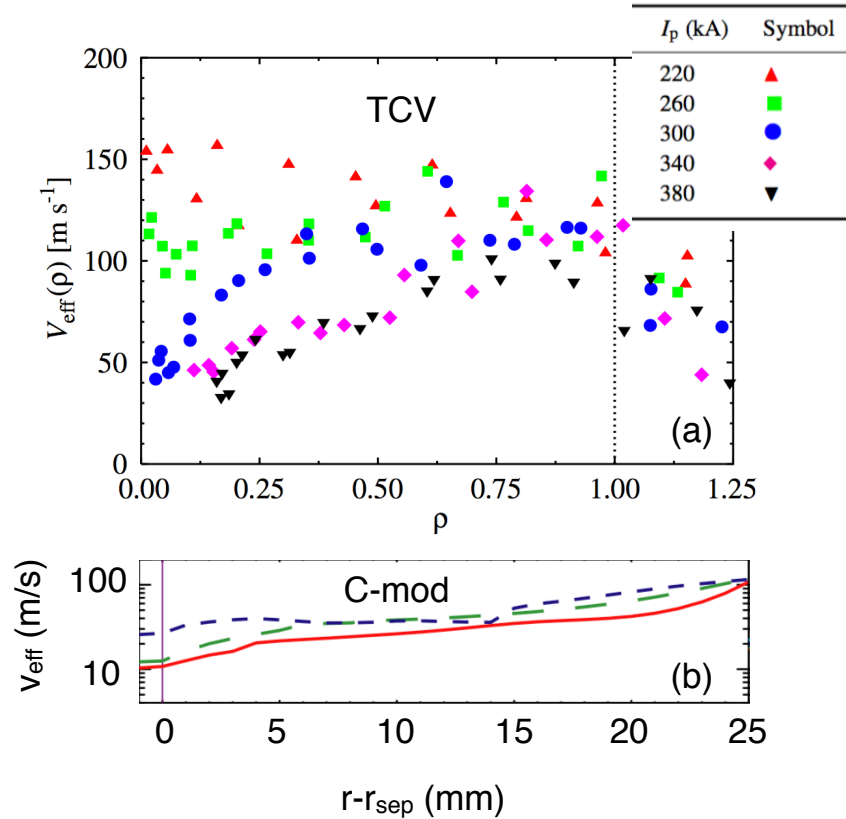


Figure 2.13: Example v_{eff} profiles taken on TCV(a) [70] and C-mod (b) [49].

2.5 Divertor physics

In this section, physics relevant to the role of divertors in this research is reviewed in order to provide a basis for results presented in this thesis, in particular chapters 5 and 6. This section is structured as follows. Section 2.5.1 gives the important plasma-neutral reaction rates for the H (also valid for D). Section 2.5.2 outlines characteristics of typical divertor operating regimes. Section 2.5.3 outlines the differences between open and closed divertor geometries.

2.5.1 Plasma-neutral interactions

After impacting the material surface, plasma ions may be retained by the material or they may reflect off the surface back into the plasma. Typically, ions recombine when contacting the surface and are released back to the plasma as a molecule or an atom. The molecule to atomic ratio is dependent upon the temperature of the surface on which they recycle [83]. The neutral hydrogen species interact with the plasma in a variety of ways. The key interactions are shown in figure 2.14 [42]. Of particular note is reaction (7), known as charge exchange (CX), where the energy of the reactant neutral and ion swap. The $H - H^+$ CX reaction is resonant and has a higher rate than atomic ionization (reaction (6)) at all temperatures. CX reactions between the fuel species and impurity species such as N are typically negligible because the reaction rate is

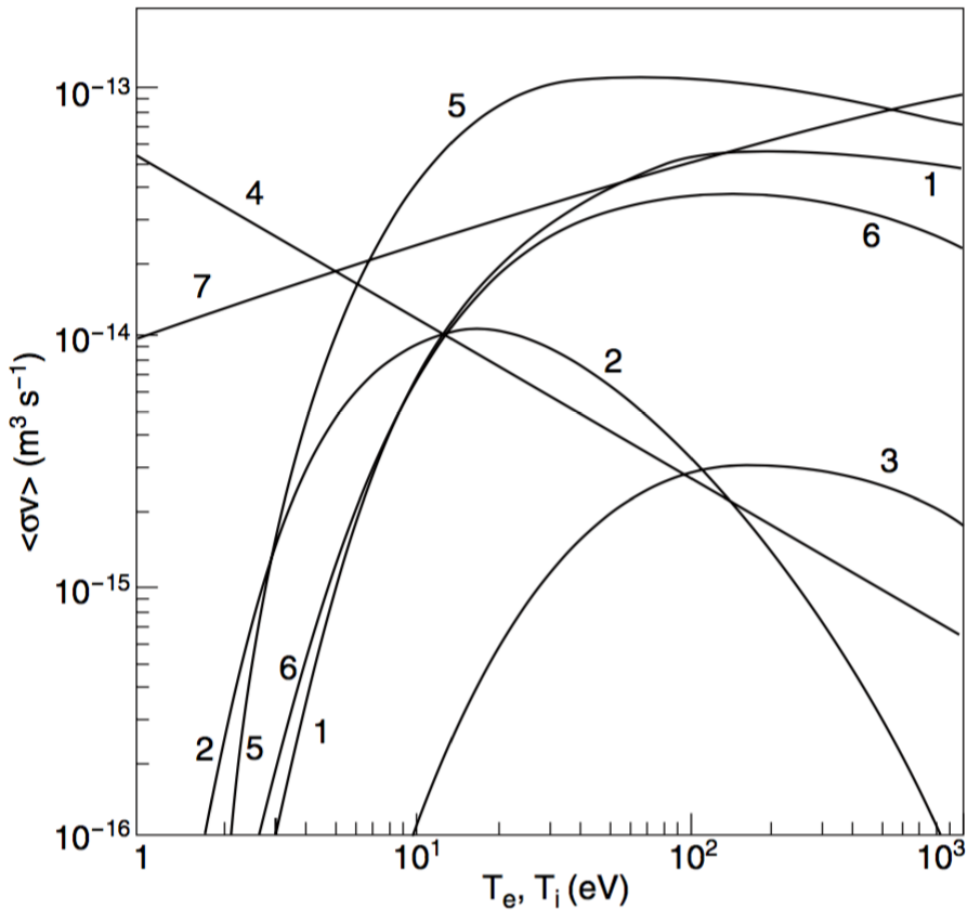


Figure 2.14: Reaction rate coefficients for atomic and molecular Hydrogen including (1) $e + \text{H}_2 \rightarrow \text{H}_2^+ + 2e$, (2) $e + \text{H}_2 \rightarrow 2\text{H}^0 + 2e$, (3) $e + \text{H}_2 \rightarrow \text{H}^0 + \text{H}^+ + 2e$, (4) $e + \text{H}_2^+ \rightarrow 2\text{H}^0$, (5) $e + \text{H}_2^+ \rightarrow \text{H}^0 + \text{H}^+ + e$, (6) $e + \text{H}^0 \rightarrow \text{H}^+ + 2e$, (7) $\text{H}^0 + \text{H}^+ \rightarrow \text{H}^+ + \text{H}^0$. Figure taken from [42]

non-resonant and also the density of the impurity species is typically much lower than the fuel species in tokamak experiments [42].

2.5.2 Divertor operating regimes

The purpose of the divertors existence is to provide a greater degree of control on the interaction between the plasma and the material surface, with particular regard to the heat flux. Experiments across multiple tokamaks suggest that the divertor conditions may be classified broadly into 3 regimes, the details of which are briefly reviewed [42].

2.5.2.1 Sheath-limited regime

In the case of low densities in the upstream SOL, the heat transport is dominated by convection of electrons. When the ions impact the divertor target and recycle, the densities sufficiently low that the subsequent neutral-plasma interaction does not act to strongly modify the local density. In other words, mean free paths are long enough such that neutrals are not ionized very shortly after leaving the target. The interaction of the plasma at the material surface is governed by the plasma sheath - hence sheath-limited (SL) regime. The electron-electron mean free path, $\lambda_{ee} > L_{\parallel}$ and results in low

temperature gradients along magnetic field lines such that the separatrix temperature at the target plates is a substantial fraction of the upstream temperature and may be of the order 30-50eV, compared to ~ 100 eV upstream.

2.5.2.2 Conduction limited (High-recycling)

Increasing the density upstream, and therefore at the target plates, simultaneously reduces the the target temperatures due to the increased plasma-neutral interaction. Below a certain temperature and above a certain density, the mean free path of particles, both neutral and plasma, becomes sufficiently short that a positive feedback loop is set up; additional density acts to shorten the mean free path, increasing the local number of ionizations, fuelling the plasma. The additional electrons act to further decrease the neutral mean free path and so on. This feed back loop acts to rapidly increase and decrease the density and temperature respectively, whilst maintaining pressure along a particular field line. Temperatures and densities can typically change by a factor 5-10. This state is the conduction limited regime. Significant parallel gradients exist and hence conduction plays a stronger role in the heat transport. The conduction limited is essentially the same as the high-recycling regime. *For the remainder of this thesis, this regime will referred to as the high-recycling (HR) regime.* It should be noted that HR regime can be induced by increased of radiation due to an injected impurity, without an associated increase in the local density of the fuel species nuclei, either charged or neutral.

2.5.2.3 Detachment

Increasing the plasma-neutral interaction still further by continued injection of the fuel species, or enhancing radiation using an impurity, local temperatures at the divertor target can continue to decrease and can be on the order 1eV or lower. Both sheath limited and HR regime conserve pressure along a field line. Detachment differs in that there is pressure loss along a field line, with the plasma pressure being lower at the target plate than upstream. Essentially, a 'cushion' of gas forms in front of the target plate which protects it from the direct effects of the plasma. The detached divertor regime is thus highly desirable in a reactor scenario. When using the fuel species to induce detachment, CX and volume recombination losses play a strong role in the reduction of the plasma pressure incident on the target via the removal of ion momentum. Volume recombination acts as a plasma particle sink and may either be two-body, where a photon removes the energy of the recombination, or three-body where an additional electron removes the recombination energy. Three-body recombination only becomes significant at $T_e < 1$ eV and high n_e and can dominate over two-body. Notably, three-body recombination has a heating effect on electrons. Ionization of the fuel species is also an energy sink. As mentioned in section 2.5.1, CX processes between D and an impurity species is negligible. The enhanced radiative ability of an impurity species acts as a strong electron energy sink. Given sufficient impurity density, the electron

population will be of low enough energy such they may recombine with the fuel species, becoming neutral atoms. Together with the radiation, the neutral particles spread the energy over a larger area.

2.5.2.4 Transitioning between regimes

The three regimes described above are not isolated states as would be energy levels in an atom. They instead provide a framework to the spectrum of divertor states. The exact behavior of the total divertor ion flux with upstream density is dependent upon the machine, but the general trend is illustrated in figure 2.15. In sheath limited regime the total ion flux to the divertor increases linearly with upstream density until the onset of HR regime where the total ion flux begins to increase with upstream density with the second power. When transitioning from HR to detachment, the total ion flux saturates and peaks. The initial decrease of the ion flux to the target is referred to as the onset of detachment in this thesis. Further reductions in the total ion flux to the target are increasing depth of detachment.

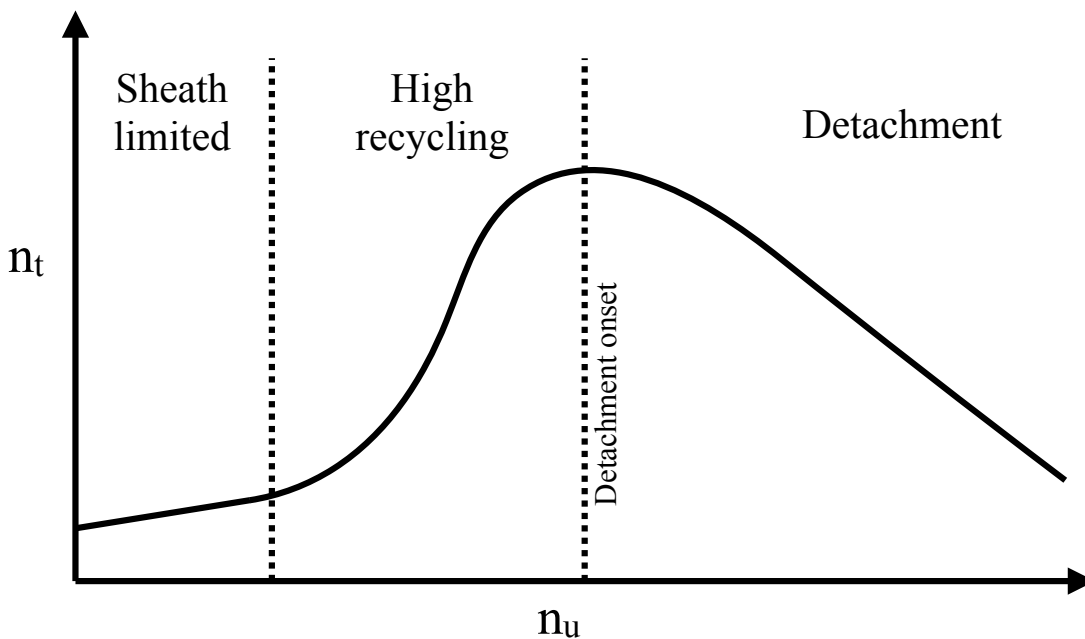


Figure 2.15: Schematic of the three divertor regimes with target density n_t shown as a function of upstream density

2.5.2.5 Detachment in H-mode

Despite the presence of filaments, progressing to detached conditions in L-mode is not an intermittent process. The presence of ELMs in H-mode, however, complicates the picture significantly. The ejected hot dense plasma can be sufficient to 'burn through' the cushion of neutrals in detachment, temporarily reattaching the plasma, with the hot ELM plasma being incident on the divertor target plates. Handling

transients under detached conditions is an important aspect of ITER. Indeed, under the currently intended ITER divertor operating conditions, there will be melting of the W monoblocks [45]. The extent of the melting depends on the level of ELM mitigation.

There is a limitation on the depth of detachment in H-mode that is practical in a reactor scenario. Using high levels impurity seeding to push the neutral cushion, also known as the detachment front, all the way to the x-point results in a substantial reduction in fusion performance due to the easy access of impurities to the core plasma, which cool the plasma via radiation.

There exists therefore a spatial window where the detachment front will have to exist if ITER is to both achieve a high performing plasma without catastrophic material damage. Understanding both the sensitivity and stability of the detachment front is therefore critical to predicting the requirements of divertor for future fusion devices. Theoretical attempts to understand this window are in progress [84], along with practical implementations of detachment control [85].

2.5.3 Divertor geometries

Of particular interest in the tokamak community is the geometry of the divertor region, both in the physical structure of the target plates and also the shape of magnetic flux surfaces. This interest is motivated by the severe challenge of handling the power in ITER and subsequent devices outlined in section 1.6.3.

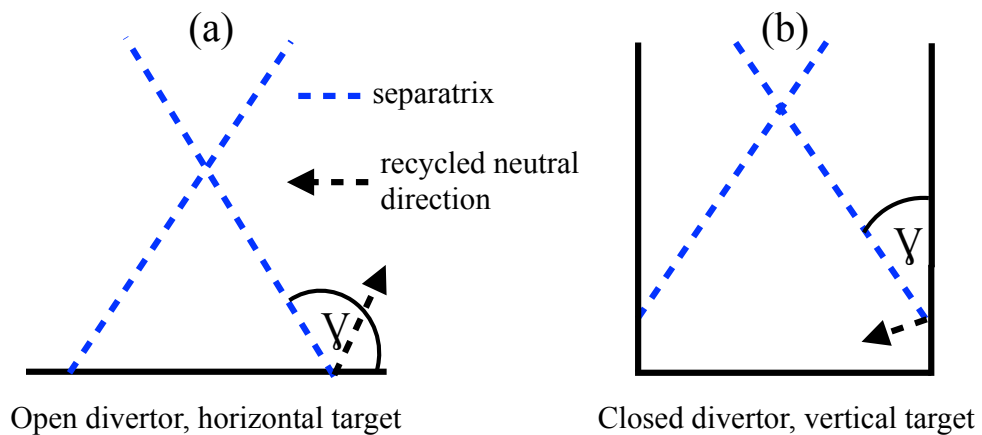


Figure 2.16: Open horizontal,(a), and closed vertical , (b), divertor geometries. The direction of recycled neutrals is also indicated.

2.5.3.1 Open and closed divertors and target plate inclination

There are two different but related aspects of conventional divertor concepts. Firstly, whether a divertor is open or closed and secondly, the target plate inclination angle relative to the separatrix.

A schematic of a typical open divertor geometry is shown in figure 2.16 (a). The open description refers to the absence of vessel structures close to the separatrix and the SOL flux surfaces. As such there is substantial room for the recycled neutrals to expand into. It is typical for open divertor geometries to have a horizontal target plate. More precisely, it is the poloidal inclination angle of the target plate relative to the separatrix, indicated by γ in figure 2.16, and the resultant preferential direction of the recycled neutrals. Neutrals are released normal to the surface on which they recycle [86]. With a horizontal target, ($\gamma > \pi/2$), the recycled neutrals are directed into the SOL onto farther out flux surfaces and interact with plasma there. Conversely, in a vertical target plate divertor ($\gamma < \pi/2$), such as shown (b), at the separatrix recycled neutrals are directed toward the PFR. Recycled neutrals from SOL flux surfaces are directed back toward the separatrix where they undergo plasma neutral interaction or pass through into the PFR. Hypothetically, it is possible to have a closed, horizontal target plate.

The closed, vertical target geometry offers multiple advantages over the open horizontal target. Firstly reflecting the neutrals back toward the separatrix aids the plasma-neutral interaction processes required for detachment such that lower upstream densities required to achieve detachment [87] were reduced by up to 40%. It should be noted however that only detachment at the separatrix was aided by the vertical target configuration. Given a narrow region around the separatrix transmits most of the power to the target, facilitating detachment in this region reduces the number of sputtered atoms from the material surface and thus the vertical target is advantageous from this perspective. SOL flux surfaces outside the separatrix remained in a more attached state. Indeed it is typical for T_e to be greater in the SOL than at the separatrix in vertical target because of this neutral effect. The closed geometry also has the benefit of aiding the confinement of sputtered material in the divertor region, reducing its access to the core. Similarly, the more closed nature improves the effect of neutral pumping which aids the removal of those impurities and potential also the He fusion products in a reactor scenario.

2.5.3.2 The JET divertor geometry

The current JET-ILW divertor design offers the unique capability of switching between horizontal and vertical target configurations as illustrated in figure 2.17. The vertical target configuration would be considered closed as described in section 2.5.3.1. Although the horizontal target configuration is more open, there is still some degree of closure incurred by the vertical target plate. The location of the extraction of neutrals via cryo-pumping is also indicated with red arrows. This capability allows the study of the effect divertor configuration on the upstream SOL.

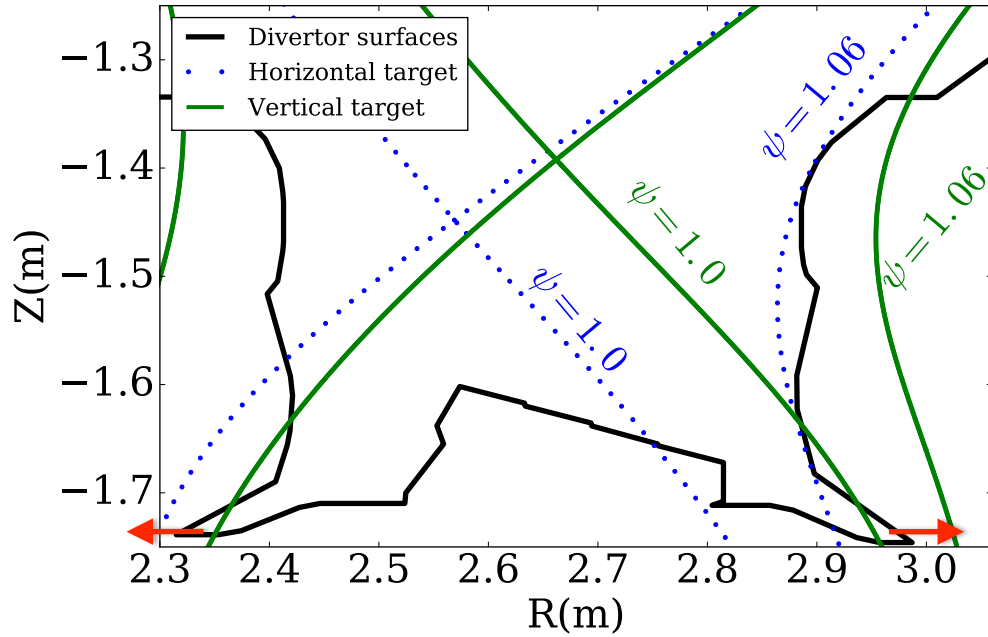


Figure 2.17: Horizontal target and vertical target divertor configurations in the JET-ILW divertor. The separatrix, $\psi = 1.0$, and an outer flux surface, $\psi = 1.06$, for each configuration are indicated. Red arrows indicate the direction of neutral pumping.

2.6 Summary

This chapter has reviewed the two areas relevant to the research undertaken in this thesis, which are summarised as follows. The first area, introduced filaments as objects which largely determine the nature of the radial transport in the SOL. Key experimental observations have been reviewed including their internal shape and the properties of statistics when measuring ensembles of filaments. The two region model, commonly used to characterize individual filaments, has been reviewed. A key point from this model is that *enhanced resistivity leads to increased velocity of filaments*, potentially increasing the net radial transport. Indeed this prediction has also been made by 3D numerical modelling of filaments [72]. Experimentally testing this prediction is one of the key subjects of this thesis. The relation between filaments and time average profiles of density and velocity has also been explored. Notably, inferred values of v_{eff} vary by around a factor 2 across a wide range of machine and operating conditions.

With regard to divertor physics, the properties of three regimes commonly used to describe the divertor conditions have been reviewed. Further, key differences between open and closed divertor geometries have been described. The JET divertor geometry, capable of operating in either horizontal or vertical target configuration, has also been detailed.

Chapter 3

Methodology

The purpose of this chapter is to firstly detail the diagnostics on JET-ILW that have been utilized and secondly to depict the techniques used to analyse data from those diagnostics. The radial flux analysis method, used to provide results for chapter 4, requires data from multiple diagnostics and is left to the end of the chapter in section 3.6. Figures 3.1 and 3.2 show the locations of all the diagnostics used in this study.

3.1 SOL density profile measurement

3.1.1 Neutral Li beam injection

Neutral Li beam injection (NLBI) is common in use as a density diagnostic on MCF devices, usually measuring the SOL and pedestal regions [88]. NLBI is a relatively non-perturbative technique that is not impacted by non-thermal electron populations.

The principle of NLBI generation is depicted in figure 3.3. Li ions are generated by heating Li- β -eucryptite to around 1600K. These ions are then collimated and accelerated using ion optics, the width of the beam being on the order 2cm. Neutralisation of the Li ions is achieved by passing the beam through a neutral gas of Na, fed by a pool of liquid Na. Na is used as it achieves the required neutralisation efficiency (80%) at a lower temperature than Li gas, extending the lifetime of components. In JET-ILW, the beam is situated around 4m vertically above the separatrix and is injected into the tokamak at the location indicated in figure 3.1[89]. Upon entering the plasma, line radiation from the Li atoms, driven by electron impact excitation, enters a periscope which views the beam from a toroidally separate location. Optical fibres transmit the collected light to a Czerny-Turner spectrometer outside torus hall. The resultant spectrum is recorded by a CCD camera. The 670.8nm wavelength light of that spectrum is used as input for a collisional radiative model which is solved numerically to provide the density [90],[91].

The intensity of the light emission is proportional to the product of the beam density and n_e . With increasing distance into the plasma, the beam attenuates and n_e of course increases. The balance of these effects results in a emission profile. It is only on the rise of this peak emission profile into the plasma that n_e can be calculated

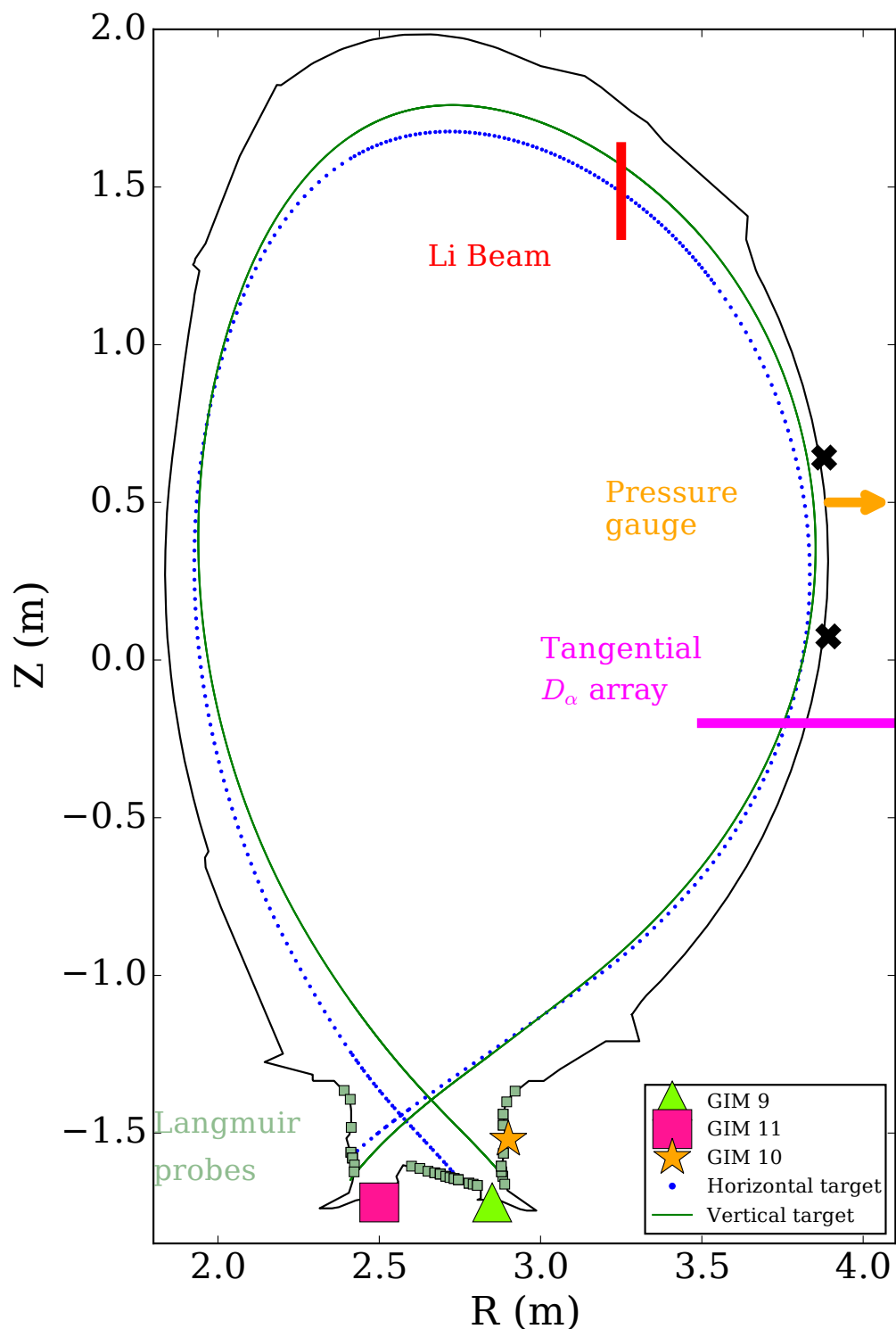


Figure 3.1: Poloidal magnetic equilibria showing vertical (green) and horizontal configuration (blue). Measurement locations of diagnostics are given. Black crosses on the LFS indicate the location of flush Langmuir probes mounted on the outer limiter.

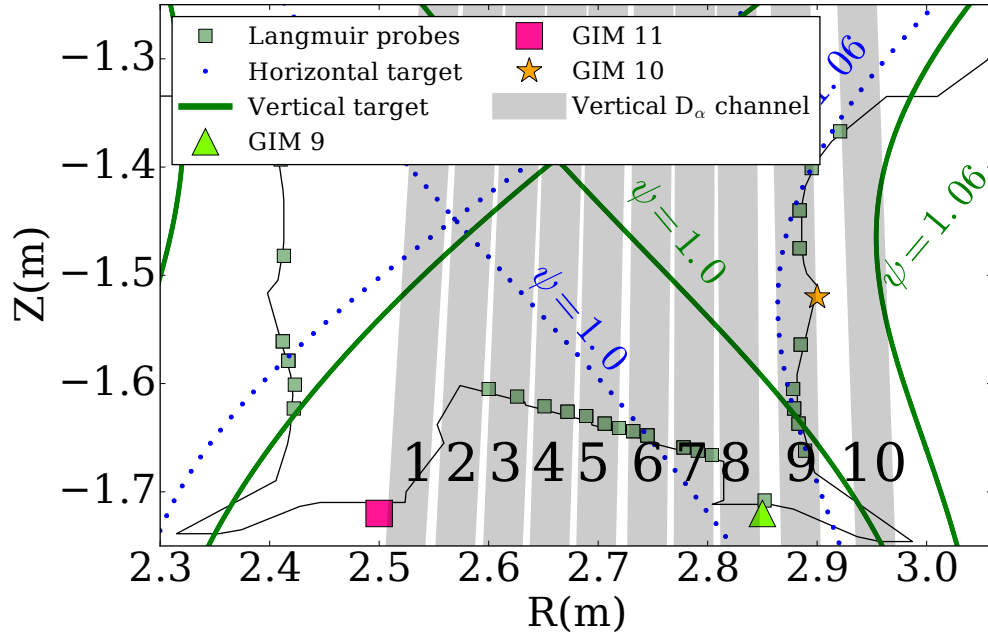


Figure 3.2: Close up of the divertor region showing the locations of the vertical viewing D_α channels, not shown on figure 3.1

accurately.

In order to solve for n_e in the collisional radiative model, values of T_e are required. However, currently, and for the discharges used in this thesis, there is no T_e measurement in the JET-ILW SOL. Instead assumed profiles are used which incorporate Thomson scattering data near the separatrix and some exponential decay into the SOL with a minimum temperature of 10eV in the far SOL which is typically measured on other tokamaks, including JET when a reciprocating Langmuir probe (RCP) was operational. Further, the resultant n_e profile was found to be in sensitive to expected range of T_e profile [92].

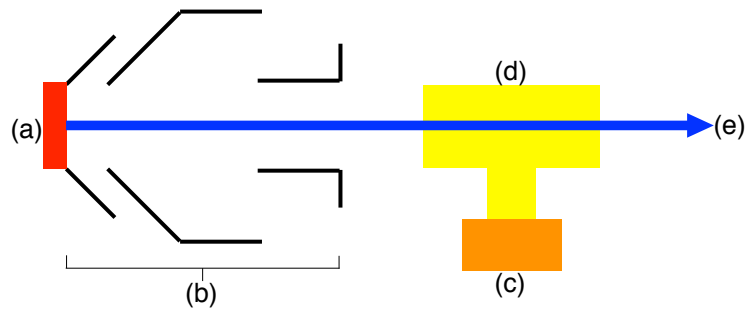


Figure 3.3: Schematic showing the principle of neutral Lithium beam generation. (a) Heated Li- β - eucryptite heated to produce Li ions. (b) ion optics to accelerate and collimate produced ions. (c) Reservoir of liquid Na and attached neutralization chamber (d) filled with Na gas. (e) Resultant Li beam

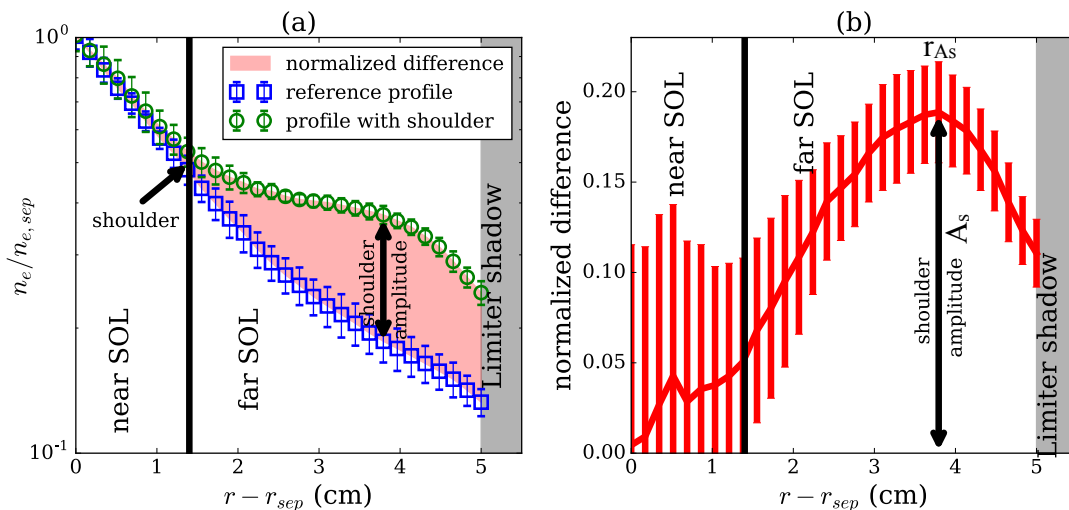


Figure 3.4: (a) Example density profiles without (blue squares) and with (green circles) a shoulder. The shaded area is shown as a profile in (b) with A_s as the peak of this profile. The location of this peak, r_{A_s} is also indicated.

3.1.2 Shoulder amplitude metric

A simple new metric of the SOL density shoulder amplitude and location based upon normalizing each SOL density profile, measured by the Li beam diagnostic, to its separatrix value is used in Chapters 5 and 6. The method, whereby we abstract out the shoulder peak amplitude and location of that peak from the Li beam data, is illustrated in figure 3.4. The horizontal co-ordinate, $r - r_{sep}$, is referenced to the mid-plane where r_{sep} is the separatrix radius. We utilize the SOL density profile at a time when the divertor is in sheath-limited (SL) regime (as discussed later, there is an absence of measurable SOL density shoulders in the SL regime) as the reference profile shape (a). This reference profile and all subsequent profiles are also normalized to their separatrix values and their difference to the reference profile is then the measured shoulder profile (b). Normalizing to the separatrix density is common [80, 93]. The maximum of the normalized difference profile is our definition of the shoulder amplitude, A_s , while the location of that peak, r_{A_s} , is used to follow shoulder expansion towards the limiter.

The method described above is advantageous over the more typical exponential decay length λ_n in that it does not tend to very large values for flat profiles. Further, the shoulder amplitude method describes the entire SOL regardless of its shape where as $\lambda_n = -n/\nabla n$ is a local measurement which cannot describes more complexly shaped profiles as in figure 3.4.

3.1.3 Profile mapping

The JET EFIT equilibrium reconstruction is known to have $\sim \pm 1$ cm uncertainty, which is incurred when mapping profiles to the midplane. It is possible to use the SOL density profiles to help constrain any required shifts as demonstrated in figure 3.5. Profiles have been taken at high density (specifically from a density limit test plasma) where the far

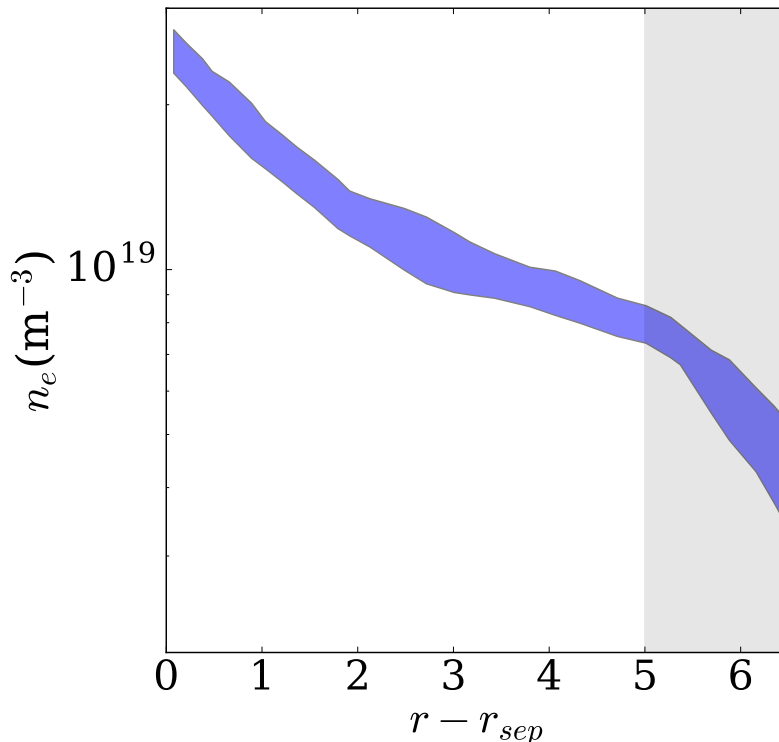


Figure 3.5: Blue shaded region comprised of five high density profiles where the far SOL extends to the limiter radius and λ_n only decreases in the limiter shadow.

SOL extends to the estimated location of the limiter radius. In the magnetic shadow of the limiter the density profile steepens, presumably due to the reduced connection length. This has been observed on multiple machines [94],[77]. Despite this effect, there is still around $\sim 0.5\text{cm}$ uncertainty in the location of the wall shadow. The shift required in this case (0.5cm outwards) was applied to all density profiles in this thesis.

3.2 SOL T_e profile estimation

The SOL T_e profile was estimated due to a lack of direct measurement. High resolution Thomson scattering (HRTS) provided reliable n_e and T_e to the separatrix, but in the SOL measurements are dominated by uncertainties. A typical radial T_e decay length, $\lambda_T = 2\text{cm}$ is used and $T_e = 10\text{eV}$ is assumed in the far SOL, based on previous measurements [49, 95].

3.3 Pressure gauges

Two types of pressure gauges have been used for this thesis. The first type, a Baratron[®] capacitance manometer is located $\sim 1\text{m}$ away from the plasma at the outboard midplane, in a 10cm diameter pipe and offers the most direct measurement of the mid-plane pressure. However, this gauge was subject to large amplitude vibrations from the

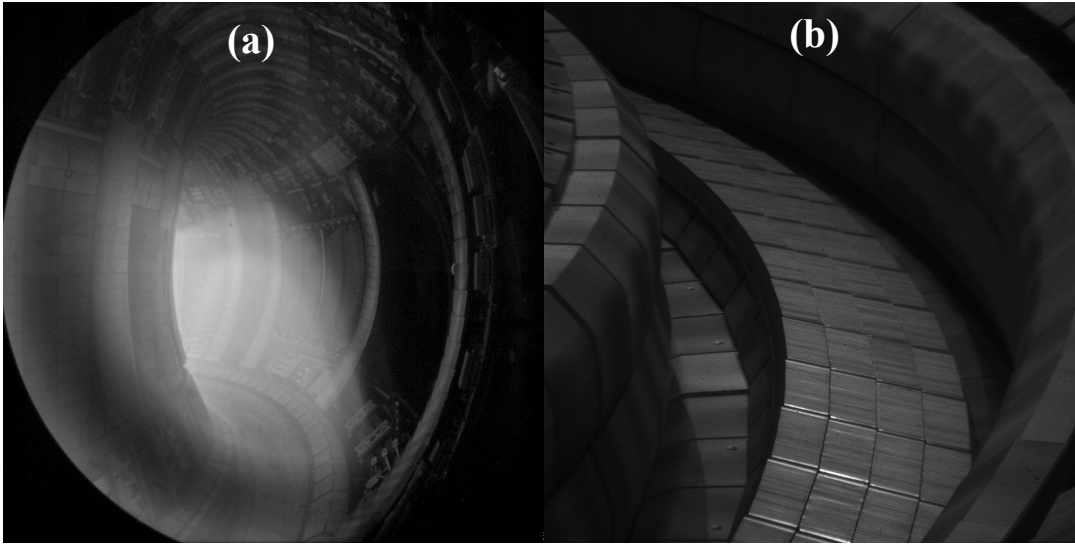


Figure 3.6: Example views of the optical cameras. (a) Wide angle main chamber (KL1). (b) Divertor view (KL11).

vacuum vessel (natural frequency $\sim 14\text{Hz}$) resulting in the signal to noise ratio (SNR) being of order ~ 1 . These large vibrations were due to inadequate insulation. Two techniques were used to remove the vibrations including a low-pass filter and a moving average. There was negligible difference between the techniques. This pressure gauge was operational only for a select number of plasmas used in this thesis.

Other pressure gauges used are of ionisation Penning type. These gauges did not suffer from large vibrations, but were more removed from the midplane by several m and were located near a vacuum pump which detracts from its validity as use as a midplane gauge.

3.4 Optical cameras

Optical cameras have been used to provide information on the spatial location of the emission from the neutral species interacting with the plasma. Two separate optical camera systems have been used. A wide angle main chamber viewing camera system, named KL1, and a divertor viewing system, named KL11, which comprise of 3 and 4 separate cameras respectively [96]. The views of KL1 and KL11 are shown in figure 3.6 (a) and (b), respectively.

Both of these systems are equipped with arrays of neutral density and atomic transition filters which may be used in conjunction to optimise for different regions of interest (ROI). The cameras are model AVT Pike 100 B with a 1000×1000 pixel CCD and have a maximum frequency of 30Hz and 60Hz in 16bit and 8bit mode, respectively.

In order to use these cameras for the purposes of inversion, both a brightness and spatial calibration are required, which are the subject of sections 3.4.1 and 3.4.2.

3.4.1 Brightness calibration

The brightness of the plasma $Br[\text{W}/(\text{str m}^2)]$ may be inferred from the cameras by the equation:

$$Br = C \frac{GV_{pulse} - GV_{BG,pulse}}{t_{exp,pulse}}, \quad (3.1)$$

where $C[\text{W}/(\text{str m}^2 \text{ count})]$ is the calibration constant, $GV_{pulse}[\text{counts}]$ is the raw count of a particular pixel measured during the plasma, $GV_{BG,pulse}[\text{counts}]$ is pixel count due to background noise, measured prior to plasma breakdown when there is no emission, and $t_{exp,pulse}(\text{s})$ is the exposure time of the camera for the specific pulse. Calibration data was taken during the 2015 calibration campaign where an in-vessel calibration light source (ICLS) was positioned [97], using the JET remote handling arm. The calibration data informs the value of C via the equation

$$C = \frac{I_{ICLS} A_{filt}}{(GV_{calib} - GV_{BG,calib})/t_{exp,calib}} \quad (3.2)$$

where $I_{ICLS}[\text{W}/(\text{m}^2 \text{ str nm})]$ is the spectral radiance of the ICLS which is known, $A_{filt}[\text{nm}^{-1}]$ is the transmission function of the filter being calibrated, $GV_{calib}[\text{counts}]$ is the pixel count measured by the CCD for the calibration light source and $t_{exp,calib}$ is the exposure time used during the recording of calibration data. $GV_{BG,calib}[\text{counts}]$ is the background recorded with the ICLS switched off. During the course of a campaign, measured background values were not found to vary outside of uncertainties.

The value of C is specific to each pixel and so the result of the calibration is a image which stores these values of C and may be used to calculate Br of any particular image recorded by the camera using the equation 3.1.

Due to the wide angle view of the wide angle KL1 cameras and the size of the ICLS, it was not possible to illuminate the entire CCD. As a compromise, the most important regions of the view were sampled. These samples also constrained a function, used to describe the unsampled regions of the CCD, of the form

$$C = d + a(x_p - x_c)^2 + b(y_p - y_c)^2 \quad (3.3)$$

where a, b, d, x_c and y_c are the model parameters and x_p and y_p are the pixel location in the horizontal and vertical directions respectively. The parabolic surface was chosen as the fitting function on the assumption of reduced sensitivity of the camera system near the edges of the CCD, known as vignetting, commonly observed in optical systems.

The sampled locations and an example fit to the data is shown in figure 3.7. The view was sampled near the centre in order to constrain the peak of the fit. The majority of the sampled locations cover those pixels which are tangent to the outer edge of the plasma, near the midplane and below. Pixels near the midplane which view the SOL are subject to reflections from a vacuum vessel structure. Robustly quantifying this reflection is challenging and therefore, pixels slightly below the midplane have been

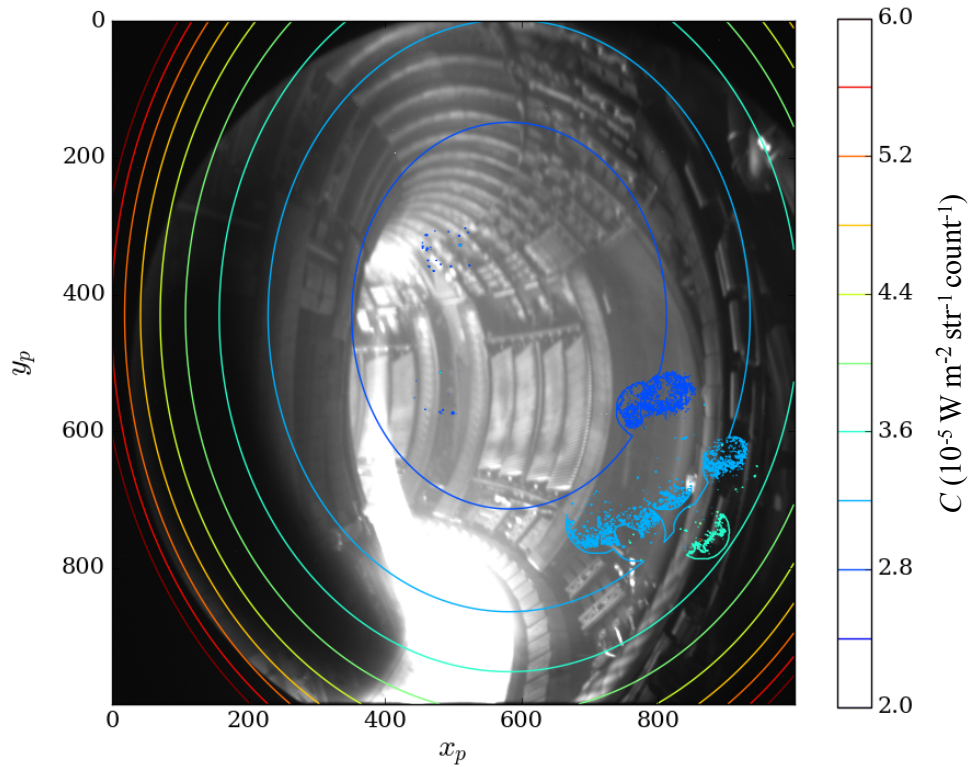


Figure 3.7: Sampled and fitted calibration data for the KL1 camera.

used to perform tomographic inversions.

In the case of the divertor viewing KL11 cameras, the entire CCD was illuminated by the ICLS and therefore no additional sampling or fitting was necessary

3.4.2 Spatial calibration

It is useful to know the line of sight (LOS) vector for each of the CCD pixels to a high degree of accuracy and precision in order to invert camera images, which record brightness, into 1D or 2D emissivity profiles which may then be used in conjunction with other diagnostics. In order to ascertain this information, a pinhole camera model has been applied which is capable of fully representing the distortion, location and orientation of the optical system via a number of parameters [98, 99] which are either intrinsic or extrinsic. Intrinsic parameters detail the optical properties of the system. Extrinsic parameters describe the modification of this reference frame into standard JET coordinates which are used by other diagnostics. The following sections describe the model and its application to the camera systems.

3.4.2.1 Intrinsic parameters

Consider a pinhole camera, the aperture of which lies at the origin with the optical axis parallel to z in standard Cartesian coordinates. A point with coordinates (X, Y, Z) , where $Z > 0$, will be projected onto the image produced by the pinhole camera in the

(x,y) plane. The normalised image location in that plane is given by

$$\begin{pmatrix} x_n \\ y_n \end{pmatrix} = \begin{pmatrix} X/Z \\ Y/Z \end{pmatrix} \quad (3.4)$$

The real image will undergo distortion passing from the endoscope in the vessel, through the optical components and to the CCD. The distorted image locations may then be expressed as

$$\begin{pmatrix} x_d \\ y_d \end{pmatrix} = [1 + k_1 r^2 + k_2 r^4] \begin{pmatrix} x_n \\ y_n \end{pmatrix} + \begin{pmatrix} 2p_1 x_n y_n + p_2 (r^2 + 2x_n^2) \\ p_1 (r^2 + 2p_2 x y) \end{pmatrix} \quad (3.5)$$

where $r^2 = x_n^2 + y_n^2$ and k_n and p_n are radial and tangential distortion coefficients, respectively. The distorted image location (x_d, y_d) must then be converted into a pixel location on the CCD (x_p, y_p) by use of

$$\begin{pmatrix} x_p \\ y_p \\ 1 \end{pmatrix} = \begin{pmatrix} f_x & 0 & c_x \\ 0 & f_y & c_y \\ 0 & 0 & 1 \end{pmatrix} \begin{pmatrix} x_d \\ y_d \\ 1 \end{pmatrix}. \quad (3.6)$$

The 3×3 matrix is known as the camera matrix where each element is in units of pixels. The effective focal length of the imaging system are f_x and f_y in the horizontal and vertical directions respectively. An object aligned with the optical axis of the camera appears at (c_x, c_y) on the detector, expected to be near the centre.

3.4.2.2 Extrinsic parameters

The coordinate system described in the section 3.4.2.1 defines the pinhole camera to be at the origin, with the optical axis aligned along the z axis. For JET, the origin is at the centre of the central column with z , as defined in figure 1.5, being along the torus rotation axis. The extrinsic parameters provide a mapping between these coordinate systems. This mapping may be described by the equation

$$\begin{pmatrix} X' \\ Y' \\ Z' \end{pmatrix} = \mathbf{R}_x(\alpha) \mathbf{R}_y(\beta) \mathbf{R}_z(\omega) \begin{pmatrix} X \\ Y \\ Z \end{pmatrix} + \begin{pmatrix} x_{cam} \\ y_{cam} \\ z_{cam} \end{pmatrix} \quad (3.7)$$

where (X', Y', Z') are the tokamak coordinates, (X, Y, Z) are the coordinates in the pinhole camera frame and $\mathbf{R}_a(\theta)$ are the rotation matrices around axis a by an amount θ in the anti-clockwise direction. The location of the pinhole in the tokamak coordinate system is given by $(x_{cam}, y_{cam}, z_{cam})$.

3.4.2.3 Model application

Together, the intrinsic and extrinsic parameters are a complete framework for calculating the LOS vector for each CCD pixel. In order to solve for the parameters to high

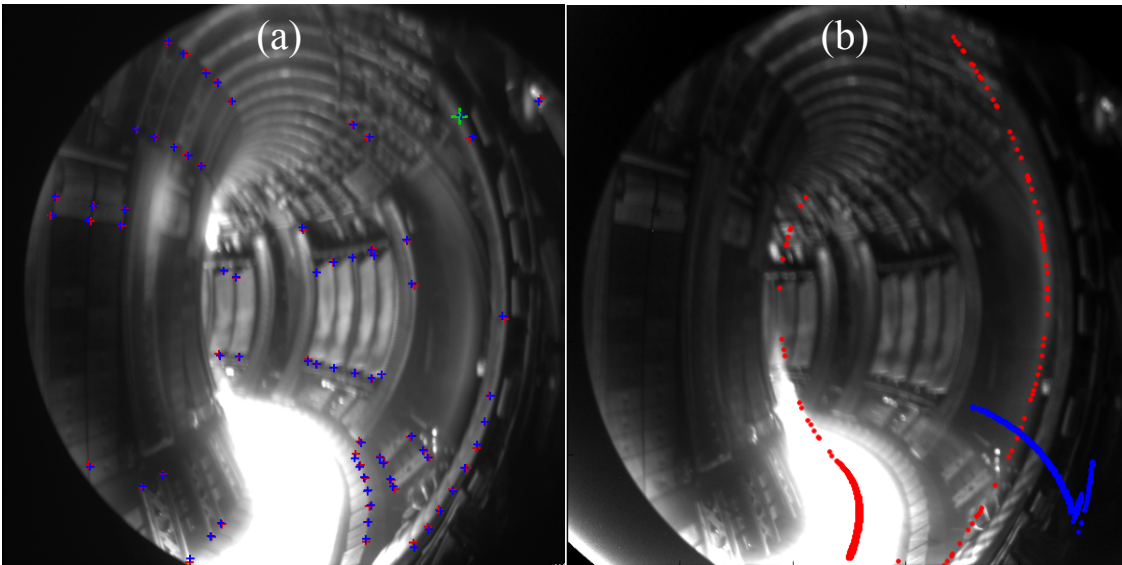


Figure 3.8: (a) Example spatial calibration showing the manually selected points (red) and the fitted and re-projected points (blue). (b) Pixels tangent to the separatrix (red) and tangent at a fixed vertical height (blue).

accuracy, a sufficient number of location pairs must be included. These locations pairs map a pixel location to the intersection of that pixel with the vessel surface. Such information was obtained by use of the calcam software [100] developed by S. Silburn at JET, where a CAD model of JET gives the coordinates of in vessel structures which may be identified in the camera image manually. Clearly, many suitable structures are visible in figure 3.6 for both camera systems.

Once a sufficient number of point pairs have been selected, the calcam software driven by the openCV module implemented in Python, minimises the error of the pixel locations produced by the camera model and re-projects those pixels onto the same image from which they have been chosen. An example of an accurate re-projection for the KL1 system is shown in figure 3.8 (a). The estimated uncertainty in the re-projection is 3-4 pixels.

The LOS vector for each pixel, calculated using the model parameters, maybe used to traces the pixel ray through Cartesian space. After converting to cylindrical polar coordinates, EFIT [101] may be used to provide the ψ along the pixel ray. The minimum of ψ along this pixel ray is the tangent flux surface of that pixel. Calculating for each pixel on the CCD, pixels which are tangent to a particular flux surface, for example the separatrix, may then be selected. Example pixels tangent to the separatrix are shown in figure 3.8 (b), showing both the inboard and outboard sides. From the point of view of performing inversions, it is more relevant to pick pixels tangent to flux surfaces at a fixed vertical height. An example selection of pixels is also shown in figure 3.8 (b).

3.4.3 Inversion methods

For the KL1 and KL11 camera systems, 1D and 2D tomographic inversion methods were applied, yielding emissivity profiles in R and (R, Z) , respectively. The 1D inversion method, developed as part of this thesis is detailed in section 3.4.3.1. The 2D inversions were performed using the *kl11* software developed by Dr. James Harrison [102].

3.4.3.1 1D inversion

A radial emissivity profile, $\epsilon(R)$, may be calculated by assuming toroidal symmetry and applying a discretized Abel inversion to the radial brightness profile. This geometry is demonstrated in figure 3.9. The emission is assumed to be structured as concentric annuli, where ϵ on each annuli is constant. Each pixel is a chord viewing through these layers and thus the brightness on each pixel is due to ϵ in each layer and the length of the pixel chord, L , in that layer. This may be expressed by the equation

$$Br_i = \sum_j L_{ij} \epsilon_j \quad (3.8)$$

where subscript i refers to the pixel and j to the emission layer. The number of emission layers is defined to be the same as the number of pixel rays. From inspection of figure 3.9, it can be seen that

$$L_{ij} = 2 \left(\sqrt{R_j^2 - R_{Ti}^2} - \sqrt{R_i^2 - R_{Ti}^2} \right) \quad (3.9)$$

where R_κ is the outer most radius of emission layer κ which has finite width $\delta R_\kappa = R_\kappa - R_{\kappa+1}$ for $\kappa = i, j$. The tangency radius of pixel i is $R_{Ti} = (R_i + R_{i+1})/2$ which is obtained using the method described in section 3.4.2.3. The innermost emission layer the pixel passes through, where $i = j$, is the exception to equation 3.9 and in this case $L_{ii} = 2 \left(\sqrt{R_j^2 - R_{Ti}^2} \right)$. Clearly the R_{Ti} requires knowledge of R_{i+1} . In practice for the inner most pixel, this may be obtained from those pixels radially inward of the set extracted from the CCD (see blue points in figure 3.8).

The entire system is described by a set of linear equations which may be expressed by the matrix equation $\vec{B}_r = \mathbf{L} \cdot \vec{\epsilon}$, where \mathbf{L} is the triangular matrix of lengths, and may be simply solved via $\vec{\epsilon} = \mathbf{L}^{-1} \cdot \vec{B}_r$.

3.4.4 Ionisation profiles

After obtaining a radial D_α emissivity profile $\epsilon(r)$, the ionisation profile, S_{ion} , may be simply obtained via $S_{ion} = \epsilon(r) \cdot (S/XB)$, where S/XB is the number of ionisations per photon and is a function of n_e and T_e . Coefficients have been taken from the ADAS database [103].

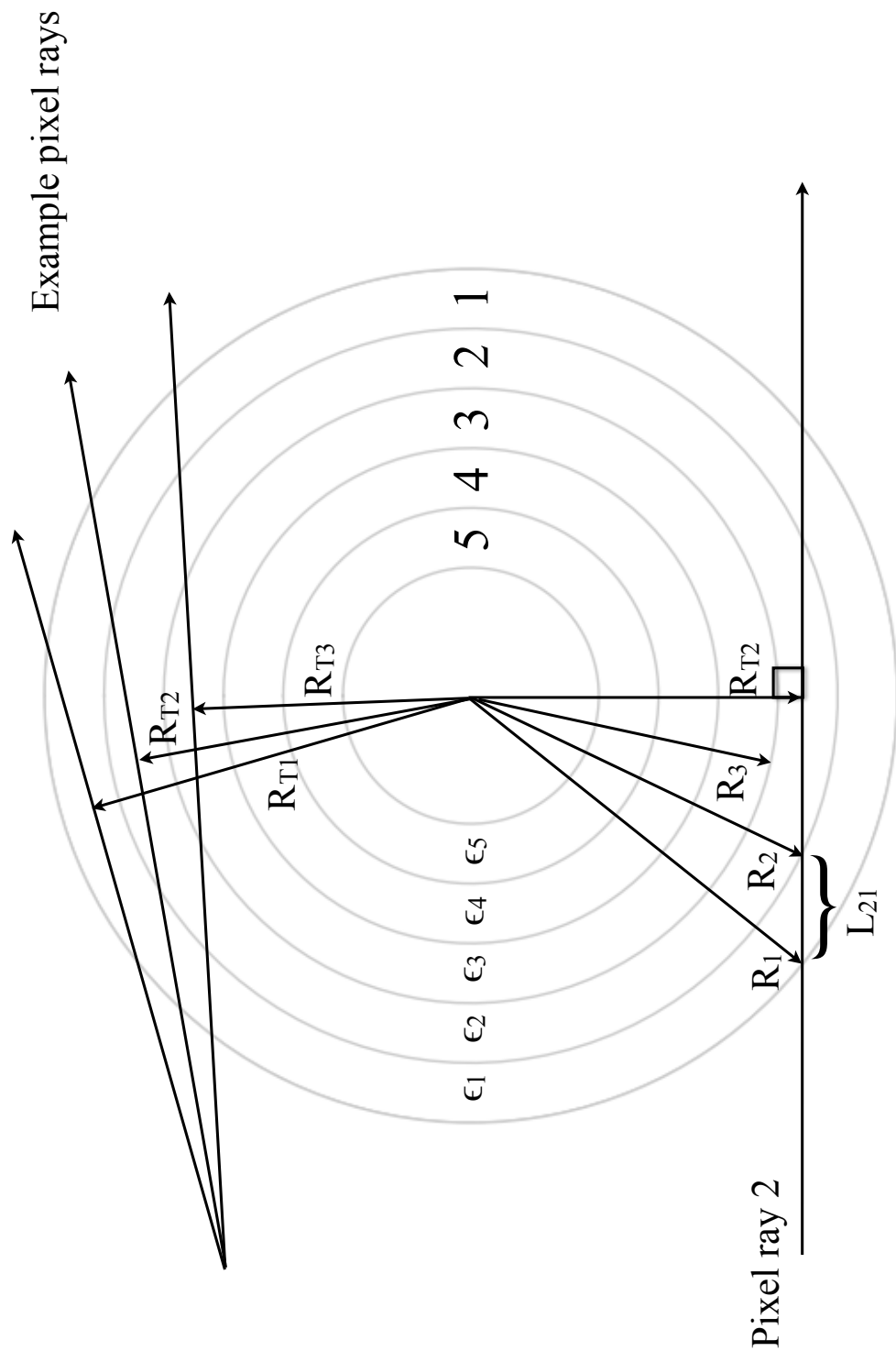


Figure 3.9: Top down view of 1D inversion model showing how the pixel ray length through each annuli of constant emission is calculated. The number of annuli layers is defined by the number of pixels over which the Abel inversion is being performed.

3.4.5 Radial D_α view-chord

An absolutely calibrated radial D_α viewchord provides a complementary measurement to the tangential viewing CCD. The view chord is toroidally separated from the tangential D_α but similar relative to the nearest limiters on the LFS. The viewchord intersects a limiter on the HFS.

3.5 Langmuir probes

Both the divertor and main chamber LFS flush mounted limiter probes have been used in this thesis. In the typical manner, a current-voltage (I-V) curve is obtained by sweeping the probe bias [19]. Both n_e and T_e may be calculated from this I-V curve, although only the divertor probes received sufficient flux to make reliable measurements of n_e and T_e .

In addition to measurement of n_e and T_e , operating the probe at constant negative bias, in so called ion-saturation mode, provides the measurement of I_{sat} which yields information on the plasma structures impacting the limiter as discussed in section 2.1.4. By taking into account the effective area of the probe projected along the direction of the total magnetic field, the current density to the probe, J_{sat} , may be calculated.

3.5.1 Identifying intermittent events

As described in section 2.1.4, it is well known from literature that the PDFs of such ion collection phases are positively skewed. Clearly it is useful to identify those regions of the signal that are associated with the filaments. One simple method is to define a threshold where regions of the signal above the threshold are considered filaments and regions below are considered part of the background plasma.

There are two commonly used thresholds. The first is an arbitrary choice of 2.5σ above the mean value of the signal in some time window where the plasma conditions do not vary significantly. An alternative method is to find the threshold which minimises the absolute value of the skewness of the data below it, referred to as the S0 method in this thesis. Events above this threshold therefore contribute to the positive skew of the data.

Using the minimum skewness is a more robust determination of the threshold than simply 2.5σ , or any multiple of σ , above the mean. For a perfectly gaussian distributed signal, shown in figure 3.10 (a), where large amplitude intermittent events are not present, the 2.5σ method would suggest that 1% of the signal is due to filaments. Comparatively, the absolute value of the skewness of such a signal would only be minimised by encompassing all of the data (shown in (c)), i.e. the upper limit of the data, and therefore no filaments would be identified using the S0 method. For the case of a positively skewed signal, shown in 3.10 (b), the 2.5σ exceeds the S0 threshold ((d)) and will therefore disregard information related to the intermittent events. For this reason, the S0 method is used in this thesis unless otherwise stated.

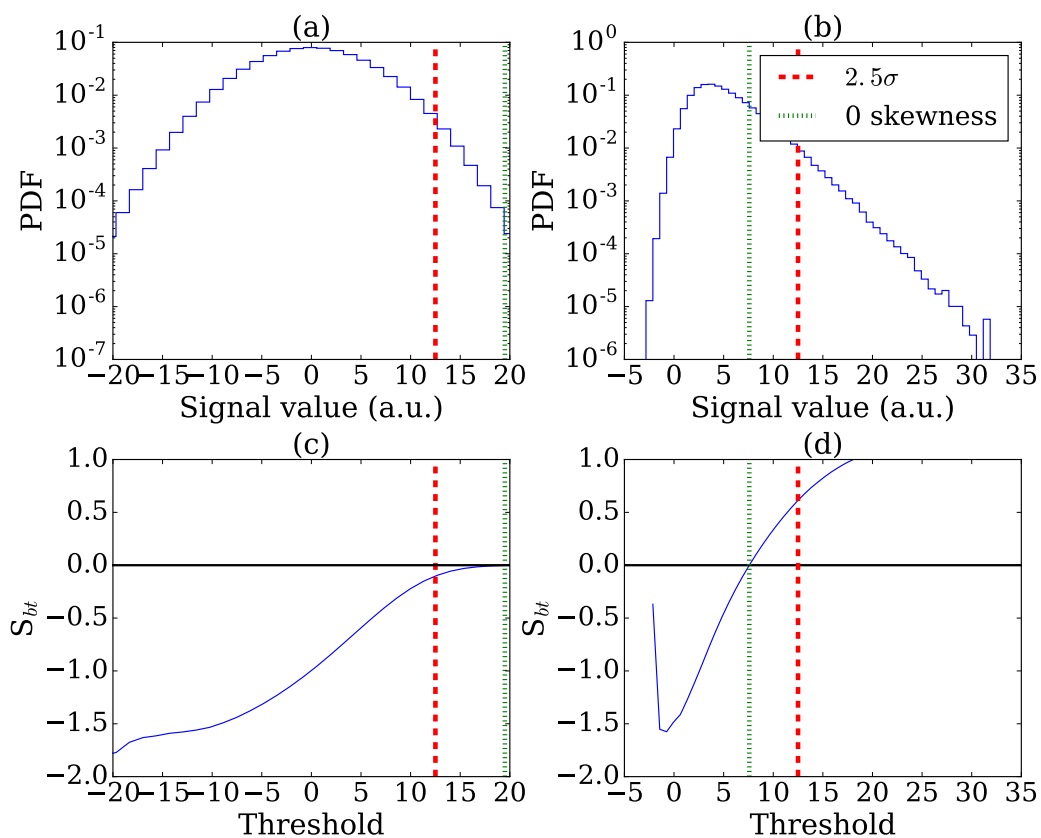


Figure 3.10: Comparison of the minimum skewness method and 2.5σ method. Gaussian, (a), and positively skewed, (b), PDFs where vertical lines indicate different thresholds. Skewness of the data below the threshold in the Gaussian, (c), and positively skewed, (d), cases.

3.5.1.1 Conditional averaging and correlations

After identifying the intermittent structures in a signal, temporally aligning the structures to their respective peaks and averaging over events produces a conditionally averaged waveform which may change dependent upon the plasma conditions. It should be noted that inevitably the S0 method will determine regions of the signal that are due to the background fluctuation as intermittent events. However, assuming the background is Gaussian distributed, those falsely identified events should have a negligible effect if using a sufficient number to average over.

Complementary to conditional averaging are autocorrelations defined by

$$\Delta(\tau) = \frac{1}{\sigma^2} \langle (x(t) - \langle x \rangle)(x(t + \tau) - \langle x \rangle) \rangle \quad (3.10)$$

where $x(t)$ is the fluctuation signal, τ is the relative shift, with angled brackets indicating the expectation value. In the context of limiter probe signals, the autocorrelation provides similar information to the conditional average, i.e. the characteristic time over which events in the signal are correlated. It is typical to consider such correlations to be reliable above $1 - 1/e \approx 0.63$ and unreliable below 0.36 (or two e-folding lengths).

Single point measurements cannot separate whether the change to the conditional average, or autocorrelation, is a result of changes to filament size or velocity. The multi-headed probe required for identifying filament velocities and sizes was removed from JET-ILW in 2013. An alternative option was to utilize the varying depth of flush mounted probes on the LFS limiter at the same Z . Cross-correlations obtained were, however, relatively poor with peak values of 0.2 and therefore analysis of such cross-correlations has not been included in this thesis.

3.5.1.2 Connection between J_{sat} and radial ion flux

It is important to connect the total radial flux toward the main chamber surface and the J_{sat} measured by the limiter probe. A method was developed in [95] to make this relation and is given by

$$I_{wall} \cong C_{geom} \cdot (n_e T_e^{1/2})_{windowpane,O} \cdot \lambda_{shadow} \quad (3.11)$$

where I_{wall} is the total flux to the wall and C_{geom} is a constant depending on the magnetic geometry and intersection with solid surfaces, which is fixed in the horizontal target cases here. J_{sat} is proportional to $(n_e T_e^{1/2})_{windowpane,O}$, the O referring to the stagnation point in parallel flows, generally assumed to be the outer midplane which is near the limiter probe in this case. The density decay length in the limiter shadow λ_{shadow} is directly measurable by the Li beam. In [95], λ_{shadow} was found to increase by around 50% for a factor two rise in \bar{n}_e . Over the same range I_{wall} increased by more than an order of magnitude. Therefore one may consider J_{sat} as a proxy for the total radial flux to the wall with the caveat of simultaneously varying λ_{shadow} .

3.6 Radial flux analysis method

A model, based on particle continuity and initially developed by LaBombard [81], has been used to infer the profile of the radial flux. This model was extended to take into account the leakage of neutrals from the divertor by Lipschultz [49], and is implemented in this thesis, with results presented in chapter 4.

The model is as follows. Considering the continuity equation at a position r in the SOL, separating out the components parallel and perpendicular to the flux surface at r :

$$\nabla_{\perp} \cdot \Gamma_{\perp}(r) + \nabla_{\parallel} \cdot \Gamma_{\parallel}(r) = S_{ion}(r). \quad (3.12)$$

Solving for the radial flux Γ_{\perp} :

$$\Gamma_{\perp}(r) = \int_{r_{sep}}^r (S_{ion} - \nabla_{\parallel} \cdot \Gamma_{\parallel}) dr + \Gamma_{\perp,sep}. \quad (3.13)$$

The drainage to the divertor along the magnetic field, $\nabla_{\parallel} \cdot \Gamma_{\parallel}$, may be approximated as $M(r)n(r)c_s(r)/L_{\parallel}$ where M is the local Mach number, $c_s = k(T_i + T_e)/m_i$ is the sound speed, n is the density and L_{\parallel} is the field line length from the midplane to the divertor target, calculated numerically using EFIT.

The flux across the separatrix, $\Gamma_{\perp,sep}$ is given by

$$\Gamma_{\perp,sep} = \int_0^{r_{sep}} S_{ion}(r) dr + f_c \int_{r_{sep}}^{r_{wall}} \frac{M(r)n(r)c_s(r)}{L_{\parallel}(r)} dr. \quad (3.14)$$

Equation 3.14 is justified as follows. In equilibrium, the total ion flux across the separatrix must be equal to the total amount of ionisation occurring inside the core. The first term on the right hand side of eq.3.14 is the ionisation occurring inside the separatrix in the main chamber. The second term on the right hand side of eq.3.14 represents the ionisation inside the separatrix in the divertor region,(i.e. the X-Point). The latter may be inferred as follows. The plasma in the SOL drains to the divertor as well as moving radially outward. The total drainage is the second term on the right hand side of eq. 3.14 without f_c . This drainage is incident upon the surfaces in the divertor and becomes neutral atoms and/or molecules. These neutrals may be ionised before entering the core, and return to the vessel surfaces, or they may enter the core, ionise and fuel that plasma. Alternatively, they may 'leak' from the divertor, through vessel structures, up to the main chamber where they contribute to the neutral pressure there along with locally recycled neutrals. The fraction of neutrals proceeding directly from the divertor to the core is f_c . The leakage fraction is therefore $1 - f_c$. Previous studies on C-mod and DIII-D have estimated $f_c=0.9$ [49]. On JET-ILW, comparing vertical target and horizontal target divertor configurations at a given density and current, the sub-divertor pressure was $\times 3$ higher in vertical target compared to horizontal, where as the mid-plane pressures from the Baratron and Penning gauges were almost identical. This suggests the leakage of neutrals from the divertor does not contribute significantly

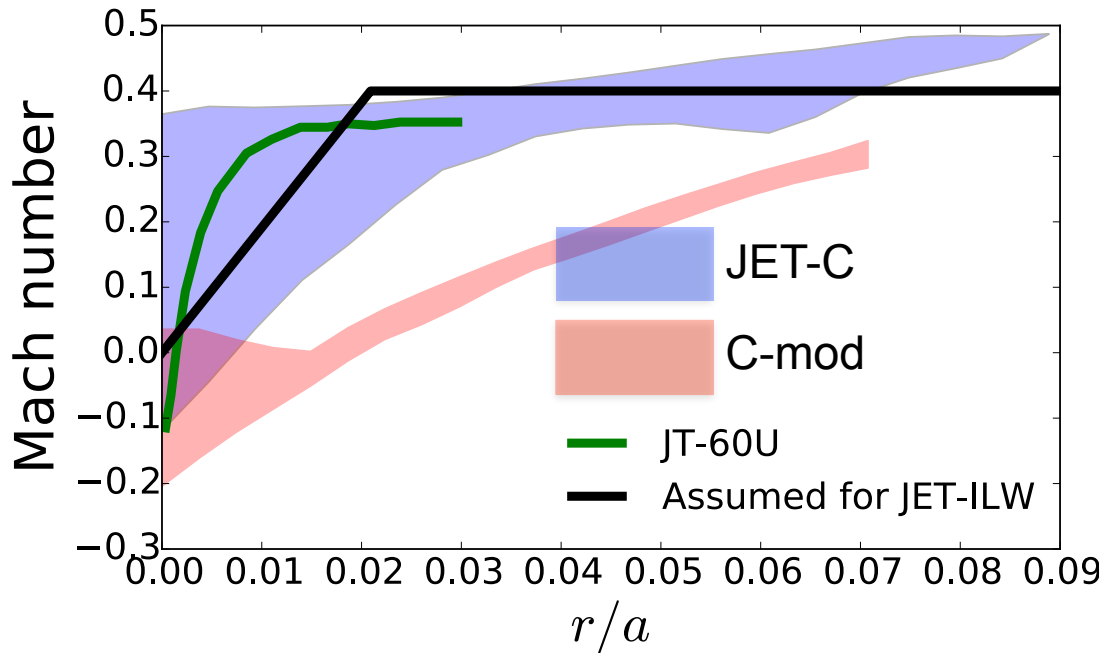


Figure 3.11: Mach profiles from multiple machines. No direct measurement of the JET-ILW was available and therefore an assumed profile (black line) was used. The radial coordinate is 0 at the separatrix and normalised to the machine minor radius.

to the neutral pressures in the main chamber, consistent with the assumptions in the analysis.

The M profile was estimated due to a lack of direct measurement. Measurements from tokamaks, including JET, have informed the choice of assumed profile (see [49] and references therein). Figure 3.11 shows the M profile used in this analysis and those from other tokamaks.

The analysis here is not identical to the method used in [49]. In that study the radial flux at the wall, $\Gamma_{\perp,wall}$, was directly measured using a 'window frame' technique, detailed in [95], and used as a boundary condition which they argued accounted for poloidal and toroidal variations of the profiles. Here, no such boundary condition is used and therefore profiles are more sensitive to the assumptions.

After obtaining a radial profile of Γ_{\perp} , an effective convective velocity, $v_{eff}(r) = \Gamma_{\perp}(r)/n(r)$ is used as a characterisation of the radial transport in the SOL.

Chapter 4

Inferring radial velocities in the SOL of the JET main chamber

4.1 Introduction

This chapter is structured into two main sections which take different approaches to assessing the radial velocity of plasma impacting the main chamber surfaces. This first section presents results obtained by applying the time averaged radial flux analysis method, detailed in 3.6. The second section presents a statistical analysis of the ion-saturation current measured by a flush mounted limiter probe. Both sections refer to the same data set, described in 4.2. A discussion is given and conclusions drawn in sections 4.5 and 4.6 respectively.

4.2 Experiments

The data used in this chapter are taken from dedicated pulses (JPN 89344-89353). Time traces of representative pulses are shown in figure 4.1. D₂ fuelling ramps were performed at plasma currents $I_p = (1.5, 2, 2.5, 3)$ MA with an equivalent toroidal field, B_t (T), such that the $q_{95} = 3.05$ for all pulses. The outer midplane separatrix to limiter gap was 5.0cm. The outer strike point was on the horizontal target. D was injected equally from GIM9 (low field side (LFS) divertor SOL) and GIM11 (private flux region (PFR)) (see figure 3.2 for locations). The fuelling ramps evolved the divertor from sheath-limited to detached conditions at all I_p . The 4Hz oscillation in figure 4.1 (c) is due to strike point sweeping which was used to obtain fully resolved divertor profiles.

4.3 Time averaged radial flux analysis

4.3.1 Results

As a validation of the radial emissivity profiles obtained from the KL1 camera, the integral of the D_α emissivity profile, a brightness, has been compared to the brightness from a radially viewing D_α view-chord, shown in figure 4.2. There is fairly good

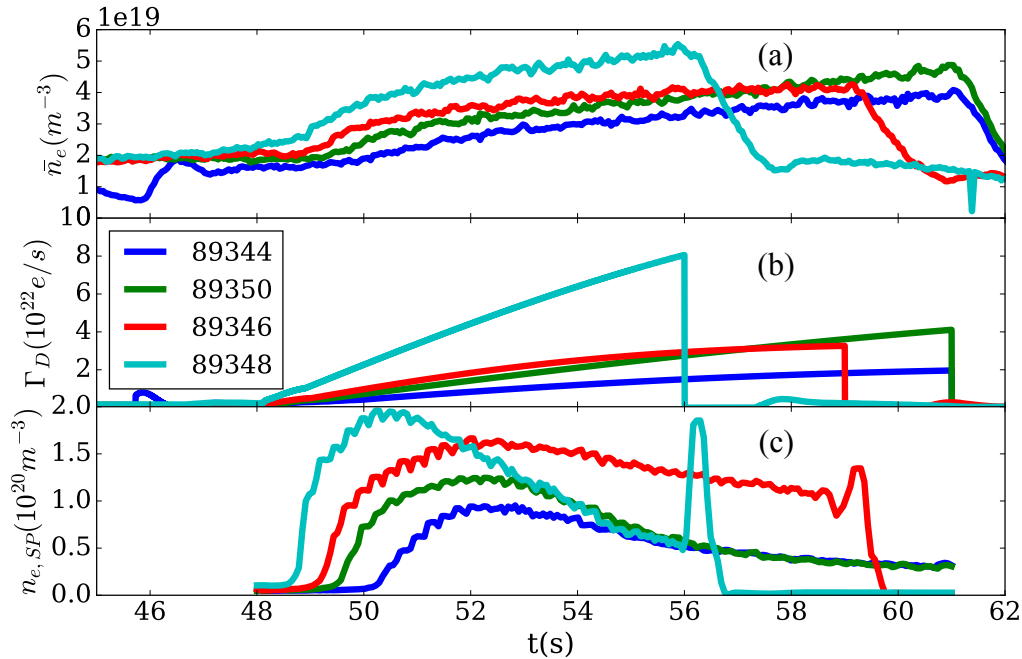


Figure 4.1: Time traces for Horizontal target L-mode D fuelling ramps line-average density \bar{n}_e , fuelling rate Γ_D and the strike point electron density $n_{e,SP}$. I_p are ordered (1.5, 2, 2.5, 3)MA for (blue, green, red, cyan).

agreement between the two diagnostics but one is not systematically higher than the other. The radial view-chord would be expected to be higher given it views the HFS in addition to the LFS, but the ratio is approximately 1:1. In any case it would suggest that the LFS and HFS brightnesses scale similarly. A systematic variation with I_p is evident, however. For a fixed integral value of the emissivity, with increasing I_p , the view-chord brightness increases slightly.

Figure 4.3 shows the input and resultant profiles of the radial flux analysis for a selection of times slices from discharges with $I_p = 1.5$ MA ((a)-(f)) and $I_p = 3$ MA ((g)-(l)). The range of \bar{n}_e span divertor conditions from sheath-limited to detached for all I_p .

Considering first the input profiles for the analysis, the n_e profiles change substantially over the selected range, being initially exponential and flattening with increasing \bar{n}_e . A study of the profile characteristics in response to changing plasma conditions is given in later chapters and is not the emphasis of this section; the density profiles are used simply as inputs into the radial flux analysis. Assumed T_e profiles are shown in (b) and (h). As expected, S_{ion} profiles (c),(i) increase with core and SOL density. Ionization is being increased both by increasing local n_e and neutral influx from plasma recycled on main chamber PFCs. S_{ion} broadens with the n_e profile into the far SOL. It should be noted that at low density, the CCD has poor SNR.

With increasing density, the $\Gamma_{\perp}/\Gamma_{\parallel}$ fraction increases. Initially, the drainage exceeds the radial transport. At the highest densities, Γ_{\perp} approaches the estimated

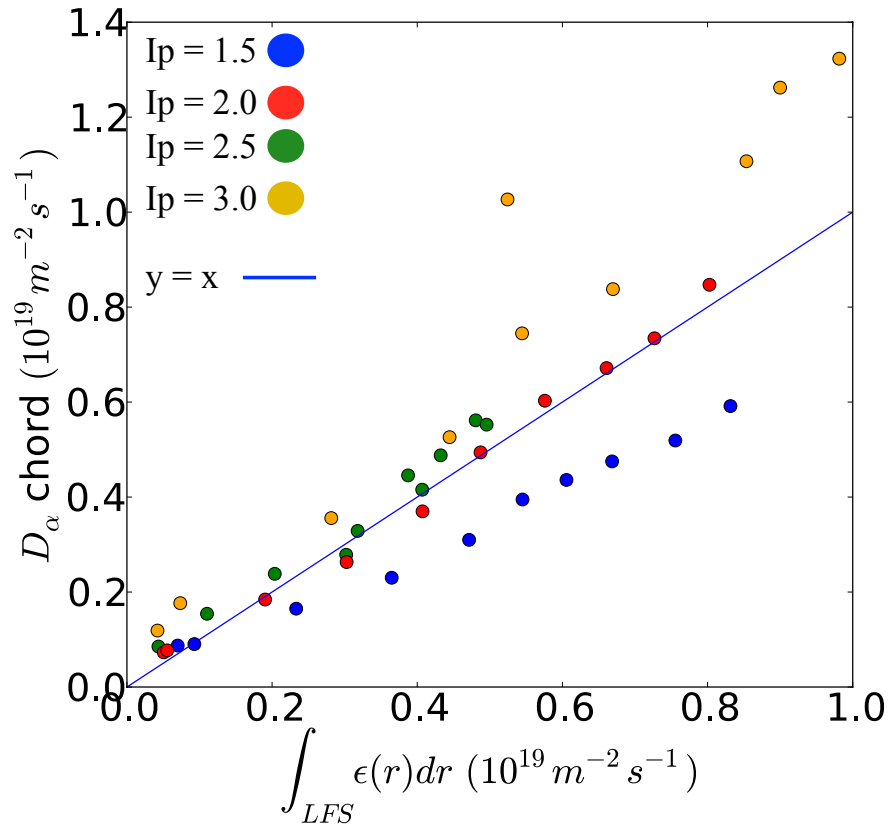


Figure 4.2: D_α radial view-chord and the integrated LFS emissivity derived from the brightness profile measured by the camera.

drainage and slightly exceeds it in the far SOL.

The inferred v_{eff} profiles are shown in (f),(l). At the separatrix, $v_{eff} = 5-10\text{ms}^{-1}$. After the shoulder has formed v_{eff} increases in the region $r - r_{sep} < 3\text{cm}$, but there is little effect near the limiter radius. These observations are consistent at all I_p .

Evident from the v_{eff} profiles in figure 4.3 is the higher value at the limiter in the higher I_p case. This effect was found to be systematic as is shown in figure 4.4. $\Gamma_{\perp,lim}$ is plotted as a function of $\bar{n}_{e,lim}$, for all I_p along with a linear fit. The gradient of the fit $\Gamma_{\perp,lim}/n_{e,lim} = v_{eff,lim}$, the velocity at the limiter radius. The approximately linear dependence of $v_{eff,lim}$ on I_p is shown inset in figure 4.4.

Using the pressure Baratron pressure gauge, it is possible to estimate the flux of neutrals back toward the plasma. Figure 4.5 shows a comparison between this neutral flux $\Gamma_{0,lim}$ and $\Gamma_{\perp,lim}$. For all I_p , $\Gamma_{0,lim}$ exceeds $\Gamma_{\perp,lim}$ by approximately factor two. The uncertainties in the neutral influx data are due to vibration of the vessel.

4.3.2 Sensitivity analysis

There are several assumptions in the analysis which include the profiles of T_e and M , the value of f_c , the n_e profiles shift and the separatrix uncertainty. In this section, the effect of these uncertainties is examined.

Γ_{\perp} and v_{eff} vary by around 50% across the potential range of T_e , depicted in figure 4.6. Plotted are experimental data from the JET-ILW and JET-C, measured using

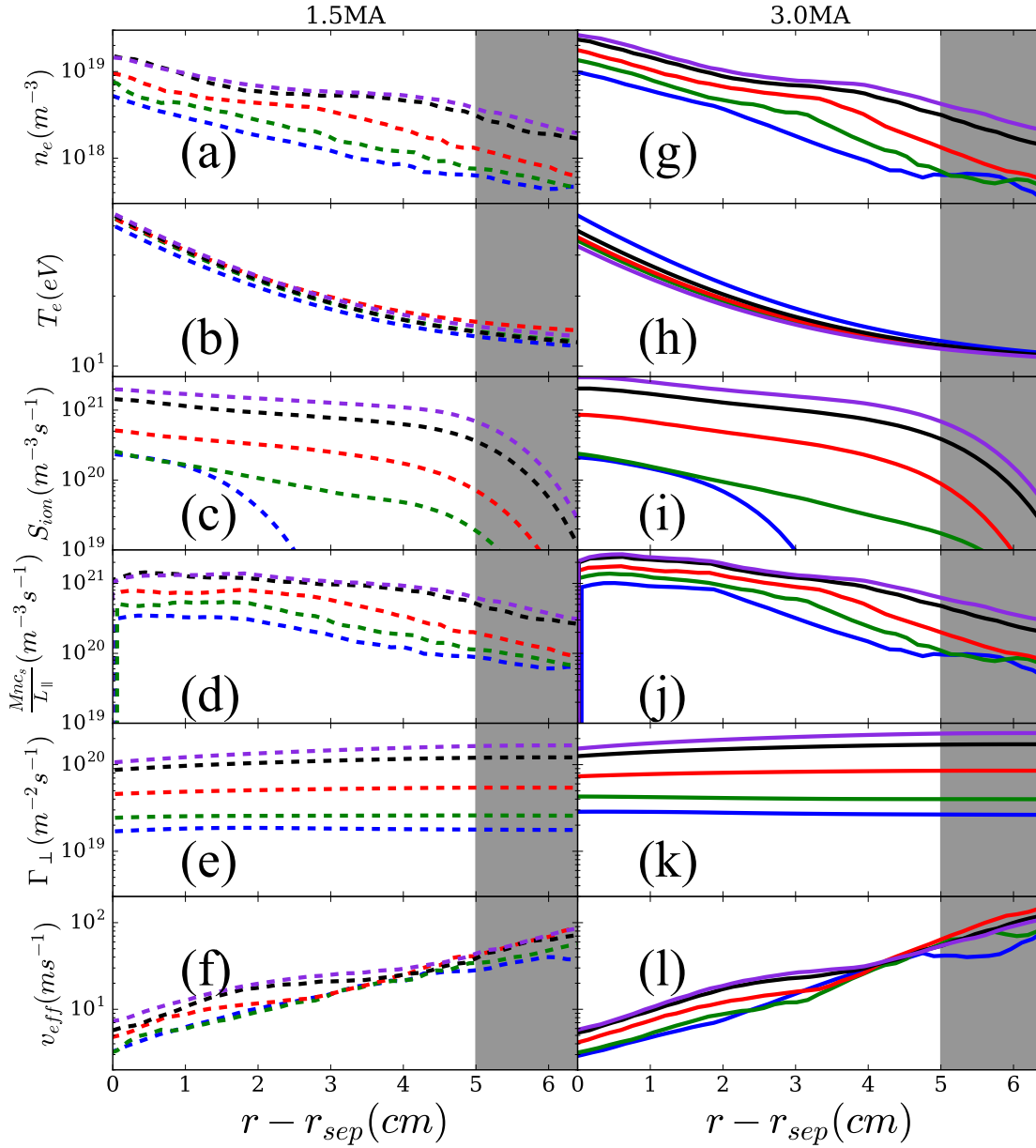


Figure 4.3: Radial profiles in the SOL of the inputs (a-d and g-j) and outputs (e,f,k,l) to the radial flux analysis. The highest and lowest I_p cases are shown. Shaded regions indicate the limiter shadow.

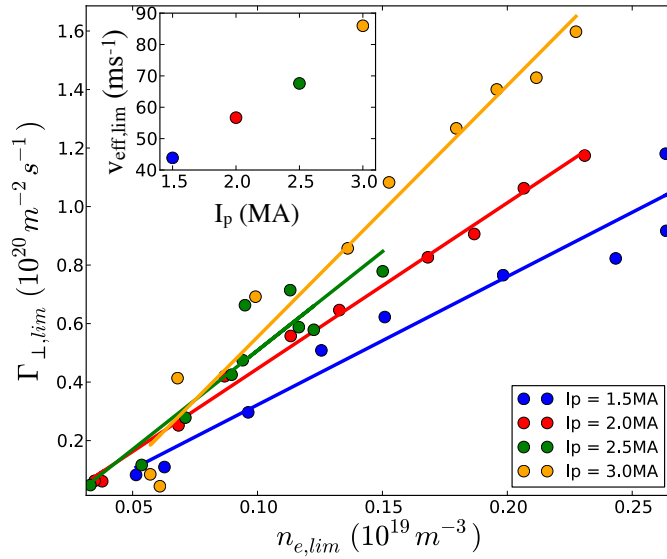


Figure 4.4: The inferred flux density at the limiter radius, $\Gamma_{\perp,lim}$, against the density at the limiter radius, $n_{e,lim}$. Solid lines show linear fits to the data points, the gradient of which is the effective velocity at the limiter radius, $v_{eff,lim}$, is shown inset as a function of I_p .

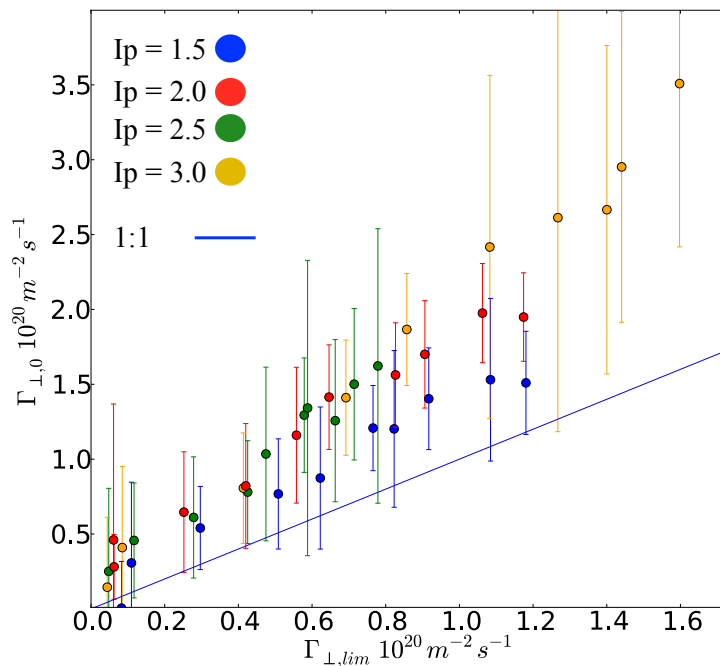


Figure 4.5: The flux of neutrals, assuming thermal velocity, $\Gamma_{0,lim}$ derived from pressure measurements (made by the Baratron), as a function of the flux density at the limiter $\Gamma_{\perp,lim}$. The 1:1 ratio is also plotted for reference.

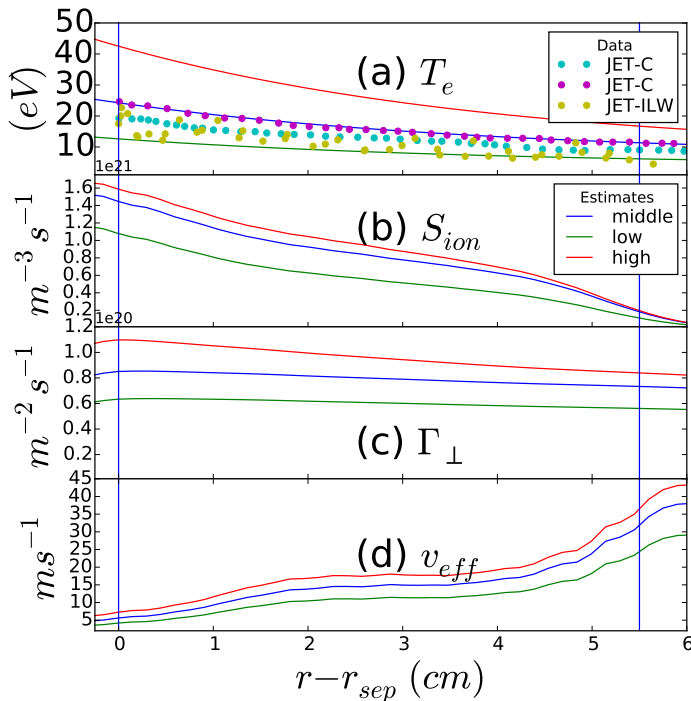


Figure 4.6: Sensitivity of radial flux analysis to T_e variation for a typical case. In (a) solid lines show the range of estimated temperatures. Points show data from the JET reciprocating probe, taken from similar discharges. The effect on the ionisation source, S_{ion} , is shown in (b). The resultant variation in radial flux density, Γ_{\perp} , and effective convective velocity, v_{eff} is shown in (c) and (d) respectively.

the RCP. The data from JET-C [104] (JPN56836,56893) and JET-ILW (JPN 81473) are taken from plasmas very similar to those used in this paper, the main difference being the addition of 1.5MW of NBI heating in the JET-ILW case. Estimates of the T_e profile are also plotted and are used in the radial flux analysis. The estimated range encompasses the measured profiles and should therefore reliably estimate the potential variation in Γ_{\perp} and v_{eff} . The T_e profile influences the radial flux analysis through both the parallel loss estimates, ($\propto T_e^{1/2}$), and the ionisation profile via the S/XB coefficient. The sensitivity of S/XB below 20eV is evident.

The sensitivity of v_{eff} to the uncertainties in the separatrix location and required shift are $\sim 30 - 40\%$. Γ_{\perp} is less sensitive, particularly in the far SOL, as shown in figure 4.7. The applied shifts encompass the potential uncertainty incurred by the equilibrium reconstruction. Both the separatrix and n_e profiles have been shifted simultaneously to maximise and minimise the parallel losses. In the maximum (minimum) case, the separatrix has been shifted inwards (outwards) by 0.5cm and the density profile shifted outwards (inwards). S/XB is a much weaker function of n_e than T_e and therefore the S_{ion} profile is not shifted in the analysis. The assumed M profile shifts with the separatrix. Despite the strong difference in parallel loss profiles, Γ_{\perp} converge in the far SOL. This is due to the increasing drainage being accounted for as a flux across the separatrix, originating from the divertor. However, the v_{eff} profiles are sensitive to the applied shifts, as would be expected due to $v_{eff}(r) = \Gamma_{\perp}(r)/n(r)$.

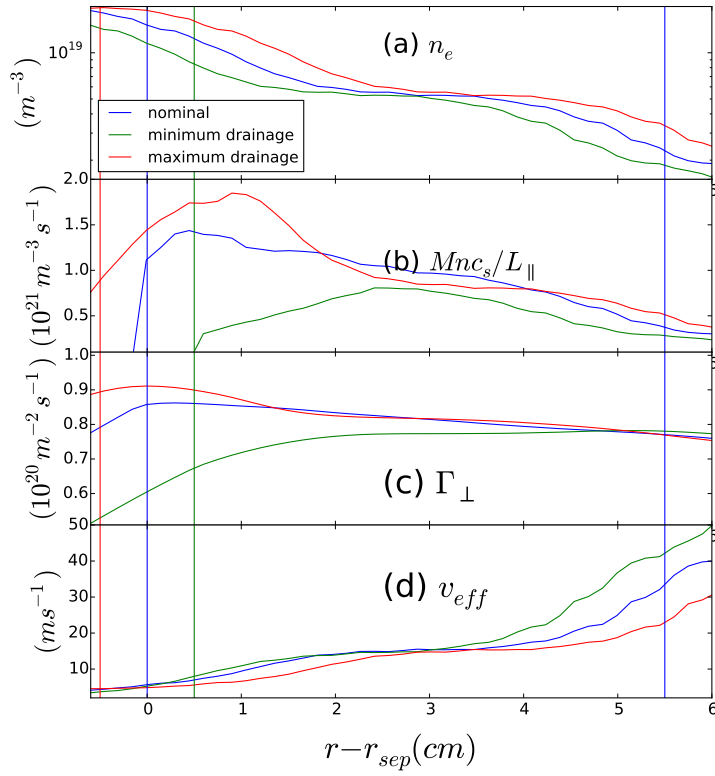


Figure 4.7: Sensitivity of radial flux analysis to variations in profile shifting and separatrix location uncertainty. The ionisation source, S_{ion} , (not shown) is assumed fixed in both location and magnitude.

Variations of the assumed M profile can incur substantial variations in both Γ_{\perp} and v_{eff} as shown in figure 4.8. In order to assess the maximum possible effect of the M profile, both an over and underestimate were used. The over estimated case was shown in figure 3.11 and the underestimated case was 0 for all r . Arguably, such a variation is a measure of the poloidal variation due to the presence of the stagnation point [95], although other plasma profiles may also vary poloidally. At low densities, there is an order of magnitude difference in Γ_{\perp} between the maximum and minimum cases in the far SOL. With increasing density, this difference would reduce to around a factor two. These differences extend to v_{eff} .

The significant number of assumptions in the analysis make estimating the net effect challenging. Simply accumulating the variation with different assumptions would suggest an uncertainty of approximately a factor three.

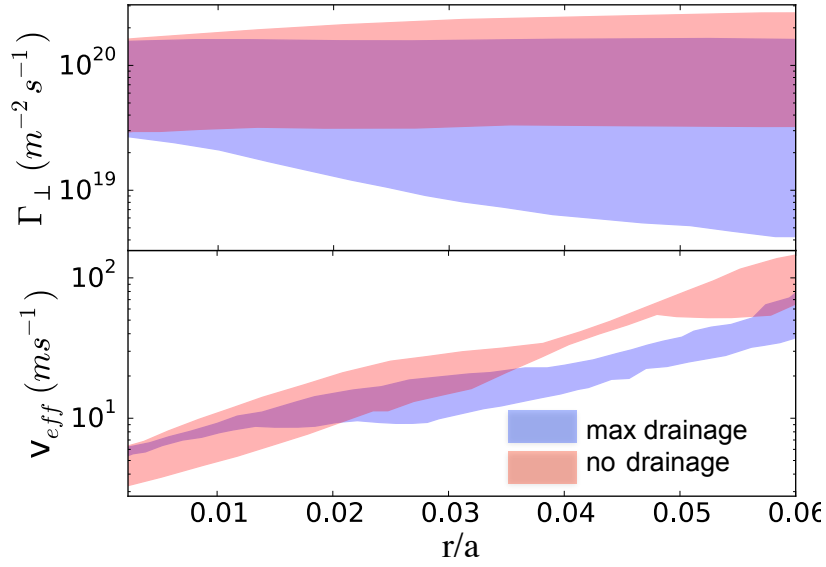


Figure 4.8: Dependence of radial flux analysis on M profile. The max drainage is the assumed profile shown in figure 3.11, with no drainage being $M = 0$ for the entire SOL.

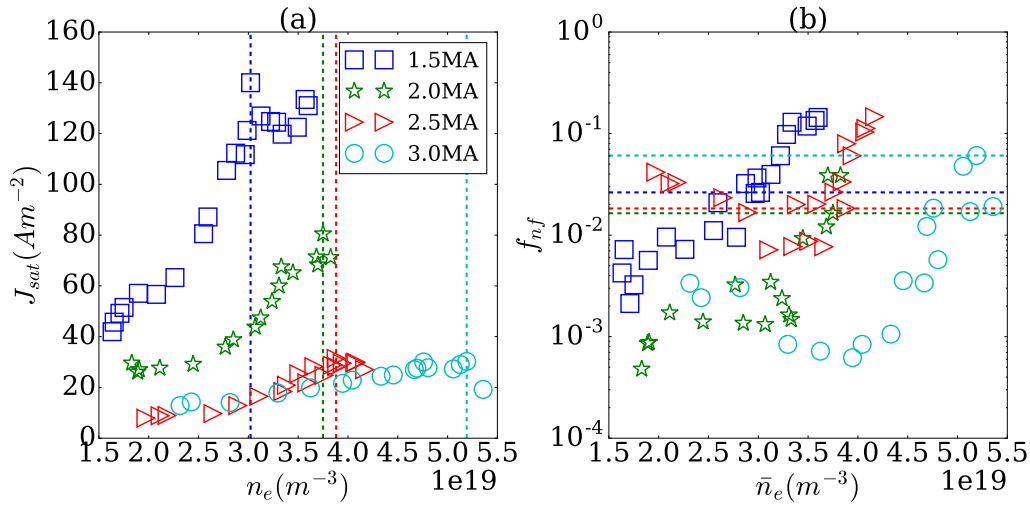


Figure 4.9: (a) Dependence of J_{sat} on \bar{n}_e for a range of I_p . Vertical dashed lines indicate the maximum J_{sat} . (b) Dependence of the signal fraction below the noise floor, f_{nf} on \bar{n}_e . Horizontal dashed lines are defined by the vertical dashed lines in (a) to indicate the value of f_{nf} before J_{sat} saturates.

4.4 Statistical analysis of limiter ion flux using the flush mounted probe

4.4.1 Results

4.4.1.1 Determining data validity

It was observed that as the radial flux toward limiter increased, as measured by J_{sat} , the fraction of the signal below the noise floor of the probe, f_{nf} , increased, often manifesting as negative currents. A study using the same data [71] states that these negative regions are due to arcing through the neutral gas present in the SOL. In order to quantify this effect J_{sat} , averaged over 0.2s time windows, and f_{nf} have been plotted as a function of \bar{n}_e in figure 4.9. With increasing density J_{sat} , (a), increases and then saturates. Vertical lines indicate the \bar{n}_e of peak J_{sat} , which determines the horizontal line in (b). Across the range of I_p , f_{nf} at the peak J_{sat} ranges from 2-6%. This is a simple determination of where the data is of 'good' or 'poor' quality. Only 'good' data (below the horizontal lines in (b)) is used in the results section. Those parts of the signal below the noise floor in the 'good' data have been removed when identifying intermittent events.

4.4.1.2 Scaling of J_{sat} with I_p

By rescaling the abscissa to f_{gw}/I_p , where f_{gw} is the Greenwald fraction [79], the data in figure 4.9 collapses onto a linear trend, shown in figure 4.10, that covers an order of magnitude in the ordinate. Data from vertical target pulses, taken from another probe, has also been included and matches well with the horizontal target. Langmuir probe data from the vertical target pulses is not used for the remainder of this chapter due to its generally poor quality ($f_{nf} \sim 0.1$)

The fraction of J_{sat} contributed by intermittent events is insensitive to both density and I_p , shown in figure 4.11. The data from figure 4.10 is repeated in black, with filament contributions, determined by different thresholds, being a fixed fraction of the total to within the scatter of the data. The minimum skewness threshold is not shown here but is typically equivalent to 0.9-1.0 σ .

As stated in section 3.5.1.2, J_{sat} is a proxy for the total radial flux with the caveat of λ_{shadow} . However, as shown in figure 4.12, there is a fairly mild difference in λ_{shadow} across I_p and in fact there is slight systematic increase in λ_{shadow} with decreasing I_p which would steepen the trend in 4.10.

Profiles in figure 4.12 have been deliberately chosen with a fixed density at the limiter radius for all I_p in order to elucidate the underlying cause of the scaling in figure 4.10. Considering the radial flux simply as $\Gamma_1 = n v_{eff}$, where n is the density and v_{eff} the effective convective velocity, such a choice of profiles isolates the dependence of filament velocities with $|B|$ (or I_p or B_t). We note that for a fixed limiter density, \bar{n}_e increases with I_p .

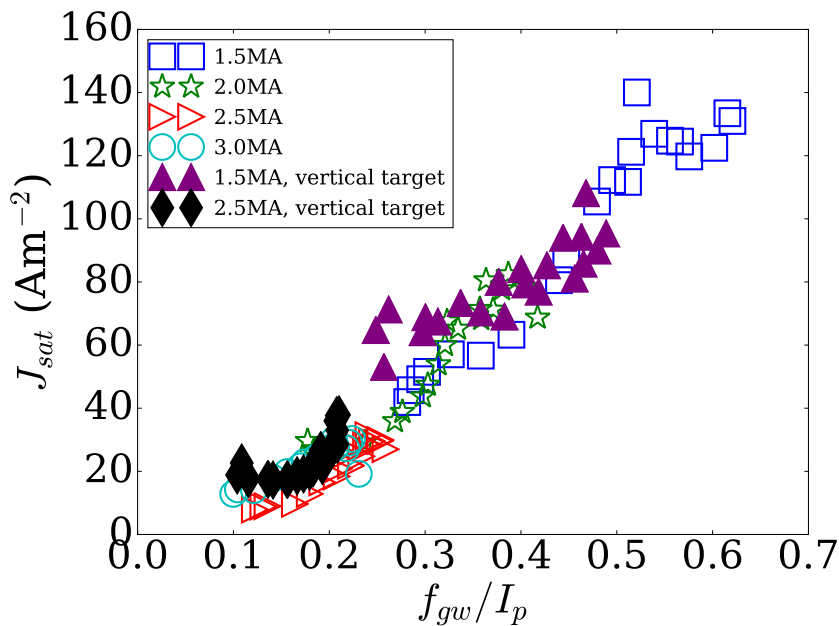


Figure 4.10: Scaling of J_{sat} with f_{gw}/I_p for a range of I_p . Data from both the horizontal (open symbols) and vertical target (filled symbols) configurations are included.

PDFs of J_{sat} taken over 0.5s windows spanning the time of profiles in figure 4.12 are shown in figure 4.13 (a). A systematic reduction in both standard deviation, σ , and mean, μ , with increasing I_p is apparent, even as \bar{n}_e is increasing simultaneously, indicating that the effect of I_p is stronger. These PDFs collapse when normalised as shown in (b), and exhibit the characteristic positive skew almost universally observed on toroidal confinement devices [63].

Conditionally averaged waveforms of the intermittent events from these time windows are presented in figure 4.14 together with the auto-correlation. Characteristic asymmetry in the rise and decay time is clear in the averaged wave form. Evident in both is the widening in temporal width with increasing I_p . Due to measurements only being taken at a single point, the velocity and size of filaments cannot be decoupled, but the observed shrinking is consistent with either velocity increases, perpendicular size reductions, or some combination of both.

This effect is demonstrated in a more statistical manner in figure 4.15 where PDFs of the waiting time between filaments, (a), and the filament duration time, (b), are shown. In accordance with stochastic models [105, 106], these parameters appear to be exponentially distributed, with fits shown by solid lines. As would be expected from figure 4.14, there is a systematic increase of the expected duration time, τ_d , with increasing I_p . The same relationship is also found with the mean waiting time τ_w . Scalings of the τ_w and τ_d against $|B|$ and $|B|^2$ are shown in figure 4.16. The uncertainties originate from the linear fits in figure 4.15 and are used to weight the linear fits (shown as solid lines). Either $|B|$ or $|B|^2$ is a plausible scaling, although the squared scaling passes slightly closer to the origin.

When incorporating data with a larger range of \bar{n}_e , the scaling of τ_w with $|B|^2$

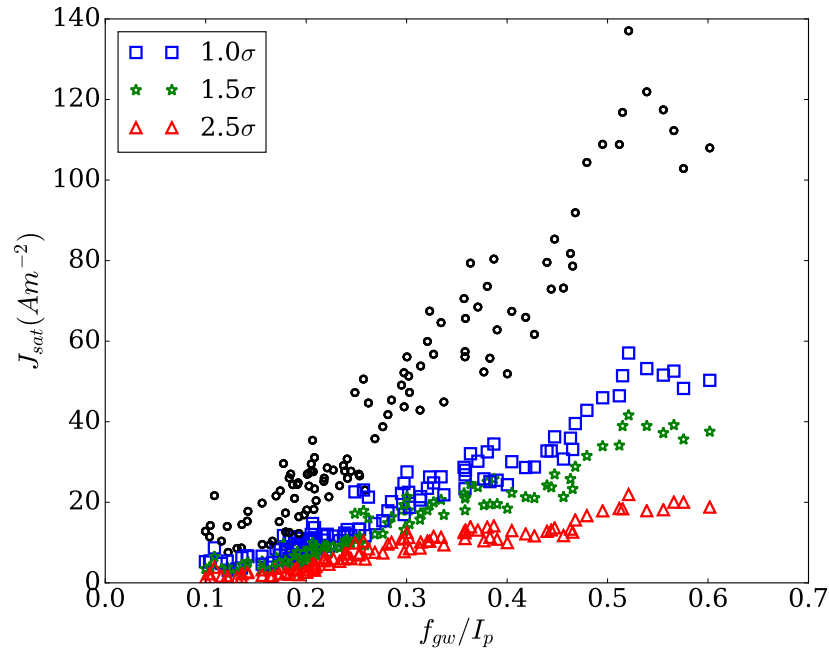


Figure 4.11: Relative contribution of intermittent events to total J_{sat} for different thresholds. Data from 4.10 is shown in black.

becomes more uncertain, but the τ_d scaling remains relatively robust, as shown in figure 4.17. Scaling with $|B|$ is not shown but the observations are generally similar. The linear fits (dashed purple lines) have been performed with the five highest \bar{n}_e , indicated by symbol size, justified by the assumption that the signal to noise ratio is generally higher at higher density, prior to the data becoming 'bad' via increasing f_{nf} . This is also evident in the lowest \bar{n}_e data contributing largely to the scatter, particularly in (b). The linear fit does not pass close to the origin, as it does in figure 4.16 (a). Given the poorly understood filament generation physics, the inability of the simple scaling to describe the data adequately is perhaps expected. The linear fit of τ_d does however pass close to the origin, and is certainly encompassed by the uncertainty of the fit. Figure 4.17 also suggests there is no general scaling of τ_d with increasing \bar{n}_e as for different I_p , the direction of increasing symbol size may be up or down or both ($I_p = 3\text{MA}$ for example).

4.5 Discussion

The first section of this chapter has attempted to characterise the radial transport in the SOL of JET-ILW Ohmically heated L-mode plasmas through the use of an effective convective velocity v_{eff} , inferred using an interpretive transport model which was initially developed by LaBombard [81], extended by Lipschultz [49] and applied here for the first time on JET-ILW.

In general, the results obtained agree well with those from other studies, in particular the relative insensitivity of v_{eff} to large increases in SOL density. As a demonstration, a collation of results from other studies is shown in figure 4.18 which includes

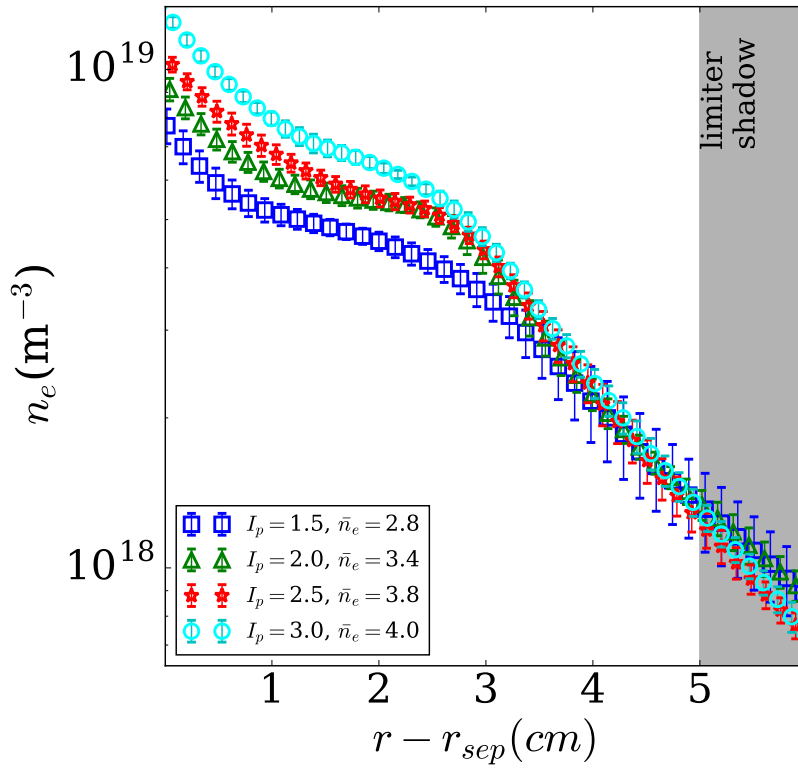


Figure 4.12: Density profiles for different I_p . Profiles have been selected such that $n_{e,lim}$ is fixed at the limiter radius.

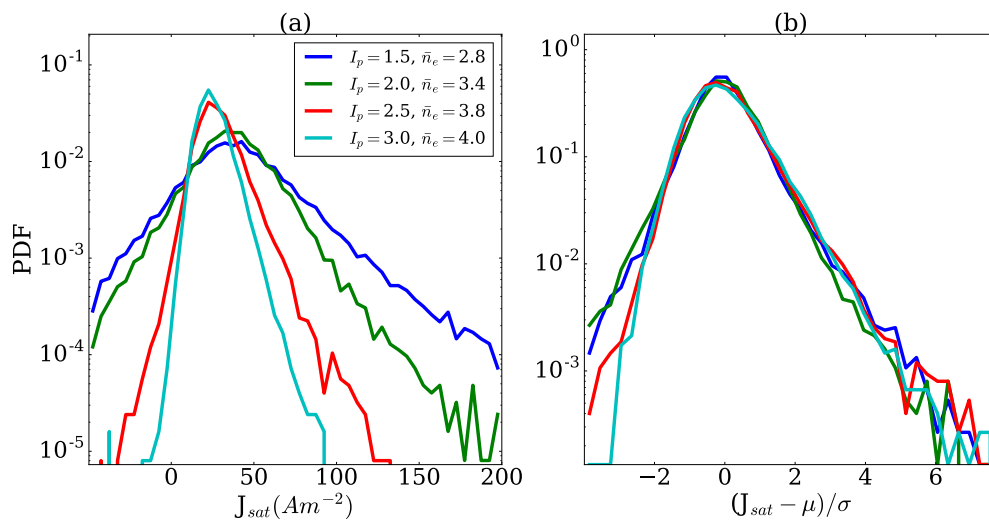


Figure 4.13: PDFs of J_{sat} taken over 0.5s windows spanning the time of profiles shown in figure 4.12. Data below the noise floor has not been removed in either the (a) or (b). In (b), μ is the signal mean and σ the standard deviation.

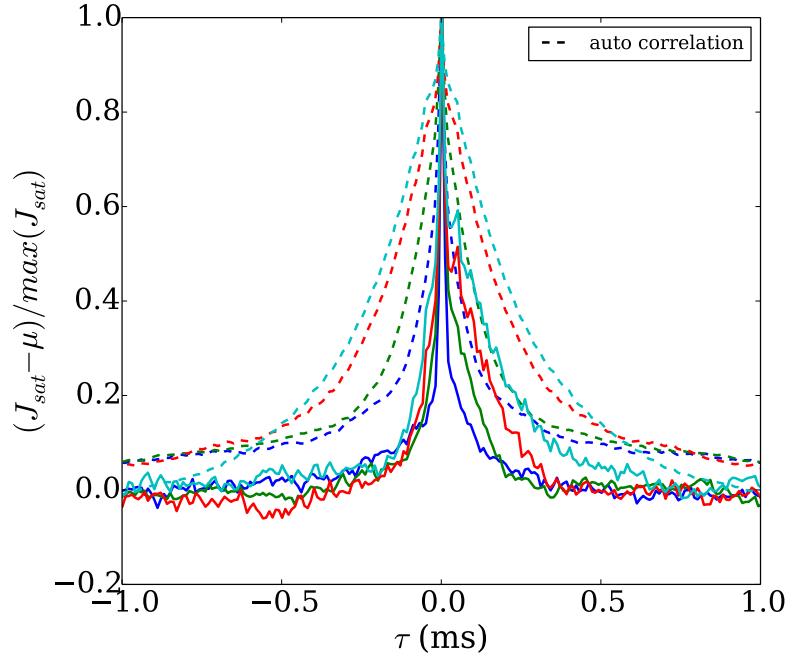


Figure 4.14: Conditional averages (solid lines) and auto-correlations (dashed lines) of J_{sat} taken over 0.5s windows spanning the time of profiles shown in figure 4.12. Colours also correspond to figure 4.12

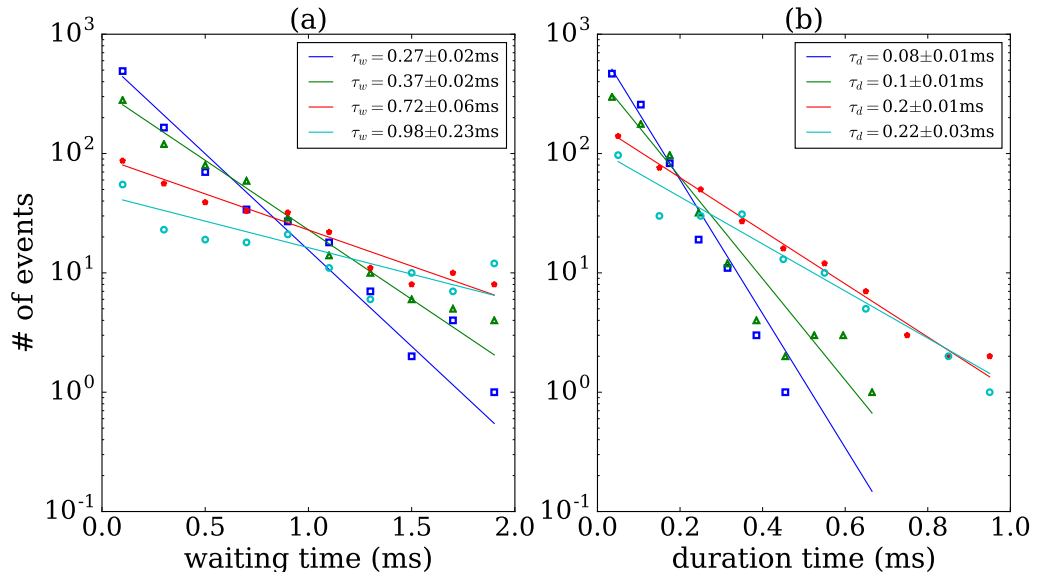


Figure 4.15: PDFs of Waiting (a) and duration (b) times for intermittent events at fixed limiter n_e . Solid lines show exponential fits to the data, weighted for \sqrt{N} , where N is the # of events. Legends show the fitted waiting time, τ_w , and duration time, τ_d , and uncertainties.

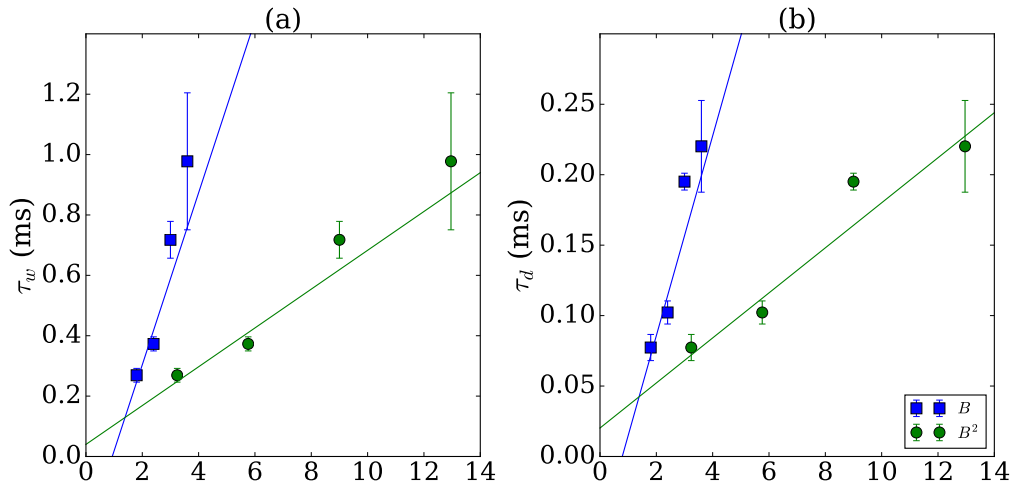


Figure 4.16: Dependence of fitted τ_w and τ_d on $|B|$ and $|B|^2$, from figure 4.15. Solid lines show linear fits.

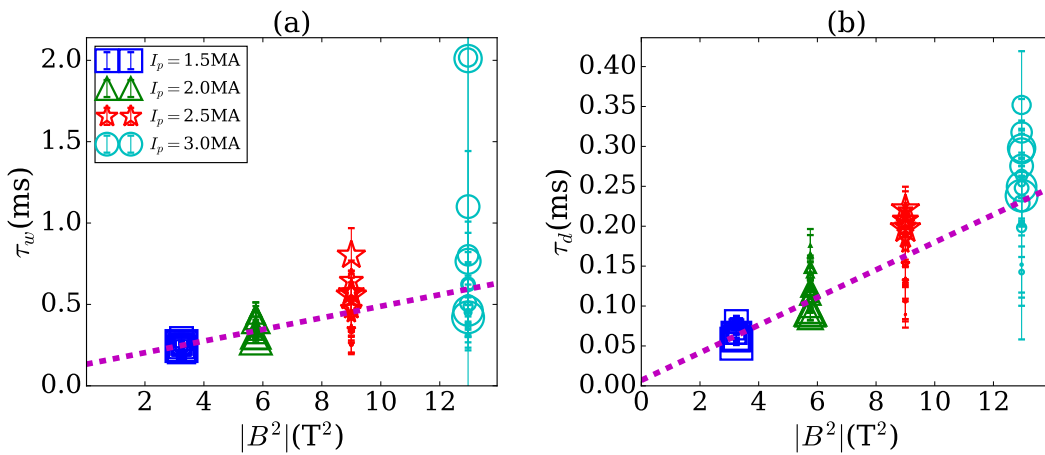


Figure 4.17: Dependence of fitted τ_w and τ_d on $|B|^2$ for a range of \bar{n}_e at each I_p . Dashed purple line shows linear fit to the five highest \bar{n}_e data points, with \bar{n}_e proportional to symbol size.

a diverse range of tokamak size, wall material and divertor configuration. The radial coordinate has been normalized to the minor radius of each tokamak for the purpose of comparison. It should also be noted that the both H-mode and L-mode plasmas are included in the DIII-D data. In the near SOL there is around an order of magnitude difference, ranging from $4\text{-}40\text{ms}^{-1}$, with the JET-ILW wall data presented here extending the lower range. With increasing radial distance from the separatrix, the range in the profiles reduces and has a factor three in range at $r/a = 1.07$. What is consistent across the profiles is the increase in v_{eff} with distance from the separatrix and the value near the limiter radius. This is consistent with the increasing dominance of filaments as the transport mechanism with increasing distance from the separatrix.

Despite being insensitive to the SOL density, $v_{eff,lim}$ for JET was found to have an approximately linear dependence of on I_p . Although this effect (factor two) is with uncertainties (factor three), the scatter is low. Comparatively, profiles of v_{eff} made using a different analysis based on Langmuir probe measurements on TCV [70] show a different I_p dependence. At the wall $v_{eff} \approx 115\text{ms}^{-1}$ for all I_p and with increasing I_p , v_{eff} at the separatrix reduced from 150ms^{-1} to 50ms^{-1} . There are significant differences in the set-up of the JET-ILW here and those TCV experiments in addition to the changing I_p . Firstly, in the TCV case the toroidal field B_t , the dominant component of the total, was fixed, where as B_t in the experiments presented here varied. Consequently, L_{\parallel} varied in the TCV experiments where as for these experiments it did not.

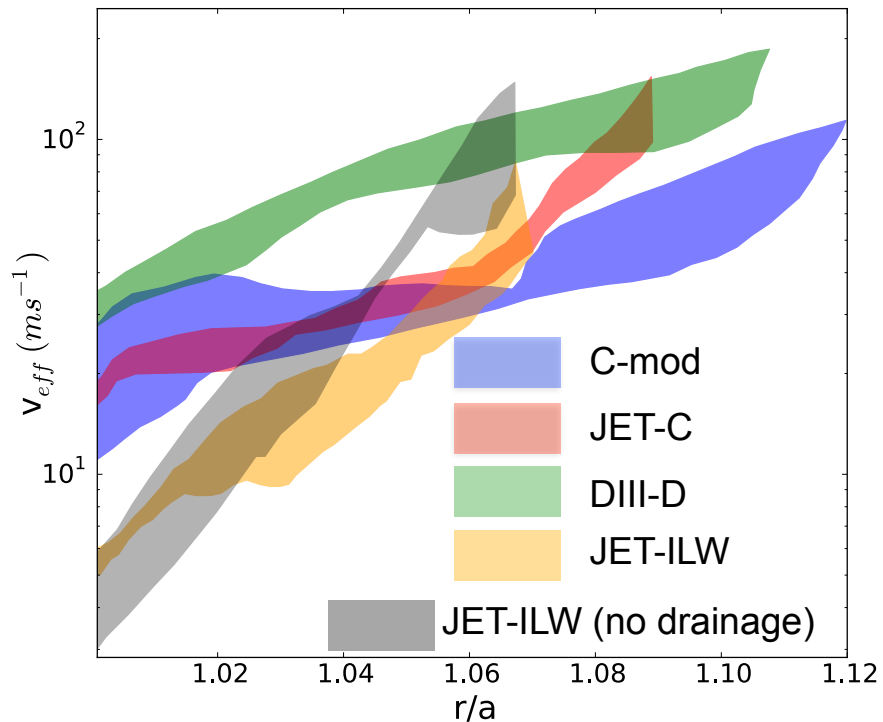


Figure 4.18: v_{eff} profiles from multiple tokamaks. The radial co-ordinate has been normalised to the minor radius.

The values of v_{eff} here are an order of magnitude lower than typical filament velocities. However, one would not expect the values to be similar as v_{eff} takes into

account filamentary and non-filamentary transport. Previous studies estimate the 50% or less of the total radial flux to be carried by filaments. Further, the non-filamentary plasma may be governed by diffusive transport, for which v_{eff} may be much lower. These effects may account for the order of magnitude difference between v_{eff} and radial filament velocities, but quantifying this effect across the SOL with filaments is beyond the capability of the Li beam diagnostic. Analysis of the high frequency (500kHz) Li beam data, which has the same view, has been performed, but the data quality was found to be poor, as detailed in appendix 1.

Turning now to the limitations of the analysis, although the measurements used to infer the transport profiles are local, the agreement with other diagnostics including the radial D_α view-chord and Baratron pressure gauge suggests the results are at least somewhat globally representative.

The sensitivity of the results to assumptions is approximately a factor two to three. The primary causes being the uncertainty in the equilibrium (and therefore profile mapping), and the assumed M profile. The uncertainty the T_e profile contributes to the uncertainty to a lesser extent due to the insensitivity of S/XB to T_e above 20eV. A principle difference between the analysis method here and previous studies is that $\Gamma_{\perp,lim}$ is not calculated separately, using a 'window frame' [95], and imposed as a boundary condition. As such, $v_{eff,lim}$ in the analysis presented here is not fixed. Nevertheless, the estimated sensitivity is in agreement with other studies using the same analysis [49, 81, 82].

A key assumption in this analysis is that the radial transport can be characterized effectively by v_{eff} . A study by Garcia et al. disputes this assumption [107], however. In that study, the radial transport was described using a mixture of a diffusive and convective ansatz given by

$$\Gamma_{\perp}/n = v_{eff} + D_{eff}/\lambda_n \quad (4.1)$$

where D_{eff} is an effective diffusion constant. It was argued that Γ_{\perp}/n should depend linearly with $1/\lambda_n$ if equation 4.1 was appropriate, with the ordinate intercept giving v_{eff} . No such dependence was found. However, data from the entire SOL was incorporated rather than at fixed $r - r_{sep}$. A similar analysis by Labombard [78] did however consider the flux-gradient relationship at a fixed distance of 2mm from the separatrix (the *near* SOL in C-mod) and also concluded that D_{eff} and v_{eff} had little value there. The inability of the diffusive and convective paradigms to describe the radial transport in the *near* SOL would be consistent with the large spread of v_{eff} there. However, the trend of v_{eff} toward $\sim 100\text{ms}^{-1}$ is persistent and may be due to its more appropriate description of the transport in the *far* SOL. A study by Militello *et al*, on the relationship between filaments and time averaged profiles is supportive of this conclusion with the radial acceleration of filaments, along with other factors, cited as part of the explanation of profile flattening, which would be consistent with the trend in v_{eff} presented here.

The second section of this chapter investigated the quantity and properties of the radial flux through the use of a Langmuir probe flush mounted on the LFS limiter.

A key assumption in the analysis is that there is no systematic effect of the ion-gyroradius, ρ_i on J_{sat} . For the lowest field cases (1.5MA), $\rho_i \sim 0.4\text{mm}$. This is similar to the vertical dimensions of the flush mounted probes (0.5mm). A study of the effect of magnetization on flush mounted probes found that the flux tube expanded with decreasing $|B|$ [108]. Application of this effect to the data in figure 4.10 made little difference to the overall trend, the main effect being a slight increase in the scatter. Even so it cannot be ruled out, with a high degree of confidence, that scaling in figure 4.10 is due at least in part to the changing magnetic field conditions.

Regardless of the potential effect of ρ_i on J_{sat} , the waiting and duration time statistics and conditionally averaged waveform are supportive of some property of the magnetic conditions having a strong effect on the filaments. Perhaps the most crucial results of the section is the linear dependence of the expected duration time

$$\tau_d = (\langle \delta_{fil} \rangle / \langle v_{fil} \rangle) \propto |B|^2 \text{ or } I_p^2, \quad (4.2)$$

where angled brackets indicate expectation values, and is stronger than the effect of \bar{n}_e . Previous studies aid the interpretation of the inherently limited single point measurements. A analysis of MAST plasmas[109] measured the filament sizes and velocities using visible imaging. The radial size of filaments was found to be insensitive to changes to either the strength or pitch angle of the magnetic field. The bi-normal (approximately the poloidal) direction filament size was however found to exhibit an approximately linear relationship with I_p . Further, the radial filament velocity was found to have an approximately negative linear relationship with I_p . Were the same scalings to apply in the cases presented here, the duration time measured by the probe would be some combination of the *radial* velocity together with the *bi-normal* size, also implying that the filaments impacting the limiter have a substantial bi-normal velocity component, similar in magnitude to the radial.

Scans of B_t and I_p performed on several tokamaks have found no explicit dependence of the radial transport on B_t [82, 110, 111, 112, 113, 114], in agreement with the MAST results, although those studies used the decay length of the time average profiles as the transport metric. Further an I_p scan performed on TCV, with B_t fixed, found both n_e and Γ_{\perp} at the limiter radius to scale linearly with $1/I_p$. The purpose of the I_p scan was to vary L_{\parallel} and in turn the collisionality defined there as $\nu_{ei}^* = L_{\parallel} / \lambda_{ei}$ where λ_{ei} is the mean free path for electron-ion collisions. That study concluded that the electrical disconnection of filaments from the target plates with increasing ν_{ei} was the cause of the observed increase in radial transport. However, a recent study, also on TCV, suggested that L_{\parallel} is not important in setting either filament dynamics or time averaged density, and that changes to both could only be induced by increasing \bar{n}_e , in that case via D₂ fuelling [115]. Those experiments did not vary either I_p or B_t , but used flux expansion in the divertor to vary L_{\parallel} .

Despite this evidence in support of I_p playing a central role, analytical and numerical modelling of filaments is consistent with the relationship between τ_d and the $|B|$ reported in this paper. Due to the $E \times B$ drive of filament, one may naively expect a $1/|B|$ scaling of the filament velocity. However in both sheath limited and resistive sheath regimes, filament velocities are predicted to scale with $1/|B|^2$ [116]. It should be noted that the uncertainties in the fitted parameters, used to determine τ_d , do not rule out a $1/|B|$ scaling.

A notable implication of the results in figure 4.17 is that there is no general trend of increasing τ_w or τ_d with increasing density, either in the core or SOL. Analysis of the same data set in [71], which used the 2.5σ threshold, concluded that τ_d decreased with *increasing* \bar{n}_e . However only the 2.0MA case was shown, and this result is consistent with 2.0MA data presented in figure 4.17, but not for all I_p in general.

A speculative interpretation, in attempt to unify the results presented here and from previous studies, is that I_p influences the turbulence that generates filaments near the separatrix as suggested in [82], and once born, filament velocities are subject to some inverse scaling with $|B|$. In other words the net radial flux, $\Gamma_1 \propto \frac{1}{BtI_p}$. In order to test this scaling, similar pulses with varying safety factors must be analysed, which would be a direction for future experiments.

Comparing the key results of each section of this chapter, if the velocity scaling with I_p in section 4.3.1 were a reliable proxy for $\langle v_{fil} \rangle$ (i.e. $v_{eff} \propto \langle v_{fil} \rangle \propto I_p$) then the scaling in equation 4.2 would imply $\langle \delta_{fil} \rangle \propto I_p^3$ which is not experimentally observed and is much stronger than the approximately linear scaling in [109]. Further, as previously mentioned, the results from [109] suggest the filament radial velocity has a negative linear relationship with the I_p , directly at odds with $v_{eff} \propto I_p$.

Together with the significant measurement uncertainties and model assumptions in the steady state radial flux analysis, which accrue to approximately a factor three, these results suggest that the radial flux analysis method does not provide a reliable measure of *either* the trend or the magnitude of the transport properties in the SOL, particularly in far SOL. However, fairly universal result is obtained in the far SOL.

4.6 Conclusions

This chapter has investigated the quantity and properties of the main chamber radial flux density in a number of Ohmically heated L-mode horizontal target plasmas using two different methods. The first method used a steady state particle continuity model and characterized the transport by the use of an effective convective velocity v_{eff} . For a fixed I_p , v_{eff} was found to be relatively insensitive to density, in agreement with previous studies. A slight positive linear trend was found between v_{eff} and I_p . However, the analysis is subject to large variations in measurement values and locations along with sensitivity to assumptions, resulting in approximately a factor of three uncertainty in v_{eff} .

This observed trend is at odds with previous studies and is also not supported by

the results of the statistical analysis of the flush mounted Langmuir probe, presented in the second section of the chapter.

The current density measured by a limiter probe was found to scale as $J_{sat} \propto f_{gw}/I_p$ for a wide range of I_p , \bar{n}_e and target configuration. Whether J_{sat} is a reliable measure of the flux density at the limiter, $\Gamma_{\perp,lim}$, as suggested by equation 3.11, is still an open question; there may be some as of yet unidentified effect of the ion gyro-radius which contributes to the observed scaling, and is an obvious direction for further investigation. Even if there is some significant effect, it would not affect the statistics of the J_{sat} , only the magnitude. Both the waiting and duration time statistics were found to be strongly influenced by some aspect of the magnetic field, most likely to be I_p based on previous studies. In particular, the duration time showed an approximately linear scaling with $|B|^2$ ($\propto I_p^2$). Notably there was no general dependence of either the waiting or duration time with density for all I_p .

Chapter 5

The role of parallel collisionality in cross-field SOL transport

5.1 Introduction

The previous chapter concluded that v_{eff} was relatively insensitive to a wide range of plasma conditions, although with a factor three uncertainty. We move onto, therefore, the potential processes that may cause the flattening of the SOL density profile, as those processes necessarily are related to the amount of perpendicular transport, but also crucially to the balance *between* the parallel and perpendicular transport.

The role of parallel collisionality is perhaps the most often used explanation for the flattening of the SOL density profile, as outlined in section 2.4, motivated by the model different current flows within filaments, shown in figure 2.7. A common interpretation is that electrical disconnection of the filaments from the target plate at high collisionality results in reduced parallel currents and an enhancement of the perpendicular transport [70]. Recently, a divertor collisionality parameter, Λ_{div} [75], has been used to quantify the divertor conditions [80, 117, 118, 119], concluding it is the general control parameter for the upstream transport. A more recent study [120] however complicated that understanding.

The focus of this chapter is to test the validity of the hypothesis of Λ_{div} as the general upstream transport control parameter in a large range of plasmas. Different methods have been used to change to parallel resistances including D₂ fuelling (or density increases), target configuration and impurity seeding with N₂. Λ_{div} is used to quantify the divertor conditions. Both L-modes and H-modes are considered.

The most crucial conclusion from the results presented in this chapter is that the parallel resistance does *not* play a strong role in setting the quantity of the perpendicular transport in the SOL. Further to this Λ_{div} is also a poor quantifier of the divertor conditions due to diagnostic limitations, but this does not detract from the insufficiency of the parallel resistance in general.

The chapter is structured as follows. Section 5.2 considers horizontal target L-mode D₂ fuelling ramp plasmas. Section 5.3 considers vertical target L-mode D₂ fuelling ramp plasmas. Section 5.4 considers Horizontal target N₂ seeded plasmas. Section 5.5

considers H-mode plasmas with D₂ fuelling and N₂ seeding, both with the horizontal target. Section 5.6 discusses the results and finally conclusions are drawn in section 5.7.

5.2 Λ_{div} in horizontal Target L-mode

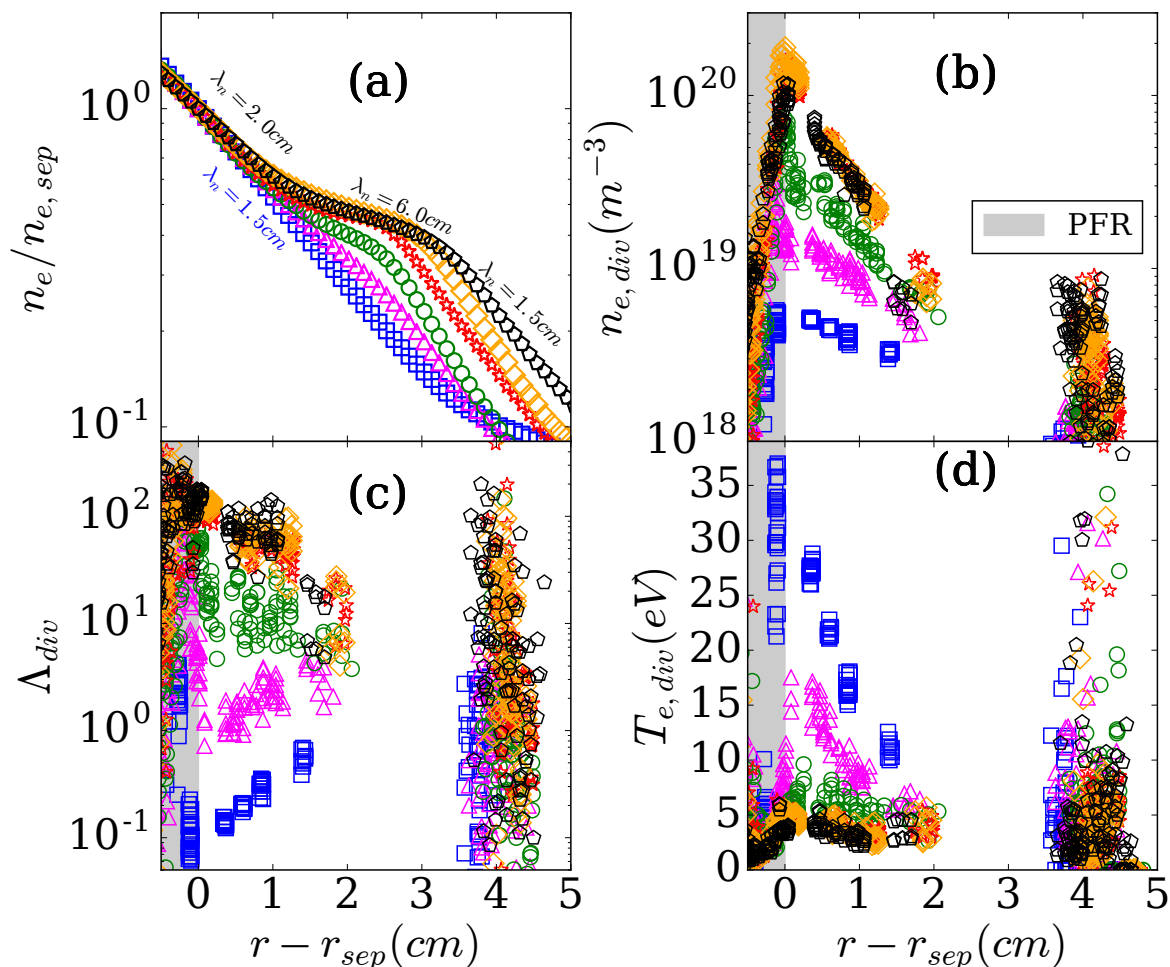


Figure 5.1: Horizontal target D₂ fuelling ramp (JPN89346) for a 2.5MA plasma: (a) normalized SOL density profiles showing the formation and growth of the shoulder. (b) Divertor target density profiles showing the transition from SL (blue squares) to peak HR (red stars), as the divertor becomes more high-recycling (green circles, red stars, orange diamonds) and detachment onset (black pentagons) (c) The resultant change to Λ_{div} ; (d) Divertor T_e profiles. Limiter radius $\sim r - r_{sep} = 5$ cm. The profiles have been shifted by 0.25cm such that the peak density and temperatures are at the separatrix.

It is only in horizontal target, Ohmically heated L-mode plasmas that enhanced parallel resistivity correlates generally with the flattening of the upstream density profile; other pulse types detailed later in this chapter do not exhibit this correlation. The pulses used are the same as outlined in the previous chapter. For clarity only the 2.5MA case (JPN89346) will be discussed.

In general, we find that the shoulder appears, or its amplitude is measurable, just after the divertor plasma transitions from sheath-limited (SL) to high-recycling (HR)

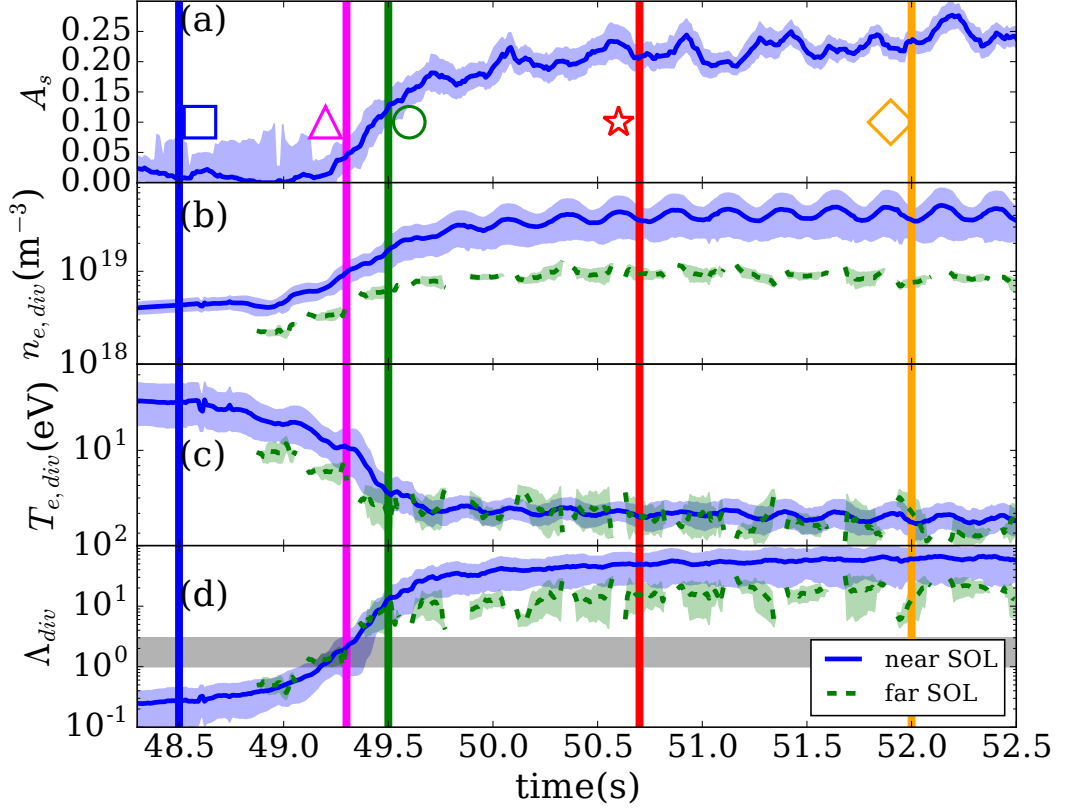


Figure 5.2: Time traces of quantities shown in figure 5.1 (JPN89346) with the same symbols and colors at times given by the vertical lines. The normalized shoulder amplitude, A_s is given in (a); (b) and (c) are the evolution of the density and temperature averaged over near ($r - r_{sep} = 0-1.5\text{cm}$) and far ($r - r_{sep} = 1.5-3\text{cm}$) SOL, referenced to the midplane; d) gives the divertor resistivities, $\Lambda_{div,near}$ and $\Lambda_{div,far}$, calculated using the data from (b) and (c). Gaps in data for far SOL are due to strike point sweeping and probe spacing.

conditions. We define the beginning of the high-recycling regime as the time when the values of density (temperature) and ion current near the separatrix start to increase (decrease) strongly as the core density is increased. One example of the transition to high-recycling is shown in figure 5.1 where colours and symbols correspond to specific times and \bar{n}_e consistently across all sub-figures as well as the time traces in figure 5.2. Figure 5.1(a) displays SOL density profiles from the Li beam mapped to the mid-plane and normalized to the separatrix density. Uncertainties are not shown but are similar to those shown in figure 3.4. At low \bar{n}_e (blue squares) SL conditions exist at the outer divertor horizontal target with $T_{e,sp} = 35\text{eV}$ (d) and $n_{e,sep} = 6 \times 10^{18}\text{m}^{-3}$ (b). The corresponding upstream density profile (a) is exponential from separatrix to limiter. The next time point (magenta triangles) corresponds to higher core and divertor densities which rise rapidly into HR conditions and the shoulder begins to form; the peak temperature and density at the target are $T_e \approx 15\text{eV}$ and $n_{e,sep} = 2 - 3 \times 10^{19}$, respectively. As the core density is increased still further, the divertor plasma becomes increasingly high recycling (green circles, orange diamonds) and the shoulder magnitude continues to increase. At the highest densities (black pentagon symbols) the divertor starts to detach (density at strike point reduces slightly) and, while the shoulder amplitude is

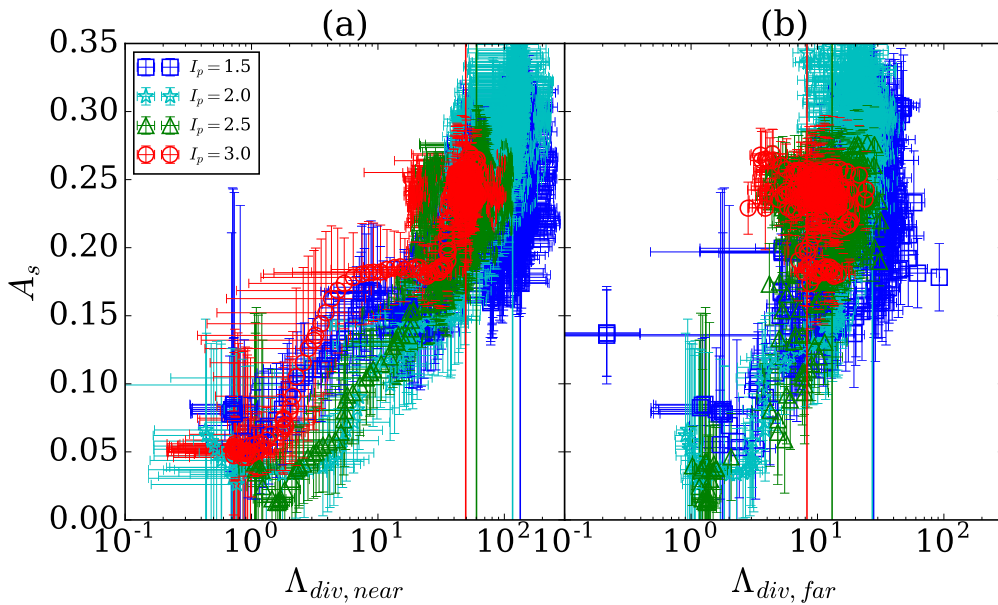


Figure 5.3: The shoulder amplitude, A_s , vs Λ_{div} , averaged over (a) near ($r - r_{sep} = 0-1.5\text{cm}$) and (b) far ($r - r_{sep} = 1.5-3\text{ cm}$) SOL regions for the four plasma currents with L-mode, horizontal target plasmas, and D_2 puffing driving a core density ramp. Vertical lines indicate the onset of detachment for corresponding colours. The error bars are representative of the standard deviation of the data in the specified regions (near and far SOL) over 0.1s. JPN893(44,50,46,48) ordered with increasing I_p .

not increasing, the shoulder peak location moves radially towards the limiter ($r - r_{sep} = 5\text{ cm}$), raising the density at the limiter radius.

Figure 5.1 (c) displays the profiles of Λ_{div} at the divertor target plate and how it changes dramatically through the transition from SL to HR regimes as well as further increases as the divertor becomes more high-recycling. Due to the strong dependence of Λ_{div} on target density and temperature, eq. (1), the transition from SL to HR also corresponds to a faster increase in Λ_{div} , transitioning from below 1 to > 10 . This correlation between shoulder formation, transition from sheath-limited to high-recycling and Λ_{div} was observed for all horizontal target L-mode \bar{n}_e scans at different values of I_p .

To emphasize the strong correlation of the transition from divertor SL to HR conditions with shoulder formation, figure 5.2 shows time traces of the quantities shown in figure 5.1. A_s in figure 2 (a) represents the upstream density shoulder magnitude evolution. Λ_{div} (d) has also been averaged over the regions corresponding to the near ($r - r_{sep} = 0-1.5\text{cm}$, $\Lambda_{div, near}$) and far SOL ($r - r_{sep} = 1.5-3\text{cm}$, $\Lambda_{div, far}$). Values and error bars shown are moving averages and standard deviations over 100ms respectively - except Λ_{div} where the error is propagated from the n_e and T_e profiles. The uncertainties at individual time points are small compared to the error bars shown.

The transition of the divertor from sheath-limited to high-recycling occurs in figure 5.2 a at $\sim 49.3\text{s}$, just before the magenta line and triangle markers, as the lower uncertainty of A_s rises above 0. At that time Λ_{div} is in the range of 1-3. After the shoulder appears, A_s increases rapidly to 0.20 while Λ_{div} essentially saturates at values

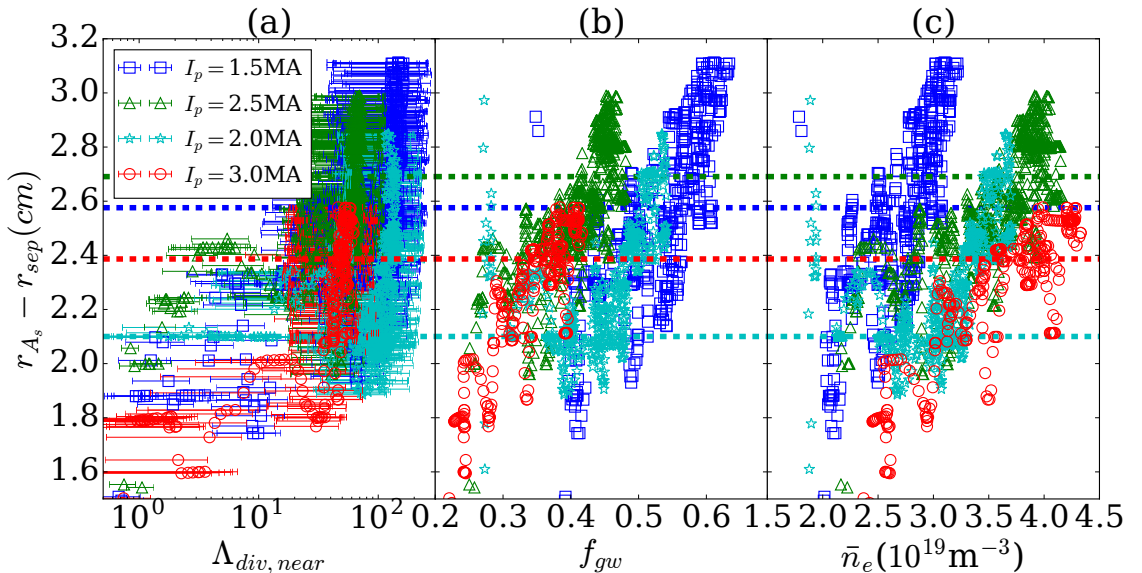


Figure 5.4: Movement of the radial location of A_s as a function of $\Lambda_{div, near}$ (a), \bar{n}_e/n_{gw} (b) and \bar{n}_e (c) for the four plasma currents with L-mode, horizontal target plasmas and D_2 puffing driving a core density ramp. (a) Indicates the 2 phases of the profile evolution, initially formation and subsequent growth. Horizontal lines indicate the onset of detachment for each plasma current.

near 50. We note that the saturation of Λ_{div} is at least partially due to $T_{e, div}$ saturating at values near 5eV, a common issue for Langmuir probe measurements in tokamaks [?]. $\Lambda_{div, far}$ follows a similar trend to $\Lambda_{div, near}$ but with slightly lower values and larger uncertainties. Gaps in the data are due to strike point sweeping.

The divertor and SOL data from all four plasma currents exhibit the same rapid increase in shoulder amplitude, A_s as $\Lambda_{div, near}$ or $\Lambda_{div, far}$ increase above approximately 1 and divertor (and parallel transport) transitions from SL to HR. The relationship between A_s , and Λ_{div} , is shown in figure 5.3 for the two cases of the abscissa being $\Lambda_{div, near}$ (a) and $\Lambda_{div, far}$ (b). Most importantly, the relationship between A_s and Λ_{div} appears to be independent of I_p . In addition, we find that a shoulder forms when Λ_{div} exceeds $\sim 1-3$ in either the near or far regions. The appearance of a shoulder above $\Lambda_{div} \sim 1-3$ is similar to the L-mode, vertical target, results from AUG [29] when the divertor detaches, as opposed to transitioning to HR. The relationship of the shoulder behaviour reported in this paper to previous results will be expanded upon in the discussion section.

While Λ_{div} may generally correlate with A_s , the radial location of the shoulder peak r_{A_s} does not and is better described by either the \bar{n}_e or Greenwald fraction n/n_{gw} . Results are given in figure 5.4. During the period when the shoulder forms and grows in amplitude ($\Lambda_{div, near} < 20-40$), r_{A_s} stays essentially constant for the various plasma currents (fig. 5.4 (a)), 1.8-2.4cm away from the separatrix. At $\Lambda_{div, near} > 40$, the divertor plasma is detached and a second phase is entered where r_{A_s} increases. The dependence of r_{A_s} on core plasma parameters, n/n_{gw} and \bar{n}_e (figures 5.4 (b and c)), are more gradual, not indicating two phases as in figure 5.4 (a). The gradual outward movement with increasing \bar{n}_e also suggests that the second change of scale length is

not due to the field line mapping to some solid surface.

5.3 Λ_{div} in vertical target L-mode

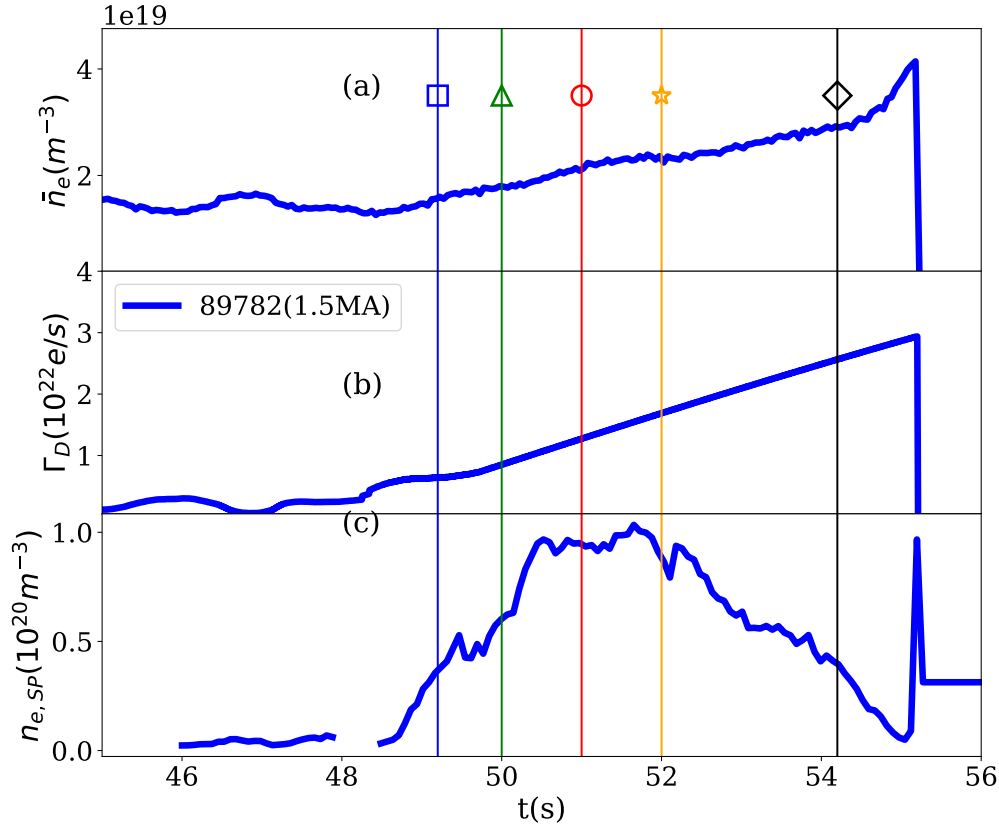


Figure 5.5: Time traces of vertical target L-mode D fuelling ramp at 1.5 MA (JPN 89782). Shown are (a) \bar{n}_e , (b) fuelling rate Γ_D , (c) and strike point density $n_{e,SP}$. Detachment is evident in the rollover in $n_{e,SP}$. Vertical lines marked with symbols indicate times used for profile shown in figure 5.6

Another test of the divertor's impact on the upstream SOL radial transport was implemented by changing the divertor *configuration* from horizontal to vertical target. It is known from both modelling and experimental studies that divertor geometry can modify the detachment threshold in upstream density [121, 122, 87]. Variations in recycling properties between vertical and horizontal targets there could lead to differences in the resistivity profile across the divertor plates. JET presents an important opportunity to study the effect of the divertor configuration on shoulders given its fairly unique capability to shift from one configuration to the other with minimal changes in the core plasma.

The L-mode discharges which utilize the vertical target were operated with the same \bar{n}_e scans (through D₂ fuelling ramps) for different I_p as for the horizontal target data of the previous section. Time traces for the 1.5MA vertical target pulse used in this section are shown in figure 5.5. The strike point density (c) rises quickly until ~ 50.5 s,

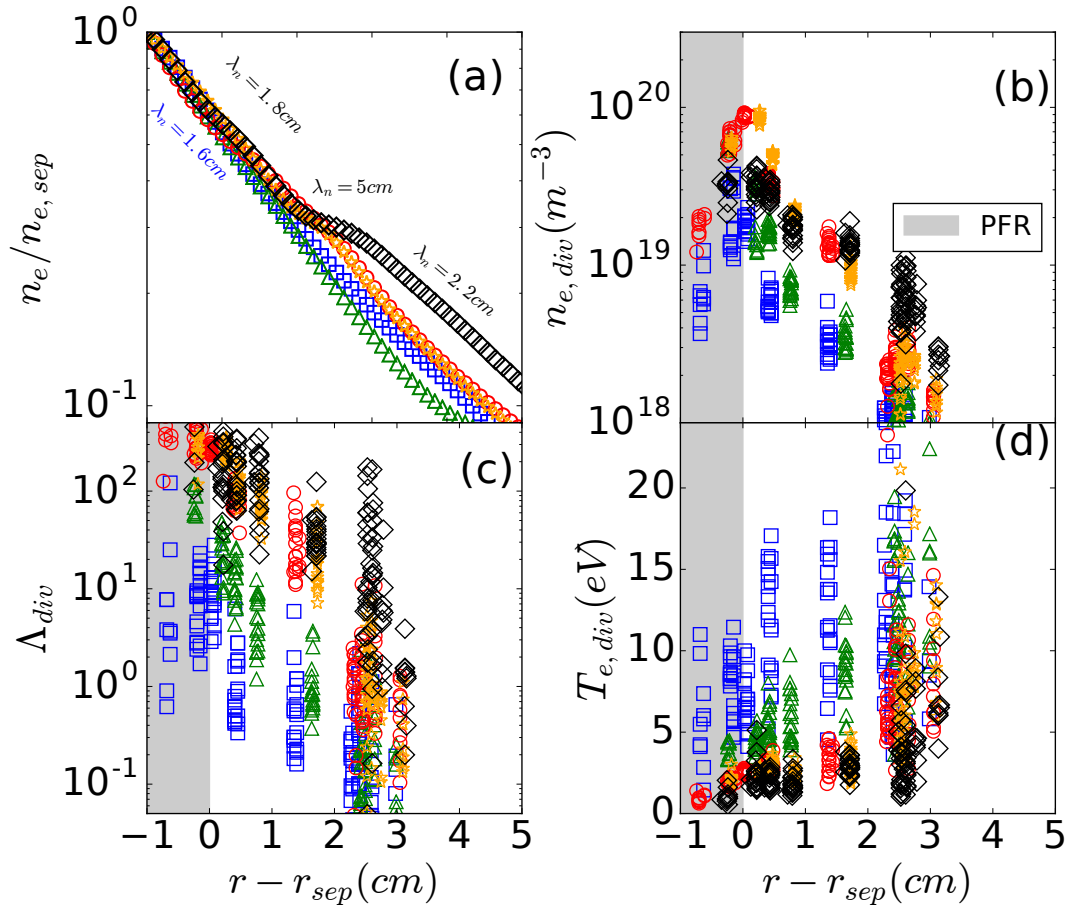


Figure 5.6: (a) Upstream density profiles, divertor probe data (b & d) and Λ_{div} (c) for a vertical target 1.5MA plasma utilizing a D₂ fuelling ramp to increase \bar{n}_e (JPN89782). The divertor condition (SL, HR or detached) is different in the near and far SOL.

after which $n_{e,sp}$ plateaus and then drops, reaching strongly detached conditions at the end of the pulse. The SOL density as well as divertor profiles are shown in figure 5.6 for the same 1.5 MA case of figure 5.5 where symbols correspond to equivalent times. The outer gap was 5cm, the same as for the horizontal target cases.

As shown in figure 5.6 (a), a small but discernible SOL density shoulder appears for operation with the vertical target. However, this occurs only at the highest \bar{n}_e when the divertor is very detached. Compared to the horizontal target case $\Lambda_{div,near}$ and $\Lambda_{div,far}$ have significantly different values; $\Lambda_{div,near}$ reaches values of order 100 as the density to the target rolls over (not shown) and the peak divertor density decreases (black diamonds). In contrast $\Lambda_{div,far}$ is of order 1-10 when the shoulder forms and thus that region of the divertor is not detached. Another difference to operation with the horizontal target is that the divertor density profile in the far SOL broadens substantially, shown in (d).

The different correlation of $\Lambda_{div,near}$ and $\Lambda_{div,far}$ with A_s is shown more clearly for the same pulse in figure 5.7. A_s does not increase further when $\Lambda_{div,far}$ increases above 10, different to the horizontal target case. In summary, for vertical target operation, $\Lambda_{div,near}$ is a poor predictor of shoulder formation and even though $\Lambda_{div,far}$ roughly shows the same threshold for shoulder formation as for the horizontal target,

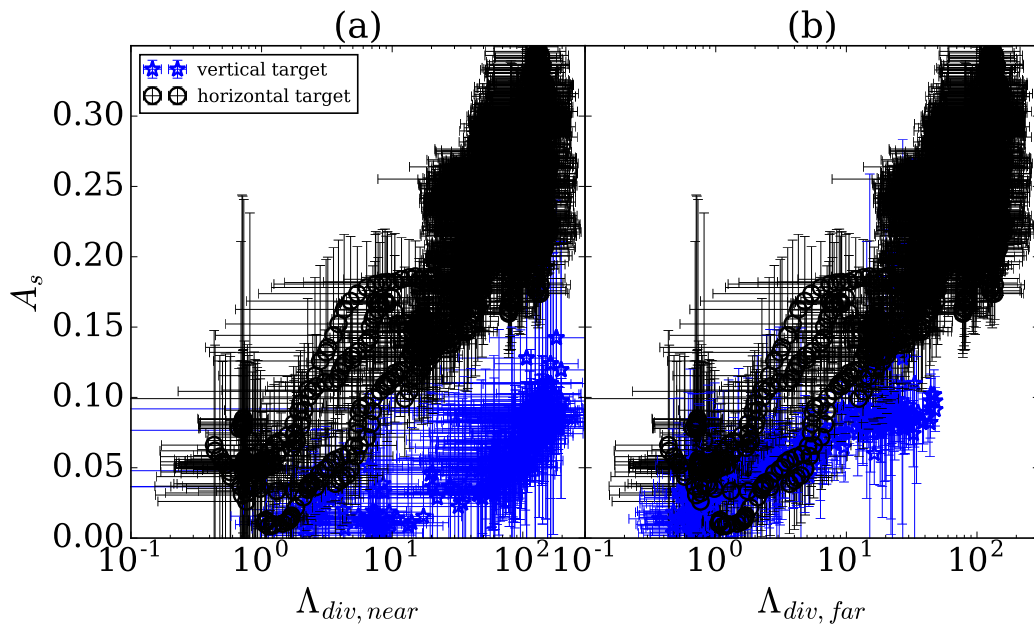


Figure 5.7: The correlation between the shoulder amplitude A_s and Λ_{div} in the near (a) and far (b) SOL for the vertical target (JPN89782). The data from all I_p in the horizontal target (figure 5.1) is also shown for reference .

the shoulder does not reach the same amplitude as the horizontal target.

The properties of J_{sat} , measured by an OLP (see figure 3.1) also suggest relatively modest changes to the filamentary transport. Figure 5.8 shows PDFs of J_{sat} taken from 0.5s time windows spanning the vertical lines in figure 5.5, with corresponding colours. Considering first (a), the mean μ (dashed vertical lines), does not systematically increase with increasing \bar{n}_e and is only positive for the green and black data. Further, the PDFs are negatively skewed. The PDFs do collapse onto a common curve when subtracting μ and rescaling by the standard deviation, σ , shown in (b), but from (a) it is clear that the negative regions of the signal are dominating. The process that caused the negative J_{sat} (likely arcing) also has an impact on those parts of the signal that remain positive, making the data quality poor with regard to extracting intermittent structures.

5.4 Λ_{div} in horizontal target nitrogen seeded L-mode

In the previous two sections, D_2 fuelling was used to change the divertor conditions while simultaneously changing the upstream conditions (\bar{n}_e , n_e , midplane pressure). In this section we utilize N_2 injection to directly modify the divertor conditions while holding upstream conditions roughly constant. The divertor strike point was on the horizontal target and conditions were evolved from SL to detached using N_2 seeding, but over that wide range there is almost no change to the upstream density profile. This is in stark contrast to the results from the D_2 fuelled horizontal target cases where

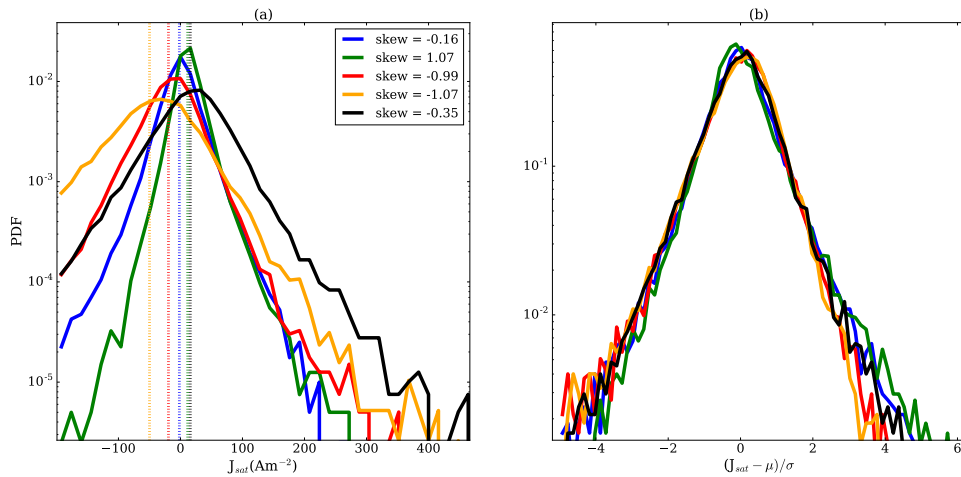


Figure 5.8: (a) PDF of J_{sat} over 0.5s windows spanning the vertical lines in figure 5.5 with corresponding colours. (b) PDF shifted by the signal mean, μ , and rescaled by the standard deviation σ .

there was a strong correlation between A_s and Λ_{div} , calculated for the near or far SOL. Time traces for the pulse used in this section are shown in figure 5.9.

Figure 5.10 shows upstream density and divertor profiles in the same format as figure 5.1 for an N seeding ramp with $I_p = 2.5\text{MA}$, where symbols correspond to the time traces. The profiles shown in (a) are not normalized to the separatrix density, unlike previous sections due to steady fuelling rate. The blue squares are from early in the discharge, before N_2 injection, when the divertor plasma is in SL conditions as evidenced by low densities (b) and high temperatures (d). The upstream SOL density profile shown in (a) has a single λ_n for the entire SOL, similar to the reference profile of figure 5.1, which had essentially the same pulse conditions. We note the slightly higher T_e at the target compared to that data due to the additional NBI heating (1.5MW).

Prior to N_2 seeding the D_2 fuelling was increased by a factor of three to four and a small SOL density shoulder forms (green triangles) corresponding to the divertor near SOL being slightly HR. Following the formation of this small shoulder, N_2 injection is initiated which leads the divertor to become even more HR (red circles). Despite this large change in the divertor conditions as well as $\Lambda_{div,near}$ and $\Lambda_{div,far}$, there is very little variation in the SOL density profiles. Finally, at the highest levels of N_2 seeding (gold stars), detachment has begun.

Detachment with N_2 seeding (Λ_{div} 20-40) corresponds to a reduction of the shoulder amplitude as well as a shift in the peak shoulder amplitude outward in major radius by roughly 1 cm. This is in contrast to strictly D_2 fuelling where A_s is much larger for the same $\Lambda_{div,near}$ or $\Lambda_{div,far}$; Neither $\Lambda_{div,near}$ nor $\Lambda_{div,far}$ are good predictors of upstream shoulder formation.

To further demonstrate the lack of effect of divertor N level on the upstream SOL density profile, we compare, from the same pulse (JPN90697), periods prior to N_2 seeding to periods during the seeding. First, we find that the pre-N injection trajectory of A_s vs $\Lambda_{div,near}$ (blue squares, 'pre-N') follows that described in figure 5.11 to within

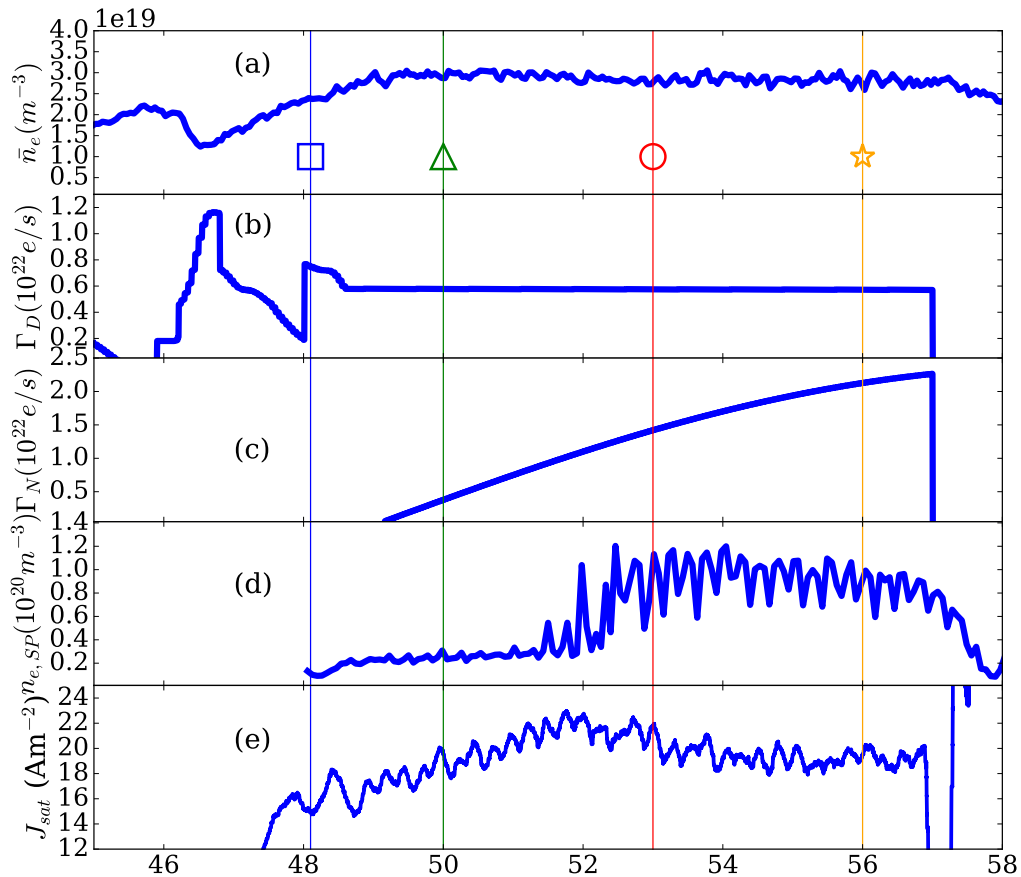


Figure 5.9: Time traces of N₂ seeding ramps showing (a) \bar{n}_e , (b) D₂ fuelling rate Γ_D , (c) N₂ seeding rate Γ_N , (d) strike point density $n_{e,SP}$ and (e) limiter J_{sat} smoothed over 0.1s windows. $I_p = 2.5\text{MA}$ (JPN90697). Coloured vertical lines marked with symbols correspond to figure 5.10.

uncertainties. As the N₂ seeding is added (gold triangles, 'post-N' later in the same discharge) the data shift to larger $\Lambda_{div,near}$ while the shoulder amplitude, A_s , drops slightly (gold triangles). In contrast, $\Lambda_{div,far}$ shows almost no change with N seeding.

Residual N, adsorbed on vessel surfaces, can strongly affect the divertor condition and SOL density shoulder in the following pulse. Figure 5.11 also displays the results (green triangles) from the early part of a different pulse (JPN90700) before N₂ seeding starts; however, the previous pulse had strong N₂ seeding and thus there is a large amount of N adsorbed on the vessel surfaces. An indirect measure of N in the divertor plasma is an NII emission line, the brightness of which is approximately the same for the early part of this pulse (90700) as during the period of HR conditions during N₂ seeding in a previous pulse (JPN90697), shown in figure 5.12. The 'N loaded' discharge (JPN90700) data follows a trajectory in (A_s vs Λ_{div}) space that is different than pulse JPN90697 and the D₂ fuelled pulses. In both the near and far SOL, Λ_{div} increases to or above 10 before A_s begins to increase. Figure 5.11 (a) and (b) thus demonstrate that there is no general relationship between Λ_{div} in either the near or far SOL that is consistent with D₂ fuelling only.

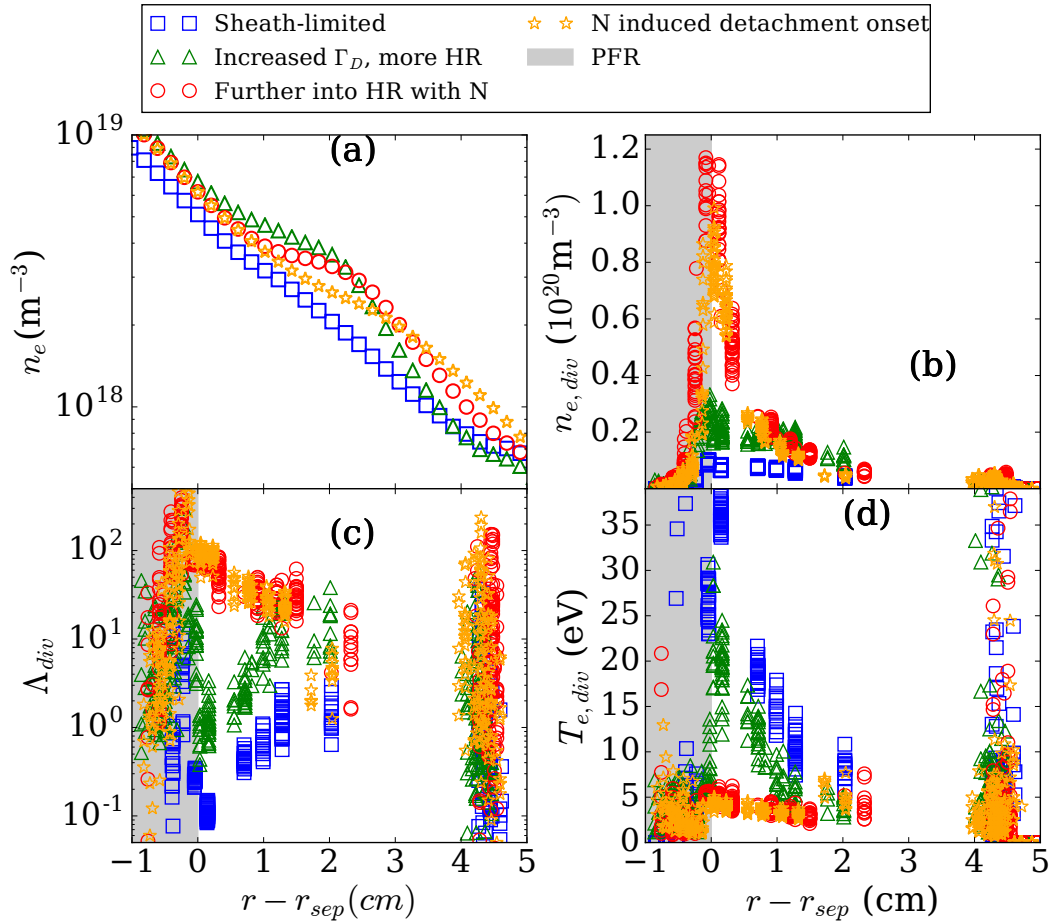


Figure 5.10: (a) Upstream density profiles, divertor probe data (b-d) and (c) for a horizontal target N_2 seeding ramp, $I_p = 2.5\text{MA}$ (JPN90697). Despite strong changes to the divertor conditions due to N_2 seeding, there is only minimal change to the upstream density profile compared to figure 5.1 for comparison.

Analysis of an OLP is broadly consistent with the implications of figures 5.10 and 5.11. Considering first figure 5.9 (e), as the increasing N_2 seeding rate drives the divertor into increasing HR conditions from 49-52s, J_{sat} increases linearly by $\sim 25\%$. Subsequently, as $n_{e,SP}$ saturates, and eventually decreases with the onset of detachment, J_{sat} initially decreases and then remains constant, as does A_s . Over this period, Λ_{div} and the collisionality in general, increases, indicating that there is no general relationship between collisionality and increased radial fluxes to the limiter probe. The 4Hz oscillation of J_{sat} present throughout the pulse is due to strike point sweeping and is explored in the next chapter.

Figure 5.13 shows analysis of the properties of J_{sat} during 0.5s time windows where times, symbols and colours correspond to those in figure 5.10. PDFs in figure 5.13 (a) show an increase in skewness simultaneous to the increase in the mean value (vertical dashed lines). However, at the latest time, where the collisionality is highest and the divertor is partially detached, the skewness has decreased slightly; the trend is not systematic.

Filaments have been identified using the zero skewness method illustrated in figure 3.10. The resultant conditional averages, shown in (b), widen slightly with increasing

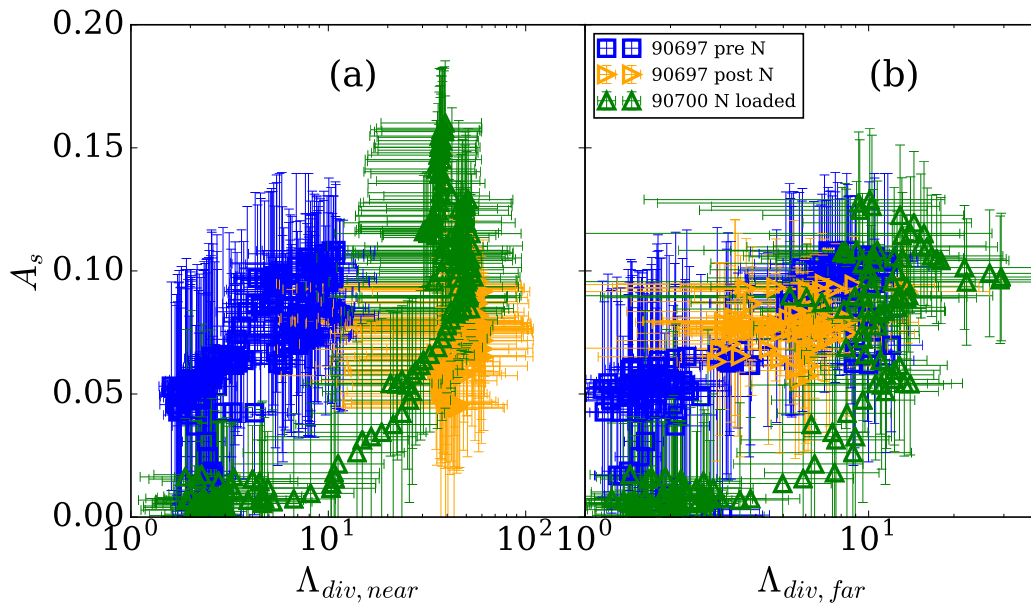


Figure 5.11: Correlation between the shoulder amplitude A_s and Λ_{div} in the near (a) and far (b) SOL for horizontal target N_2 seeded pulses. Data from JPN90700 is for N-loaded vessel surfaces and increasing D_2 fuelling.

N_2 seeding rate, but the effect is not strong. The visible beat frequency is due to the alternating measurement time interval of the probe between 8 and $12\mu s$. The auto-correlations (dashed lines in (b)) have the opposite trend, but again the orange data is not the narrowest. Filament waiting times, (c), do increase systematically with N_2 seeding rate outside of the uncertainties of the fits to the data. Importantly, there is essentially no variation of the expected duration time, (d), of intermittent events across the wide range in collisionality.

5.5 Density shoulder in H-mode

While the research focus of the previous sections of this paper focus on L-mode plasmas, we have studied a few H-mode discharges where the ELM frequency was low enough to make measurements between ELMs. ELMs are major perturbations on the SOL and divertor plasma, where plasma characteristics are strongly varying within the measurement time resolution. The H-mode plasmas we show correspond to the outer strike point on the horizontal target. Ramps in fuelling and nitrogen seeding were available and thus are easily compared to the equivalent L-mode discharges. In general, the behaviour in H-modes was similar to that of a comparable L-mode.

5.5.1 D_2 fuelling ramp in Horizontal target H-mode

The first case addressed is where shoulders are also most evident in L-mode - a D_2 fuelling ramp, which moves the divertor condition from SL through HR. Figure 5.14 displays the time dependence of several core and divertor plasma parameters. Despite

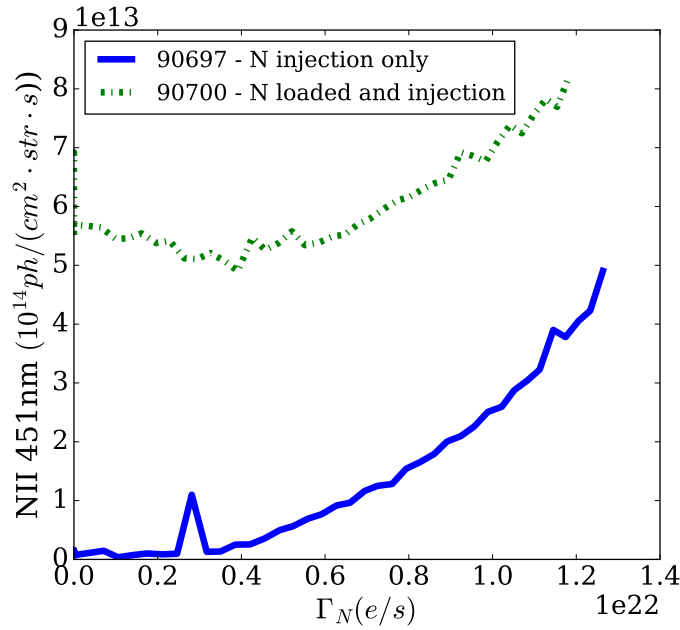


Figure 5.12: The effect of N loading of the vessel surfaces on *NII* brightness as a function of N_2 seeding rate Γ_N .

the factor of eight increase in fuelling rate, there was little change to \bar{n}_e . The time averaged Γ_{div} (integral of ion current over the outer divertor), however, increased somewhat with increasing D_2 fuelling rate. The D_2 gas was injected through GIMs 10 and 11 different from the L-mode cases. In the course of the fuelling ramp, the ELM frequency increased from 25 to 100Hz. Vertical shaded bars with corresponding symbols indicate periods where the divertor and SOL data has been analyzed; the width of the shaded regions corresponds to the length of time over which data is averaged.

The evolution of the divertor profiles of n_e , T_e and Λ_{div} during an H-mode fuelling scan shows little difference to L-mode horizontal target plasmas. The profiles with different symbols/colors shown in figure 5.15 correspond to the color shaded regions of figure 5.14. All profiles correspond to inter-ELM periods. In the L-mode phase (blue squares) the divertor n_e (b) and T_e (d) profiles indicate slightly high-recycling conditions and a small upstream density shoulder. Upon transitioning to H-mode (green triangles), the density profile in both the near and the far SOL becomes steeper, consistent with the H-mode reduction in radial particle transport. Simultaneously, the divertor target n_e reduces, and T_e increases strongly (leading to Λ_{div} decreasing), despite a significant increase (>2) in the separatrix density (not shown). Therefore, in transitioning from L-mode to H-mode, the divertor has also transitioned from HR to SL conditions and the small shoulder disappears; thus the L-mode relationship between the upstream density profiles and target conditions holds across the L-H mode transition for the case of horizontal target D_2 -fuelling ramp).

With increasing gas fuelling, the divertor becomes more high recycling (red circles to black diamonds) and the corresponding Λ_{div} increases. In line with similar L-mode

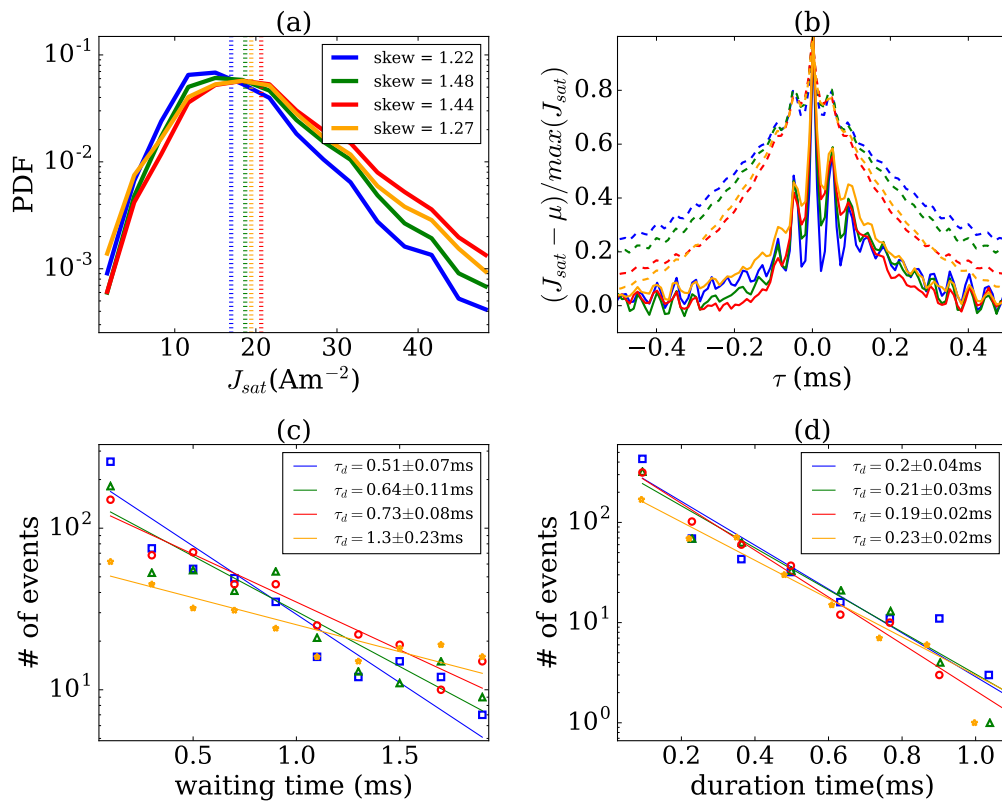


Figure 5.13: Colours and symbols correspond figure 5.10. (a) PDFs of J_{sat} where vertical dashed lines give the mean value. (b) Conditional averages (solid lines) and auto-correlations (dashed lines). (c) and (d) show waiting and duration time statistics. Solid lines are exponential fits with the time scales shown in the legend. The uncertainty originates from the least squares fitting variance estimate.

discharges, a density shoulder forms in the upstream SOL beyond 1.5cm from the separatrix. With further increases in the D₂ fuelling rate, the shoulder amplitude and ion current at the limiter radius substantially increase, and while the shoulder moves inwards (broadening), the near SOL region contracts by ~ 1 cm (red circles to black diamonds).

In addition to the time average density profiles, analysis of the limiter probe J_{sat} has also been performed. Figure 5.16 shows example ELM window identification using the outer divertor BeII brightness. The ELM is clearly visible in limiter J_{sat} along with intermittent events in the inter-ELM period. Application of the 0 skewness method to the inter-ELM periods results in a threshold that is below the mean of the signal. This is persistent across different time windows. Even though the threshold has been validly determined, the resultant conditional averages (not shown) are almost entirely negative, except at $\tau = 0.0$ s. Therefore duration and waiting time statistics have been calculated using thresholds of multiples of σ . In line with the density profiles of 5.15, with increasing D₂ fuelling rate, the mean inter-ELM J_{sat} increases as shown in figure 5.17. Inclusion of the ELMs increases the mean by $\sim 20\%$. The PDFs do not rescale as precisely as is commonly observed in L-mode although the positively skewed shape is broadly similar.

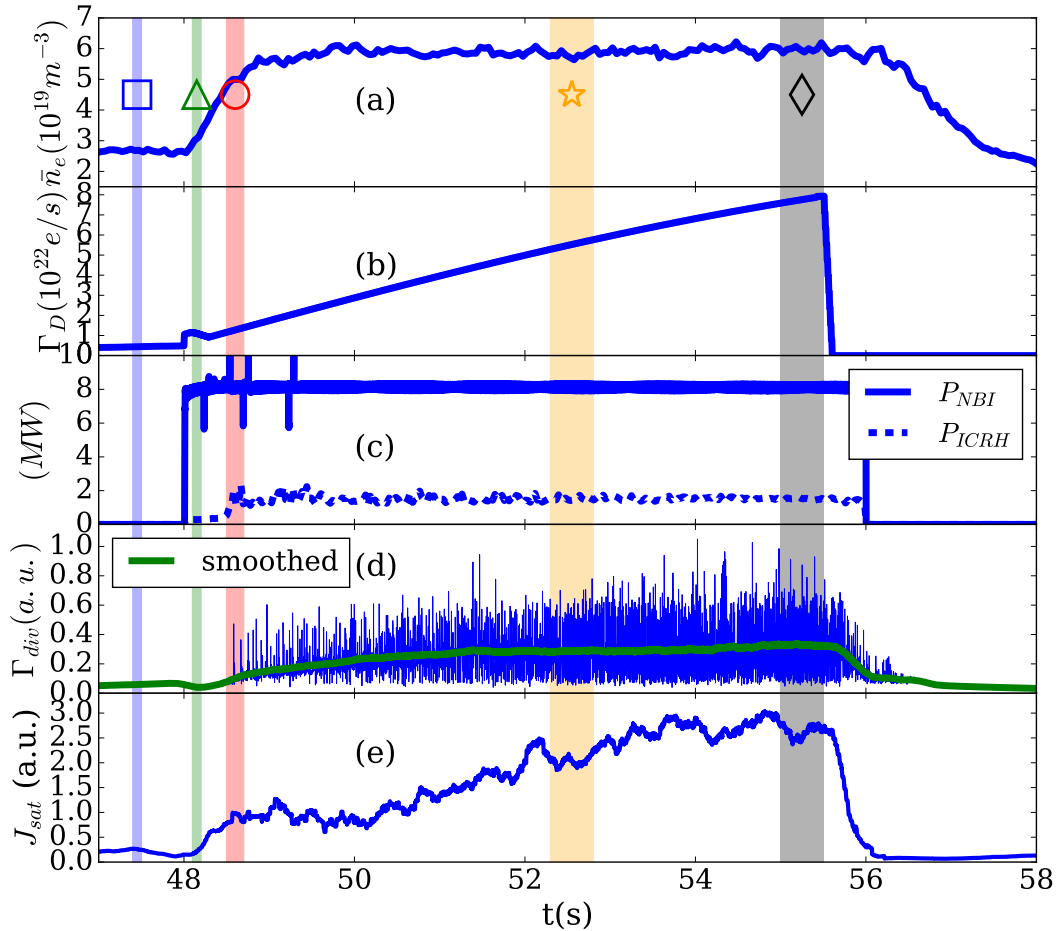


Figure 5.14: Pulse time traces for horizontal target H-mode D₂ fuelling ramp. Smoothed data in (d) is a 0.1s window moving average. J_{sat} , (e), has been smoothed by the same method.

Figure 5.18 shows the expected τ_w and τ_d over time with increasing D₂ fuelling rate for various thresholds. Both τ_w and τ_d have been determined in the same manner as for L-mode pulses (the e-folding length of exponential fits to PDFs of the waiting and duration times). In general, both τ_w and τ_d increase with D₂ fuelling rate. The widening of the conditional average, shown in figure 5.19 is consistent with the increases in τ_d .

5.5.2 H-mode N₂ seeding ramp

As for the L-mode cases, divertor N₂ seeding of H-mode plasmas does not lead to further flattening of the upstream density profile. Figure 5.20 displays time traces for an N₂ seeding ramp where vertical shaded regions (time window of averaging inter-ELM periods) and symbols correspond to the profiles shown in figure 5.21. D₂ fuelling was held constant. The ELM frequency was substantially lower than for the D₂ fuelling ramp case of figure 5.14.

The density profiles at the lowest Λ_{div} already show substantial flattening and therefore any inferred value of A_s cannot be directly compared to the the L-mode

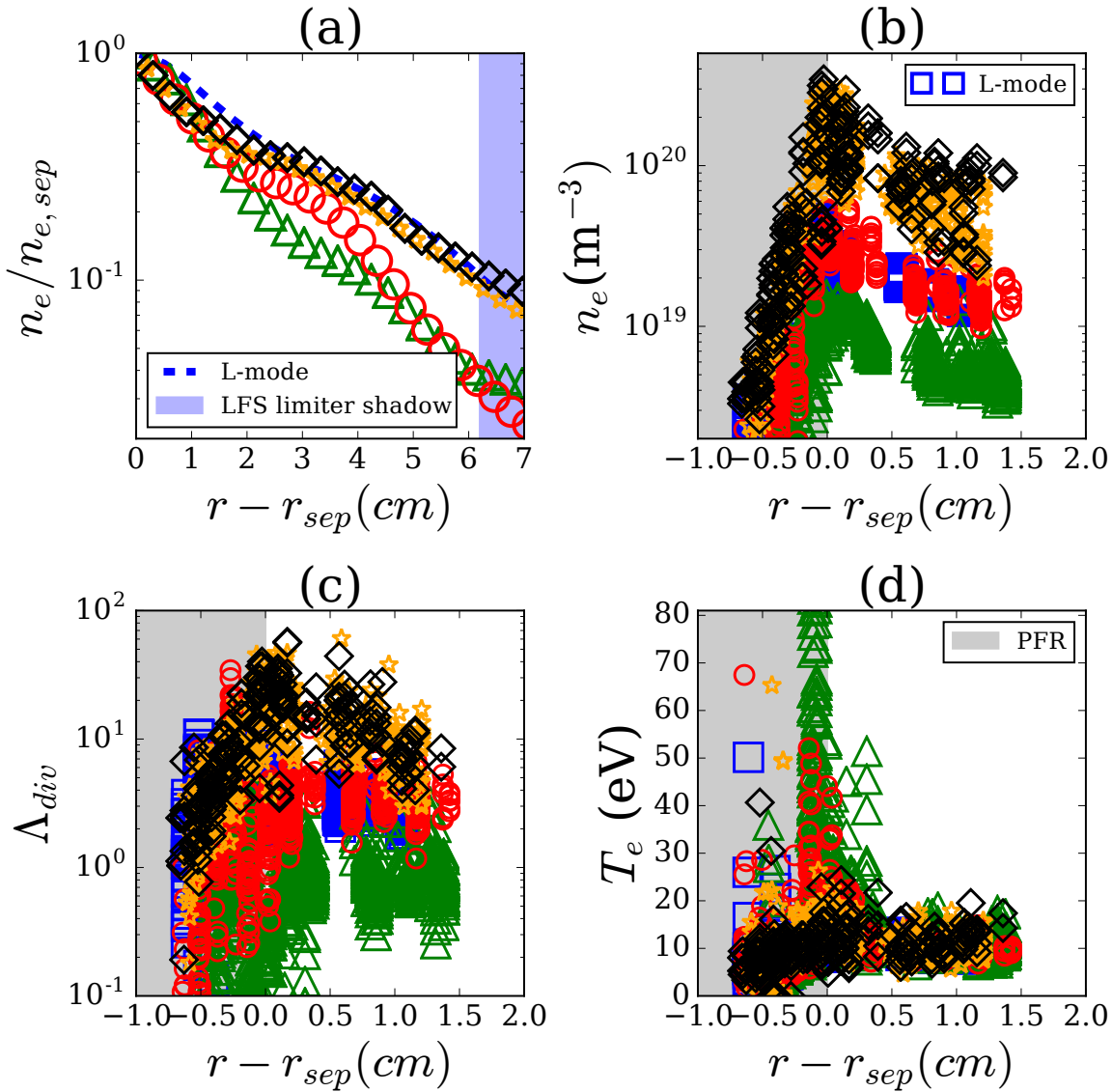


Figure 5.15: Horizontal target H-mode D₂ fuelling ramp upstream and divertor profiles (JPN89786). L-mode prior to the H-mode transition is shown in blue (dashed line in (a)). The shaded region in (a) is the shadow of the LFS limiter.

cases. For this reason, we do not interpret the profiles in the same manner as previous sections via the use of A_s .

As in the D₂ fuelled case, during the transition to H-mode (green triangles) the density profile steepens generally. The divertor conditions are SL, indicated by high T_e . Further into the development of the H-mode, with increased \bar{n}_e (red circles), the density profile in the far SOL is essentially the same as the L-mode. The near SOL, however, does differ with larger $n_{e,sep}$ and gradients in the H-mode.

Higher subsequent N₂ seeding does not modify the upstream density profile outside of uncertainties, yet there are strong changes to the divertor conditions and also Λ_{div} . Divertor densities peak (black stars) and then reduce by an order of magnitude (cyan pentagons). In this most detached case, \bar{n}_e and $n_{e,sep}$ are higher and yet there is no appreciable increase in the far SOL density. The only significant change appears in the near SOL where the gradient increases.

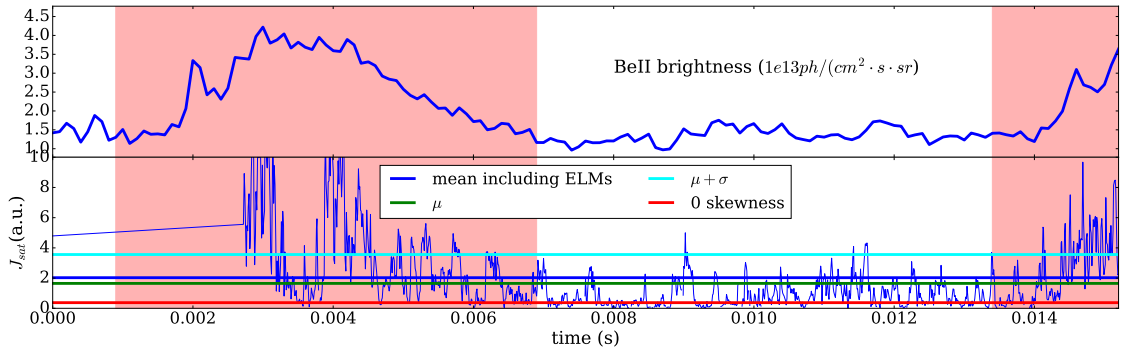


Figure 5.16: Horizontal target H-mode D₂ fuelling ramp ELM removal and thresholds example (JPN89786). Shaded regions are during ELMs, as indicated by the BeII brightness. Only the mean including ELMs (blue horizontal line) takes into account ELMs. 52.6073s has been subtracted from the time.

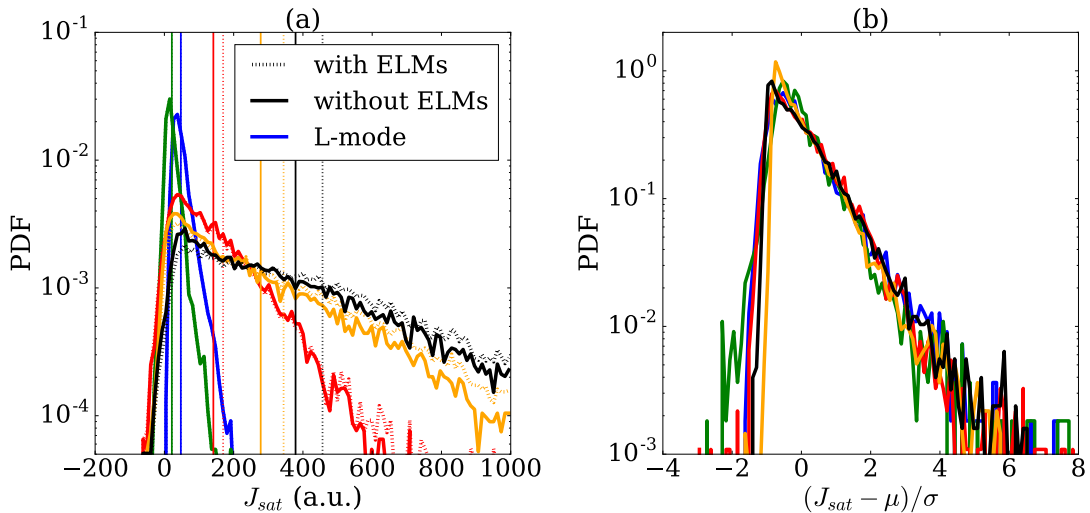


Figure 5.17: Unscaled (a) and rescaled (b) PDFs from a Horizontal target H-mode D₂ fuelling ramp (JPN89786). Colours correspond to figure 5.14. Dashed and solid lines in (a) have ELMs included and removed respectively. Vertical lines indicate the mean of the corresponding colour. ELMs have been removed from data in (b).

Considering now the fluxes measured by the limiter probe, broadly, they agree with the density profiles in that there is no systematic increase of wall flux with increasing collisionality, but the dependence is more complex than suggested by the density profiles. Time traces of the limiter probe J_{sat} (10ms moving average) and the integrated flux to the outer divertor (10ms moving average and full time resolution) are shown in figure 5.22 (a) and (b) respectively. It should be noted that the colours do *not* correspond to figure 5.20, but have instead been coloured for each second. Following the transition to H-mode at 48s, the total divertor flux decreases by approximately a factor two rapidly over a 0.1s window, whereas the wall flux shows an *increase*. This is opposite to the expectation of increased confinement in H-mode. Indeed after \bar{n}_e has stopped increasing when transitioning to H-mode, the current to the limiter probe has increased by around a factor of four, even with the removal of ELMs. The N₂ seeding, beginning at 48.5s, initially increases the flux to the divertor, presumably due to

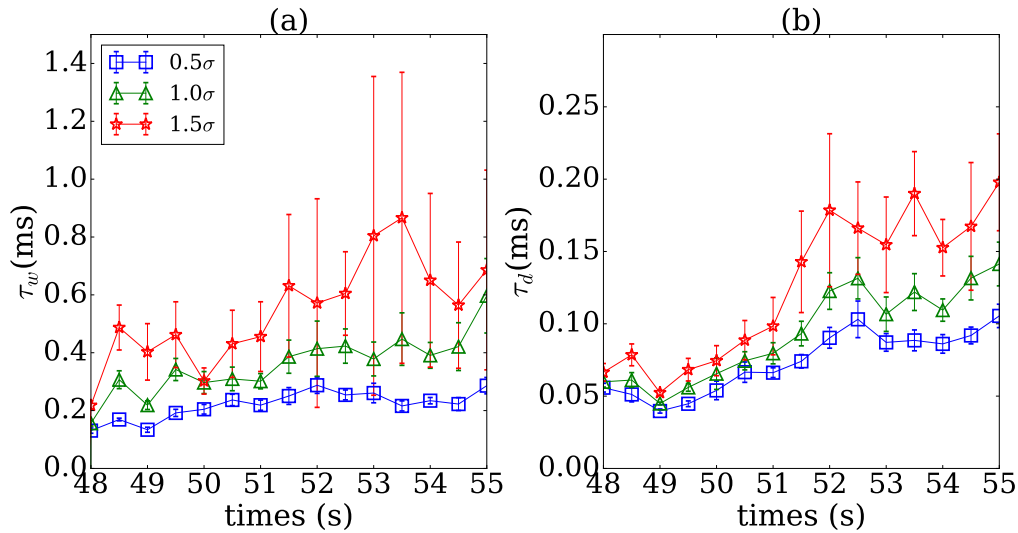


Figure 5.18: Time traces of τ_w and τ_d , for different intermittent thresholds, in a Horizontal target H-mode D₂ fuelling ramp (JPN89786). Errorbars are the uncertainty of the exponential fits of PDFs used to determine τ_w and τ_d .

increasingly HR condition, and then decreases as the divertor detaches. During the period 48.5-49.5s, there is no increases in the limiter probe J_{sat} and, in fact, after 49.5s there is a systematic decrease which occurs during detachment, when the divertor collisionality will undoubtedly be increasing. Just after 52s, there is an almost immediate increase in the limiter probe J_{sat} by around a factor four. This occurs simultaneously to a decrease in the the ELM frequency, visible in (b). It should be noted that this occurs simultaneously to an increase in \bar{n}_e , shown in figure 5.20 (a). For the limiter probe J_{sat} , this effect is transient and reduces by around a factor of four just before 53s, although the ELM frequency does not correspondingly increase.

PDFs of the limiter probe J_{sat} , with colours corresponding to figure 5.22, are shown in figure 5.23, where dashed lines show the effect of including ELMs. When renormalising, shown in (b), there is some agreement, but the collapse is poorer than the L-mode case. The properties of intermittent events, isolated using $\mu + 0.5\sigma$ as a threshold, are shown in figures 5.24 and 5.25. Regarding first the waiting and duration time statistics, when transitioning to H-mode, both τ_w and τ_d decrease by around a factor three. There is no systematic effect of the increasing N₂ seeding on either τ_w or τ_d that is outside the uncertainties of the fit. This extends to the conditional average and auto-correlation shown in 5.25 (a) and (b) respectively.

5.6 Discussion

This chapter has addressed the role divertor collisionality, quantified through Λ_{div} , in setting the properties of the upstream transport. The divertor collisionality has been modified in a number of ways including fuelling ramps in different target plate inclinations and N₂ seeding in L-modes and H-modes. The key result is that increases in Λ_{div} , and more generally collisionality, is not sufficient to increase the amount of

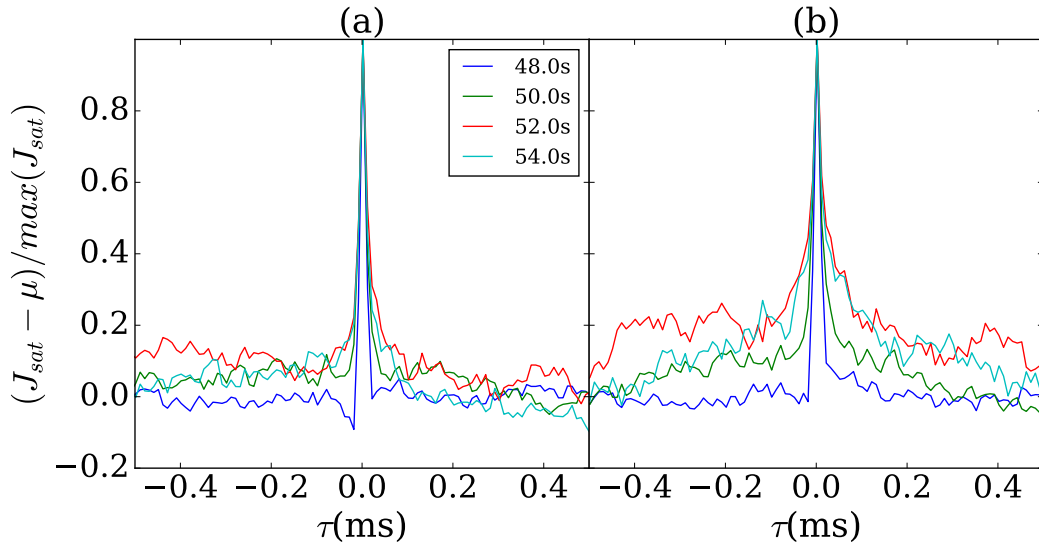


Figure 5.19: Conditional averages of intermittent events (JPN89786). Thresholds of $\mu+0.5\sigma$ and $\mu+1.5\sigma$ are shown in (a) and (b), respectively.

radial transport, as measured by either time average density profiles or the current measured by a flush mounted limiter probe near the outboard mid-plane.

There is only correlation between Λ_{div} and upstream transport (A_s or J_{sat}) when using D_2 fuelling in either L-modes or H-mode. The L-mode horizontal target results presented in this chapter are consistent with analysis of similar JET plasmas in [80], which act as a benchmark for the analysis method, although λ_n was used to quantify density profile changes. This relationship, however, does not apply generally to the vertical target and is dependent upon the region used (either the near or far SOL mapped region). Only in the far SOL mapped region does the correlation between A_s and Λ_{div} remain, and even then appears to diverge from the horizontal target results. This highlights a potential short coming of Λ_{div} , namely the ambiguity over which region should be used. In the two region model, Λ_{div} is modelled at the x-point [75]. This would suggest the use of Λ_{div} in the far SOL is not appropriate.

The insufficiency of Λ_{div} , and also collisionality more generally, as a control parameter on upstream radial transport is most starkly demonstrated by the use of N_2 seeding in both L-modes and H-modes. In both confinement regimes, Λ_{div} was increased by over an order of magnitude as measured by the divertor LPs. Further, this increase is likely an underestimate due to the measurement floor of the probes. Given that detachment is reached in both L-mode and H-mode, and so divertor $T_e < 1\text{eV}$, Λ_{div} is likely an order of magnitude higher. The L-mode results presented here contrast to those from comparable L-mode N_2 seeded plasmas on AUG [80]. However, recently, N_2 seeding was reported as ineffective in inducing shoulder formation in AUG N_2 seeded H-modes, which is consistent with the H-mode results presented here, although it should be noted that those AUG plasmas were performed in vertical target.

Recently, the same conclusion on the insufficiency of Λ_{div} was made when using L_{\parallel} to vary Λ_{div} in L-mode plasmas on TCv [115]. That study considered the near and far SOL upstream density profiles separately. In the near SOL, λ_n was found to

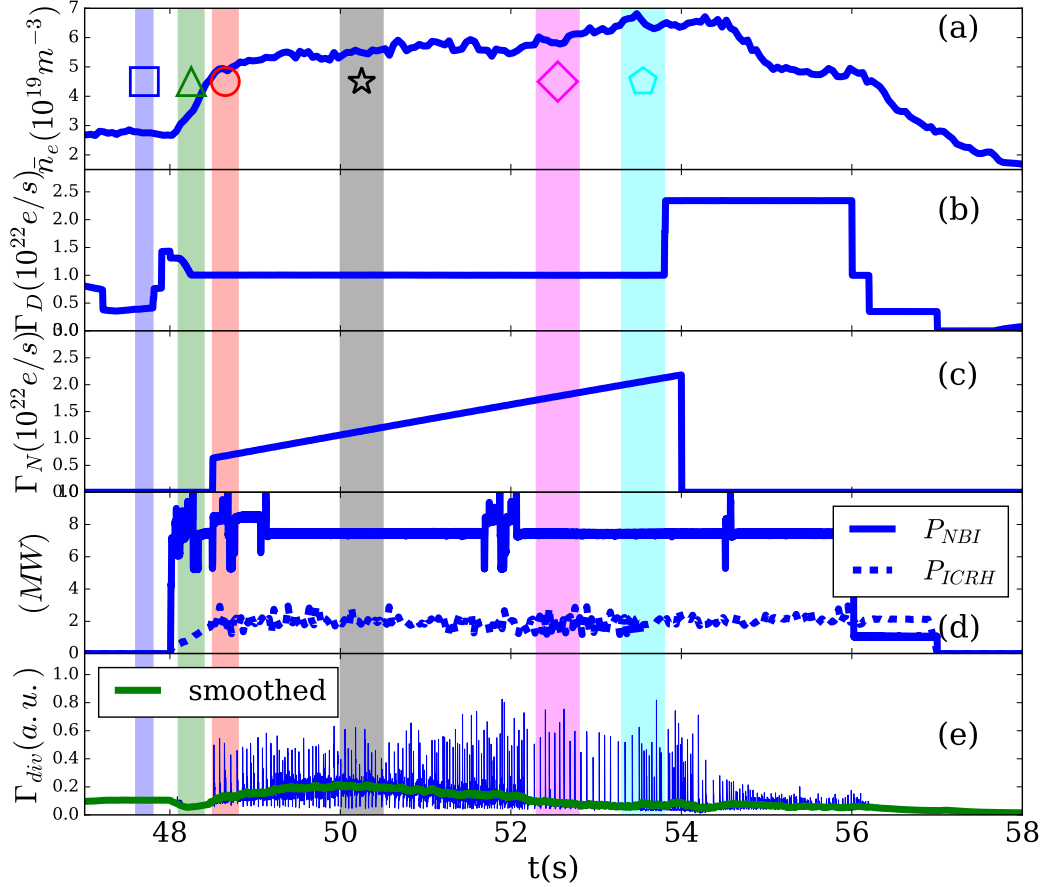


Figure 5.20: Pulse time traces of a Horizontal target H-mode N_2 seeding ramp (JPN89241). Shaded regions and symbols correspond to those used in later figures in this section. The total flux to the outer target Γ_{div} , is smoothed using a 0.1s moving average in order to show detachment with increasing N_2 seeding.

not depend on either the blob size, Λ_{div} , or the connection length; Λ_{div} was neither necessary nor sufficient. In the far SOL, $\Lambda_{div} > 1$ was found to be necessary but not sufficient. Notably, only increases in density, through D_2 fuelling were sufficient to modify the SOL properties, in line with the results presented in this chapter.

In addition to the experimental investigations from various tokamaks, the effect of changing the filaments electrical resistivity has been investigated numerically using the BOUT++ framework in 3D slab geometry [72, 116]. Increasing the parallel resistance, $\hat{\eta}_{\parallel} \propto n_e/T_e^{3/2}$, was found to generally enhance the radial velocity of the filaments. However, [116] adds the strong caveat that $\hat{\eta}_{\parallel}$ required increasing by three orders of magnitude, in the last 25% of the parallel domain with $T_e \sim 1\text{eV}$, in order to yield only a factor two increase in the radial velocity. Such conditions correspond to almost complete detachment, with the temperature at the x-point being only a few eV.

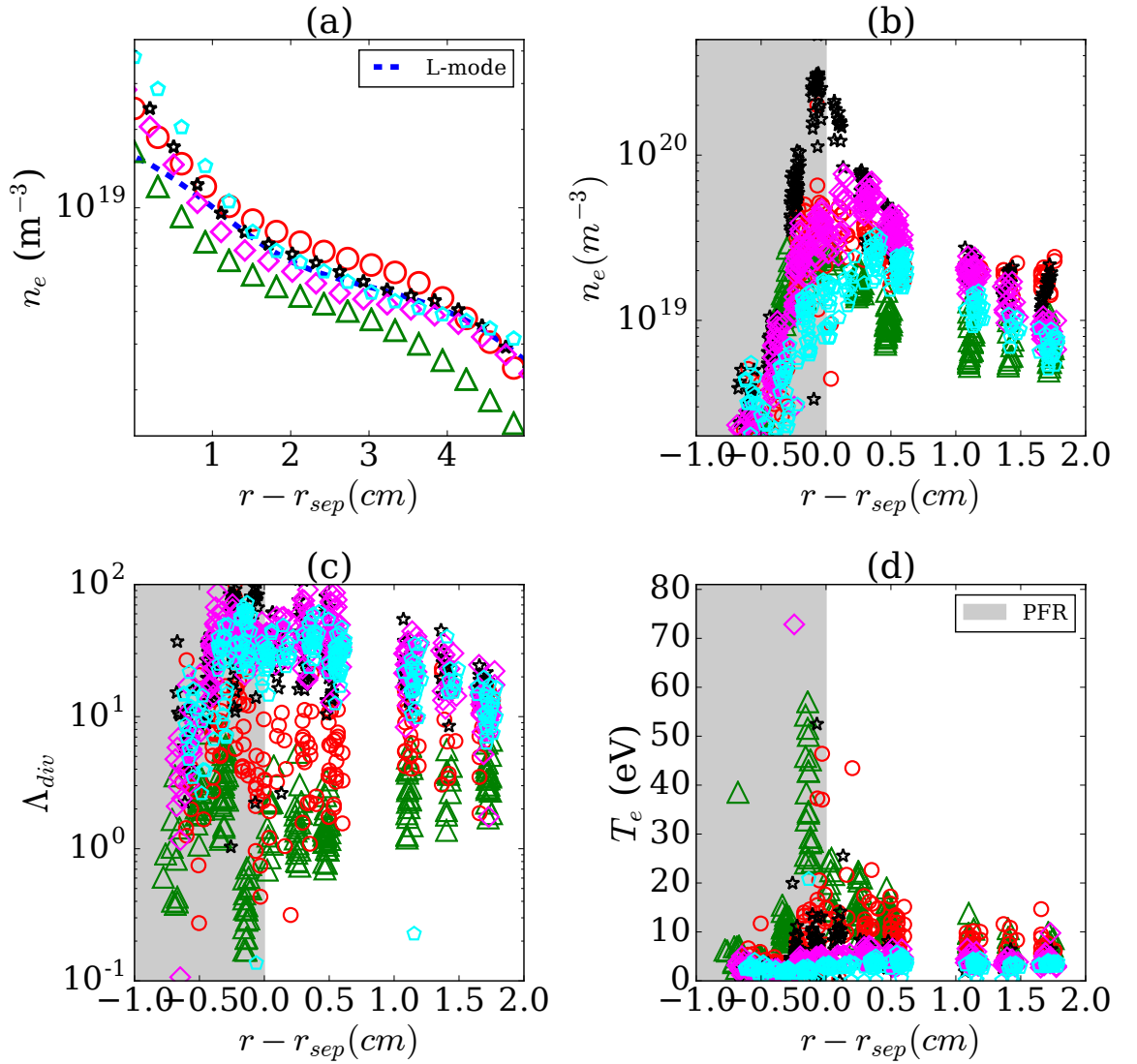


Figure 5.21: Upstream and divertor profiles in a Horizontal target H-mode N_2 seeding ramp (JPN89241). Symbols correspond to figure 5.20.

5.7 Conclusion

The SOL properties of a diverse range of plasmas have been studied using the divertor Langmuir probes, a flush mounted LFS limiter probe and main chamber Li-beam. The results presented challenge the central role of collisionality, and therefore Λ_{div} , in determining the quantity and nature of the main chamber SOL radial transport and the flattening of the density profile. More precisely, Λ_{div} increasing above some threshold **may** be a necessary condition, **but it is not sufficient**. Together with the TCV and AUG H-mode results, the results here motivate a change of direction of investigation, away from collisionality and towards the role of neutrals. The next chapter presents initial results in this direction.

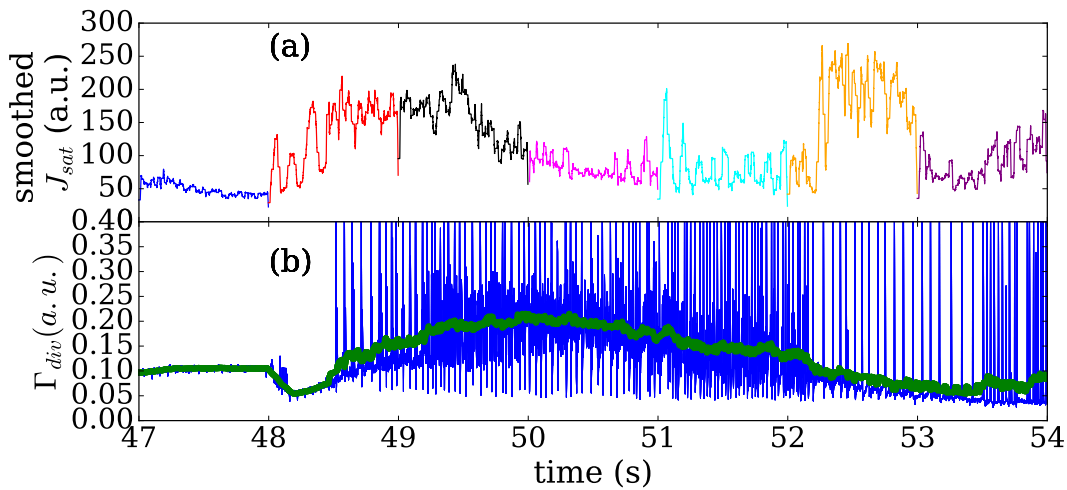


Figure 5.22: Limiter probe J_{sat} , (a), and integrated divertor probe flux Γ_{div} , (b). Colours in (a) correspond to figure 5.23. Both unsmoothed, (a), and smoothed, (b), traces of Γ_{div} , are shown in order to indicate changes to ELM frequency and the detachment evolution.

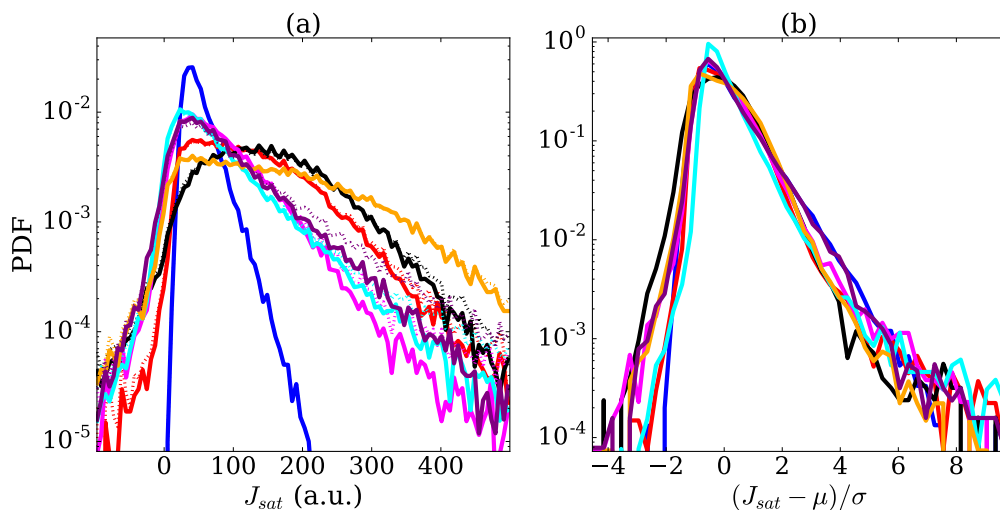


Figure 5.23: Unnormalised, (a), and normalised, (b), PDFs of the limiter probe J_{sat} . In (a) dashed lines include ELMs, solid lines have ELMs removed. ELMs have been removed in (b). Colours correspond to figure 5.22. L-mode is shown in blue.

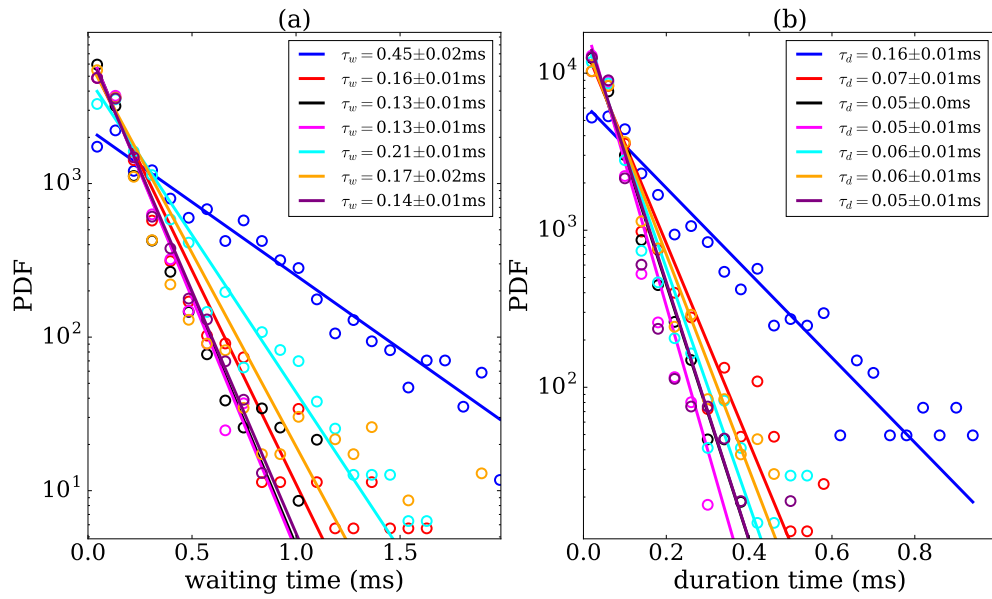


Figure 5.24: Waiting time and duration time distributions in a horizontal target H-mode N_2 seeding ramp. Solid lines show exponential fits to the data. L-mode is in dark blue

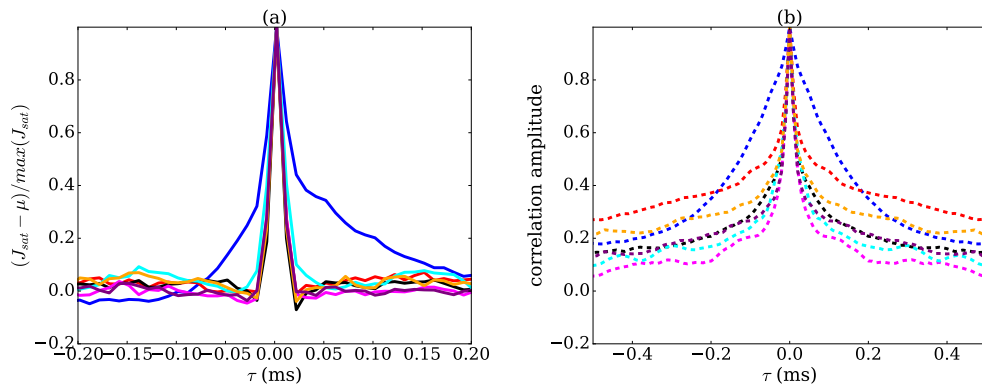


Figure 5.25: Conditional averages, (a), and auto-correlations, (b), in a horizontal target H-mode N_2 seeding ramp. L-mode is in dark blue.

Chapter 6

The influence of divertor neutrals

6.1 Introduction

The insufficiency of the parallel collisionality, quantified by Λ_{div} or otherwise, to generally predict the SOL density profiles naturally leads to the search for an alternative mechanism which is more consistent with the observed shoulder characteristics.

Perhaps the most basic and intuitive observation, however, is the increase in perpendicular particle flux density with \bar{n}_e . However, returning to the case of deuterium fuelled horizontal target L-modes, the shoulder was observed to form rapidly as the divertor transitioned from SL to HR (shown in section 5.2). This extended to comparable H-mode pulses (shown in section 5.5.1). The simultaneous increase of divertor and upstream densities make it difficult to identify the location where the most important processes are occurring.

This chapter presents results which separate the main chamber and divertor effects. It is found that the divertor conditions *do* play a substantial role in setting the upstream radial transport. This is achieved primarily through examining the effect of strike point sweeping of different amplitudes in both L-mode and H-mode (section 6.2). Additionally, the impact of N₂ seeding, main chamber neutrals and are considered. The horizontal and vertical target divertor configurations are also compared. A discussion of the results is provided and conclusions drawn where possible in attempt to prove a consistent picture of the shoulder formation.

6.2 Strike point sweeping

6.2.1 Small amplitude sweeping

Through minimal sweeping of the radial strike point location, R_{SP} , across the horizontal target (total target distance of 5 cm) we find that the changes in the total D _{α} emission integrated across the outer divertor ($I-D_\alpha$, the sum of multiple chordal D _{α} brightnesses across the outer divertor target) also oscillate in the same sawtooth fashion. The close correlation between movement of the strike point, A_s , and $I - D_\alpha$, is shown in figure 6.1 versus time. It should be noted that the fuelling rate, (d), and \bar{n}_e (not shown) is

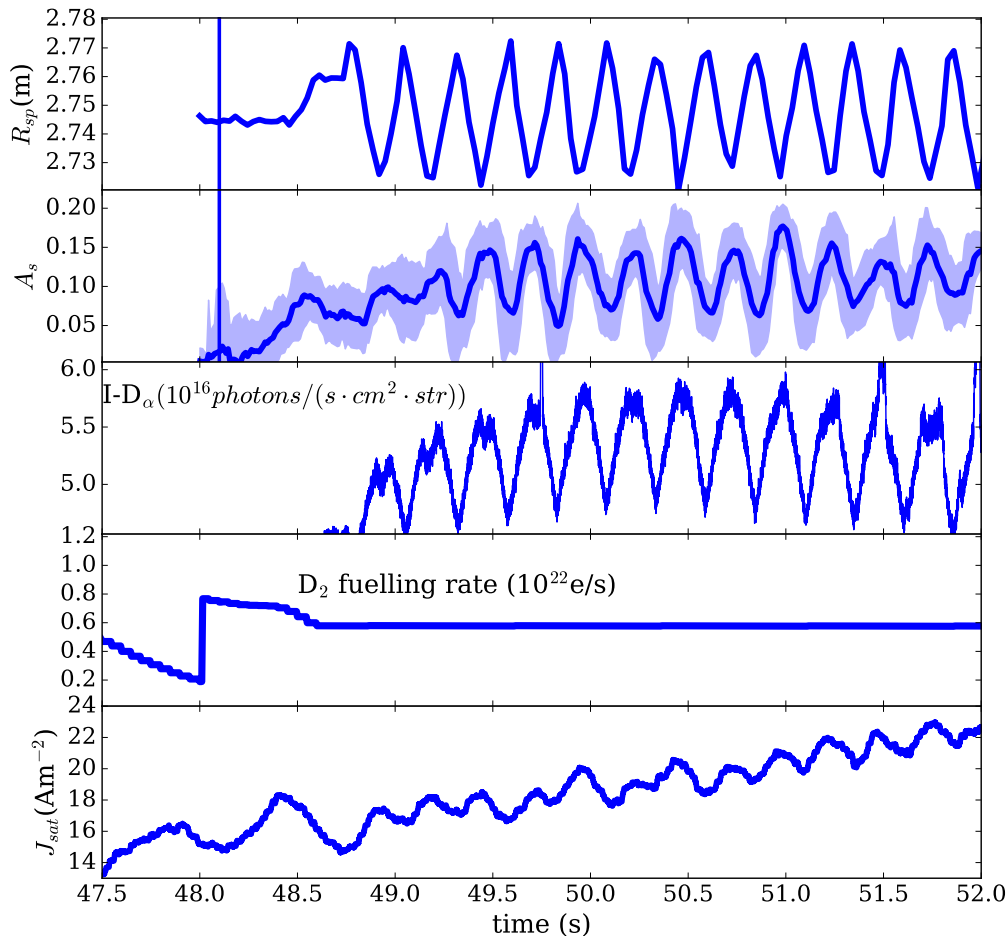


Figure 6.1: Time traces of quantities varying with strike point sweeping. Uncertainties in A_s are the standard deviation of profiles averaged over 0.1s time windows. J_{sat} as measured by the flush mounted limiter probes.

constant during this period.

Following the formation of a small shoulder (figure 6.1 (b), 48.5s) with core density rise due to initial high D_2 fuelling rate, both A_s (b) and $I - D_\alpha$ (c) oscillate in anti-phase with respect to the radius of the outer strike point, R_{sp} . In other words, $I - D_\alpha$ (and A_s) are both maximized when R_{sp} is smallest. The flush mounted limiter probe J_{sat} , shown in (e), also exhibits the 4Hz sweep, with the steady increase being due to N_2 seeding as detailed in 5.4.

Figure 6.2 displays the correlation between the different characteristics given in figure 6.1. The strong correlation between A_s and $I - D_\alpha$ (b) as well as between $I - D_\alpha$ and R_{sp} quantitatively reflect what is evident from figure 6.1; small changes in the divertor D_α (and thus neutral processes such as ionization and charge exchange) correlate with observable changes in A_s upstream. As further evidence against Λ_{div} , to within error bars Λ_{div} does not change with A_s when using either the near or the far SOL (figure 6.2 (d)).

Although the relative changes presented in figures 6.1 and 6.2 are small, they nonetheless provide direct evidence of the influence of the downstream conditions on

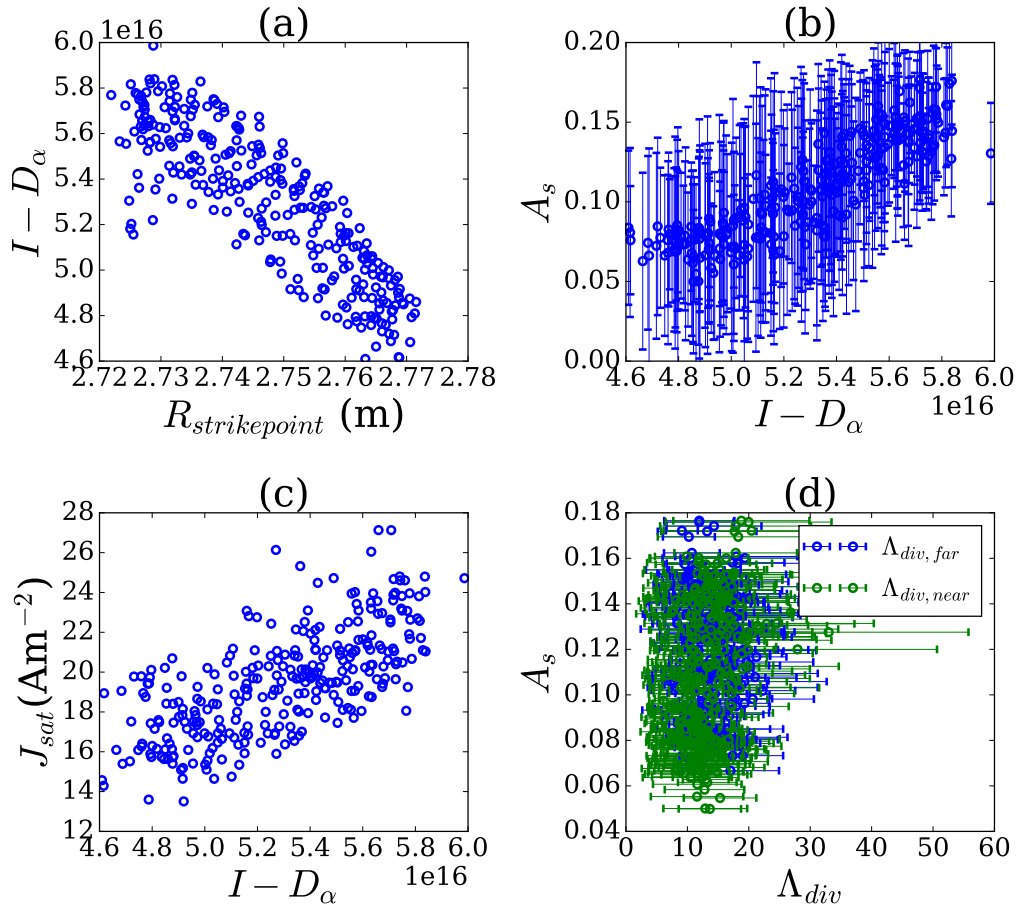


Figure 6.2: Correlations of divertor and main chamber quantities varying with strike point sweeping. Units of $I - D_\alpha$ are $ph/(cm^2 \cdot sr \cdot s)$. Uncertainties in A_s are the standard deviation of profiles averaged over 0.1s time windows.

the *upstream* of radial transport. In the next section, a more extreme example of this effect is investigated.

6.2.2 Large amplitude sweeping

Even larger sweeps with an amplitude of ~ 20 cm were performed in a D_2 fuelling ramp L-mode. The extremes of the strike point sweeping are shown in figure 6.3. The amplitude is sufficiently large that divertor configuration is considered to have changed from horizontal configuration (tile 5) at the minimum R_{SP} to corner configuration (tile 6) at the maximum as shown in the legend.

Sweeping of this amplitude was observed to have a profound effect on the radial transport in the main chamber SOL. Time traces of relevant parameters are shown in figure 6.4. The occasional skip in the minima of Z_{SP} is due to the strike point intersecting the vertical target (tile 7). The increasing plasma density is evident in the growth of the peaks of the limiter J_{sat} , (c), and divertor D_α , (d). The sweeping modulates limiter J_{sat} and divertor D_α by approximately a factor five. The large amplitude of the sweeps also results in a modulation of the separatrix to limiter gap (raw outer gap (ROG)) (e). However, this variation is only 10-15% of the total gap

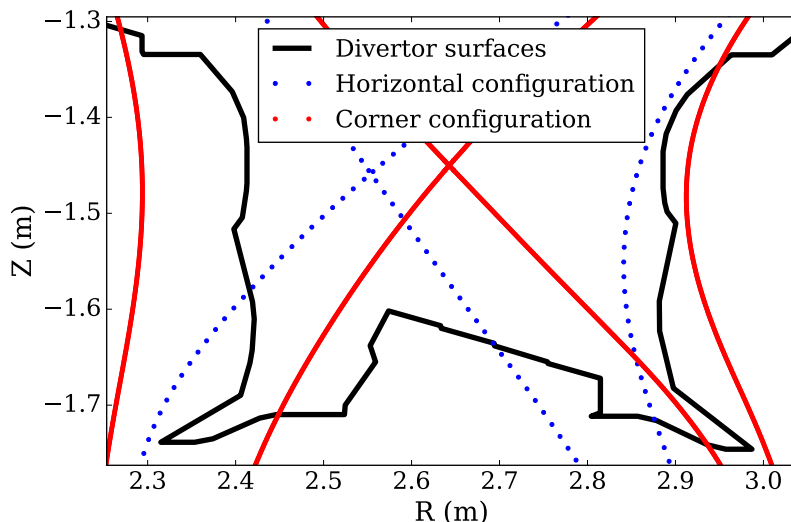


Figure 6.3: Large amplitude sweeping strike point extrema. At minima in R_{SP} , the divertor is in horizontal configuration (blue dots), while at the maxima, it is in corner configuration (solid red). Sweeping occurs at 4Hz.

and would unlikely cause the factor five variation. As additional evidence of the effect of the strike point sweeping, figure 6.5 shows SOL density profiles selected from the extrema of the strike point sweeping. Consistent with the large modulation of J_{sat} , the density profile is strongly dependent upon the strike point location, being much flatter when at lower R_{SP} . Fewer density profiles were available at large strike point sweeping as the upstream movement of the plasma (amplitude 5mm at the midplane) was sufficient to misalign the views of the Li-beam periscope.

The relationships between the variable in figure 6.4 is not as simple as the small amplitude sweep case, as shown in figure 6.6. When plotted against spatial parameters (either ROG or R_{SP}) both J_{sat} and the divertor D_α are multi valued ((a), (c) and (d)). Red arrows indicate the direction in time. J_{sat} and the divertor D_α appears to be more single valued although the highest values occur when the R_{SP} is *increasing*, indicated by green ovals, opposite to the trend observed in the small amplitude sweep. With continued increases in R_{SP} , J_{sat} and the divertor D_α saturate and begin to decrease. When the strike point travels off the outer edge of the horizontal target (tile 5), $R_{SP} > 2.8m$, towards the corner of the divertor region, the decrease becomes steeper, consistent with the removal of neutrals by pumping.

The asymmetry between sweeping toward and away from the neutral pump suggest a more complex picture potentially involving neutral expansion and compression and/or the switching between kinetic and fluid neutral regimes. Nevertheless, the key observation is that the divertor conditions modified in this way have a strong effect on the net radial transport upstream and are supportive of the hypothesis of drainage clogging by plasma-neutral interaction of the fuel species.

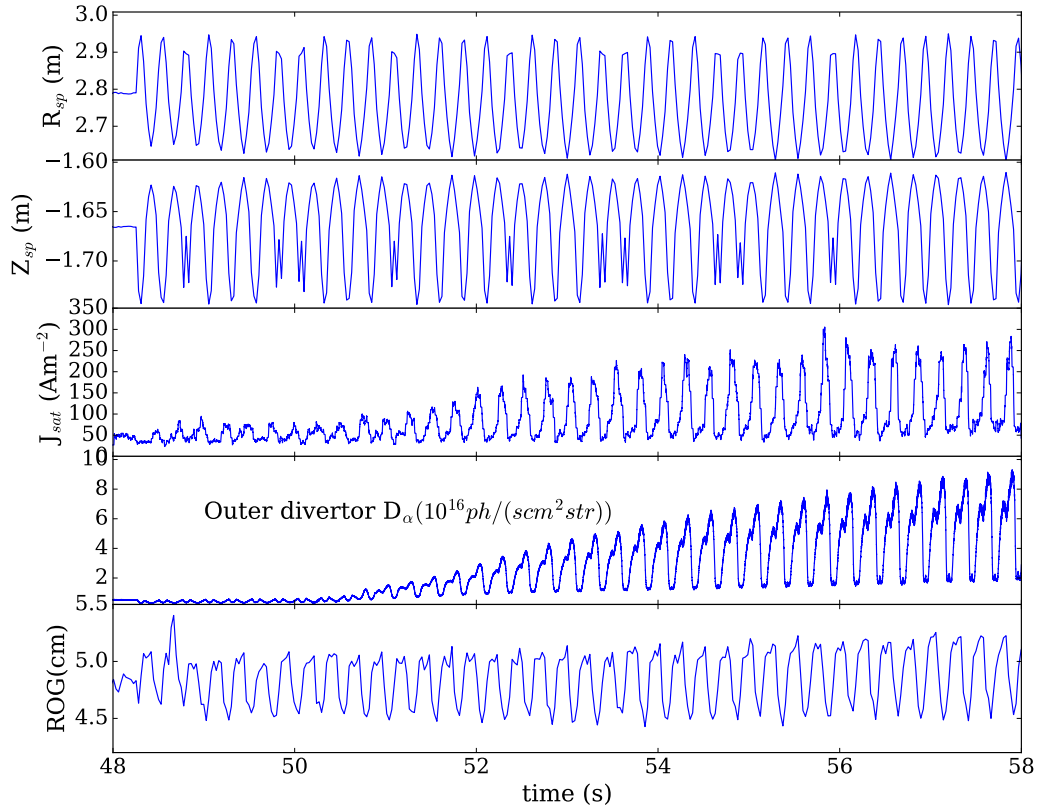


Figure 6.4: Time traces of upstream and divertor parameters during strike point sweeping, extrema of which are shown in figure 6.3. Note the Outer divertor D_α is different to $I - D_\alpha$; it views the entire divertor, not just the horizontal target. A 10ms moving average is used to smooth the limiter J_{sat}

6.2.3 Strike point sweeping in H-mode

In addition to L-mode plasmas, the effect of the strike point sweeping on the main chamber radial transport has also been observed in an H-mode plasma, relevant parameters of which are shown in figure 6.7. ELMs have been removed from J_{sat} , shown in (a), and smoothed using a 10ms moving average. ELMs have not been removed from the divertor D_α , but have been smoothed also using a 10ms moving average in order to reveal the underlying oscillation with strike point sweeping.

6.3 D_α in the presence of N

The level of N in the divertor region influences the neutral processes occurring there. In this section, the effect of N on divertor recycling in the N_2 seeded L-mode case (JPN90697) from the previous chapter is investigated.

Increasing N_2 seeding rate results in a shrinking of radial extent of the divertor D_α emission region as well as total D_α . Time traces demonstrating this are shown in figure 6.8. Changes to the upstream transport also occur, indicated by A_s and J_{sat} which peak at around 51-52s. Before 52s, the strike point oscillation is visible on all

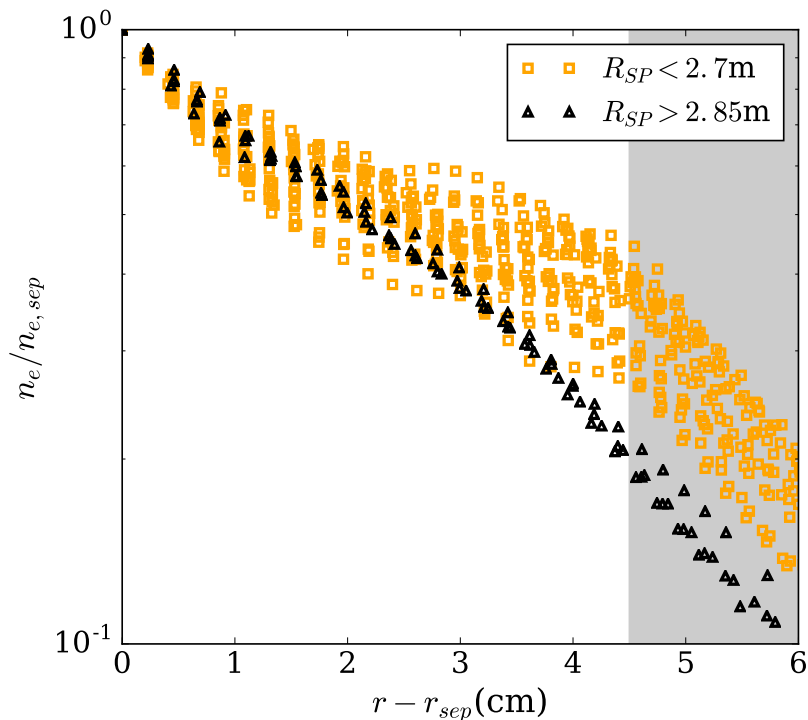


Figure 6.5: Normalised density profiles at the large amplitude strike point sweeping extrema over the time window 54-56s. At $R_{SP} < 2.7\text{m}$, strike point is on the horizontal target and for $R_{SP} > 2.85\text{m}$, the strike point is in either corner configuration, or occasionally on the vertical target.

channels of the vertical D_α view chords. After 52s, the oscillation on the radially outer most channel (C7) dies away and the average levels also reduces. With increasing NII brightness, this effect moves progressively inwards. As the D_α emission region shrinks toward the separatrix, A_s decreases together with limiter J_{sat} . The sub-divertor neutral pressure (not shown) remains constant over this time range indicating the total density of Deuterons in the divertor region is also fixed suggesting observations in figure 6.8 are due to the changing reaction rates.

Complementary observations to those of figure 6.8 are given in figure 6.9 which shows 2D emission maps, obtained from tomographically inverting images from the tangentially viewing camera system, in D_α (a-c) and NII (d-f). Going from left to right follows increasing N_2 seeding rate with inset symbols corresponding to those in figure 5.10, such that each column is at a different divertor condition. The discrepancies between the inversion positions and the flux surfaces throughout figure 6.9 is of the order 2-3cm and is due to both uncertainties in the mapping of optical camera pixels to vessel structures and also equilibrium reconstruction. The evolution of the D_α emission profiles closely resemble the time traces of figure 6.8; the emission is strongest at the peak HR and then radially narrows as N_2 is further increased. Unlike figure 6.8 however, figure 6.9 (c) suggests a reduction in the peak emission at the strike point by around a factor of 2 at the onset of detachment.

In the previous chapter, the presence of N on vessel surfaces was sufficient to increase Λ_{div} by an order of magnitude without corresponding change to the upstream

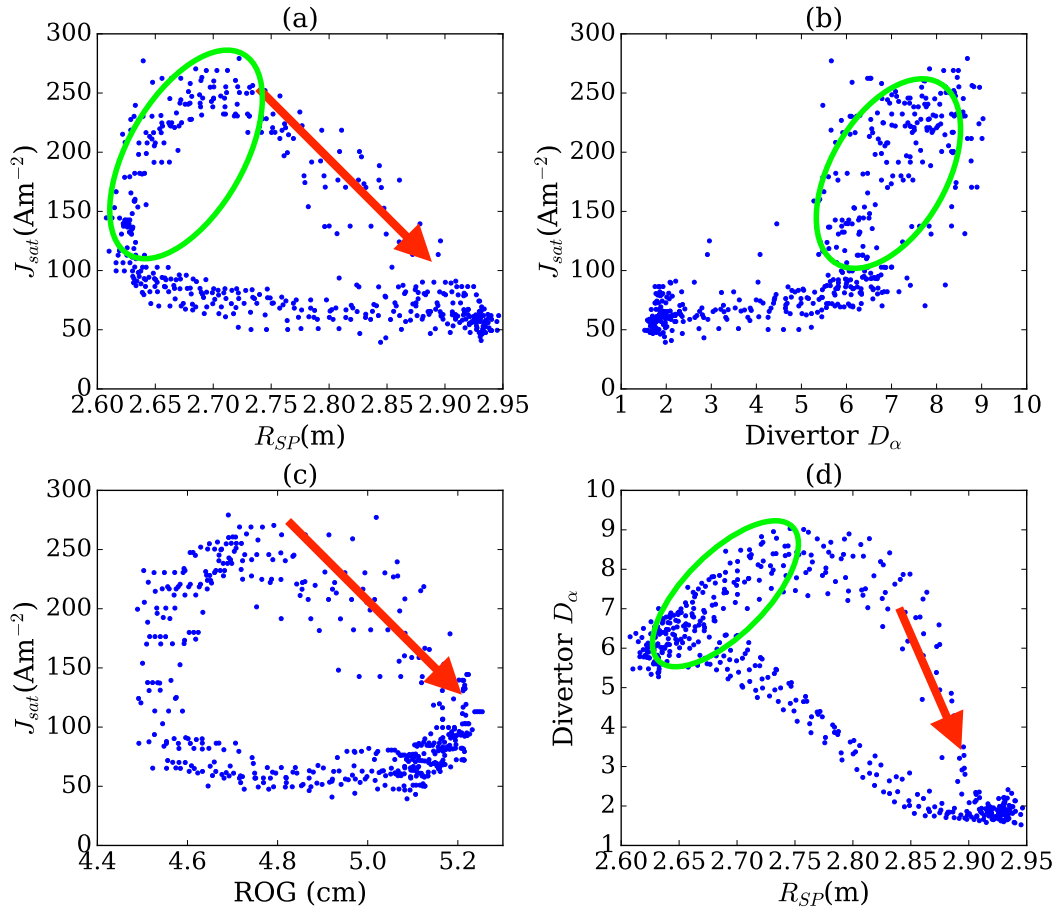


Figure 6.6: Large amplitude strike point sweeping correlations. Data in green ovals correspond to each other. The direction of progression in time is indicated by red arrows. Units for Divertor D_α are 10^{16} ph/($\text{cm}^2 \cdot \text{sr} \cdot \text{s}$).

density profile (section 5.4). Despite being a crude metric of the plasma-neutral interaction, measurements of $I - D_\alpha$ for the same discharges consistently correlate with the amplitude of the shoulder measured by A_s , regardless of the presence of N. Shown in figure 6.10 are the same pulses as figure 5.10, with the addition of the fuelling ramp of figure 5.1. The effect of strike point sweeping, discussed in section 6.2, is also indicated.

6.4 The role of mid-plane neutrals

This section briefly digresses onto the influence of main chamber neutrals. The results presented suggest local ionization does strongly influence the shoulder formation or the quantity of radial transport.

Figure 6.11 compares pulses with vertical and horizontal divertor targets. Normalized density profiles are shown in (a) and S_{ion} profiles in (b). The mid-plane pressure as a function of \bar{n}_e is shown in (c). The vertical lines in (c) correspond in colour to the profiles in (a) and (b) such that colours correspond to a fixed \bar{n}_e . Separatrix densities were also equivalent for each \bar{n}_e . Clearly evident is the slight flattening of the density profile in the horizontal target case, which corresponds to generally higher SOL den-

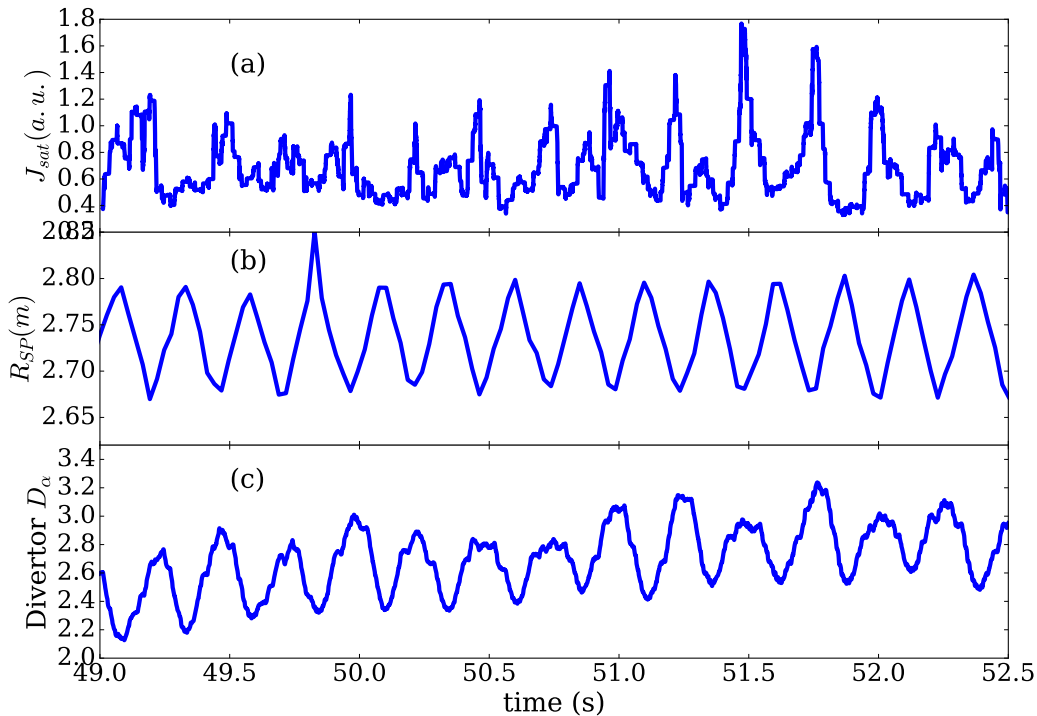


Figure 6.7: Time traces of (a) limiter J_{sat} , (b) R_{SP} , (c) Divertor D_α for an horizontal target H-mode with constant input power and D_2 fuelling rate. ELMs have been removed in (a) and smoothed in (c) using 10ms window moving average.

sities compared to the vertical target. The *shape* of the ionisation profile mimics the density profile between the two target configurations, but overall the magnitude in the vertical target case is higher. In other words, a higher ionisation does not necessarily lead to a higher density. Regarding the total flux of neutrals toward the separatrix, despite the penning gauge being a relatively poor measure due to its large distance from the midplane, the functional dependence with \bar{n}_e is essentially identical, suggesting a similar number of neutrals are approaching the plasma from the LFS main chamber in both divertor configurations.

The general implication of the results is that the ionisation occurring locally in the SOL is not having a strong effect on either the magnitude or shape of the density profiles. That is not to say that local fuelling is not occurring, but that other effects dominate. These results in the context of other studies will be explored in section 6.6

6.5 Comparison of vertical and horizontal target

The previous section showed that divertor configuration influenced the upstream radial transport in a manner that was not explainable by local ionisation. In this section, results of divertor D_α distributions in the horizontal and vertical target are presented which may consistently explain these differences.

Figure 6.12 shows 2D emission contours in D_α for the horizontal (a-c) and vertical (d-f) targets. Each column corresponds to the vertical line in figure 6.11, with ascending

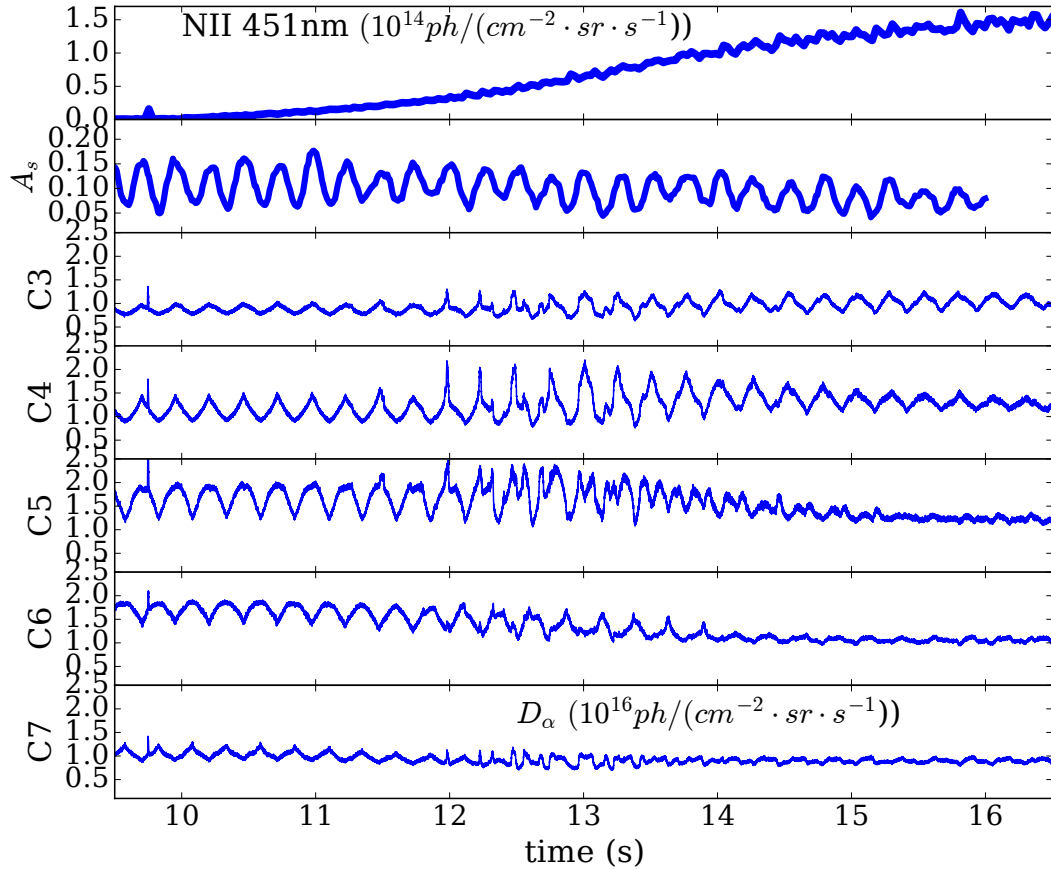


Figure 6.8: Time traces of the later half of JPN90697 including NII brightness, A_s , limiter J_{sat} and the five vertical view-chords on the horizontal target with increasing radius from C3-C7.

density from left to right. The D_α emission region is wider both in real space and flux space in the horizontal target compared to the vertical target. Comparing the first column (a and d), when the divertor is in the SL regime, immediately evident is the difference in radiation region. It should be noted that the peak emission is not located at the strike point, but rather slightly into the PFR. This may be due to the combination of equilibrium and tomographic inversion errors. However the D_γ emissivity (figure 6.13) radiates primarily at the strike point as might be expected. If the inversion is correct then it could be explained by the neutrals attacking the separatrix from the PFR as well as LFS SOL. Higher sub-divertor pressures (by a factor two to three) are measured in the vertical target compared to the horizontal target for a given \bar{n}_e . Further, as can be seen in figure 6.12 (e) and (f), the emission appears to spread into the PFR for the vertical target with increasing \bar{n}_e . Figure 6.12 (b and e) correspond to where both configurations have transitioned to HR divertor conditions. The shoulder has formed in the horizontal target, but not in the vertical. The peak emissivity in the horizontal target configuration is $\sim 2\times$ higher than the vertical target and there is a strong difference in the shape of the emission region; the equivalent contour line (e.g. red) for the horizontal target extends over a wider region in the common flux region of

SOL than for the vertical target. As the core density is increased further (c and f), the shoulder amplitude saturates in the horizontal target. In vertical target, the emission region shape remains relatively unchanged, spreading slightly into the PFR. On the other hand, the horizontal configuration continues to spread across flux surfaces and also to larger R, and over the edge of the horizontal target ($R > 2.82m$).

A more direct comparison of the D_α emission is shown in figure 6.14. The emission in flux tubes of width 0.01 in ψ , extending 0.2m off the target along the poloidal flux surface, is integrated in both the vertical and horizontal targets. In general the emission is higher for a given flux tube in horizontal target compared to the vertical. However, the emission in vertical target does reach and exceed values when shoulder formation occurs in the horizontal target ($t = 49.2s$) and so one might expect a shoulder to form in vertical target. This highlights the insufficiency of simple measures D_α to generally explain the observed upstream transport, despite the correlations detailed in previous sections of this chapter.

Nevertheless, the observed differences in both the shape and magnitude of the emission region between the different divertor configurations and the corresponding differences to the upstream density profile could be meaningful in that there is more plasma-neutral interaction in the region where the upstream density shoulder should form for the horizontal target. In the horizontal target, recycled neutrals would be preferentially directed toward the SOL where they may clog the flow, whereas in the vertical target configuration, recycled neutrals would be directed toward either the separatrix PFR.

6.6 Discussion

The insufficiency of Λ_{div} , and parallel collisionality in general, in controlling the properties of radial transport led to the search for an alternative mechanism. Based on the results presented in this chapter and chapter 5, it may be speculated that 'recycling' or 'neutral processes' in the divertor modify flows out of the SOL.

Expanding further on this hypothesis, it is the neutral density in the *divertor* LFS SOL which may act to control the drainage of plasma along field lines. This 'clogging' of the flow acts to preserve the density of filaments as the travel outwards, thus enhancing the net radial ion transport. Controlling the number of removed neutrals would influence this clogging effect and is consistent with the strike point sweeping results. In a similar vein, the vertical target would act to ballistically reflect neutrals back toward the PFR, aiding the pumping of neutrals, reducing clogging, consistent with reduced upstream transport

EDGE2D-EIRENE modelling of unseeded H-mode plasmas with vertical and horizontal targets [50] shows a strong similarity to the experimental results presented here. The modelled divertor ionization distribution at the target is much broader in horizontal compared to the vertical configuration. The density across the entire SOL was increased for the horizontal target compared to the vertical, although the profile shape

was generally the same. The lack of a localized effect in the region of the upstream density shoulder may not be surprising given such fluid codes do not take into account cross-field transport due to turbulence or even convection. It should also be noted that the ionisation distributions reported in that study are also good indicators of the CX reactions.

Ionization in the divertor plasma has been shown in several other models (fluid and analytic) to affect flow magnitude and direction, and would lead to flow reversal out of the divertor towards the SOL [123, 124, 125, 126]. Variations in flows can be localized and could correspond to those regions which map to upstream SOL shoulder.

More recent analytical studies [127, 128] support the 'clogging' or parallel flow reduction hypothesis. The authors noted CX as the likely mechanism over ionisation [127, 128] due in part to its higher reaction rate. CX would act to reduce T_i but have minimal effect on the local T_e . Although divertor T_e reduces with increasingly HR divertor conditions, reductions in T_i in the midplane have been observed using an $E \times B$ analyser and correlated with the formation of the shoulder [117]. The stochastic model from [128] was implemented in 1D in [129] and demonstrates that reduced filament drainage rates could be used to match the time averaged density profiles. However, at the highest densities, both reduced drainage rates and increased radial filament velocities were required. That study also ruled out collisionality as the main control parameter influencing the profile shape.

In short, the results presented in this chapter offer no direct proof that divertor neutral processes are leading to shoulder formation through reductions in parallel flows out of the upstream SOL via 'clogging', however, the results presented are more generally consistent with 'clogging' than collisionality.

Regarding the role of midplane neutrals, the results of section 6.4 indicate that local ionization in the main chamber SOL is not the dominant mechanism influencing the formation of the density shoulder. This mechanism is perhaps the most intuitive in that one can envision setting up a SOL 'radial recycling condition' [81] such that as the core density is increased, the ionization mean free path in the main chamber SOL shortens, leading to an increase in ionization and a SOL density rise, followed by the ionization mean free path shortening. This positive feedback loop would act rapidly after the ionization mean free path reduced below some critical value (presumably the SOL width) and is supportive of the strong increases in density associated with shoulder formation. The results here contradict this hypothesis. Other studies also point to the lack of importance of main chamber neutrals. Experiments using CD4 puffing into the JET-C SOL concluded that local ionization in EDGE2D-EIRENE modelling could not reproduce the observed enhancement of the far SOL density [130]. Only an increase in the radial transport, in that case diffusion, could reproduce the profiles. Further, a study of shoulder formation on MAST found no correlation between the mid-plane radial D_α chord and changes to the profile flatness [93]. The authors of that study pointed out that the local ionization hypothesis is not consistent with the widespread observation of the insensitivity of the SOL T_e profiles to the shoulder formation; local ionisation

is not sufficient to observably cool the SOL. That said, the neutral processes in the main chamber may possibly add to the clogging effect, but most of the effect is likely to occur in the divertor where the neutral densities are the highest. Further, modelling of the SOL using diffusive and convective paradigms also suggest local ionisation is not an important effect [131]. The 2D turbulence code ESEL (and also HESEL) routinely observes the flattening of the density profile but includes no neutral physics.

6.7 Conclusions

This chapter provides evidence that is supportive of plasma-neutral interactions of the fuel species in the divertor region having an influence on the main chamber radial transport. This hypothesis was explored as an alternative to the role of collisionality which was challenged in chapter 5.

Firstly, in section 6.2, strike point sweeping of various amplitudes in both L-mode and H-mode was found to modulate the radial transport upstream, measured by both A_s and J_{sat} , consistent with the removal of neutrals being dependent on the proximity of the strike point to the pump entrance. Also, divertor radiation distributions in horizontal and vertical target may plausibly explain the observed differences in upstream transport between the two configurations.

Secondly, the presence of N was found to reduce both the D_α emission in the divertor and the upstream radial transport, although the effect was relatively modest. Importantly, the formation of the shoulder correlated with the divertor D_α regardless of the presence of N (figure 6.10).

It should be noted that the the measurements of D_α are only estimates of the magnitude of the plasma-neutral interaction; without knowing the local density and temperatures, quantifying the total number of reactions occurring is challenging. Modelling may help to quantify different neutral effects.

Lastly it is likely that the ionization of midplane neutrals do not strongly influence either the shape or the magnitude of the main chamber density profile, consistent with the results of other studies.

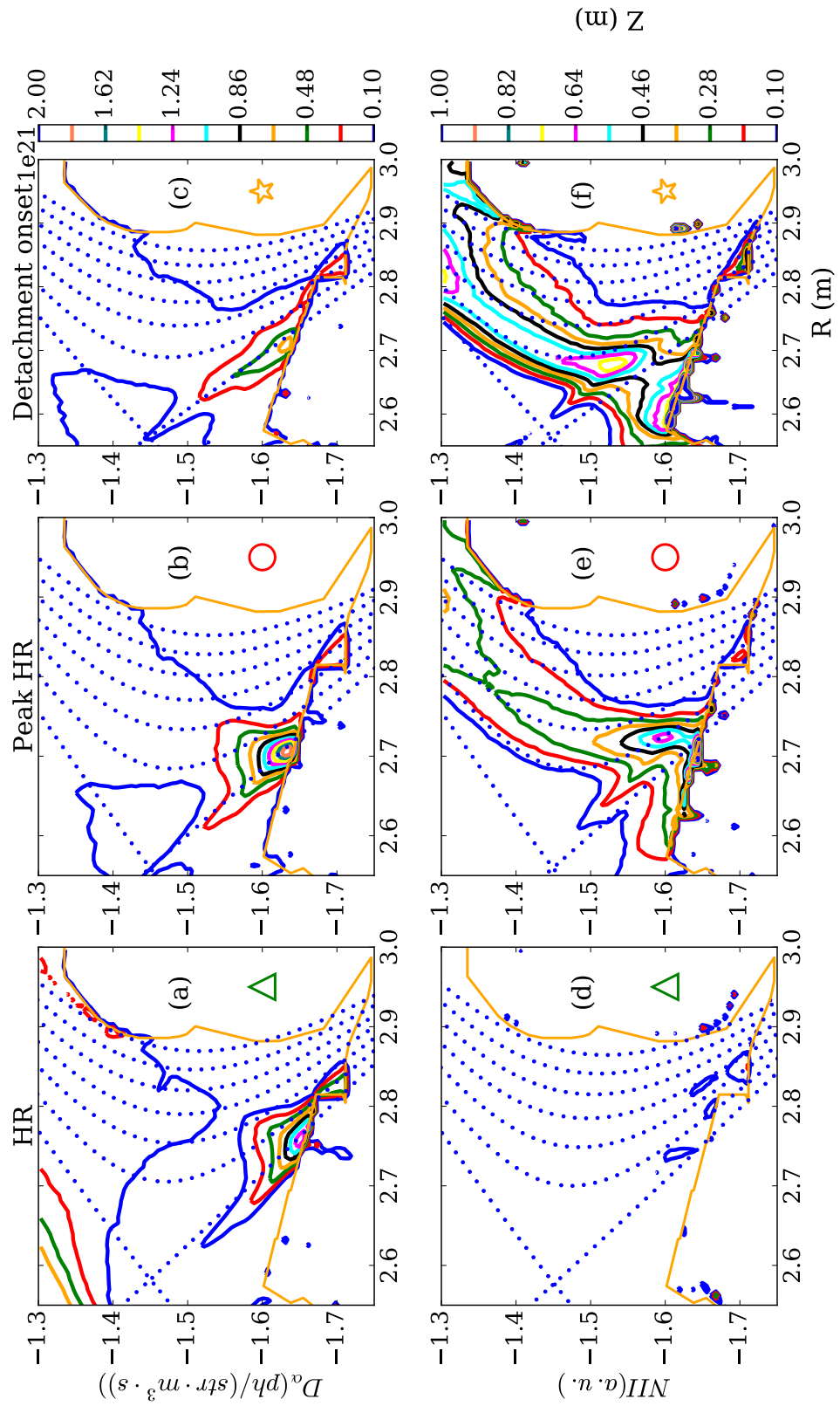


Figure 6.9: 2D emission maps of D_α (a-c) and NII (d-f). N_2 seeding rate increases from left to right. Inset symbols correspond in time to those in figure 5.10.

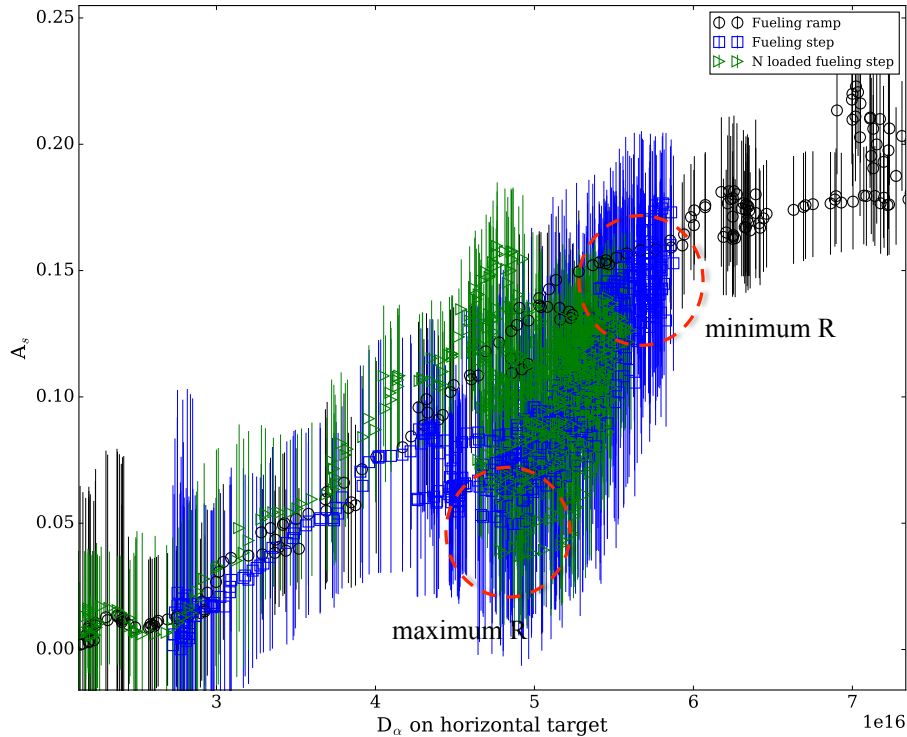


Figure 6.10: A_s dependence on D_α in cases with and without the presence of N 'loaded' vessel surfaces. The fuelling ramp (JPN89346) and fuelling step (JPN90697) have no Nitrogen present. The N loaded data (green triangles) follows several previous N_2 seeded shots. All pulses have the same I_p .

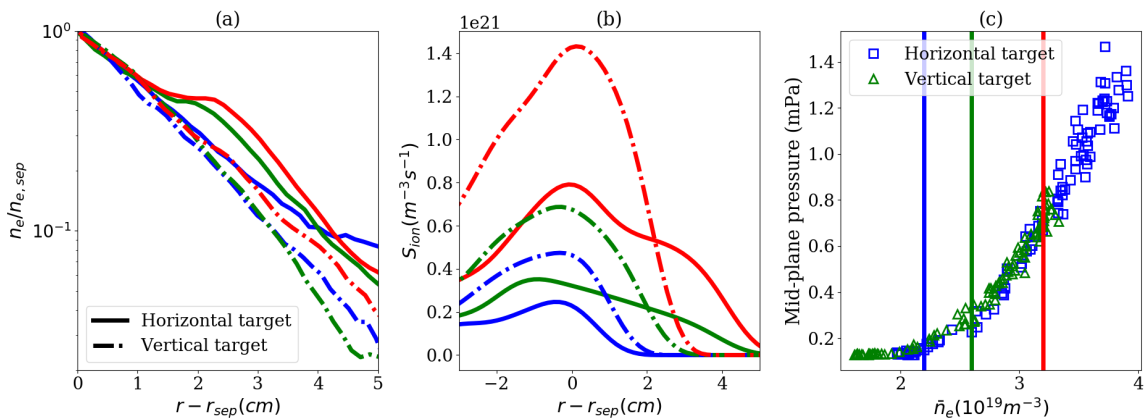


Figure 6.11: (a) Normalized n_e profiles for the horizontal (JPN89346) and vertical (JPN 89783) divertor target. (b) Corresponding S_{ion} profiles. (c) Dependence of mid-plane pressure on \bar{n}_e . Coloured vertical lines correspond in \bar{n}_e to profiles in (a) and (b).

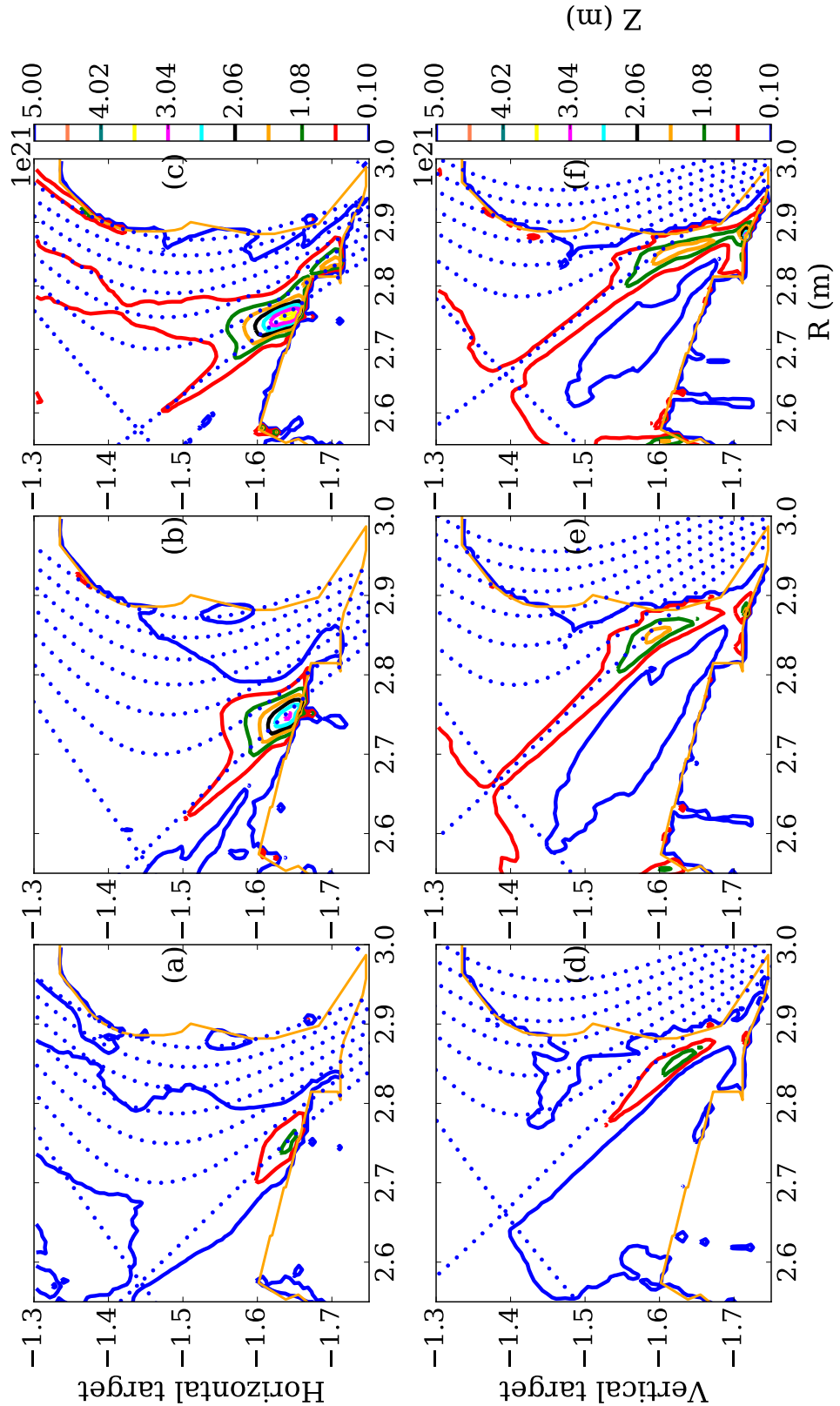


Figure 6.12: Comparison of 2D D_α emission maps of horizontal (JPN89346) (a-c) and vertical (JPN89783) (d-f) target. Flux surfaces are dotted and are separated in normalized flux ψ by 0.01 ($\psi_{sep} = 1.0$). \bar{n}_e increases from left to right with each column corresponding in time to the profiles in figure 6.11.

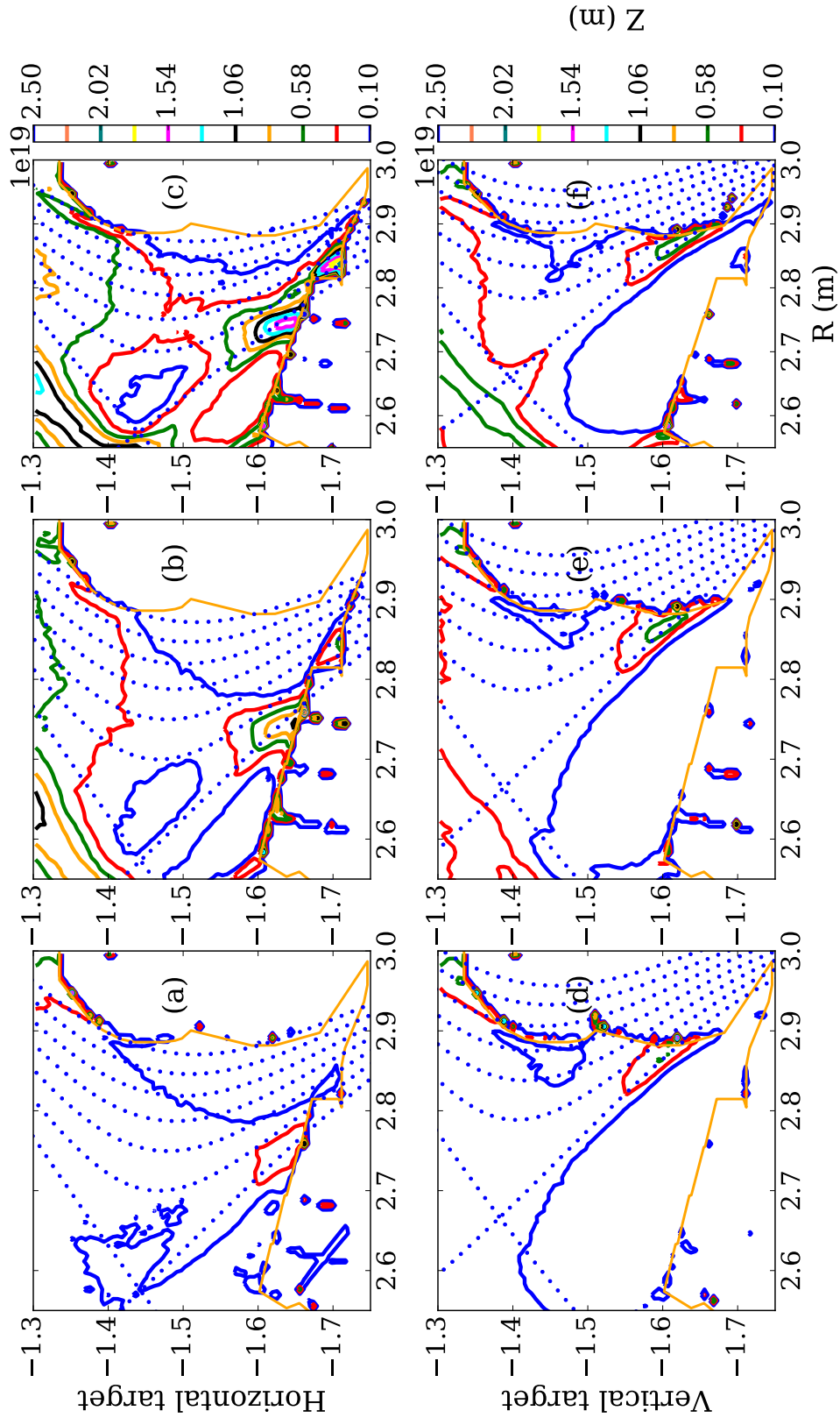


Figure 6.13: Comparison of 2D D_γ emission maps of horizontal (a-c) and vertical (d-f) target. Flux surfaces are dotted and are separated in normalized flux ψ by 0.01 ($\psi_{sep} = 1.0$). \bar{n}_e increases from left to right with each column corresponding in time to the profiles in figure 6.11.

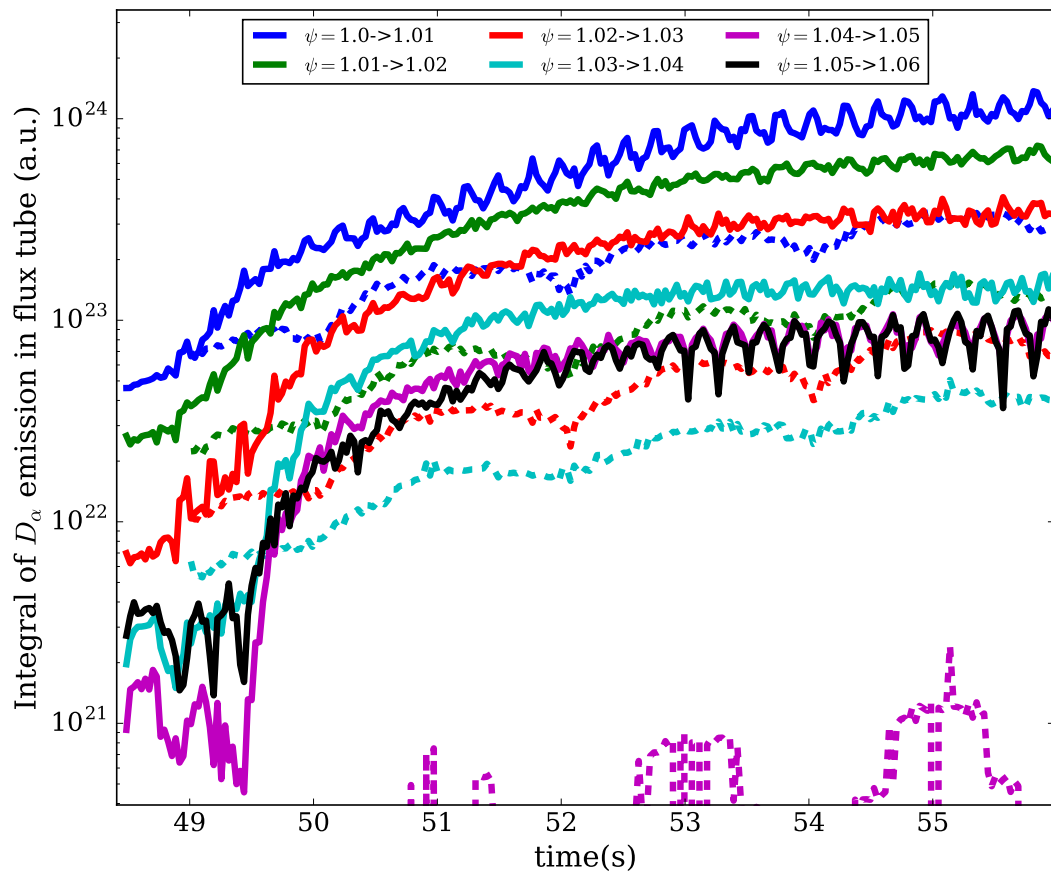


Figure 6.14: Time traces of 2D D_α emission profiles integrated in flux tubes of widths specified in the legend. The horizontal target (solid lines) and vertical target (dashed lines) are from pulses JPN89346 and JPN89355 respectively.

Chapter 7

Conclusions and future work

This thesis has experimentally investigated the quantity and nature of the radial transport in the main chamber SOL, and the physics governing it. Dedicated experiments have been performed on the JET-ILW which were designed to test potential control mechanisms. Broadly, these can be thought of in four areas, two upstream in the main chamber and two downstream in the divertor region, and are shown in table 7.1.

	Mechanism	Conclusion drawn for (✓) or against (✗)	Chapter
1	Main chamber SOL ionisation	✗	6
2	Core plasma properties ($\bar{n}_e, I_p \dots$)	✓	4
3	Parallel resistance or collisionality (Λ_{div})	✗	5
4	Plasma-neutral interaction of the fuel species in the divertor	✓	6

Table 7.1: A summary of the potential mechanisms that may influence main chamber radial transport and whether the results presented in this thesis support or contest a given mechanism. Relevant chapters are also given for reference.

For each of these mechanisms, their respective conclusions, limitations on these conclusions and potential for future work is considered.

1. Main chamber SOL ionisation

Local fuelling of the density profile through ionisation in the main chamber SOL was found not to be the dominant mechanism in the formation of flattened density profiles. This conclusion was drawn when comparing the density and ionisation profiles in L-mode fuelling ramps in horizontal and vertical target configurations. The density profile flattened with increasing D₂ fuelling rate in the horizontal configuration, but not in the vertical. Comparatively, the ionisation rate was *higher* in the vertical target. Were the positive feedback loop hypothesis of ionisation driving down the mean free path true, then the local ionisation rate would be sufficient to predict the state of the density profile. The results presented indicate otherwise.

Given that separate studies draw similar conclusions on the role of *main chamber* ionisation, pursuit of this mechanism may yield little return on understanding of the SOL transport in the context of other mechanisms which show more potential.

2. Core plasma properties

Unsurprisingly the magnitude of the cross field particle flux density increased with increasing \bar{n}_e , although perhaps more notable was the linear dependence. Regarding the measurement of the cross field transport, the particle continuity method, outlined in section 3.6, has significant uncertainty (factor three) due to the model assumptions and measurement uncertainties and also fails to capture the expected trend of the transport with I_p . Consequently, the method cannot be used to further improve the predictions of ion fluxes to main chamber surfaces in future fusion devices; more first principals and time resolved approaches should be taken to understand the governing physics.

Although the effect of different the ion-gyroradii at different $|B|$ cannot be discounted, $J_{sat} \propto \Gamma_{\perp,lim} \propto f_{gw}/I_p$ across a wide range of plasma conditions in L-mode. Regarding filament properties, the expected duration time was found to scale linearly with I_p . No general dependence with increasing \bar{n}_e was found. These results motivate further experiments and studies with varying safety factors to determine the relative roles of I_p and B_t . Investigating these effects in H-mode is also an open line of enquiry.

3. Parallel resistance or collisionality (Λ_{div})

A key conclusion that may be drawn from the results presented in this thesis is that the parallel collisionality in the SOL, quantified by Λ_{div} or otherwise, is *not* the general control parameter of the main chamber cross field transport. This conclusion runs against the conventional understanding of the electrical resistances inside the filament governing its motion and similarly that electrical disconnection of filaments from the target enhances radial transport upstream. The conclusion made here is however supported by other recent experimental studies, namely [115] and [117], and also 3D simulations of filaments [116]. Further testing of Λ_{div} , and more generally the collisionality, should not be central to the design of future experiments seeking to explore the effect of the divertor conditions on main chamber radial transport. The use of N as the divertor impurity may not be extensible to ITER which may use Ne or potentially other elements. The most ITER relevant impurities should be used to confirm the generality of this result, with emphasis on H-mode.

4. Plasma-neutral interaction of the fuel species in the divertor

Although the exact mechanism is not understood, the plasma-neutral interaction of the fuel species in the divertor was found to play a significant role in setting cross field particle flux density. Decoupling changes in \bar{n}_e and the downstream divertor neutral density was achieved by sweeping the strike point across the target thus modulating the quantity of neutrals removed via pumping. In the most extreme case, sweeping between horizontal and corner configuration modulated the upstream transport by around a factor five as measured by the limiter probe. The upstream density profiles were also strongly affected by the strike point modulation, the sweeping essentially acting as a switch for the presence of the shoulder. The comparison between the horizontal and vertical target are consistent, the results essentially being the same except in steady state. The effect of the sweeping on upstream transport also extended to H-modes. The D_α measurements used to draw these conclusions are a rather blunt measure of the plasma neutral interaction in the divertor.

Nevertheless, the conclusions drawn motivate further experiments. Discharges analysed in this thesis were not specifically designed around testing the plasma-neutral interaction in the divertor region. For example the original purpose of the strike point sweeping was to fully resolve the divertor profiles for calculating Λ_{div} . There are many options that could be explored in terms of new experiment design. Some preliminary ideas for JET are as follows. Performing slow sweeps from the horizontal up to the vertical target, potentially pausing at certain locations for periods of 1s in order to collect steady state Langmuir probe data. This experiment may potentially aid the explanation of the observed hysteresis in the large amplitude sweep presented in section 6.2.2, and also allow for the response time of the sub-divertor neutral pressure which may be ~ 1 s. Direct modulation of the pumping rate is also a simple experiment, if possible to perform. Modulating the gas puffing rate, may be a simpler alternative. From the perspective of future fusion devices, extending experiments to H-mode is also vital.

Appendix 1 - High frequency Li-beam measurements

In addition to the 100Hz measurements of the density profile, made using the spectrometer, an APD camera also measures the beam emission at the higher rate of 500kHz, referred to the the Fast Li-Beam (FLB). However, as will be detailed in this appendix, deficiencies with the diagnostic prevented data being incorporated into the analysis presented in this thesis.

Firstly, 50Hz oscillations dominated the signal fluctuations, shown in the Fourier spectrum in figure 1. These were caused by the electrical power supply being too close to Li ion beam. 40Hz oscillations were also present, the origins of which are unknown. A high pass filter, with cut-off frequency 100Hz, was used to filter out these signal. Although these oscillations detract from the quality of the data they do not prevent further analysis.

The signal to noise ratio of the FLB was low, being ~ 1 in the far SOL, rising up to ~ 5 near the separatrix. Figures 2 and 3 demonstrate the dominance of the photon noise. In figure 2, normalised PDFs of a Li-beam channel, which maps to the far SOL, and from the limiter probe are compared over the same time window (54-56s JPN89344). The PDF of the FLB does not rescale to match that of the limiter probe. Other channels farther into the SOL also do not rescale. Consequently, intermittent events cannot be reliably extracted from the data set.

The low cross-correlation values in (a) and (c) in figure 3, with (b) being an auto-correlation, also suggest photon noise dominates the signal. Despite the relatively low amplitudes, cross-correlating to the reference channel and linearly fitting the peaks by introducing the channel viewing location, a cross correlation velocity, v_{cc} , is obtained.

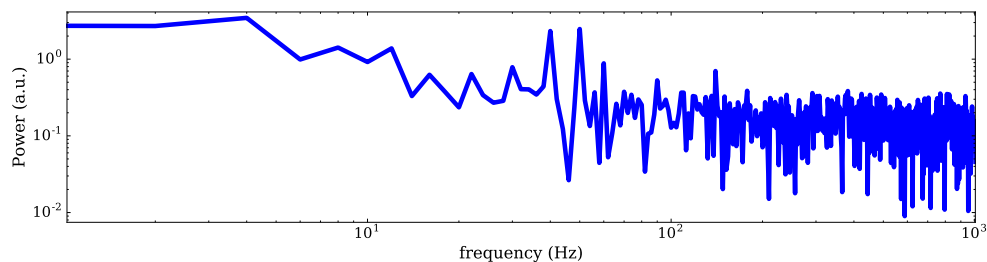


Figure 1: Comparison of scaled PDFs from the outer limiter probe (OLP) and fast Li-beam diagnostic.

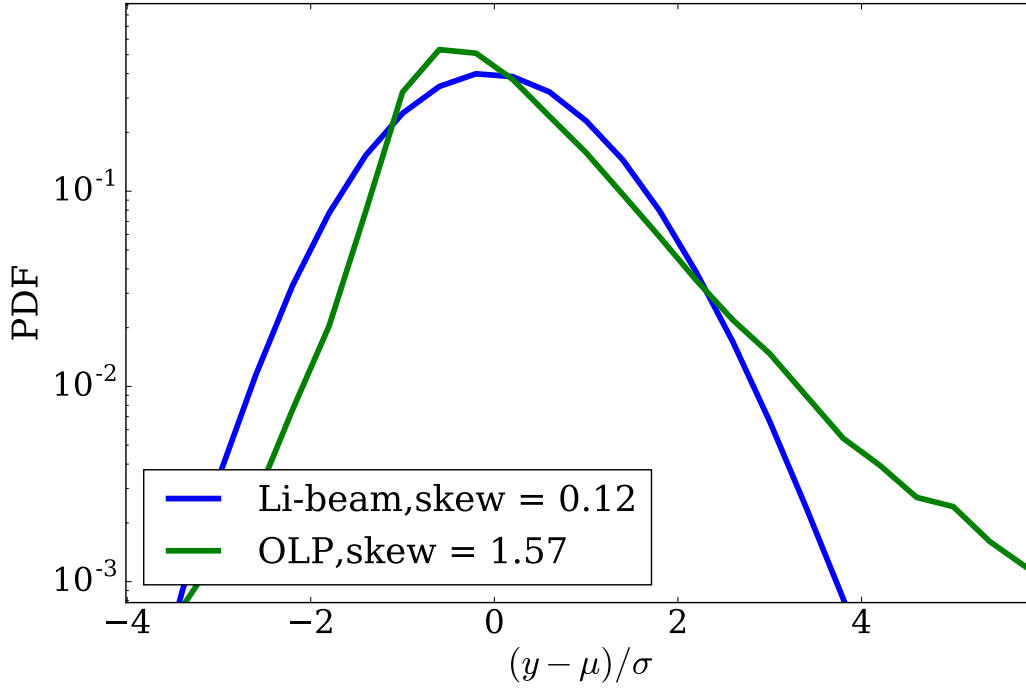


Figure 2: Comparison of scaled PDFs from the outer limiter probe (OLP) and fast Li-beam diagnostic.

An example is shown in figure 4. The value of v_{cc} is somewhat lower than those obtained in other studies, such as [132], but in the same order of magnitude.

Efforts are underway to improve the FLB for the forthcoming JET campaign and if successful will provide a wealth of information for the study of SOL transport.

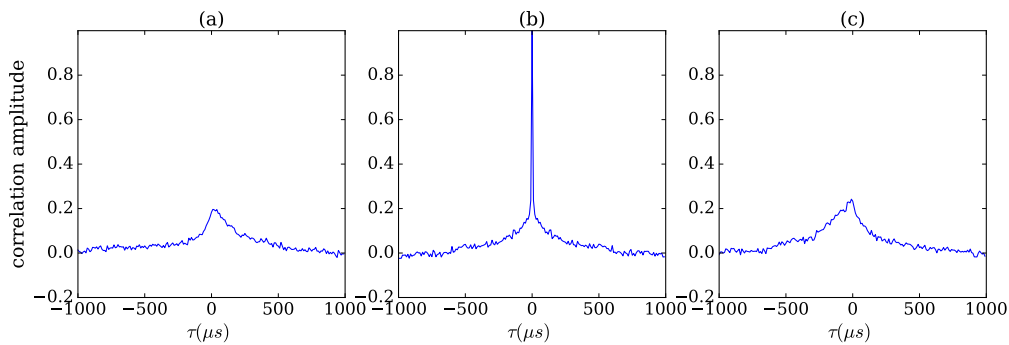


Figure 3: Correlations of three adjacent channels, which map to the flattened region of the density profile, of the high frequency Li-beam diagnostic. Cross-correlations are shown in (a) and (c) are, where as (b) is a an auto-correlation.

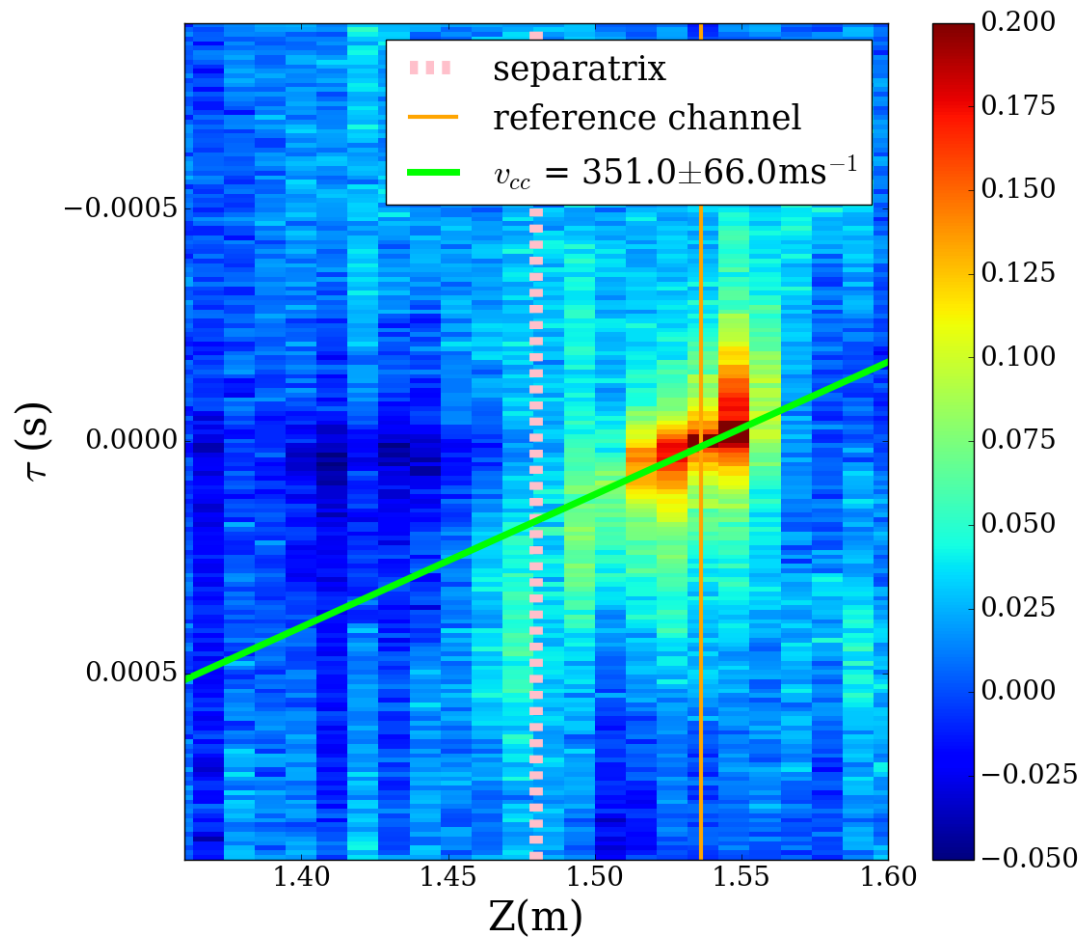


Figure 4: Cross-correlations of high frequency Li-beam diagnostic with a chosen reference channel (the same as figure 3), indicated by the orange vertical line. The colour scale give the correlation amplitude.

Bibliography

- [1] World bank energy consumption data. <http://data.worldbank.org/indicator>. Accessed: 17-3-2017.
- [2] United nations world population projections. <https://esa.un.org/unpd/wpp/>. Accessed: 17-3-2017.
- [3] Mikael Höök and Xu Tang. Depletion of fossil fuels and anthropogenic climate change - a review. *Energy Policy*, 52:797–809, 2013.
- [4] Ipcc report, 2013. <http://www.ipcc.ch/report/ar5/wg1/>. Accessed: 17-3-2017.
- [5] Ipcc sea level changes, 2013. https://www.ipcc.ch/pdf/assessment-report/ar5/wg1/WG1AR5_Chapter13_FINAL.pdf. Accessed: 17-3-2017.
- [6] Shahriar Shafiee and Erkan Topal. When will fossil fuel reserves be diminished? *Energy policy*, 37(1):181–189, 2009.
- [7] Clean energy’s dirty secret. wind and solar power are disrupting electricity systems. <https://tinyurl.com/jenjph2>. Accessed: 17-3-2017.
- [8] Bridging the gap: Do fast reacting fossil technologies facilitate renewable energy diffusion? <http://www.nber.org/papers/w22454.pdf>. Accessed: 17-3-2017.
- [9] Duncan Brack. Woody biomass for power and heat impacts on the global climate. 2017.
- [10] Sebastiaan Luyssaert, E-Detlef Schulze, Annett Börner, Alexander Knohl, Dominik Hessenmöller, Beverly E Law, Philippe Ciais, and John Grace. Old-growth forests as global carbon sinks. *Nature*, 455(7210):213–215, 2008.
- [11] Hinckley point c, electricity strike price. <https://www.theguardian.com/uk-news/2016/sep/15/hinkley-point-c-guide-uk-first-new-nuclear-plant-for-20-years>. Accessed: 17-3-2017.
- [12] Jessica R Lovering, Arthur Yip, and Ted Nordhaus. Historical construction costs of global nuclear power reactors. *Energy Policy*, 91:371–382, 2016.

- [13] Iaea uranium reserves estimate. <https://www.iaea.org/OurWork/ST/NE/NEFW/Technical-Areas/NFC/uranium-production-cycle-redbook.html>. Accessed: 17-3-2017.
- [14] Chancellor george osborne's spending review and autumn statement 2015 speech. <https://tinyurl.com/pfrygs9>. Accessed: 17-3-2017.
- [15] China starts building smr-based floating nuclear plant. <http://www.powermag.com/china-starts-building-smr-based-floating-nuclear-plant/>. Accessed: 17-3-2017.
- [16] Arthur S Eddington. The internal constitution of the stars. *The Scientific Monthly*, pages 297–303, 1920.
- [17] Hans Albrecht Bethe. Energy production in stars. *Physical Review*, 55(5):434, 1939.
- [18] Archie A Harms, Donald R Kingdon, KF Schoepf, and George H Miley. *Principles of fusion energy: an introduction to fusion energy for students of science and engineering*. World Scientific Publishing Co Inc, 2000.
- [19] John Wesson and DJ Campbell. *Tokamaks*, volume 149. Oxford University Press, 2011.
- [20] Sustainable energy without the hot air. <https://www.withouthotair.com/>. Accessed: 17-3-2017.
- [21] MR Gilbert and J-Ch Sublet. Neutron-induced transmutation effects in w and w-alloys in a fusion environment. *Nuclear Fusion*, 51(4):043005, 2011.
- [22] Some criteria for a useful thermonuclear reactor. <https://www.euro-fusion.org/wp-content/uploads/2012/10/dec05-aere-gpr1807.pdf>. Accessed: 17-3-2017.
- [23] Some criteria for a useful thermonuclear reactor. <https://www.euro-fusion.org/glossary/triple-product/>. Accessed: 17-3-2017.
- [24] George H Miller, Edward I Moses, and Craig R Wuest. The national ignition facility. *Optical Engineering*, 43(12):2841–2853, 2004.
- [25] OA Hurricane, DA Callahan, DT Casey, PM Celliers, Charles Cerjan, EL Dewald, TR Dittrich, T Döppner, DE Hinkel, LF Berzak Hopkins, et al. Fuel gain exceeding unity in an inertially confined fusion implosion. *Nature*, 506(7488):343–348, 2014.
- [26] Tokamak principle. <https://www.euro-fusion.org/2011/09/tokamak-principle-2/>. Accessed: 17-3-2017.

- [27] G Gibson, WC Jordan, EJ Lauer, and CH Woods. Guiding center motion and plasma behavior in the bumpy torus. *The Physics of Fluids*, 7(4):548–556, 1964.
- [28] F. Wagner, G. Becker, K. Behringer, D. Campbell, A. Eberhagen, W. Engelhardt, G. Fussmann, O. Gehre, J. Gernhardt, G. v. Gierke, G. Haas, M. Huang, F. Karger, M. Keilhacker, O. Klüber, M. Kornherr, K. Lackner, G. Lisitano, G. G. Lister, H. M. Mayer, D. Meisel, E. R. Müller, H. Murmann, H. Niedermeyer, W. Poschenrieder, H. Rapp, H. Röhr, F. Schneider, G. Siller, E. Speth, A. Stäbler, K. H. Steuer, G. Venus, O. Vollmer, and Z. Yü. Regime of improved confinement and high beta in neutral-beam-heated divertor discharges of the asdex tokamak. *Phys. Rev. Lett.*, 49:1408–1412, Nov 1982.
- [29] HR Wilson, PB Snyder, GTA Huysmans, and RL Miller. Numerical studies of edge localized instabilities in tokamaks. *Physics of Plasmas*, 9(4):1277–1286, 2002.
- [30] PB Snyder, HR Wilson, JR Ferron, LL Lao, AW Leonard, TH Osborne, AD Turnbull, D Mossessian, M Murakami, and XQ Xu. Edge localized modes and the pedestal: a model based on coupled peeling–ballooning modes. *Physics of Plasmas*, 9(5):2037–2043, 2002.
- [31] TE Evans, ME Fenstermacher, RA Moyer, TH Osborne, JG Watkins, P Gohil, I Joseph, MJ Schaffer, Larry R Baylor, M Becoulet, et al. Rmp elm suppression in diiii-d plasmas with iter similar shapes and collisionalities. *Nuclear fusion*, 48(2):024002, 2008.
- [32] KH Burrell, ME Austin, DP Brennan, JC DeBoo, EJ Doyle, P Gohil, CM Greenfield, RJ Groebner, LL Lao, TC Luce, et al. Quiescent h-mode plasmas in the diiii-d tokamak. *Plasma Physics and Controlled Fusion*, 44(5A):A253, 2002.
- [33] DG Whyte, AE Hubbard, JW Hughes, B Lipschultz, JE Rice, ES Marmor, M Greenwald, I Cziegler, A Dominguez, T Golfopoulos, et al. I-mode: an h-mode energy confinement regime with l-mode particle transport in alcator c-mod. *Nuclear Fusion*, 50(10):105005, 2010.
- [34] H-S Bosch, RC Wolf, T Andreeva, J Baldzuhn, D Birus, T Bluhm, T Bräuer, H Braune, V Bykov, A Cardella, et al. Technical challenges in the construction of the steady-state stellarator wendelstein 7-x. *Nuclear Fusion*, 53(12):126001, 2013.
- [35] T Sunn Pedersen, M Otte, S Lazerson, P Helander, S Bozhnikov, C Biedermann, T Klinger, RC Wolf, H-S Bosch, The Wendelstein, et al. Confirmation of the topology of the wendelstein 7-x magnetic field to better than 1: 100,000. *Nature Communications*, 7, 2016.

- [36] Efd: A roadmap to the realisation of fusion energy. <https://www.euro-fusion.org/wpcms/wp-content/uploads/2013/01/JG12.356-web.pdf>. Accessed: 17-3-2017.
- [37] GF Matthews, M Beurskens, S Brezinsek, M Groth, E Joffrin, A Loving, M Kear, ML Mayoral, R Neu, P Prior, et al. Jet iter-like wall - overview and experimental programme. *Physica Scripta*, 2011(T145):014001, 2011.
- [38] A Gibson. Deuterium–tritium plasmas in the joint european torus (jet): Behavior and implications. *Physics of Plasmas*, 5(5):1839–1847, 1998.
- [39] RJ Hawryluk, DJ Campbell, G Janeschitz, PR Thomas, R Albanese, R Ambrosino, C Bachmann, L Baylor, M Becoulet, I Benfatto, et al. Principal physics developments evaluated in the iter design review. *Nuclear Fusion*, 49(6):065012, 2009.
- [40] RA Pitts, S Carpentier, F Escourbiac, T Hirai, V Komarov, S Lisgo, AS Kukushkin, A Loarte, M Merola, A Sashala Naik, et al. A full tungsten divertor for iter: physics issues and design status. *Journal of Nuclear Materials*, 438:S48–S56, 2013.
- [41] The iter project. <https://www.iter.org/proj/inafewlines>. Accessed: 17-3-2017.
- [42] P. Stangeby. *The plasma boundary of magnetic fusion devices*. Institute of Physics Pub., 1 edition, 2000.
- [43] Thomas Eich, AW Leonard, RA Pitts, W Fundamenski, RJ Goldston, TK Gray, A Herrmann, A Kirk, A Kallenbach, O Kardaun, et al. Scaling of the tokamak near the scrape-off layer h-mode power width and implications for iter. *Nuclear fusion*, 53(9):093031, 2013.
- [44] RA Pitts, A Kukushkin, A Loarte, A Martin, M Merola, CE Kessel, V Komarov, and M Shimada. Status and physics basis of the iter divertor. *Physica Scripta*, 2009(T138):014001, 2009.
- [45] JP Gunn, S Carpentier-Chouchana, F Escourbiac, T Hirai, S Panayotis, RA Pitts, Y Corre, R Dejarnac, M Firdaouss, M Kocan, et al. Surface heat loads on the iter divertor vertical targets. *Nuclear Fusion*, 57(4):046025, 2017.
- [46] DHJ Goodall. High speed cine film studies of plasma behaviour and plasma surface interactions in tokamaks. *Journal of Nuclear Materials*, 111:11–22, 1982.
- [47] SJ Zweben. Search for coherent structure within tokamak plasma turbulence. *The Physics of fluids*, 28(3):974–982, 1985.

- [48] MV Umansky, SI Krasheninnikov, B LaBombard, and JL Terry. Comments on particle and energy balance in the edge plasma of alcator c-mod. *Physics of Plasmas*, 5(9):3373–3376, 1998.
- [49] B Lipschultz, D Whyte, and Brian LaBombard. Comparison of particle transport in the scrape-off layer plasmas of alcator c-mod and diiii-d. *Plasma physics and controlled fusion*, 47(10):1559, 2005.
- [50] AE Jaervinen, S Brezinsek, C Giroud, M Groth, C Guillemaut, P Belo, M Brix, G Corrigan, P Drewelow, D Harting, et al. Impact of divertor geometry on radiative divertor performance in jet h-mode plasmas. *Plasma Physics and Controlled Fusion*, 58(4):045011, 2016.
- [51] N Ben Ayed, A Kirk, B Dudson, S Tallents, RGL Vann, HR Wilson, et al. Inter-elm filaments and turbulent transport in the mega-amp spherical tokamak. *Plasma Physics and Controlled Fusion*, 51(3):035016, 2009.
- [52] BD Dudson, N Ben Ayed, A Kirk, HR Wilson, G Counsell, X Xu, M Umansky, PB Snyder, B Lloyd, et al. Experiments and simulation of edge turbulence and filaments in mast. *Plasma Physics and Controlled Fusion*, 50(12):124012, 2008.
- [53] DA D’Ippolito, JR Myra, and SJ Zweben. Convective transport by intermittent blob-filaments: Comparison of theory and experiment. *Physics of Plasmas*, 18(6):060501, 2011.
- [54] GS Xu, Volker Naulin, W Fundamenski, C Hidalgo, JA Alonso, C Silva, B Goncalves, Anders Henry Nielsen, J Juul Rasmussen, SI Krasheninnikov, et al. Blob/hole formation and zonal-flow generation in the edge plasma of the jet tokamak. *Nuclear Fusion*, 49(9):092002, 2009.
- [55] Odd Erik Garcia, J Horacek, RA Pitts, Anders Henry Nielsen, W Fundamenski, Volker Naulin, and J Juul Rasmussen. Fluctuations and transport in the tcv scrape-off layer. *Nuclear fusion*, 47(7):667, 2007.
- [56] Y Hamada, T Watari, A Nishizawa, K Narihara, Y Kawasumi, T Ido, M Kojima, K Toi, et al. Streamers in the jipp t-llu tokamak plasmas. *Physical review letters*, 96(11):115003, 2006.
- [57] I Nanobashvili, P Devynck, JP Gunn, S Nanobashvili, J Stöckel, and G Van Oost. Comparative analysis of intermittent burst temporal characteristics at the edge of the castor and tore supra tokamaks. *Physics of Plasmas*, 16(2):022309, 2009.
- [58] T Yamada, S-I Itoh, S Inagaki, Y Nagashima, N Kasuya, K Kamataki, H Arakawa, T Kobayashi, M Yagi, A Fujisawa, et al. Observation of quasi-two-dimensional nonlinear interactions in a drift-wave streamer. *Physical review letters*, 105(22):225002, 2010.

- [59] Ph Ghendrih, Y Sarazin, G Attuel, S Benkadda, P Beyer, G Falchetto, C Figarella, X Garbet, V Grandgirard, and M Ottaviani. Theoretical analysis of the influence of external biasing on long range turbulent transport in the scrape-off layer. *Nuclear fusion*, 43(10):1013, 2003.
- [60] JR Myra, DA D'Ippolito, DP Stotler, SJ Zweben, BP LeBlanc, JE Menard, RJ Maqueda, and J Boedo. Blob birth and transport in the tokamak edge plasma: Analysis of imaging data. *Physics of plasmas*, 13(9):092509, 2006.
- [61] JP Graves, J Horacek, RA Pitts, and KI Hopcraft. Self-similar density turbulence in the tcv tokamak scrape-off layer. *Plasma physics and controlled fusion*, 47(3):L1, 2005.
- [62] JA Boedo, JR Myra, S Zweben, R Maingi, RJ Maqueda, VA Soukhanovskii, JW Ahn, J Canik, N Crocker, DA D'Ippolito, et al. Edge transport studies in the edge and scrape-off layer of the national spherical torus experiment with langmuir probes. *Physics of Plasmas*, 21(4):042309, 2014.
- [63] Ghassan Y Antar, Glenn Counsell, Yang Yu, Brian Labombard, and Pascal Devynck. Universality of intermittent convective transport in the scrape-off layer of magnetically confined devices. *Physics of Plasmas*, 10(2):419–428, 2003.
- [64] J Ernest Wilkins. A note on skewness and kurtosis. *The Annals of Mathematical Statistics*, 15(3):333–335, 1944.
- [65] Istvan Cziegler. *Turbulence and Transport Phenomena in Edge and Scrape-Off-Layer Plasmas*. PhD thesis, Massachusetts Institute of Technology, 2011.
- [66] Noam Katz, Jan Egedal, Will Fox, Ari Le, and Miklos Porkolab. Experiments on the propagation of plasma filaments. *Physical review letters*, 101(1):015003, 2008.
- [67] SH Müller, Ahmed Diallo, Ambrogio Fasoli, Ivo Furno, Benoît Labit, and Mario Podesta. Plasma blobs in a basic toroidal experiment: Origin, dynamics, and induced transport. *Physics of plasmas*, 14(11):110704, 2007.
- [68] C Theiler, I Furno, P Ricci, A Fasoli, B Labit, SH Müller, and G Plyushchev. Cross-field motion of plasma blobs in an open magnetic field line configuration. *Physical review letters*, 103(6):065001, 2009.
- [69] OE Garcia, J Horacek, and RA Pitts. Intermittent fluctuations in the tcv scrape-off layer. *Nuclear Fusion*, 55(6):062002, 2015.
- [70] Odd Erik Garcia, RA Pitts, J Horacek, Jens Madsen, Volker Naulin, Anders Henry Nielsen, and J Juul Rasmussen. Collisionality dependent transport in tcv sol plasmas. *Plasma Physics and Controlled Fusion*, 49(12B):B47, 2007.

- [71] NR Walkden, A Wynn, F Militello, B Lipschultz, G Matthews, C Guillemaut, J Harrison, D Moulton, and JET Contributors. Statistical analysis of the ion flux to the jet outer wall. *Nuclear Fusion*, 57(3):036016, 2017.
- [72] Luke Easy, Fulvio Militello, John Omotani, NR Walkden, and Benjamin Dudson. Investigation of the effect of resistivity on scrape off layer filaments using three-dimensional simulations. *Physics of Plasmas*, 23(1):012512, 2016.
- [73] SI Krasheninnikov, DD Ryutov, and Guanghui Yu. Large plasma pressure perturbations and radial convective transport in a tokamak. *J. Plasma Fusion Res.(Japan)*, 6:139–143, 2004.
- [74] SI Krasheninnikov, DA D’ippolito, and JR Myra. Recent theoretical progress in understanding coherent structures in edge and sol turbulence. *Journal of Plasma Physics*, 74(5):679, 2008.
- [75] JR Myra, DA Russell, and DA D’Ippolito. Collisionality and magnetic geometry effects on tokamak edge turbulent transport. i. a two-region model with application to blobs. *Physics of plasmas*, 13(11):112502, 2006.
- [76] B LaBombard, RL Boivin, M Greenwald, J Hughes, B Lipschultz, D Mossessian, CS Pitcher, JL Terry, and SJ Zweben. Particle transport in the scrape-off layer and its relationship to discharge density limit in alcator c-mod. *Physics of Plasmas*, 8(5):2107–2117, 2001.
- [77] B Lipschultz, B LaBombard, CS Pitcher, and R Boivin. Investigation of the origin of neutrals in the main chamber of alcator c-mod. *Plasma physics and controlled fusion*, 44(6):733, 2002.
- [78] Brian Labombard, JW Hughes, N Smick, A Graf, K Marr, R McDermott, M Reinke, M Greenwald, B Lipschultz, JL Terry, et al. Critical gradients and plasma flows in the edge plasma of alcator c-mod a. *Physics of Plasmas*, 15(5):056106, 2008.
- [79] Martin Greenwald, JL Terry, SM Wolfe, S Ejima, MG Bell, SM Kaye, and GH Neilson. A new look at density limits in tokamaks. *Nuclear Fusion*, 28(12):2199, 1988.
- [80] D Carralero, P Manz, L Aho-Mantila, G Birkenmeier, M Brix, M Groth, HW M’uller, U Stroth, N Vianello, E Wolfrum, et al. Experimental validation of a filament transport model in turbulent magnetized plasmas. *Physical review letters*, 115(21):215002, 2015.
- [81] B LaBombard, MV Umansky, RL Boivin, JA Goetz, J Hughes, B Lipschultz, D Mossessian, CS Pitcher, JL Terry, et al. Cross-field plasma transport and main-chamber recycling in diverted plasmas on alcator c-mod. *Nuclear Fusion*, 40(12):2041, 2000.

- [82] B LaBombard, JW Hughes, D Mossessian, M Greenwald, B Lipschultz, JL Terry, Alcator C-Mod Team, et al. Evidence for electromagnetic fluid drift turbulence controlling the edge plasma state in the alcator c-mod tokamak. *Nuclear fusion*, 45(12):1658, 2005.
- [83] S Brezinsek, G Sergienko, A Pospieszczyk, Ph Mertens, U Samm, and PT Greenland. Characterization of the deuterium recycling flux in front of a graphite surface in the textor tokamak. *Plasma physics and controlled fusion*, 47(4):615, 2005.
- [84] Bruce Lipschultz, Felix I Parra, and Ian H Hutchinson. Sensitivity of detachment extent to magnetic configuration and external parameters. *Nuclear Fusion*, 56(5):056007, 2016.
- [85] C Guillemaut, M Lennholm, J Harrison, I Carvalho, D Valcarcel, R Felton, S Griph, C Hogben, R Lucock, GF Matthews, et al. Real-time control of divertor detachment in h-mode with impurity seeding using langmuir probe feedback in jet-iter-like wall. *Plasma Physics and Controlled Fusion*, 59(4):045001, 2017.
- [86] Charles Spencer Pitcher and PC Stangeby. Experimental divertor physics. *Plasma Physics and Controlled Fusion*, 39(6):779, 1997.
- [87] Alberto Loarte. Effects of divertor geometry on tokamak plasmas. *Plasma Physics and Controlled Fusion*, 43(6):R183, 2001.
- [88] K McCormick, S Fiedler, G Kocsis, J Schweinzer, and S Zoletnik. Edge density measurements with a fast li beam probe in tokamak and stellarator experiments. *Fusion Engineering and Design*, 34:125–134, 1997.
- [89] M Brix, A Korotkov, M Lehnen, P Morgan, K McCormick, J Schweinzer, D Summers, J Vince, and JET EFDA Contributors. Determination of edge density profiles in jet using a 50 kv lithium beam. In *Proc. 28th Conf. on Control. Fusion Plasma Phys. (Madeira) Europhys. Conf. Abstracts A*, volume 25, page 389, 2001.
- [90] J Schweinzer, E Wolfrum, F Aumayr, M Pockl, H Winter, RP Schorn, E Hintz, and A Unterreiter. Reconstruction of plasma edge density profiles from li i (2s-2p) emission profiles. *Plasma physics and controlled fusion*, 34(7):1173, 1992.
- [91] ZA Pietrzyk, P Breger, and DDR Summers. Deconvolution of electron density from lithium beam emission profiles in high edge density plasmas. *Plasma physics and controlled fusion*, 35(12):1725, 1993.
- [92] Mathias Brix, D Dodt, D Dunai, I Lupelli, S Marsen, TF Melson, B Meszaros, P Morgan, G Petravich, DI Refy, et al. Recent improvements of the jet lithium beam diagnostic a. *Review of Scientific Instruments*, 83(10):10D533, 2012.

- [93] F Militello, L Garzotti, J Harrison, JT Omotani, R Scannell, S Allan, A Kirk, I Lupelli, AJ Thornton, et al. Characterisation of the l-mode scrape off layer in mast: decay lengths. *Nuclear Fusion*, 56(1):016006, 2015.
- [94] DL Rudakov, JA Boedo, RA Moyer, Peter C Stangeby, JG Watkins, DG Whyte, L Zeng, NH Brooks, RP Doerner, TE Evans, et al. Far sol transport and main wall plasma interaction in diii-d. *Nuclear fusion*, 45(12):1589, 2005.
- [95] DG Whyte, BL Lipschultz, PC Stangeby, J Boedo, DL Rudakov, JG Watkins, and WP West. The magnitude of plasma flux to the main-wall in the diii-d tokamak. *Plasma physics and controlled fusion*, 47(10):1579, 2005.
- [96] A Huber, S Brezinsek, Ph Mertens, B Schweer, G Sergienko, A Terra, G Arnoux, N Balshaw, M Clever, T Edlingdon, et al. Development of a mirror-based endoscope for divertor spectroscopy on jet with the new iter-like wall (invited) a. *Review of scientific instruments*, 83(10):10D511, 2012.
- [97] Theodore M Biewer, C Belcher, I Hassall, DL Hillis, G Kaveney, D Scharpf, MF Stamp, C Stunell, K-D Zastrow, and JET-EFDA Contributors. Implementation of an in-vessel calibration light source for jet a. *Review of Scientific Instruments*, 83(10):10D505, 2012.
- [98] D Brown. Decentering distortion of lenses. *Photogrammetric Engineering*, 32(3):444.
- [99] AE Conrady. Lens-systems, decentered. *Monthly notices of the royal astronomical society*, 79:384–390, 1919.
- [100] calcam, image calibration software. <https://github.com/euratom-software/calcam>. Accessed: 25-2-2018.
- [101] LL Lao, H St John, RD Stambaugh, AG Kellman, and W Pfeiffer. Reconstruction of current profile parameters and plasma shapes in tokamaks. *Nuclear fusion*, 25(11):1611, 1985.
- [102] Kl11 image inversion software. <https://git.ccfе.ac.uk/jrh/kl11>. Accessed: 17-3-2017.
- [103] Open-adas database. <http://open.adas.ac.uk/adf13>. Accessed: 17-3-2017.
- [104] B Lipschultz. A study of jet sol radial transport based on particle balance. In *European Physical Society Conference on Contributions to Fusion and Plasma Physics, St. Petersburg 2003*, pages P–3.197.
- [105] OE Garcia. Stochastic modeling of intermittent scrape-off layer plasma fluctuations. *Physical review letters*, 108(26):265001, 2012.

- [106] Ralph Kube and Odd Erik Garcia. Convergence of statistical moments of particle density time series in scrape-off layer plasmas. *Physics of Plasmas*, 22(1):012502, 2015.
- [107] Odd Erik Garcia, RA Pitts, J Horacek, AH Nielsen, W Fundamenski, JP Graves, V Naulin, and J Juul Rasmussen. Turbulent transport in the tcv sol. *Journal of Nuclear Materials*, 363:575–580, 2007.
- [108] JP Gunn. The influence of magnetization strength on the sheath: Implications for flush-mounted probes. *Physics of Plasmas*, 4(12):4435–4446, 1997.
- [109] A Kirk, AJ Thornton, JR Harrison, F Militello, NR Walkden, MAST Team, EUROfusion MST1 Team, et al. L-mode filament characteristics on mast as a function of plasma current measured using visible imaging. *Plasma Physics and Controlled Fusion*, 58(8):085008, 2016.
- [110] B LaBombard, JA Goetz, I Hutchinson, D Jablonski, J Kesner, C Kurz, B Lipschultz, GM McCracken, A Niemczewski, J Terry, et al. Experimental investigation of transport phenomena in the scrape-off layer and divertor. *Journal of Nuclear Materials*, 241:149–166, 1997.
- [111] JW Connor, GF Counsell, SK Erents, SJ Fielding, B LaBombard, and K Morel. Comparison of theoretical models for scrape-off layer widths with data from compass-d, jet and alcator c-mod. *Nuclear fusion*, 39(2):169, 1999.
- [112] GF Counsell, JW Connor, SK Erents, AR Field, SJ Fielding, B La Bombard, and KM Morel. Sol width scaling from consideration of edge transport in tokamaks. *Journal of nuclear materials*, 266:91–98, 1999.
- [113] K McCormick, N Asakura, S Bosch, S Davies, S Fielding, K Itami, H Kawashima, B LaBombard, B Lipschultz, A Loarte, et al. Iter edge database investigations of the sol width. *Journal of nuclear materials*, 266:99–108, 1999.
- [114] SK Erents and PC Stangeby. Heat transport in the jet scrape-off layer. *Nuclear fusion*, 38(11):1637, 1998.
- [115] N. Vianello, C. Tsui, C. Theiler, S. Allan, J. Boedo, B. Labit, H. Reimerdes, K. Verhaegh, W.A.J. Vijvers, N. Walkden, S. Costea, J. Kovacic, C. Ionita, V. Naulin, A.H. Nielsen, J. Juul Rasmussen, B. Schneider, R. Schrittwieser, M. Spolaore, D. Carralero, J. Madsen, B. Lipschultz, F. Militello, The TCV Team, and The EUROfusion MST1 Team. Modification of sol profiles and fluctuations with line-average density and divertor flux expansion in tcv. *Nuclear Fusion*, 57(11):116014, 2017.
- [116] Luke Easy. *Three Dimensional Simulations of Scrape-Off Layer Filaments*. PhD thesis, University of York, 2016.

- [117] D Carralero, M Siccino, M Komm, SA Artene, FA D’Isa, J Adamek, L Aho-Mantila, G Birkenmeier, M Brix, G Fuchert, et al. Recent progress towards a quantitative description of filamentary sol transport. *Nuclear Fusion*, 57(5):056044, 2017.
- [118] D Carralero, HW Müller, M Groth, M Komm, Jiri Adamek, G Birkenmeier, M Brix, F Janky, P Hacek, S Marsen, et al. Implications of high density operation on sol transport: a multimachine investigation. *Journal of Nuclear Materials*, 463:123–127, 2015.
- [119] D Carralero, G Birkenmeier, HW Müller, P Manz, SH Müller, F Reimold, U Stroth, M Wischmeier, E Wolfrum, et al. An experimental investigation of the high density transition of the scrape-off layer transport in asdex upgrade. *Nuclear Fusion*, 54(12):123005, 2014.
- [120] D Carralero, J Madsen, SA Artene, M Bernert, G Birkenmeier, T Eich, G Fuchert, F Laggner, V Naulin, P Manz, et al. A study on the density shoulder formation in the sol of h-mode plasmas. *Nuclear Materials and Energy*, 2016.
- [121] *Proc 16th International Conf. Plasma Physics and Controlled Fusion Research, Montreal, Canada*, volume 1 of *FI-CN-640A4-5*. IAEA, 1996.
- [122] B Lipschultz, B LaBombard, JL Terry, C Boswell, and IH Hutchinson. Divertor physics research on alcator c-mod. *Fusion science and technology*, 51(3):369–389, 2007.
- [123] PIH Cooke and AK Prinja. An analytic model for flow reversal in divertor plasmas. *Nuclear fusion*, 27(7):1165, 1987.
- [124] Nobuyuki Asakura, ITPA SOL, and Divertor Topical Group. Understanding the sol flow in l-mode plasma on divertor tokamaks, and its influence on the plasma transport. *Journal of nuclear materials*, 363:41–51, 2007.
- [125] R Schneider, X Bonnin, K Borrass, DP Coster, H Kastelewicz, D Reiter, VA Rozhansky, and BJ Braams. Plasma edge physics with b2-eirene. *Contributions to Plasma Physics*, 46(1-2):3–191, 2006.
- [126] JA Boedo, GD Porter, MJ Schaffer, R Lehmer, RA Moyer, JG Watkins, TE Evans, CJ Lasnier, AW Leonard, and SL Allen. Flow reversal, convection, and modeling in the diii-d divertor. *Physics of Plasmas*, 5(12):4305–4310, 1998.
- [127] F Militello and JT Omotani. Scrape off layer profiles interpreted with filament dynamics. *Nuclear Fusion*, 56(10):104004, 2016.
- [128] F Militello and JT Omotani. On the relation between non-exponential scrape off layer profiles and the dynamics of filaments. *Plasma Physics and Controlled Fusion*, 58(12):125004, 2016.

- [129] N R Walkden, A Wynn, F Militello, B Lipschultz, G Matthews, C Guillemaut, J Harrison, D Moulton, and JET Contributors. Interpretation of scrape-off layer profile evolution and first-wall ion flux statistics on jet using a stochastic framework based on filamentary motion. *Plasma Physics and Controlled Fusion*, 59(8):085009, 2017.
- [130] GF Matthews, SK Erents, G Corrigan, W Fundamenski, I Garcia-Cortes, J Mailoux, C Hidalgo, MA Pedrosa, V Pericoli, J Spence, et al. The effect of cd4 puffing on the peripheral scrape-off layer in jet. *Plasma physics and controlled fusion*, 44(6):689, 2002.
- [131] PC Stangeby. Modeling plasma contact with the main vessel walls of a divertor tokamak. *Physics of Plasmas*, 9(8):3489–3507, 2002.
- [132] M Agostini, JL Terry, P Scarin, and SJ Zweben. Edge turbulence in different density regimes in alcator c-mod experiment. *Nuclear Fusion*, 51(5):053020, 2011.